

Sheffield Hallam University

Mesh-free methods for liquid crystal simulation.

YAKUTOVICH, Mikhail.

Available from the Sheffield Hallam University Research Archive (SHURA) at:

<http://shura.shu.ac.uk/20580/>

A Sheffield Hallam University thesis

This thesis is protected by copyright which belongs to the author.

The content must not be changed in any way or sold commercially in any format or medium without the formal permission of the author.

When referring to this work, full bibliographic details including the author, title, awarding institution and date of the thesis must be given.

Please visit <http://shura.shu.ac.uk/20580/> and <http://shura.shu.ac.uk/information.html> for further details about copyright and re-use permissions.

Sheffield S1 1WB

26081

101 923 047 9



Sheffield Hallam University
Learning and IT Services
Adsetts Centre City Campus
Sheffield S1 1WB

REFERENCE

ProQuest Number: 10701227

All rights reserved

INFORMATION TO ALL USERS

The quality of this reproduction is dependent upon the quality of the copy submitted.

In the unlikely event that the author did not send a complete manuscript and there are missing pages, these will be noted. Also, if material had to be removed, a note will indicate the deletion.



ProQuest 10701227

Published by ProQuest LLC (2017). Copyright of the Dissertation is held by the Author.

All rights reserved.

This work is protected against unauthorized copying under Title 17, United States Code
Microform Edition © ProQuest LLC.

ProQuest LLC.
789 East Eisenhower Parkway
P.O. Box 1346
Ann Arbor, MI 48106 – 1346

Mesh-Free Methods for Liquid Crystal Simulation

Mikhail Yakutovich

A thesis submitted in partial fulfilment of the requirements of
Sheffield Hallam University
for the degree of Doctor of Philosophy

May 2009

Abstract

The key aim of this Thesis is the development and implementation of a set of simulation techniques for LCs capable of tackling mesoscopic phenomena. In this, we concentrate only on mesh-free particle numerical techniques. Two broad approaches are used, namely bottom-up and top-down.

While adopting the bottom-up approach, we employ the DPD method as a foundation for devising a novel LC simulation technique. In this, we associate a traceless symmetric order tensor, Q , with each DPD particle. We then further extend the DPD forces to directly incorporate the Q tensor description so as to recover a more complete representation of LC behaviour. The devised model is verified against a number of qualitative examples and applied to the simulation of colloidal particles immersed in a nematic LC. We also discuss advantages of the developed model for simulation of dynamic mesoscopic LC phenomena.

In the top-down approach, we utilise recently emergent numerical mesh-free methods. Specifically, we use the SPH method and its variants. The developed method includes hydrodynamics, variable order parameter and external electric and magnetic fields. The developed technique is validated against a number of analytical and numerical solutions.

Subsequently, we apply our top-down methods to the simulation of the complex 3D post-aligned bistable nematic (PABN) device. This includes a smooth geometry representation in order to fully exploit the developed mesh-free numerical techniques. We study both the static and dynamic behaviours of the PABN device for a number of distinct post shapes.

Моим родителям посвящается¹

¹To my parents

Acknowledgements

First of all I would like to express my sincere gratitude to my supervisors, Dr D.J. Cleaver and Prof C.M. Care, for their constant support and guidance throughout this project. All the time they provided me with clear explanations, important advice and lots of good ideas, without which I would have been lost. I would also like to thank Dr I. Halliday, Dr T.J. Spencer, Dr C.J.P. Newton and colleagues from Hewlett-Packard for their useful comments and advice.

I am grateful to David, Christina, Anna and Sergey who, from the very beginning, helped me to acclimatise in Sheffield and then made it such a great place to study. Many thanks to all colleagues from Sheffield Hallam University with whom I spent last three years or so. So thanks to Laurence, Fatima, Candy, Adam, Stephen, Vin, Alena, Alex and Pavel. I would also like to thank an endless stream of my friends who made Sheffield such an enjoyable place to stay. So thank you to Will, Lee, Olesya, Sasha, Juri, Dima, Sveta, Viktor and Iryna Yarmolenko, Masha, Maksim, Antonia, Paul, Taras, Gena, Artem, Viktor Nikitin, Nastya Sheiko, Nastya Dontsova, Irchik and many others.

Last but not least, I wish to say big thank you to my family. To my Babushka, for her love and great empathy. To my sister Lena and her husband Viktor, for their love and encouragement. And, to my parents, for their love, understanding and support, without which I would have not achieved all that I have – I dedicate this Thesis to them.

Advanced Studies

The following is a chronological list of related postgraduate work undertaken and meetings attended during the course of study:

- “DL POLY Training Day”, Sheffield University (April 2006).
- “Applied Numerical Algorithms” course, Edinburgh Parallel Computing Centre (June 2006).
- CCP5 Summer School 2006 “Methods in Molecular Simulation”, Cardiff University (July 2006).
- Graduate Training Assistant Workshops, Sheffield Hallam University (November 2006 – February 2007).
- MERI Research Methods module, Sheffield Hallam University (February 2007).
- Advanced Measurement Techniques training module, MERI, Sheffield Hallam University (March 2007).
- “Mainz Materials Simulation Days”, Mainz, Germany (June 2007). Poster presentation “Smoothed dissipative particle nemato dynamics: from atomistic to application scale”.
- MERI 2nd Year Student Seminar Day, Sheffield Hallam University (20th June 2007). Oral presentation “Mesh free simulation of liquid crystals using modified smoothed particle hydrodynamics”
- 9th European Conference on Liquid Crystals, Lisbon, Portugal (July 2007). Poster presentation “Smoothed dissipative particle nemato dynamics: from atomistic to application scale”.
- CCP5 Annual General Meeting 2007 “Multiscale Modelling: simulation methods and applications spanning time and length scales”, Cambridge. Poster

presentation “Smoothed dissipative particle nemato dynamics: from atomistic to application scale”.

- Computer Modelling Seminar at Sheffield University (November 2007). Invited talk “Smoothed dissipative particle nemato dynamics: from continuum to mesoscale”.
- ‘Liquid Crystal Micro- and Nano-Composites’ meeting, Manchester (9th January 2008). Poster presentation “Smoothed dissipative particle nemato dynamics: from atomistic to application scale”.
- “Bistable displays: technologies & application” conference, Hewlett Packard Laboratories, Bristol (25th June 2008).
- “Dissipative Particle Dynamics” CECAM workshop, Lausanne, Switzerland (July 2008). Poster presentation “Smoothed dissipative particle nemato dynamics: from atomistic to application scale”.
- “Liquid Crystals for Photonics” workshop, Cambridge (July 2008). Oral presentation “Mesh free simulation of liquid crystals using modified smoothed particle hydrodynamics”.
- 23rd BLCS Conference 2009, Hewlett Packard Laboratories, Bristol (April 2009). Oral presentation “Studying bistability in liquid crystal devices with complex 3-D topologies using mesh-free methods”.

Publications

This thesis contains some work published in the following journals:

- M. V. Yakutovich, C. J. P. Newton, and D. J. Cleaver. Mesh-Free Simulation of Complex LCD Geometries. *Molecular Crystals and Liquid Crystals*, 502:1, 245–257, 2009.
- M. V. Yakutovich, C. M. Care and D. J. Cleaver. Mesh-free modelling of liquid crystals using modified smoothed particle hydrodynamics. Submitted to PRE.

Contents

List of Acronyms	xi
1 Introduction	1
1.1 Aims & Objectives	2
1.2 Thesis Structure	2
1.3 Liquid Crystals	3
1.3.1 The Fundamentals of Liquid Crystals	3
1.3.2 Physical Properties of Liquid Crystals	6
1.3.3 Computer Simulation of Liquid Crystals	8
1.3.4 Liquid Crystal Displays	11
1.4 Bistability	13
1.4.1 Zenithal Bistable Device (ZBD)	14
1.4.2 Post Aligned Bistable Nematic (PABN)	15
1.5 Basics of Mesh-free Methods	15
1.5.1 Mesh-free Particle Methods	16
1.5.2 Consistency, Completeness and Reproducing Conditions	16
2 Landau-de Gennes Theory of Liquid Crystals	19
2.1 Introduction	19
2.1.1 The Nematic Order Parameter	19
2.1.2 The Biaxiality	20
2.1.3 The Tensor Order Parameter Q	22
2.1.4 The Nematic-Isotropic Phase Transition	23
2.2 Static Theory of Liquid Crystals	26
2.2.1 Elasticity	26
2.2.2 Electric and Magnetic Fields	27
2.2.3 Flexoelectricity	29
2.2.4 Boundary Conditions and Anchoring	30
2.2.5 The Equilibrium States	31

2.2.6	Defects	33
2.3	Dynamic Theory of Liquid Crystals	34
2.3.1	Dynamic Equations	37
3	Mesoscopic Mesh-free Particle Techniques	39
3.1	Introduction	39
3.2	Dissipative Particle Dynamics	40
3.2.1	DPD Formalism	41
3.2.2	Equilibrium Properties	43
3.2.3	Hydrodynamics	45
3.2.4	Fluid Particle Model	50
3.2.5	DPD Drawbacks	53
3.3	Smoothed Particle Hydrodynamics	55
3.3.1	SPH Formalism	55
3.3.2	SPH Conservation Law Equations	59
3.3.3	SPH Artificial Viscosity	60
3.3.4	Completeness of the SPH	62
3.3.5	SPH Drawbacks and Improvements	64
3.3.6	Corrective Smoothed Particle Method	67
3.3.7	Modified Smoothed Particle Hydrodynamics	68
3.4	Smoothed Dissipative Particle Dynamics	70
3.5	Other Mesoscopic Mesh-free Particle Techniques	72
3.5.1	Direct Simulation Monte Carlo	72
3.5.2	Stochastic Rotational Dynamics	74
4	Implementation of Bottom-up Approaches	76
4.1	Practical Aspects in DPD/FPM Implementation	76
4.1.1	Reduced Units	77
4.1.2	Periodic Boundary Conditions / Minimum Image Convention	78
4.1.3	Integrators	79
4.1.4	Quaternions	80
4.1.5	Verlet Neighbour List	82
4.1.6	Calculation of Observables	83
4.2	DPD/FPM Testing and Verification	85
4.3	Extending DPD for the Simulation of Liquid Crystals	90
4.3.1	Incorporation of a Q-tensor into DPD Formalism	92
4.3.2	Extending Conservative Forces	93
4.3.3	Fokker-Planck Equation and Equilibrium State	94

4.3.4	Extending the Thermostat Forces	96
4.4	Simulation Results	98
4.4.1	Recovering the Isotropic-Nematic Phase Transition	98
4.4.2	Diffusion Coefficients	98
4.4.3	Simulation of Colloidal Particles Immersed in LCs	99
4.5	Discussion	101
4.6	Conclusions and Future Work	103
5	Implementation of Top-down Approaches	104
5.1	Revising the Governing Equations	104
5.2	Description of the Algorithm	106
5.3	Major Practical Implementation Aspects	108
5.3.1	Boundary Conditions	108
5.3.2	Time Integration Scheme	109
5.3.3	Smoothing Length	110
5.3.4	Smoothing Kernel	111
5.3.5	Reduced Units	112
5.4	Implementation Details For Individual Methods	112
5.4.1	Smoothed Particle Hydrodynamics	112
5.4.2	Modified Smoothed Particle Hydrodynamics	113
5.5	Electric Field Solvers	114
5.6	SPH Simulation Attempts	117
5.7	MSPH Testing and Verification	121
5.7.1	Equilibrium Phase Behaviour	121
5.7.2	Fréedericksz Transition	122
5.7.3	Transverse Flow Effect	124
5.7.4	Fast Switching Dual-Frequency Chiral HAN Cell	126
5.8	Conclusions	129
6	Modelling of the PABN Device	130
6.1	Overview of PABN Operation	130
6.1.1	Experimental Studies	130
6.1.2	Theoretical and Simulation Studies	132
6.2	Post Geometry Representation	133
6.2.1	Geometry Model	133
6.2.2	Geometry Discretisation	135
6.2.3	Implementation Details	139
6.3	Static Configurations	140

6.3.1	Tilted State \mathcal{T}	142
6.3.2	Planar State \mathcal{P}_1	142
6.4	Studying Effects of the Post Topography	145
6.4.1	Circular Posts	145
6.4.2	Effect of the Post Smoothness	146
6.4.3	Effect of the Post Height	148
6.5	Switching Behaviour	150
6.5.1	$\mathcal{T} - \mathcal{P}$ Transition	151
6.5.2	$\mathcal{P} - \mathcal{T}$ Transition	153
6.6	Conclusions	153
7	Conclusions and Further Work	156
7.1	Conclusions and Discussions	156
7.2	Further Work	158
A	Moving Least Squares Shape Functions	160
	Bibliography	163

List of Acronyms

CSPM	Corrective smoothed particle method
DPD	Dissipative particle dynamics
DSMC	Direct simulation Monte Carlo
ELP	Ericksen-Leslie-Parodi theory
FDM	Finite-difference method
FEM	Finite-elements method
FPE	Fokker-Planck equation
FPM	Fluid particle model
GCMC	Grand Canonical Monte Carlo
HAN	Hybrid-aligned nematic
LB	Lattice Boltzmann
LC	Liquid crystal
LCD	Liquid crystal display
LJ	Lennard-Jones
MC	Monte Carlo
MD	Molecular dynamics
MSPH	Modified smoothed particle hydrodynamics
PABN	Post-aligned bistable nematic
SDPD	Smoothed dissipative particle dynamics
SPH	Smoothed particle hydrodynamics
SRD	Stochastic rotational dynamics
ZBD	Zenithal bistable device

Chapter 1

Introduction

Liquid crystals (LC) are fascinating materials which combine the usual properties of conventional fluids with an inherent orientational ordering. This leads to LCs exhibiting a range of anisotropic properties, which give them a marked technological significance. LCs have found applications in many areas of physical and biological science and engineering, such as in liquid crystal displays (LCDs), optoelectronic devices, sensors, commercial detergents (soap), biological self-assembly of micelles etc.

Some aspects of LC behaviour have been well-studied since they were first discovered in 1890. In theoretical studies, computer modelling plays an important part in aiding understanding of many processes on atomistic and mesoscopic levels. It also certainly helps with explaining and predicting behaviour of LC devices on continuum length-scales. For example, the multi-billion pound LCD industry has motivated the development of LC solvers based on Ericksen-Leslie-Parodi continuum theory. However, there are still some important gaps in our understanding of the physics behind LCs. This is due, in part, to the complex interplay of distinct physical phenomena on different time- and length-scales in these systems, e.g. inter-molecule interactions, orientational order, continuum velocity field etc are all coupled. This makes it impossible to fully study LCs with only one chosen simulation technique.

Thus, nowadays the predominant issue in the computer modelling of materials and, particularly, of LCs, is the problem of bridging the length- and time-scales between the underlying molecular motions and the consequent application-scale behaviour. A wide range of techniques have been developed to address this amongst which may be included accelerated molecular dynamics (MD) methods, Brownian dynamics, dissipative particle dynamics (DPD), Lattice Boltzmann (LB), smoothed particle hydrodynamics (SPH) and a suite of methods which combine elements of

these approaches. While it is unlikely that a single unified framework will be emergent from this multiplicity of developments, a common approach is to develop “overlap” methods which allow a particular coarse grained method to be parameterised using a finer grained method. Given this broad context, the work presented in this Thesis can be viewed as an attempt to identify and fill gaps in the current spectrum of LC modelling approaches.

1.1 Aims & Objectives

This Thesis mainly deals with the development of novel mesoscopic simulation techniques for simulating LCs. This direction was primarily determined at the start of this project, when the following objectives were set:

- to determine which mesoscopic simulation techniques can be applied to simulation of LCs, both from bottom-up and top-down points of view, in order to bridge the gaps between existing simulation methodologies.
- to consider bottom-up approach simulation techniques and to determine if a comprehensive link with the atomistic level can be established.
- to consider top-down simulation techniques and to investigate how thermal noise can be incorporated into the model, so as to properly recover the mesoscopic behaviour.
- to determine how these models compare to conventional numerical techniques in terms of computational requirements.
- to investigate if the developed simulation techniques are computationally viable and whether they can address LC phenomena which are non-achievable with the currently available simulation techniques.

1.2 Thesis Structure

The remainder of this Chapter is devoted to a brief introduction to LCs and LCDs. This is followed by a précis of the basics of mesh-free simulation methods.

In Chapter 2 we summarise the phenomenological continuum theory for the Landau-de Gennes order parameter. We then describe relevant LC properties using this theory and review the literature relating to the governing equations for both static and dynamic LC behaviours.

In Chapter 3 we give an overview of mesoscopic simulations using mesh-free particle techniques. We place a particular emphasis on dissipative particle dynamics (DPD) and smoothed particle hydrodynamics (SPH), the relevant specifics of which are considered in more detail.

In Chapter 4 we describe a novel LC simulation technique based on a bottom-up DPD approach. We first show how this novel approach can be tuned to yield anisotropic static and dynamic behaviour of LCs. We then apply this method to the demanding scenario of 3-D simulation of dynamic behaviour of colloidal particles immersed in a nematic LC.

In Chapter 5 we follow a top-down approach, in which we apply the modified smoothed particle hydrodynamics (MSPH) mesh-free numerical technique to the simulation of LCs. We first describe our unsuccessful attempts to model LCs with a number of simpler techniques, such as with SPH, corrective smoothed particle method (CSPM) and some of their variants. Then, we provide results obtained using our MSPH approach for a number of test cases so as to address the validity of the newly developed solver.

In Chapter 6 we present a study performed using our mesh-free simulation approach to investigate the statics and dynamics of the post-aligned bistable nematic (PABN) device. Here, we briefly describe the PABN device, our model geometry representation and the approach we use to discretise it. We then provide results obtained on static configurations for a number of different post geometries. Finally, we provide some results on the PABN device switching behaviour.

In Chapter 7 we conclude with a summary of this Thesis and suggest some ideas for future work. A bibliography is included.

1.3 Liquid Crystals

In this section we give a short introduction to the physics of liquid crystals (LCs), provide a brief overview of the available LC simulation techniques and describe the most common application of LCs in liquid crystal displays (LCDs).

1.3.1 The Fundamentals of Liquid Crystals

The term *liquid crystals* denotes materials which exhibit intermediate stages of order between liquid and crystalline phases. They were first discovered at the end of nineteenth century and, in a certain sense, can be considered as a fourth state of matter. The term LC consists of two parts, namely liquid, which specifies that the

matter possesses some fluidity, and crystal, which indicates the presence of long-range order in the system. In the crystalline solid state, the order is both positional and orientational, i.e. molecules occupy specific positions and their molecular axes are pointed in a certain direction. In a liquid phase, in contrast, there is no long-range order and the matter is fully isotropic. Molecules in LC phases, however, have orientational order and either no or only partial positional order. In almost all cases, these phases are only formed when molecules are anisotropic in shape – usually they are rod-like or disk-like. Most LC materials are organic compounds, and the classical example is *p*-azoxyanisole (PAA) shown in Fig. 1.1. From a steric point of view, this molecule is a rigid rod of length ~ 20 Å and width ~ 5 Å [1].

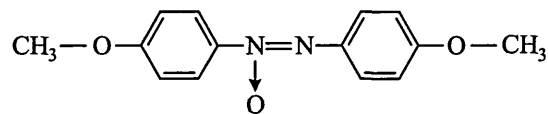


Figure 1.1: Formula of *p*-azoxyanisole.

LC phases are often called *mesophases* (from *mesomorphic* – of intermediate form), and, from the same root, their constituent molecules are called *mesogens*. This is a well-established nomenclature nowadays.

LCs can be divided in two classes, namely *thermotropic* and *lyotropic*. Thermotropic LCs are formed by mesogens in a certain range of temperatures $T_M < T < T_{IN}$, where T_M is the melting temperature of the crystalline phase and T_{IN} is the temperature of isotropic-nematic LC phase transition. The properties of thermotropic LCs are very dependant on temperature, and that is why they have *thermo-* in their name – it indicates the importance of thermal effects. Lyotropic LCs phases, however, form in solution (*lyo-* refers to concentration), and the concentration governs most of their properties. Below only thermotropic LCs are considered.

The main types of mesogen, as mentioned above, are rod-like, or *calamitic*, and disk-like, or *discotic*. Thermotropic mesophases can be subdivided into three classes (phases) which are nematic, smectic and chiral nematic (cholesteric) according to their molecular order, see Fig. 1.2.

The nematic phase is the simplest LC phase. Here, the molecules have no long-range positional order, just as in any normal liquid. However, they do possess long-range orientational order, unlike an isotropic liquid. In the nematic phase, the molecular axes tend to point along a preferred direction, called the *director*. This is usually denoted by a unit vector \mathbf{n} . The directions \mathbf{n} and $-\mathbf{n}$ are usually equivalent and indistinguishable. We can define the degree of this alignment using

the parameter S , which is called the *order parameter*. Thus,

$$S = \frac{1}{2} \langle 3 \cos^2 \gamma - 1 \rangle, \quad (1.1)$$

where γ is the angle which each long molecular axis makes with \mathbf{n} , and the angular brackets denote a statistical average. For perfect alignment $S = 1$, while for the random (isotropic) alignment $S = 0$. In thermotropic LCs $S = S(T)$, where T is the system's temperature. Usually, in real systems, S decreases as the temperature T is raised, and $0.3 < S < 0.8$. At the transition from the nematic to the isotropic phase at the temperature T_{IN} , S discontinuously jumps to zero, indicating a first order phase transition.

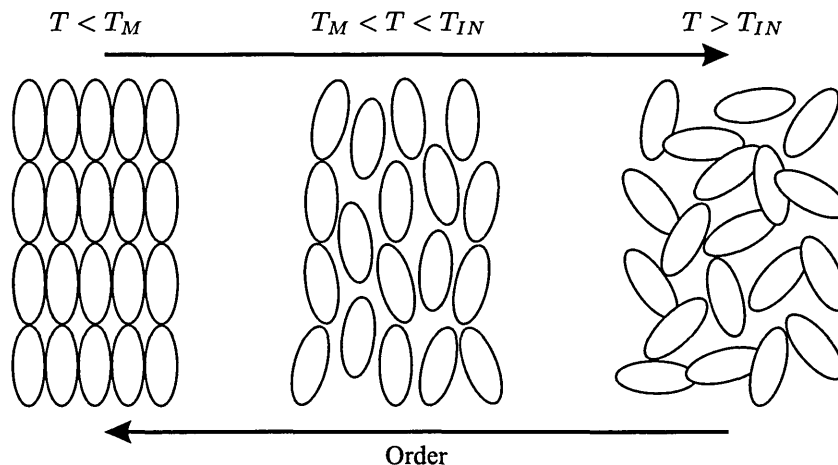


Figure 1.2: Two-dimensional sketch of solid, nematic LC and isotropic liquid phases.

Smectic phases are usually formed by rod-like molecules arranged in layers, so that in this phase there is one or two dimensional positional as well as orientational order. There are many types of smectic phase, the most common being smectic A, where the director is perpendicular to the layers, and smectic C, where the director makes an angle other than 90° with layers. The chiral nematic phase is similar to the nematic phase but has an additional property – the director has a spatial variation that leads to a helical structure. It should be noted that this relates to an average molecular orientation, but not to individual molecules. Both nematic and chiral nematic phases can also be formed by discotic molecules. Some substances may exhibit more than one mesophase as the temperature is varied in the $T_M < T < T_{IN}$ region, e.g. with increasing temperature a substance may change from a smectic to a nematic, and then finally to an isotropic liquid above T_{IN} .

1.3.2 Physical Properties of Liquid Crystals

The orientational ordering of a LC makes many of its properties anisotropic. This means that different physical parameters, such as the dielectric constant ϵ , refractive index n , viscosity η etc. have different values when measured in the directions parallel (\parallel) or perpendicular (\perp) to the director. Below we consider some of the most important anisotropic properties of LCs, and so illustrate what makes them such attractive materials to use in displays [2].

Birefringence

Birefringence is the anisotropy of the refractive index. LCs usually have two principal refractive indices. In uniaxial nematic LCs, for example, these are measured along (n_{\parallel}) and perpendicular (n_{\perp}) to the director and, thus, optical anisotropy is defined as $\Delta n = n_{\parallel} - n_{\perp}$. It is dependant on the temperature, since temperature directly influences the order parameter which, in turn, characterises the degree of anisotropy. Typical values of birefringence in LCs are ≈ 0.15 .

Dielectric Anisotropy

Dielectric anisotropy $\Delta\epsilon$ in LCs is defined as $\Delta\epsilon = \epsilon_{\parallel} - \epsilon_{\perp}$, where ϵ_{\parallel} and ϵ_{\perp} are, respectively, the relative dielectric permittivity parallel and perpendicular to the director. LC molecules with positive dielectric anisotropy align themselves along the field lines of applied external electric fields. LC molecules with negative dielectric anisotropy, on the other hand, align their axes perpendicular to such externally applied fields. In both cases, these effects are the same no matter what the sign of the applied fields is, positive or negative.

Dielectric anisotropy is a function of frequency. Usually, the dielectric constant ϵ_{\parallel} decreases with increased frequency [3] and ϵ_{\perp} varies little over large frequency ranges. Certain LCs exhibit both positive and negative dielectric anisotropies over a working frequency range. These are called dual frequency materials. Dielectric anisotropy is also a function of order parameter and, thus, temperature.

Elasticity

An unperturbed nematic LC sample always tries to align itself uniformly, so that the director has the same orientation everywhere. Different external influences, such as boundary conditions and various applied fields, can, however, distort the LC sample and create a spatial variation in the orientation of the LC director. There are three different principal distortions, which are splay, twist and bend. These are depicted in

Fig. 1.3. A common assumption is that the order parameter is constant throughout the sample. There are corresponding elastic constants K_{ii} associated with each type of distortion, which were first identified by Frank [4] in the context of his seminal continuum theory of LCs. These elastic constants are dependant on the temperature and on the order parameter.

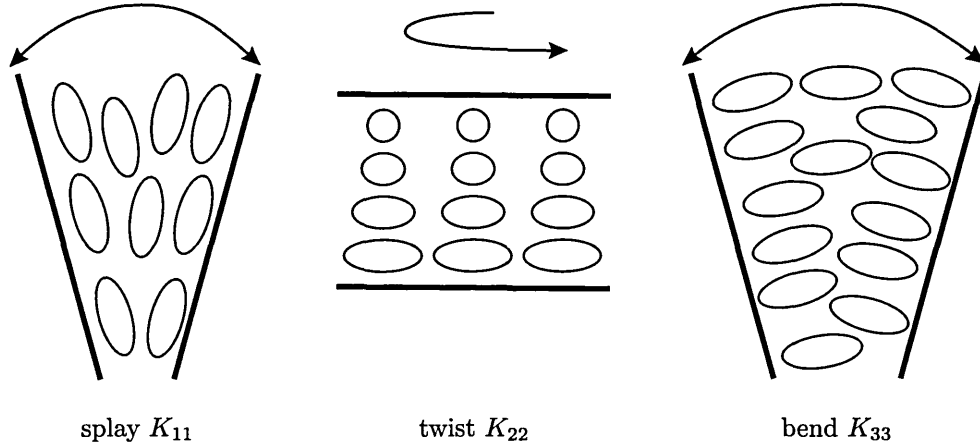


Figure 1.3: Sketch of splay, twist and bend elastic distortions.

Viscous Anisotropy

Viscosity is the measure of the fluid resistance to shear stress. It is an important parameter which should be taken into account when manufacturing devices involving any kind of LC switching. Experimentally, viscosity is commonly measured using a device which consists of two parallel plates, between which the studied material is placed. This is sketched in Fig. 1.4. The measured viscosity η then can be found as

$$\eta = \frac{F}{A \frac{dv}{dz}}, \quad (1.2)$$

where F is the force needed to be applied to the upper plate in order to impose the LC velocity gradient $\frac{dv}{dz}$ and A is the plates area.

If the director field of the LC sample is fixed (by an applied field) to lie in one of the x , y or z directions, then the force needed to move the upper plate in Fig. 1.4 is different for each case. Thus, there are three different viscosities which are called Miesowicz viscosities. In general, there are five independent LC viscosities, which are all dependant on temperature. The magnitude of these viscosities is of the same order as that of water.

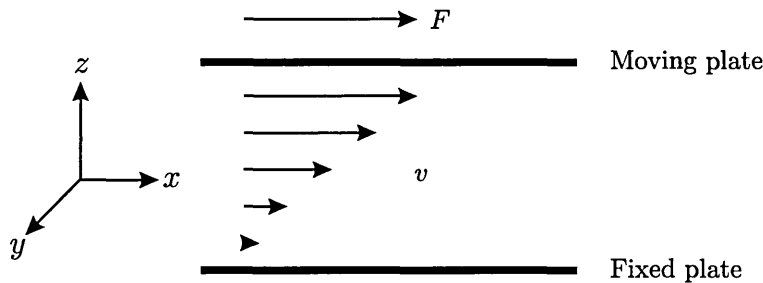


Figure 1.4: Sketch of the device for measuring viscosities.

1.3.3 Computer Simulation of Liquid Crystals

Computer simulations help to establish a two-way link between theory and experiment. Simulations are like virtual “experiments” which allow one to look inside matter at the level which is beyond the reach of real experiments. This allows system behaviour to be analysed more deeply and novel phases to be discovered, so broadening our understanding of the underlying processes and, potentially, opening up advances in both science and industrial applications. Depending on a problem’s time- and length-scales, totally different simulation techniques should be employed. We sketch this concept in Fig. 1.5, where we broadly classify all simulation techniques into three distinct categories: microscopic, mesoscopic and continuum. Below we briefly consider each of these categories separately.

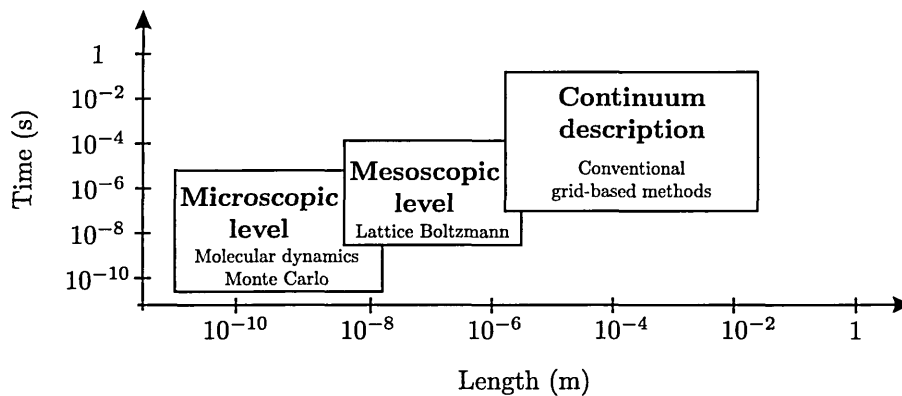


Figure 1.5: Broad categorisation of LC simulation techniques depending on their respective time- and length-scales.

LC Microscopic Simulation Techniques

Microscopic simulation of LCs is a particularly challenging task. Firstly, mesogens usually consist of a number of atoms and have a reasonably complex structure. Consequently, realistic atomistic simulations are very expensive. Secondly, many

LC phenomena occur on large length- and time-scales. For this reason, proper simulations of LCs were not achieved until the 1980s, at which point the computational power available became adequate to access these scales.

The two most popular simulation techniques at the microscopic level are molecular dynamics (MD) and Monte Carlo (MC). Largely, these yield essentially equivalent results, although MD allows one to simulate true non-equilibrium dynamic behaviour and MC can offer advantages in terms of better sampling of configurational space in situations where conventional MD is inefficient. These simulation methods can be applied to a number of different models. Here by model we mean the level of theoretical description used to define a given system. Below we consider only those models which are applicable to the simulation of LCs.

The models used in microscopic simulations of LCs can be classified into four different classes [5]: realistic atom-atom potential models, hard nonspherical models, soft nonspherical models and lattice models. The first of these is the most realistic but is also the most expensive – one needs to specify all atoms in every molecule and to use realistic atom-atom potentials. So in order to simulate only two molecules of PAA, depicted in Fig. 1.1, using a realistic model, at every time step $\mathcal{O}(10^3)$ interactions have to be calculated. In the hard particle model, by contrast, every particle has an infinitely repulsive core and contains no attractive forces. This core retrains the basic shape of the molecule (i.e. rod-like or disk-like), but neglects all chemical detail. Its simplicity makes this an attractive class of model for use in MC simulations. However, in real systems there are both repulsions and attractions between molecules; soft particle models have been therefore developed including both of these components. Finally, lattice models are different from the methods just described. Here, LCs are represented using classical spin vectors located on the sites of a cubic lattice. These spins are allowed to rotate and to interact with neighbouring particles via a given potential. Effects such as flow and density variations are usually ignored in small models, however.

LC Mesoscopic Simulation Techniques

Simulations of LCs in the mesoscopic regime are not yet achievable to the microscopic techniques just described, because they cannot access the higher orders of magnitude required for both the time- and length-scales. There are a number of mesoscopic simulation techniques available for simulations of fluids, such as dissipative particle dynamics (DPD) [6, 7], the lattice Boltzmann (LB) method [8], smoothed particle hydrodynamics (SPH) [9, 10] and others. Of these, the LB method is the only mesoscopic technique for which a concerted effort has been made to apply to simulations

of LCs [11, 12, 13]. In this, essentially a top-down approach has been adopted due to the high complexity of the task. This means that the developed LB techniques recover macroscopic equations, rather than allow these equations to emerge from some underlying mesoscopic behaviour. A proper development of a bottom-up approach is still missing.

Whereas LC simulation techniques in each of these three categories identified above still have some challenges to overcome, the mesoscopic regime seems to be the mostly underdeveloped. This partly stems from the fact that mesoscopic simulation techniques are not yet mature in their own right. For example, proper parametrisation of the DPD technique even for water simulations is not yet developed. A second reason arises due to the complexity of LC phenomena. The introduction of orientational degrees of freedom and the coupling of these to translation motion make it extremely difficult to develop appropriate mesoscopic behaviours and to prove that they recover the target continuum equations, i.e. to establish a bottom-up connection.

LC Continuum Simulation Techniques

For length-scales greater than $1\ \mu\text{m}$ and time-scales above $1\ \text{ms}$, which is the main region where device operations are studied, continuum equations for nematic LCs can be solved numerically. In this, there are two main steps. The first step is to choose the appropriate partial differential equations (PDEs) to solve and the second step is to apply a suitable numerical technique for their solution.

For many LC systems, it is reasonable to assume that the LC order parameter is constant. If this is the case, then the Ericksen-Leslie-Parodi formalism [1] is a relevant set of governing equations. However, if variations in ordering are important, such as in systems involving defects, then there are a number of alternative formalisms. In this context, the most commonly used sets of PDEs are those due to Qian and Sheng [14] and Beris and Edwards [15]. A recent paper by Sonnet [16] provides a framework against which different descriptions can be compared.

Once a target set of equations has been chosen, it can, in principle, then be solved using any conventional numerical technique. The most popular numerical techniques employed for this are the LB method, the finite-elements method (FEM) and the finite difference method (FDM). For example, a LB technique has been used to solve ELP equations [12], the meshless local Petrov-Galerkin method has been applied to solving the Q-tensor equations of nematostatics [17] and, more recently, a dynamic finite-element simulation has been applied to solve Landau-de Gennes theory of LCs with variable order parameter in 3D [18].

1.3.4 Liquid Crystal Displays

The optical properties of LCs, along with their orientational behaviour, makes them very popular for use in display devices. A number of advantages, e.g. low power consumption, light weight, thin form factor, full colour etc. have contributed to make liquid crystal displays (LCDs) the dominant technology in several markets. LCD technology is also in its early stages of development to achieve electronic paper. In this section we briefly outline the essential techniques used in the manufacturing of LCDs [2].

A typical LC display consists of a thin layer (1 to 10 μm) of a LC sandwiched between two plates, usually made of a glass. Different treatments are applied to glass plates in order to impose a preferred LC alignment. The plates are also coated with transparent electrodes by depositing indium tin oxide (ITO) on these via evaporation or sputtering techniques.

Twisted Nematic (TN) Display

Many different types of display exist. We consider the twisted nematic (TN) display [19] as an illustrative example. This was devised in the early 1970s but still remains the most commonly produced type of LCD. The arrangement of a typical TN cell is depicted in Fig. 1.6. Glass plates are treated so as to impose uniform planar orientation of the LC but these are arranged such that there is a 90° orientational twist between the opposite plates. This causes the polarisation of incident light to rotate by 90° when traversing the cell. As a result, if the cell is placed between crossed polarisers, light is still transmitted. When an external voltage is applied, however, all LC molecules align along it (assuming that the LC has a positive dielectric anisotropy, $\Delta\epsilon > 0$), as depicted in Fig. 1.6b. This state appears dark when the cell is located between cross-polarisers.

Display Addressing

Any LCD consists of hundreds of pixels, which need to be separately addressed. There are three main types of addressing used in real devices: direct addressing, passive addressing and active addressing.

The direct addressing approach is usually used in simple displays. In this, each pixel is directly connected to a controlling electronic device. A calculator display with seven pixels could be given as an example here. However, when the number of pixels grows this approach simply becomes very difficult and expensive to implement.

The next simplest common approach is to use a passive matrix, or multiplex,

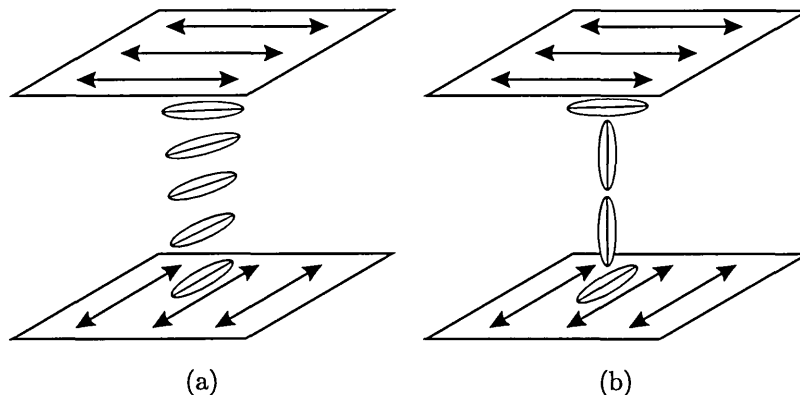


Figure 1.6: Twisted nematic cell with (a) no applied voltage and (b) an applied voltage.

addressing, which is schematically depicted in Fig. 1.7. In this, matrix of transparent conducting rows and columns interconnects all LCD pixels. In the switching process, a voltage $+V_r$ is applied sequentially to each row. Then, pixels in this row are switched in parallel by applying voltages $\pm V_c$ to the corresponding columns. The pixels are switched to “on” or “off” states depending on the total voltage applied, i.e. $V_r \pm V_c$. Thus, it is very important that pixels have some switching threshold value, otherwise the applied column voltages V_c would erroneously switch pixels in other rows. This approach is also limited by the fact that in an N row display, over a given time frame t , each pixel receives its full voltage over the time period $t_f = t/N$. In this class of multiplexed addressing, $M \times N$ pixels can be addressed using $M + N$ different lines.

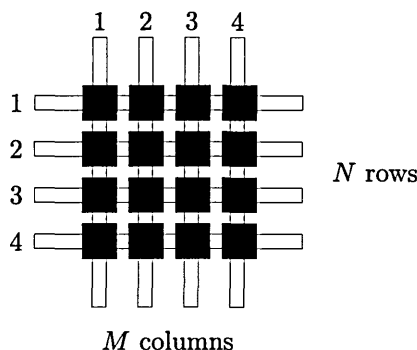


Figure 1.7: Sketch of the multiplex addressing in LCDs.

The major disadvantage of passive matrix technology is that as the number of rows, N , grows, the time t_f during which each pixel is addressed decreases. This reduces the difference between the “on” and “off” states and, as a result, decreases the display’s contrast ratio. This can be partially overcome by splitting the display into a number of separate regions, such that these regions are updated independently,

or by using the active addressing approach considered below.

A thin film transistor (TFT) is put next to every pixel in the active addressing technology. TFTs maintain the state of pixels and update them only when corresponding rows are being accessed. The voltage across each pixel is maintained by storage capacitors which are located next to each TFT. Thus, the manufacturing process needed for active addressing technology is much more complicated than that used to implement passive matrix technology, because an active transistor and a capacitor is required next to each pixel. Despite this, use of TFTs in commercial displays is widespread because they give high contrast ratios, fast switching times and high resolutions.

1.4 Bistability

Bistability is a property of a LC device by which the LC can reside in two or more distinct stable configurations under the same external conditions. Provided that these two stable LC configurations are optically distinct, e.g. form black and white in a bistable reflective display. There are two main benefits of bistability for display applications:

- *Reduced power consumption.* Bistable displays consume energy only when switching process occurs between two states and, consequently, do not use any energy to hold a static image. Conventional monostable displays require a constant power for their operation, but they usually require less energy for switching between optically distinct states. Thus, if a display device does not needed to be updated frequently, then there is a significant advantage in terms of power consumption in employing the bistability. This aspect is especially pertinent to mobile held devices, such as electronic book readers.
- *Unlimited multiplexing capabilities.* Bistable pixels do not require a continuously applied voltage over some threshold to retrain a static image. As a result, they can be used with cheaper passive matrix technologies which can potentially support an arbitrary number of rows. Thus, very high resolutions can be easily achieved, as compared to TN technology, where very complex active matrix addressing needs to be used.

A number of possible mechanisms to achieve bistability have been researched in recent years, exploiting both physical properties of LCs and/or non-trivial boundary conditions. One early work in this area [20] used evaporated SiO layers as boundary conditions which lead to bistability; a sign dependant applied voltage was used to

switch between states. Bistable twisted nematics [21] is another example, which has one state homogeneous and the other with a 360° twist; switching between these is achieved using voltages with different threshold values. Cholesteric LCD's [22] have two stable states, which are a planar twisted state and a state with a focal conic texture; switching between these is achieved by electric field pulses of different lengths.

Below we consider two of the relatively recent developments in this area, namely the zenithal bistable device (ZBD) and post aligned bistable nematic (PABN). These both employ complex alignment surfaces to achieve their bistability.

1.4.1 Zenithal Bistable Device (ZBD)

The zenithal bistable device (ZBD) uses an asymmetric grating on one of the cell's surfaces to obtain bistability [23]. A schematic illustration of the ZBD cell is depicted in Fig. 1.8. Here, both surfaces are treated so as to impose local homeotropic alignment. There are two stable states in the ZBD device, which are called the defect state (planar) and the continuous state (vertical). Depending on the pitch to groove ratio, the ZBD cell can be made to favour the planar state only, the vertical state only or both states bistably. The final case is the one used when producing devices.

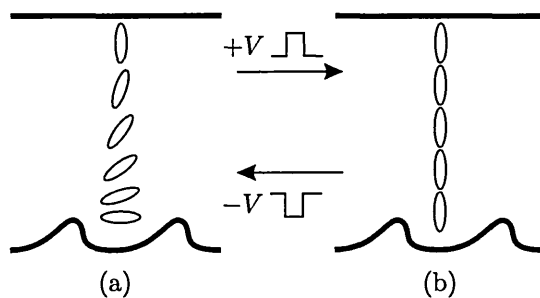


Figure 1.8: Sketch of ZBD stable configurations, (a) planar state (b) vertical state.

Switching between the two stable states of the ZBD is achieved using sign-dependant field pulses on LCs with positive dielectric anisotropy $\Delta\epsilon > 0$. The switching mechanism involves a non-trivial creation and annihilation of defects near to the grated surface. Defect dynamics in this processes is governed mainly by the flexoelectric coefficients and the dielectric constant, as was recently shown by 2D simulations which used theory of LCs with variable order parameter [11].

1.4.2 Post Aligned Bistable Nematic (PABN)

The post aligned bistable nematic (PABN) device [24] uses an array of 3-dimensional posts on one of the cell sides to achieve bistability. When posts are low, the system favors only planar configurations and when posts are high, only tilted states are stable. For some intermediate post heights, however, both states are stable.

Switching between the two stable states is achieved using sign-dependant pulses. In these, a LC with negative dielectric anisotropy is usually employed, $\Delta\epsilon < 0$. The driving mechanism behind the switching is not yet fully understood, although it is assumed that flexoelectricity is involved and that the switching process involves creation and annihilation of defects [18]. We describe our study of the PABN device operation in more detail in §6.

1.5 Basics of Mesh-free Methods

As their name suggests, the main idea behind mesh-free methods is that they do not rely on a grid. This is a big advantage over traditional grid-based methods since it fully eliminates the computational cost associated with mesh creation. In mesh-free methods, then, the spatial domain and its boundaries are represented by a set of scattered nodes without any specified intra-connectivity. As such, any confining geometry can be represented very accurately, even if the shape functions utilised within the mesh-free method are of low order.

Many types of mesh-free methods have been devised so far. The different classifications of these are set out in the extensive reviews which have been published in a number of books [25, 26]. Depending on the details of their formulation procedures, mesh-free methods can be classified into three categories: those based on weak-forms, those based on collocation techniques (also called strong form) and mesh-free particle methods.

Strong-form methods are usually easy to implement, computationally efficient and have the advantage that the procedure they use for discretising PDEs is straightforward. In these, the numerical error is minimised on the simulation points themselves. The biggest issue preventing collocation methods from becoming more popular is their inability to handle derivative boundary conditions. Another issue with strong-form methods is that they have a tendency to be unstable, especially when the final solution contains high-frequency modes.

In weak-form mesh-free methods, the error of solution is minimised in a certain region around the point, rather than on point itself as in strong-form methods.

This integral operation effectively smears out the numerical error, resulting in the discretised system being more accurate and stable. The only disadvantage of weak-form methods is their decreased computational efficiency, which arises due to the numerical integration procedure outlined above.

1.5.1 Mesh-free Particle Methods

Mesh-free particle methods (MPMs) can be seen as a certain sub-set of mesh-free methods, in which a finite set of particles is used to represent the state of a system [27]. These particles can represent some discrete physical objects (e.g., atoms) or they can represent parts of the continuum problem domain (e.g., when solving a PDE).

MPMs can be classified into three different categories based on length scales, which are atomistic, mesoscopic and macroscopic. Classical examples of atomistic MPMs are molecular dynamics and Monte Carlo methods, in which each particle typically represents an atom. Dissipative particle dynamics (DPD) [6, 7], direct simulation Monte Carlo (DSMC) [28, 29] etc. can be seen as examples of mesoscopic MPMs. Macroscopic MPMs include smoothed particle hydrodynamics (SPH) [9, 10], Particle-in-Cell [30], Reproducing kernel particle methods (RKPM) [31] and others.

There is also a second classification of MPMs based on the mathematical model employed. This divides MPMs into deterministic and probabilistic classes. Many MPMs are probabilistic in its nature, such as DSMC, DPD etc. In deterministic techniques, on the other hand, once all initial conditions have been set, the particle's position and properties at later simulation stages can be exactly predicted based on physical laws governing the system. Some MPMs can belong to both classes, such as SPH. SPH was originally presented as a probabilistic technique, but now it is widely used as a deterministic mesh-free particle method.

1.5.2 Consistency, Completeness and Reproducing Conditions

The following three terms are often used in the study of the convergence of numerical methods: consistency, completeness and reproducing conditions. The consistency condition is used in finite-difference methods, whereas the reproducing condition (or completeness) is used in Galerkin methods for convergence proofs [32]. In this section we state the definitions of these three conditions and define the ways in which we use them to analyse the completeness of mesh-free particle methods.

The consistency condition is used in the analysis of finite-difference approximations. It states that a scheme $L_h u = f$ is consistent (accurate) with the differential equation $Lu = f$ to order p , where u is any sufficiently smooth function, if $\|Lu - L_h u\| = O(h^p)$. In this definition, h is the distance between the nodes in the regular FDM grid. It is easy to see that the approximation error $\|Lu - L_h u\|$ goes to zero when $p > 0$ and $h \rightarrow 0$.

The consistency condition is difficult to apply to mesh-free methods, where there are no predefined connections between the randomly distributed nodes and the node spacing h is not clearly defined. Thus, the reproducing condition (or completeness) is usually used in the analysis of mesh-free methods.

The reproducing condition (or, alternatively, completeness) states that an approximation $u^h(x)$ is complete to order p if polynomials up to order p can be reproduced exactly. This can be illustrated by considering $u^h(x)$ as being approximated by a sum of certain basis functions, i.e.

$$u^h(x) = \sum_I \Phi_I(x) u_I, \quad (1.3)$$

where $\Phi_I(x)$ are basis functions and u_I are nodal values. If the values of u_I are set according to some polynomial of order p , then $u^h(x)$ should reproduce this polynomial exactly. For example, if in one dimension, the nodal values are given by the polynomial

$$u_I = a_0 + a_1 x_I + a_2 x_I^2 + \dots + a_p x_I^p, \quad (1.4)$$

then the reproducing condition of order p is met if

$$u^h(x) = \sum_I \Phi_I(x) u_I = a_0 + a_1 x + a_2 x^2 + \dots + a_p x^p. \quad (1.5)$$

Consideration of an arbitrary choice of the coefficients, a_i , then leads to the following set of conditions on the basis functions:

$$\sum_I \Phi_I(x) = 1, \quad \sum_I \Phi_I(x) x_I = x, \quad \dots, \quad \sum_I \Phi_I(x) x_I^p = x^p. \quad (1.6)$$

The set of basis functions $\{\Phi_I\}$ also satisfies what is called the partition of unity (PU) of order p . For instance, the PU of order 0 satisfies $\sum_I \Phi_I(x) = 1$.

It is often also necessary for the derivatives of polynomials to be correctly reproduced. This is called the derivative requirement condition and can be found from eqs. (1.6) by straightforward differentiation of both sides. For example application

of the first derivative yields:

$$\sum_I \Phi_{I,x}(x) = 0, \quad \sum_I \Phi_{I,x}(x)x_I = 1, \quad \dots, \quad \sum_I \Phi_{I,x}(x)x_I^p = px^{p-1}. \quad (1.7)$$

It can be reasonably argued that the terms completeness and reproducing condition are closely related to consistency [32]. Indeed any differences between them are not relevant to the remainder of this Thesis so that these terms will be used interchangeably from this point to denote the reproducing condition defined above.

Chapter 2

Landau-de Gennes Theory of Liquid Crystals

2.1 Introduction

2.1.1 The Nematic Order Parameter

Quantitatively, the behaviour of LCs is best described using the concepts of the director and the associated order parameters [1]. In the nematic phase, the molecular axes of a LC tend to point along a preferred direction, called the *director*. The director is denoted by a unit vector \hat{n} pointing along the average molecular orientation, as sketched in Fig. 2.1. The directions \hat{n} and $-\hat{n}$ are usually equivalent and indistinguishable; that is why the vector \hat{n} is drawn with two arrows in Fig. 2.1. Generally, the director is a function of both space and time coordinates, i.e. $\hat{n} = \hat{n}(\mathbf{x}, t)$.

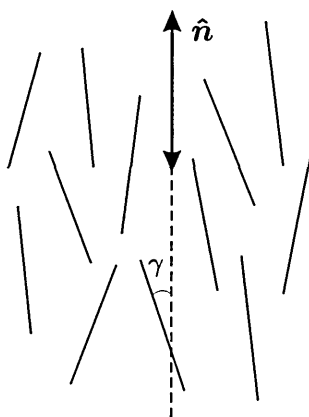


Figure 2.1: A schematic illustration of molecular axis around the average alignment direction.

The degree of LC alignment can be described quantitatively using the scalar S ,

which is called the *order parameter*. Formally, this order parameter is a second-rank quantity, but this detail is not pertinent to the remainder of this Thesis. In order to define the order parameter, we consider some sample of a LC, e.g. that depicted in Fig. 2.1. If γ is the angle which a given molecule's long axis makes with the director, then the degree of order can be quantified via the set of even Legendre polynomials of $\cos \gamma$, averaged over an appropriate volume. Odd Legendre polynomials average to zero in uniform bulk nematic due to the head-tail symmetry of the phase. The leading non-zero number of this set is, therefore, the second averaged Legendre polynomial. This is also called the microscopic order parameter:

$$S = \langle P_2(\cos \gamma) \rangle = \frac{1}{2} \langle 3 \cos^2 \gamma - 1 \rangle, \quad (2.1)$$

in which $\langle \dots \rangle$ denotes the statistical average and, thus, this equation can be equivalently rewritten in the continuum form such as

$$S = \frac{1}{2} \int (3 \cos^2 \gamma - 1) f(\gamma) dV, \quad (2.2)$$

where $f(\gamma)$ is the statistical distribution function of the molecular angle γ . The function $f(\gamma)$ is even and periodic due to the head-tail symmetry of the phase, i.e. $f(\gamma + \pi) = f(\gamma)$.

In a perfectly ordered fluid where all molecules are ideally aligned with the director, i.e. all angles $\gamma = 0$ and the order parameter is equal to 1. In an isotropic fluid, conversely, all molecules are randomly oriented, so $\langle \cos^2 \gamma \rangle = 1/3$ and the order parameter is equal to 0. When all molecules lie in the plane perpendicular to the director, the order parameter $S = -1/2$. Although mathematically it is possible to have a negative S , in real systems the order parameter usually takes values $0 < S < 1$, with typical values for a nematic being around 0.6. This order parameter is usually sufficient to describe systems composed of molecules possessing cylindrical or rotational symmetry around their long axes.

2.1.2 The Biaxiality

Molecules, in practice, do not usually have axes of complete rotational symmetry. Systems composed of such molecules, thus, might not have an axis such that rotation around it will leave the system's state unchanged. Sometimes, this can also be the case for systems composed of uniaxial molecules. Such systems are called *biaxial*. In these, a uniaxial order parameter S alone is not enough to describe the system. However, in such systems two perpendicular axes \hat{n} and \hat{m} of translational symmetry

can always be identified, with the third axis \hat{l} being always perpendicular to these two, $\hat{l} = \hat{n} \times \hat{m}$. In these, each axis has a reflection symmetry, i.e. $\hat{n} \rightarrow -\hat{n}$, $\hat{m} \rightarrow -\hat{m}$ and $\hat{l} \rightarrow -\hat{l}$.

A uniaxial arrangement of both uniaxial and biaxial molecules is easy to imagine, as well as the biaxial arrangement of biaxial molecules. A biaxial arrangement of uniaxial molecules is more complicated, and this situation is pertinent to defects in nematic liquid crystals. The latter situation is illustrated in Fig. 2.2, where the ordering of molecules is different depending on the axis along which the system is viewed. The distinct feature of this configuration, when viewed from the “top” in the xy -plane, is that the projections of molecules are ordered. We call the associated order parameter S_2 the biaxial order parameter, which is equal to $\frac{3}{2}\langle \sin^2 \gamma \cos 2\gamma \rangle$. There is also a third order parameter, $S_3(\mathbf{x}, t)$, which is related to $S_1(\mathbf{x}, t)$ and $S_2(\mathbf{x}, t)$. For example, in the uniaxial case one of these order parameters will normally be zero and two others will be equal to each other, e.g. $S_1 = S_2$ and $S_3 = 0$.

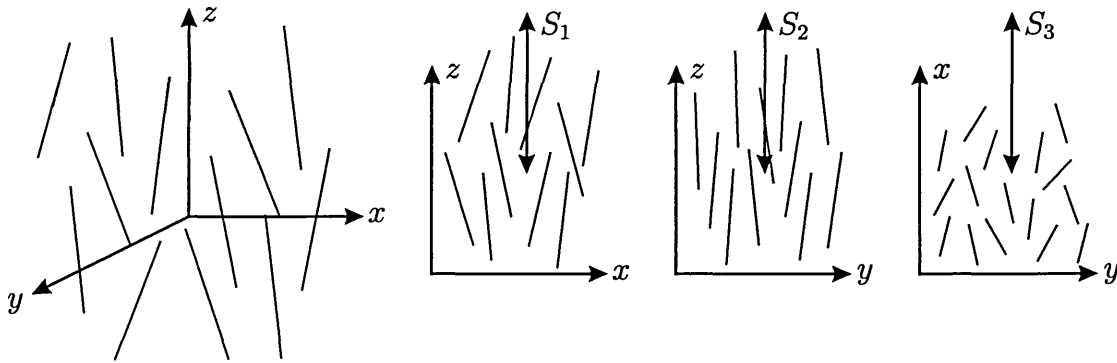


Figure 2.2: A schematic illustration of a biaxial arrangement of uniaxial molecules viewed along three different principle axes.

Thus, in order to fully describe a biaxial system, two directors, $\hat{n}(\mathbf{x}, t)$ and $\hat{m}(\mathbf{x}, t)$, and two corresponding order parameters, $S(\mathbf{x}, t) \equiv S_1(\mathbf{x}, t)$ and $P_B(\mathbf{x}, t) \equiv S_2(\mathbf{x}, t)$, should be defined. The directors can be represented by three Euler angles, namely zenithal angle θ , azimuthal angle ϕ and another zenithal angle ψ for the second director. Using the assumption that all directors are of unit length, we can then represent them using Euler angles as

$$\hat{n} = (\cos \theta \cos \phi, \cos \theta \sin \phi, \sin \theta),$$

$$\hat{m} = (\sin \phi \cos \psi - \cos \phi \sin \psi \sin \theta, -\sin \phi \sin \psi \sin \theta - \cos \phi \cos \psi, \sin \psi \cos \theta).$$

The complete description of a biaxial system can then be achieved by using five

independent variables, which are

$$\theta(\mathbf{x}, t), \phi(\mathbf{x}, t), \psi(\mathbf{x}, t), S_1(\mathbf{x}, t), S_2(\mathbf{x}, t). \quad (2.3)$$

However, there can be problems with theories based on Euler angles. For instance, when the zenithal angle $\theta = \pi/2$, then the azimuthal angle ϕ is undefined. Thus, extra care should be taken when solving differential equations based on this description.

2.1.3 The Tensor Order Parameter \mathbf{Q}

In this subsection we describe an alternative approach for describing a nematic system, which removes problems associated with descriptions based on Euler angles. In this, instead of defining the five independent variables listed in eq. (2.3), a matrix \mathbf{Q} is constructed which includes all of the information about the nematic state. This matrix is the second rank, traceless, symmetric tensor \mathbf{Q} which can be written in terms of previously defined directors and order parameters as

$$Q_{\alpha\beta} = \frac{S}{2} (3\hat{n}_\alpha\hat{n}_\beta - \delta_{\alpha\beta}) + \frac{P_B}{2} (\hat{l}_\alpha\hat{l}_\beta - \hat{m}_\alpha\hat{m}_\beta). \quad (2.4)$$

In the uniaxial state, the biaxiality P_B is equal to zero and \mathbf{Q} is simplified as

$$Q_{\alpha\beta} = \frac{S}{2} (3\hat{n}_\alpha\hat{n}_\beta - \delta_{\alpha\beta}). \quad (2.5)$$

The eigenvalues of the matrix \mathbf{Q} described by eq. (2.4) are S , $-\frac{1}{2}(S + P_B)$ and $-\frac{1}{2}(S - P_B)$. In the isotropic state, all of these eigenvalues are equal to zero and $\mathbf{Q} = \mathbf{0}$. Since \mathbf{Q} is symmetric and traceless, it contains five independent variables fully describing the nematic system. But, unlike the Euler description, which is also described by five independent variables, it is free of the description problem noted in §2.1.2.

While \mathbf{Q} describes the level of microscopic ordering in LCs, there is also an intimate connection between \mathbf{Q} and macroscopic quantities such as the dielectric and magnetic susceptibility, refractive index and conductivity. This provides a number of experimental ways of determining \mathbf{Q} . Various techniques based on the above macroscopic quantities provide comparable results, with a maximum difference of 10% [1].

For example, by considering the diagonalised macroscopic susceptibility tensor

and by making it traceless we obtain:

$$\Delta\chi_{\alpha\beta} = \begin{pmatrix} -\frac{1}{3}(\chi_{\parallel} - \chi_{\perp}) & & \\ & -\frac{1}{3}(\chi_{\parallel} - \chi_{\perp}) & \\ & & \frac{2}{3}(\chi_{\parallel} - \chi_{\perp}) \end{pmatrix}. \quad (2.6)$$

Normalisation of the above equation with the maximum anisotropy $\Delta\chi^{max} = (\chi_{\parallel} - \chi_{\perp})/S$ gives the following form for \mathbf{Q} :

$$Q_{\alpha\beta} = \frac{3}{2\Delta\chi^{max}} \left(\chi_{\alpha\beta} - \frac{\chi_{\gamma\gamma}\delta_{\alpha\beta}}{3} \right). \quad (2.7)$$

The tensor order parameter regarded in this way does not contain any assumption on the microscopic structure of the LC under consideration. It also provides a straightforward connection between changes in microscopic ordering and variation of the associated macroscopic quantity.

2.1.4 The Nematic-Isotropic Phase Transition

The nematic-isotropic phase transition in LCs is weakly first order. This type of transition is characterised by a discontinuous change in the order parameter at the critical temperature. Phenomenologically, we follow Landau [33] in describing this by using the Taylor expansion of the free energy density f in powers of the tensor order parameter \mathbf{Q} . This expansion is usually written near $\mathbf{Q} = \mathbf{0}$ as [1]

$$f_{LdG} = f_{iso} + \frac{1}{2}AQ_{\alpha\beta}Q_{\beta\alpha} + \frac{1}{3}BQ_{\alpha\beta}Q_{\beta\gamma}Q_{\gamma\alpha} + \frac{1}{4}C(Q_{\alpha\beta}Q_{\alpha\beta})^2 + \mathcal{O}(\mathbf{Q}^5), \quad (2.8)$$

where f_{iso} is the free energy density of the isotropic fluid. The coefficients A , B and C are all temperature dependant, but usually the coefficients B and C are set to be independent of temperature, while the coefficient A is chosen to depend on temperature as $A = \alpha(T - T^*)$, where $\alpha > 0$ and T^* is the temperature at which the isotropic state becomes unstable. All terms in equation (2.8) for the free energy density are invariant under rotations and reflections of coordinate axes, as they should be, since the symmetry of the phase needs to be preserved. Normally, eq. (2.8) for free energy is truncated at the fourth-order terms, which provides a general description effectively representing the uniaxial phase [34]. In order to match notations, we rewrite the above Landau-de Gennes form of the free energy

density in the form equivalent to that given in [14]:

$$f_{LdG}(\mathbf{Q}) = f_{iso} + \frac{1}{2}\alpha_F Q_{\alpha\beta} Q_{\beta\alpha} - \beta_F Q_{\alpha\beta} Q_{\beta\gamma} Q_{\gamma\alpha} + \gamma_F Q_{\alpha\beta} Q_{\beta\alpha} Q_{\mu\nu} Q_{\nu\mu}. \quad (2.9)$$

Here, α_F , β_F and γ_F are the Landau-de Gennes coefficients. Thus, equation (2.9) is our main working equation for the free energy density of a thermotropic LC. It can be readily used to predict the preferred phase of the material, i.e. isotropic, uniaxial or biaxial.

We now proceed to the analysis of eq. (2.9). For this, we insert the uniaxial order tensor definition given by eqs. (2.5) into eq. (2.9), which yields:

$$f_{LdG}(S, T) = f_{iso} + a(T - T^*)S^2 - BS^3 + CS^4, \quad (2.10)$$

where $a(T - T^*) = \frac{3\alpha_F}{4}$, $B = \frac{3\beta_F}{4}$ and $C = \frac{9\gamma_F}{4}$. By calculating the first order derivative $df_{LdG}(S, T)/dS$, setting it to zero and solving the obtained equation with respect to S , three stationary points are found:

$$S = 0, \quad (2.11)$$

$$S = \frac{1}{8C} \left(3B + \sqrt{9B^2 - 32aC(T - T^*)} \right), \quad (2.12)$$

$$S = \frac{1}{8C} \left(3B - \sqrt{9B^2 - 32aC(T - T^*)} \right). \quad (2.13)$$

Examination of the second order derivative $d^2 f_{LdG}(S, T)/dS^2$ leads to the following conclusions about these stationary points:

- $S = 0$, the LC is in the isotropic state. This phase is stable for $T > T_{IN} = T^* + \frac{B^2}{4aC}$, metastable for $T^* < T < T_{IN}$ and unstable for $T < T^*$.
- $S = \frac{1}{8C} \left(3B + \sqrt{9B^2 - 32aC(T - T^*)} \right)$, the LC is in the nematic state. It is stable for $T < T_{IN}$, metastable for $T_{IN} < T < T^{**} = T^* + \frac{9B^2}{32aC}$ and not defined for $T > T^{**}$.
- $S = \frac{1}{8C} \left(3B - \sqrt{9B^2 - 32aC(T - T^*)} \right)$, this state is metastable with a negative S value for $T < T^*$, unstable for $T_{IN} < T < T^{**}$ and not defined for $T > T^{**}$.

Based on the above analysis, the LC behaviour can be summarised as follows. For $T \gg T_{IN}$ the LC is in the isotropic state and for $T \ll T_{IN}$ it is in the nematic phase. In between these states, close to the transition temperature T^* , the behaviour is dependant on whether the LC is being heated or cooled. In the former case, the

nematic phase becomes unstable at T^{**} and in the latter case the isotropic state becomes unstable at T^* . Fig. 2.3 shows the S dependance of the free energy density for different temperature values, according to eq. (2.10), where all troughs can be clearly seen.

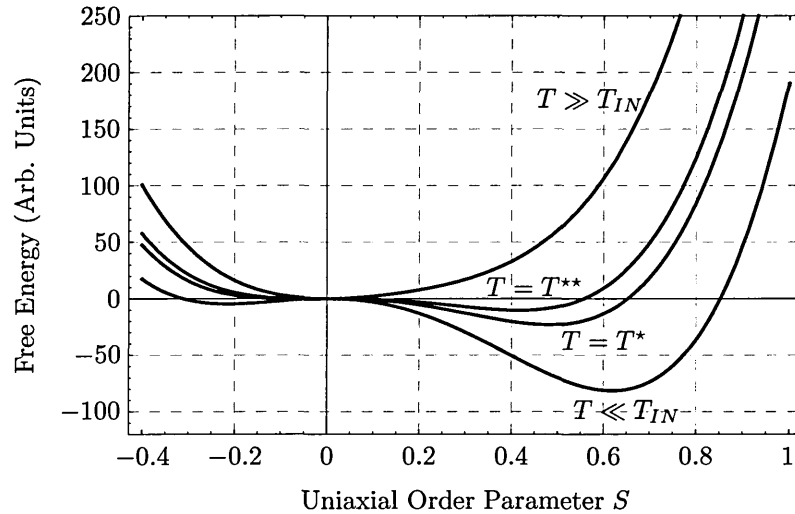


Figure 2.3: The dependance of the free energy density on the order parameter for various temperatures.

The order parameter given by eq. (2.12) is plotted in Fig. 2.4 as a function of temperature, where the discontinuity at $T = T^{**}$ can be clearly seen. It should be

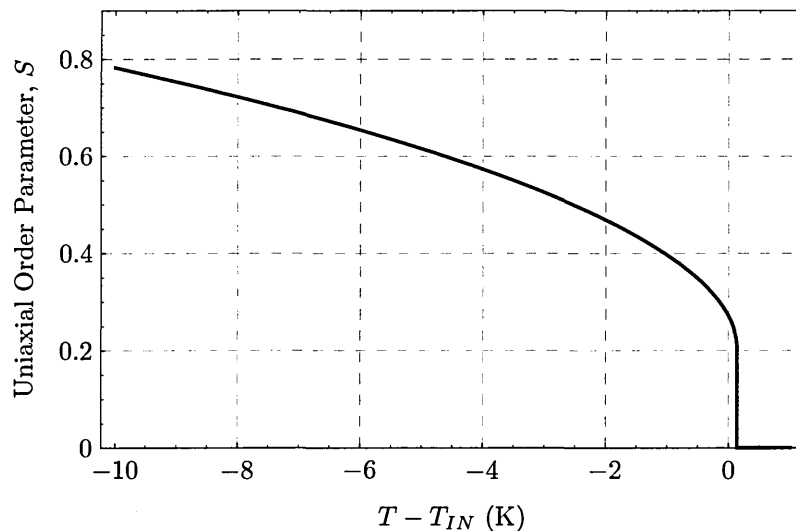


Figure 2.4: The dependance of equilibrium order parameter S on the temperature for a set of Landau coefficients suitable for 5CB [14].

noted that the Taylor expansion of the free energy density (2.8) is valid only for small values of order parameter S . That is why all terms containing higher powers

of \mathbf{Q} were neglected in this expansion. Thus, formally this theory should be applied only in situations where S does not take large values. However, as it can be seen from Fig. 2.4, the theory provides reasonable values of order parameter deep in the nematic phase. Thus, in this thesis we apply this theory without any limitations, since we work only in the nematic phase ($S \simeq 0.6$).

2.2 Static Theory of Liquid Crystals

2.2.1 Elasticity

A nematic LC prefers to remain in an undistorted state with \mathbf{Q} remaining uniform throughout the sample. Various external influences, such as boundary conditions, may, though, produce spatial variations in ordering. But the LC returns to the undistorted state once these external influences have been removed. This tendency can be explained through a free energy density f_D , also called the distortional or elastic energy density, associated with distortions which depends on the spatial derivatives of \mathbf{Q} . Derivatives of \mathbf{Q} are assumed to be weak, provided that the characteristic length scale associated with changes in \mathbf{Q} is much longer than the molecular dimensions. A linear expansion yields the free energy density:

$$f_D = f_D(\partial\mathbf{Q}) = f_0 + L_{\alpha\beta\gamma}\partial_\gamma Q_{\alpha\beta} + \frac{K_{\alpha\beta\gamma\theta\mu\nu}}{2}\partial_\alpha Q_{\beta\gamma}\partial_\theta Q_{\mu\nu}, \quad (2.14)$$

where f_0 is the energy of the undistorted LC, $L_{\alpha\beta\gamma}$ controls distortions corresponding to a chiral nematic phase and $K_{\alpha\beta\gamma\theta\mu\nu}$ represents the nematic elasticity. The elastic free energy density should be the same when described in different frames of reference, i.e. it should be invariant to arbitrary rotations or translations. This implies that not all of the combinations of \mathbf{Q} derivatives are allowed and, in fact, the elastic free energy (2.14) can be reduced to:

$$\begin{aligned} f_D = & \frac{L_1}{2}\partial_\mu Q_{\nu\gamma}\partial_\mu Q_{\nu\gamma} + \frac{L_2}{2}\partial_\mu Q_{\nu\mu}\partial_\gamma Q_{\nu\gamma} + \frac{L_3}{2}\partial_\mu Q_{\nu\gamma}\partial_\gamma Q_{\nu\mu} \\ & + \frac{L_4}{2}Q_{\mu\nu}\partial_\mu Q_{\gamma\tau}\partial_\nu Q_{\gamma\tau} + \frac{4\pi L_1}{P_{ch}}\varepsilon_{\mu\nu\gamma}Q_{\mu\tau}\partial_\nu Q_{\gamma\tau} \\ & - \frac{4\pi L_4}{P_{ch}}\varepsilon_{\mu\nu\gamma}Q_{\mu\eta}Q_{\eta\tau}\partial_\nu Q_{\gamma\tau} + \frac{6\pi^2}{P_{ch}^2}(L_1Q_{\mu\nu}Q_{\nu\mu} - L_4Q_{\mu\nu}Q_{\nu\tau}Q_{\tau\mu}), \end{aligned} \quad (2.15)$$

where P_{ch} denotes the helix pitch. Although there are seven third-order terms in \mathbf{Q} , we keep only one in order to prevent having undefined constants [15], i.e. to remove the degeneracy in elastic constants when mapping them from \mathbf{Q} tensor to experimental values K_{ii} in the Frank energy approach. The elastic parameters L_i

are related to the Frank elastic constants by the following identities [35]:

$$K_{11} = \frac{9S_0^2}{4} (2L_1 + L_2 + L_3 - S_0L_4), \quad (2.16)$$

$$K_{22} = \frac{9S_0^2}{4} (2L_1 - S_0L_4), \quad (2.17)$$

$$K_{33} = \frac{9S_0^2}{4} (2L_1 + L_2 + L_3 + 2S_0L_4), \quad (2.18)$$

$$K_{24} = \frac{9S_0^2}{4} L_3, \quad (2.19)$$

where S_0 is the uniaxial order parameter at which the experimental measurements of the elastic constants were taken and is not necessary equal to the current equilibrium order parameter S of the LC. The saddle-splay contribution K_{24} is a divergence term and does not influence the bulk behaviour. However, if the anchoring is weak at the surface, this term may contribute to surface ordering and thus change the bulk ordering.

2.2.2 Electric and Magnetic Fields

LCs interact strongly with externally applied electric and magnetic fields. The response of LCs to magnetic fields is relatively simple and depends only on the anisotropy of the magnetic susceptibility. Electric fields, on the other hand, produce many physical effects in nematics in addition to that due to dielectric anisotropy [1]. Below we consider the influence of both fields separately.

Magnetic Fields

LCs are anisotropic diamagnetic media and their magnetic susceptibilities are different along the directions parallel (χ_{\parallel}) and perpendicular (χ_{\perp}) to the LC director. In nematics, the difference $\Delta\chi = \chi_{\parallel} - \chi_{\perp}$ is usually positive. If an external magnetic field \mathbf{H} is applied to a LC sample, then the magnetisation \mathbf{M} induced by \mathbf{H} can be written as:

$$M_{\alpha} = \mu_0\chi_{\alpha\beta}H_{\beta} = \frac{2}{3}\Delta\chi^{max}Q_{\alpha\beta}H_{\beta} + \frac{1}{3}\mu_0\chi_{\gamma\gamma}\delta_{\alpha\beta}H_{\beta}, \quad (2.20)$$

where $\chi_{\alpha\beta}$ is expressed following eq. (2.7). The free energy density due to the applied magnetic field can then be derived from eq. (2.20):

$$f_M = - \int_0^{\mathbf{H}} \mathbf{M} \cdot d\mathbf{H} = -\frac{1}{3}\mu_0\Delta\chi^{max}H_{\alpha}Q_{\alpha\beta}H_{\beta} - \frac{1}{6}\mu_0\chi_{\gamma\gamma}H^2. \quad (2.21)$$

In the above equation the second term is independent of the ordering. The first term, on the other hand, explicitly contains the \mathbf{Q} tensor and it is minimised when the director is collinear with the applied magnetic field (for positive $\Delta\chi$).

Electric Fields

In order to describe the effect of electric fields, we consider an ideal situation of a static electric field \mathbf{E} applied to a nematic LC. In this simple set-up, two different physical processes take place. The first is due to the dielectric anisotropy and it is very similar to the effect of the diamagnetic anisotropy described above. The second effect is more complicated and arises in deformed nematics where a spontaneous dielectric polarization appears. This is the so-called flexoelectric effect and we consider it in the next section.

The derivation for the dielectric anisotropy effect is very similar to that for the diamagnetic anisotropy. The dielectric anisotropy $\Delta\epsilon = \epsilon_{\parallel} - \epsilon_{\perp}$, where ϵ_{\parallel} and ϵ_{\perp} are the dielectric constant measured along and perpendicular to the nematic axis, can be positive or negative depending on the structure of the constituent molecules. If an electric field \mathbf{E} is applied to a nematic LC, then the electric displacement \mathbf{D} has the following form

$$D_{\alpha} = \epsilon_0 \epsilon_{\alpha\beta} E_{\beta} = \frac{2}{3} \Delta\epsilon^{max} Q_{\alpha\beta} E_{\beta} + \frac{1}{3} \epsilon_0 \epsilon_{\gamma\gamma} \delta_{\alpha\beta} E_{\beta}. \quad (2.22)$$

The free energy density due to the electric field is then given by:

$$f_E = - \int \mathbf{D} \cdot d\mathbf{E} = -\frac{1}{3} \epsilon_0 \Delta\epsilon^{max} E_{\alpha} Q_{\alpha\beta} E_{\beta} - \frac{1}{6} \epsilon_0 \epsilon_{\gamma\gamma} E^2. \quad (2.23)$$

For LCs with a positive anisotropy, i.e. with those having $\epsilon_{\parallel} - \epsilon_{\perp} > 0$, the lowest energy state is when the director is parallel to the applied electric field and, thus, the molecules align along the field. In case of the negative anisotropy, $\epsilon_{\parallel} - \epsilon_{\perp} < 0$, the lowest energy is achieved when the director is perpendicular to the electric field.

In real LC devices, however, the presence of an electric field produces a more complicated behaviour. For example, there are always conducting impurities present which aggregate into regions of charge when an electric field is applied. Also, the dielectric anisotropy of a LC is much greater than the diamagnetic anisotropy. Thus, for any distortion of the ordering in the sample, the Maxwell's electrostatic equations

need to be solved:

$$\begin{cases} \partial_\alpha D_\alpha = \sigma_f, \\ D_\alpha = \epsilon_0 \epsilon_{\alpha\beta} E_\beta, \\ E_\beta = -\partial_\beta \phi, \\ \nabla \times \mathbf{E} = 0, \end{cases} \quad (2.24)$$

where ϕ is the electric potential (voltage) and σ_f is the free charge which is in this thesis assumed to be always equal to zero. Strictly speaking, Maxwell's equations ($\partial_\alpha B_\alpha = 0$, $\nabla \times \mathbf{H} = 0$) need also to be solved for magnetic fields for higher accuracy.

2.2.3 Flexoelectricity

In some liquid crystals a splay or bend distortion can create a spontaneous dielectric polarisation which is equivalent to a local electric field. An applied electric field, on the other hand, may induce distortions which will induce a corresponding polarisation. This effect is called flexoelectricity and it was first discovered by Meyer [36]. In order to quantify this, the most general form of polarisation P_θ is constructed which is proportional to the first-order spatial derivatives of the director [1]:

$$P_\theta = e_{11} \hat{n}_\theta \partial_\mu \hat{n}_\mu + e_{33} \hat{n}_\gamma \partial_\gamma \hat{n}_\theta, \quad (2.25)$$

where e_{11} and e_{33} are flexoelectric coefficients with the dimensions of an electric potential. There are no flexoelectric terms arising from second order derivatives due to symmetry principles. Whereas eq. (2.25) includes only the derivatives of the director, a more general expression accounting for order parameter can be written as [37]:

$$P_\theta = C_1 \partial_\gamma Q_{\theta\gamma} + C_2 Q_{\theta\gamma} \partial_\mu Q_{\gamma\mu}. \quad (2.26)$$

In this, C_1 and C_2 are 'weakly' temperature dependent flexoelectric coefficients. Only one second order term in \mathbf{Q} (the C_2 term) out of a possible three was included in eq. (2.26) in order to remove ambiguity. This allows one to directly match experimental parameters without introducing unknown coefficients, similar to the expression for elasticity. Substitution of \mathbf{Q} from eq. (2.5) into eq. (2.26) yields:

$$P_\theta = \left(\frac{3S_0 C_1}{2} + \frac{3S_0^2 C_2}{2} \right) \hat{n}_\theta \partial_\mu \hat{n}_\mu + \left(\frac{3S_0 C_1}{2} - \frac{3S_0^2 C_2}{4} \right) \hat{n}_\gamma \partial_\gamma \hat{n}_\theta. \quad (2.27)$$

Matching this equation with that by Meyer (2.25) provides the following relations between flexoelectric coefficients:

$$e_{11} = \left(\frac{3S_0C_1}{2} + \frac{3S_0^2C_2}{2} \right), \quad e_{33} = \left(\frac{3S_0C_1}{2} - \frac{3S_0^2C_2}{4} \right). \quad (2.28)$$

The free energy density due to the flexoelectric contribution has the following form:

$$f_{flexo} = -E_\theta P_\theta = -C_1 E_\theta \partial_\gamma Q_{\theta\gamma} - C_2 E_\theta Q_{\theta\gamma} \partial_\mu Q_{\gamma\mu}. \quad (2.29)$$

There is an effect similar to flexoelectricity, which is called the order electric effect [38]. It happens when there is a spatial gradient in the ordering S and there are no significant variations of the director. The polarisation in this case is found by again substituting \mathbf{Q} from eq. (2.5) into eq. (2.26) with assumption that S is a variable and $\hat{\mathbf{n}}$ is constant. This yields

$$P_\theta = \left(\frac{3C_1}{2} + \frac{3C_2S}{4} \right) \hat{n}_\theta \hat{n}_\mu \partial_\mu S + \left(-\frac{C_1}{2} + \frac{C_2S}{4} \right) \partial_\theta S. \quad (2.30)$$

2.2.4 Boundary Conditions and Anchoring

When liquid crystal molecules are close to a solid boundary they experience an influence which is dependent on type of the boundary treatment. For example, a boundary treated by rubbing can impose a preferred direction of the director. In some cases, boundaries can also change the value of the order parameter. Thus, a full continuum description of LCs should include a free energy density term which will account for boundaries. This then should be minimised together with the bulk terms in order to find the LC preferred state.

Strong anchoring is the simplest type of LC boundary condition. In this, the boundary strictly imposes both the preferred orientation and the degree of ordering of the LC molecules. In the continuum limit this corresponds to a classical Dirichlet boundary condition and is imposed in simulations by fixing the \mathbf{Q} tensor on the boundaries. In this, \mathbf{Q} is determined by substituting the desired values of the order parameter S and the director \mathbf{n} into eq. (2.5). Thus, for this type of anchoring the free energy density expression to be minimised contains no extra terms.

Weak anchoring also imposes preferred direction and ordering of a LC at a boundary. Unlike strong anchoring, however, it does so by including an extra term in the free energy density which penalises any deviations from the preferred orientation or ordering. One of the most widely used forms for this free energy density that

involves \mathbf{Q} tensor can be written as [39]:

$$f_S = \frac{W}{2} (Q_{\alpha\beta} - Q_{\alpha\beta}^\circ)^2, \quad (2.31)$$

where W is the only anchoring coefficient and \mathbf{Q}° is a preferred alignment tensor on the surface given by eq. (2.5). The magnitude of the anchoring coefficient W determines how strongly the preferred orientation is imposed. It is obvious that the strong anchoring corresponds to the limit when $W \rightarrow \infty$. In case of the uniaxial constant order limit, which can be derived by substituting eq. (2.5) into eq. (2.31), the free energy density takes the following form:

$$f_S = \frac{9S_0^2 W}{4} (1 - (\hat{n}_\alpha \hat{n}_\alpha^\circ)^2) = -\frac{A}{2} (\hat{n}_\alpha \hat{n}_\alpha^\circ)^2, \quad (2.32)$$

where A is the Rapini-Papoular anchoring coefficient [40] and $W = \frac{2A}{9S_0^2}$.

Planar degenerate anchoring is another important class of anchoring. In this, the director lies parallel to the surface. There is no single preferred direction at the surface, though, and the only condition is that the director should prefer to lie parallel to the surface. The most general surface free energy density in this case is given by [41]:

$$f_S = c_1 \boldsymbol{\nu} \cdot \mathbf{Q} \cdot \boldsymbol{\nu} + c_2 (\boldsymbol{\nu} \cdot \mathbf{Q} \cdot \boldsymbol{\nu})^2 + c_3 \boldsymbol{\nu} \cdot \mathbf{Q}^2 \cdot \boldsymbol{\nu}, \quad (2.33)$$

where the c_i are anchoring coefficients and $\boldsymbol{\nu}$ is the vector of the surface normal. Here, the effective anchoring strength, as compared to Rapini-Papoular energy, can be shown to be $W = \frac{2}{3} S_0 (3c_1 + (c_3 - 2c_2) S_0)$.

2.2.5 The Equilibrium States

In the previous sections of this chapter we have provided expressions for the free energy density of a LC that describe different aspects of nematic behaviour. The total free energy of a given state is then found by integrating the free energy density over the whole domain including bounding surfaces:

$$\begin{aligned} \mathcal{F}_{Global} &\equiv \mathcal{F}_{Global}(\mathbf{Q}, \boldsymbol{\partial}\mathbf{Q}) = \mathcal{F}_{Bulk} + \mathcal{F}_{Surface} = \int_{\Omega} f_B dV + \int_{\Gamma} f_S dS \\ &= \int_{\Omega} (f_{LdG} + f_D + f_{EM} + f_{flexo}) dV + \int_{\Gamma} f_S dS, \end{aligned} \quad (2.34)$$

where Ω is an open-bounded set with boundary Γ . In order to find the free energy density which minimises eq. (2.34), variational calculus needs to be applied. For that, we first construct an expression for variations in \mathcal{F} , $\delta\mathcal{F}$, for all virtual variations of

the alignment field:

$$\begin{aligned}\delta\mathcal{F} &= \delta \int_V f_B(Q_{\alpha\beta}, \partial_\gamma Q_{\alpha\beta}) dV + \delta \int_S f_S(Q_{\alpha\beta}) dS \\ &= \int_V \left(\frac{\partial f_B}{\partial Q_{\alpha\beta}} \delta Q_{\alpha\beta} + \frac{\partial f_B}{\partial \partial_\gamma Q_{\alpha\beta}} \delta(\partial_\gamma Q_{\alpha\beta}) \right) dV + \int_S \frac{\partial f_S}{\partial Q_{\alpha\beta}} \delta Q_{\alpha\beta} dS,\end{aligned}\quad (2.35)$$

where we used the fact that the variation operator commutes, i.e. $\delta(\partial_\gamma Q_{\alpha\beta}) = \partial_\gamma(\delta Q_{\alpha\beta})$.

The following identity can be derived from the divergence theorem:

$$\int_V \partial_\alpha (f_{\alpha\beta} g_\beta) dV = \int_V g_\beta \partial_\alpha f_{\alpha\beta} dV + \int_V f_{\alpha\beta} \partial_\alpha g_\beta dV = \int_S \nu_\alpha f_{\alpha\beta} g_\beta dS,\quad (2.36)$$

where ν is, again, an outward pointing unit normal vector from the surface. Application of the above equation to eq. (2.35) yields:

$$\delta\mathcal{F} = \int_V \left(\frac{\partial f_B}{\partial Q_{\alpha\beta}} - \partial_\gamma \frac{\partial f_B}{\partial(\partial_\gamma Q_{\alpha\beta})} \right) \delta Q_{\alpha\beta} dV + \int_S \left(\nu_\gamma \frac{\partial f_B}{\partial(\partial_\gamma Q_{\alpha\beta})} + \frac{\partial f_S}{\partial Q_{\alpha\beta}} \right) \delta Q_{\alpha\beta} dS.\quad (2.37)$$

This minimisation should also account for the \mathbf{Q} tensor being symmetric and traceless, which is achieved by introducing Lagrange multipliers λ^B and λ^S . Thus, finally the following equilibrium conditions for LCs can be written:

$$\frac{\partial f_B}{\partial Q_{\alpha\beta}} - \partial_\gamma \frac{\partial f_B}{\partial(\partial_\gamma Q_{\alpha\beta})} + \lambda^B \delta_{\alpha\beta} + \lambda_\gamma^B \varepsilon_{\alpha\beta\gamma} = 0\quad (2.38)$$

$$\nu_\gamma \frac{\partial f_B}{\partial(\partial_\gamma Q_{\alpha\beta})} + \frac{\partial f_S}{\partial Q_{\alpha\beta}} + \lambda^S \delta_{\alpha\beta} + \lambda_\gamma^S \varepsilon_{\alpha\beta\gamma} = 0\quad (2.39)$$

Solutions to eqs. (2.38) and (2.39) yield the equilibrium states of the LC system. In the case of strong anchoring eq. (2.39) can simply be ignored, since here the free energy density $f_S = 0$ as was previously discussed in §2.2.4. When, on the other hand, the boundary conditions are complicated and f_S is not equal to zero, both equations should be taken into account. The complexity of eqs. (2.38) and (2.39) makes them impossible to solve analytically for all but the simplest geometries. For this reason, numerical techniques are routinely applied. Very often more than one solution exists corresponding to the local minima in the free energy density. Thus, in order to find all solutions for real systems, different random starting conditions are often considered within the minimisation process.

2.2.6 Defects

In this section we consider common defects in LCs. These are characterised by distortions in the local director field entailing a significant decrease in the local order parameter and an increase in the biaxiality parameter. These are directly observed through optical microscopy, the nematic itself being named due to “thread like” defects [1]. The defects can be points, lines (sometimes called as disclinations) or walls, but usually walls are unstable, tending to break into a number of line defects [1]. The free energy of defects is higher than that of the uniform nematic, but their formation can lead to the total free energy of the system finding a global minimum.

Defects in real LC systems may occur, for example, due to applied electromagnetic fields or varying boundary conditions. When there are external influences acting on a LC, the minimum of the free energy density is achieved via one of two different mechanisms. In the first, the eigenvectors of the \mathbf{Q} tensor change as a function of space and/or time coordinates. This simply corresponds to the director varying in space but the order parameter staying constant. For example, this is what happens in a cell which imposes different uniaxial orientations on its boundaries. The second mechanism is manifested via change of the eigenvalues of the \mathbf{Q} tensor. In this case the orientation of the director remains fixed, but the order parameter is decreased and the biaxiality is increased. Sometimes there may be a combination of these two mechanisms, depending on the interplay between the elastic free energy f_D and the Landau-de Gennes free energy f_{LDG} .

In order to quantitatively describe defects, we consider a two-dimensional plane. We assume that the order parameter is constant and the director is described as $\hat{n}_\alpha = \hat{n}_\alpha(x, y) = (\cos \theta, \sin \theta)$. Then, using a coordinate system with the origin at the defect core, we imagine a closed loop encircling the defect. Moving along this loop, the director \hat{n}_α rotates, and after a complete circle the director is required to return to its initial state. Thus, $\theta(\phi + 2\pi) = \theta(\phi) + 2\pi m$, where ϕ is a polar angle position along the circle and m is an integer or half integer, called the defect strength [1].

A simple expression for the bulk elastic energy of a defect can be written as $F = (K/2) \int (\partial_\gamma \partial_\gamma \theta)^2 dV$, where the one elastic constant approximation is assumed ($K_{ii} = K$). Minimisation of the free energy yields the far-field solution $\theta(\phi) = m\phi + \theta_0$, where θ_0 is the director angle at the start of the enclosing circle. The director fields for different m are shown in Fig. 2.5 for this solution.

The energy of defects is proportional to m^2 , and, thus, usually lower m states are preferred over higher ones [2]. The creation and annihilation of defects happens

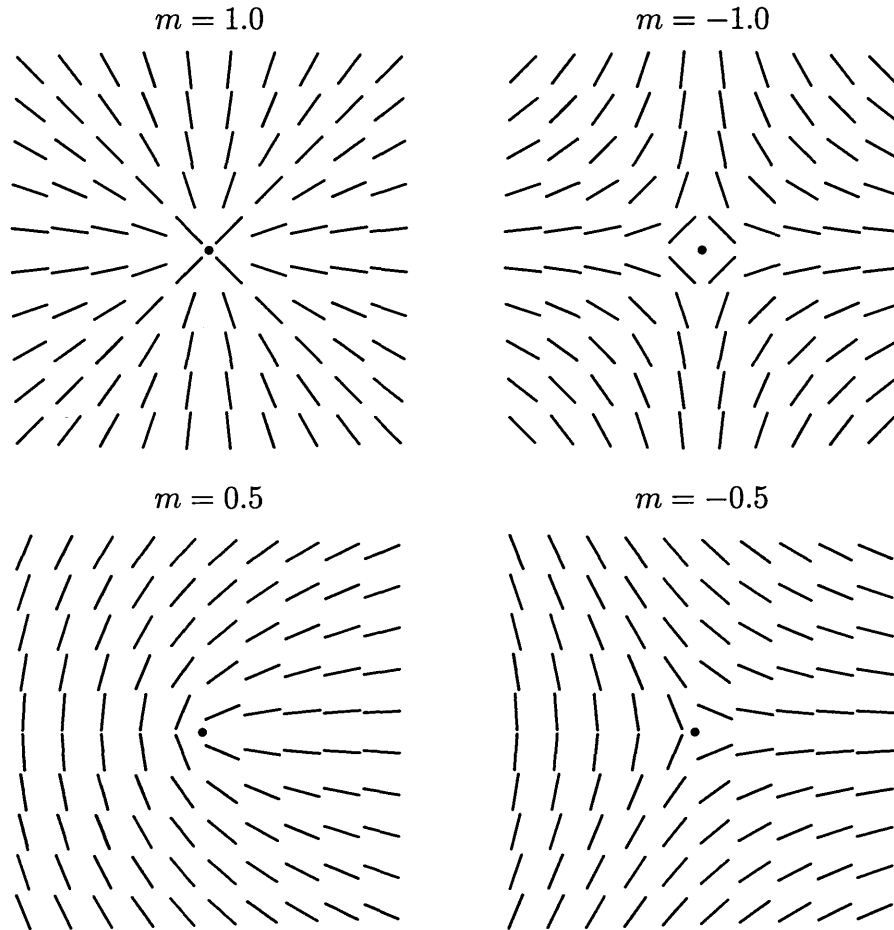


Figure 2.5: Director fields for some topological defects of different strengths m .

between defects of opposite strengths.

It should be noted that half integer defects cannot be recovered in simulations using vector director theories [42], since the vector representation leads to miscalculation of derivatives due to head-tail symmetry. Thus, a \mathbf{Q} tensor based description is necessary in order to properly recover phenomena involving defects.

2.3 Dynamic Theory of Liquid Crystals

In this section we consider the theoretical description of the dynamics of nematic LCs, which is usually called ‘nematodynamics’. The flow of nematics is much more complicated than that of isotropic fluids and it is very difficult to study experimentally. This is due to a reciprocal coupling between translational motion and rotational degrees of freedom, i.e. flow of a LC affects the alignment and, at the same time, distortions of alignment affect the flow. From a theoretical point view this also presents a significant challenge, since it is necessary to describe both the

alignment and flow simultaneously. The published literature surrounding the governing equations for nematodynamics is complex and there is, as yet, no unifying methodology for deriving the complete description of LCs.

The first phenomenological continuum theory for nematics was developed by Ericksen [43], Leslie [44] and Parodi [45]. This employs the director to describe molecular alignment. We further refer to this theory using the commonly used abbreviation ELP. It consists of equations which fully couple orientation and flow, using the assumptions that LC is uniaxial and that the order parameter is constant everywhere. The original derivations of ELP theory are based on conservation laws for energy, linear momentum and angular momentum.

Since the appearance of ELP theory, the governing equations for nematodynamics based on the vector description have been developed in a number of different ways. De Gennes [1] presented ELP in the framework of irreversible thermodynamics by de Groot [46]. Sonnet [47] applied a variational principle to such input parameters as the free energy density and dissipation in order to derive governing equations which, in the limit of the uniaxial constant order parameter, were shown to reduce to ELP equations. Forster [48] considered hydrodynamic Goldstone modes using Poisson brackets to derive the governing equations. Thus, it was shown that fundamentally different derivations can be cast in the ELP form and, eventually, this theory has been accepted by experimentalists as being a reliable one. Five independent viscosities, namely Leslie viscosities, were measured and verified. Also, calculations of the optical transmission through a LCD cell using the ELP model were proven to be very accurate [49].

While ELP theory is sufficient for describing many of the effects present in LCs, it unfortunately fails to provide a complete description of the LC phenomena. The major shortcoming of the ELP description centres on its inability to properly describe defects in LCs. The ELP model also does not include effects relating to order parameter and biaxiality. All of these limitations can be seen as been due to the vector description of ordering. A few extensions to the ELP model were suggested to alleviate some of these problems. For example, Ericksen [50] extended the ELP director theory to include a variable order parameter, but the resulting model is still uniaxial and lacks the correct director symmetry. Another different approach aims at restoring the director symmetry by employing the dyad $\hat{n}_\alpha \hat{n}_\beta$ [51]. This avoids effects like artificial derivatives when directors are almost antiparallel, but essentially this technique is equivalent to using the \mathbf{Q} tensor with constant eigenvalues. Whilst they are helpful in certain situations, these enhanced methods still fail to address a range of complex situations, e.g. half-integer defects, where variable order,

biaxiality and the symmetry of the director need to be considered. All of these can, though, be fully recovered by using \mathbf{Q} tensor theory.

The foundations of a LC representation using the \mathbf{Q} tensor as a macroscopic variable were laid down by de Gennes [52] and Lubensky [53]. De Gennes also introduced the framework of irreversible thermodynamics needed to derive the ELP equations in the equivalent \mathbf{Q} form [1, 52].

Further progress in the development of a continuum theory based on \mathbf{Q} tensor theory was made by Hess [54] and Olmsted [55], who derived the constitutive equations for homogeneous alignments. These equations have subsequently been generalised by Hess and Pardowitz [56] to include spatial variation of alignment. These attempts, however, failed to yield the full anisotropy in viscosities predicted by ELP theory. Further model extensions by Hess [57, 58] produced the complete anisotropy of viscosities but failed to be consistent with ELP theory in other ways, e.g. the viscosity coefficients were not fully independent.

A completely different approach which has been adopted by Hess in the search for a full continuum model used the Fokker-Planck equation for the orientational distribution function as a starting point [59]. In this, closure approximations were used to obtain equations for the second rank order tensor [59, 60, 61]. The initial derivation described the dynamics of nematics in given external fixed flows, whereas later extensions of this model by Tsuji and Rey [62] included spatial variations of the alignment.

Lastly, a few promising methods were published more recently to describe the evolution of the alignment with variable ordering; these are often employed in simulations. Berris and Edwards [15] used Poisson brackets on a macroscopic scale, including their own introduced dissipative bracket, to derive the governing equations. Qian and Sheng [14] presented equations for the evolution of both the velocity field and the alignment tensor. Most recently, Sonnet and Vigna [47] introduced an elegant framework based on the variational principle and on a Rayleigh dissipation function which allows one to directly derive and compare most of the previously described methods.

In this Thesis for all of our simulations we employ the constitutive equations due to Qian and Sheng [14]. This enables the simulation of thermotropic LCs using the \mathbf{Q} tensor description while retaining five independent ELP viscosities.

2.3.1 Dynamic Equations

The central equations in the Qian-Sheng formalism, which describe the evolution of momentum and order for incompressible ($\partial_\alpha u_\alpha = 0$) nematodynamics, are

$$\rho \dot{u}_\beta = \partial_\alpha (-P \delta_{\alpha\beta} + \sigma_{\alpha\beta}^v + \sigma_{\alpha\beta}^d + \sigma_{\alpha\beta}^{EM}), \quad (2.40)$$

and

$$J \ddot{Q}_{\alpha\beta} = h_{\alpha\beta} + h_{\alpha\beta}^v - \lambda \delta_{\alpha\beta} - \varepsilon_{\alpha\beta\gamma} \lambda_\gamma, \quad (2.41)$$

where the superposed dot ($\dot{}$) denotes the material time derivative: $\partial_t + u_\alpha \partial_\alpha$. Here, the local variables are ρ , the LC density, \mathbf{u} , the fluid velocity, P , the pressure, and J , the moment of inertia. λ and λ_γ are Lagrange multipliers chosen to ensure that \mathbf{Q} remains symmetric and traceless. Direct calculation of the trace and off-diagonal elements of eq. (2.41) shows that the Lagrange multipliers are given by $\lambda = \frac{1}{3} (h_{\gamma\gamma})$ and $\lambda_\gamma = \frac{1}{2} \varepsilon_{\alpha\beta\gamma} h_{\alpha\beta}$. σ^d and \mathbf{h} are the distortion stress tensor and molecular field defined by the free energy as

$$\sigma_{\alpha\beta}^d = - \frac{\partial f_B}{\partial (\partial_\alpha Q_{\mu\nu})} \partial_\beta Q_{\mu\nu}, \quad (2.42)$$

$$h_{\alpha\beta}^B = - \frac{\partial f_B}{\partial Q_{\alpha\beta}} + \partial_\gamma \frac{\partial f_B}{\partial (\partial_\gamma Q_{\alpha\beta})}. \quad (2.43)$$

σ^v and \mathbf{h}^v , the viscous stress tensor and viscous molecular field, are given by

$$\begin{aligned} \sigma_{\alpha\beta}^v &= \beta_1 Q_{\alpha\beta} Q_{\mu\nu} A_{\mu\nu} + \beta_4 A_{\alpha\beta} + \beta_5 Q_{\alpha\mu} A_{\mu\beta} + \beta_6 Q_{\beta\mu} A_{\mu\alpha} \\ &+ \frac{\mu_2 N_{\alpha\beta}}{2} - \mu_1 Q_{\alpha\mu} N_{\mu\beta} + \mu_1 Q_{\beta\mu} N_{\mu\alpha}, \end{aligned} \quad (2.44)$$

and

$$h_{\alpha\beta}^v = - \frac{1}{2} \mu_2 A_{\alpha\beta} - \mu_1 N_{\alpha\beta}. \quad (2.45)$$

Here β_i , μ_i are viscosities coefficients which can be directly mapped on to ELP viscosities using the dependencies given in [14], while $N_{\alpha\beta} = \dot{Q}_{\alpha\beta} - \varepsilon_{\alpha\mu\nu} \omega_\mu Q_{\nu\beta} - \varepsilon_{\beta\mu\nu} \omega_\mu Q_{\alpha\nu}$. $A_{\alpha\beta} = \frac{1}{2} (\partial_\alpha u_\beta + \partial_\beta u_\alpha)$ and $W_{\alpha\beta} = \frac{1}{2} (\partial_\alpha u_\beta - \partial_\beta u_\alpha)$ are the symmetric and anti-symmetric velocity gradient tensors with the vorticity being $\omega_\gamma = \frac{1}{2} \varepsilon_{\gamma\alpha\beta} W_{\alpha\beta}$.

σ^{EM} is the stress tensor arising from externally applied electromagnetic fields

$$\sigma_{\alpha\beta}^{EM} = \frac{1}{2} (H_\alpha B_\beta + H_\beta B_\alpha) - \frac{H_\gamma B_\gamma}{2} \delta_{\alpha\beta} + \frac{1}{2} (E_\alpha D_\beta + E_\beta D_\alpha) - \frac{E_\gamma D_\gamma}{2} \delta_{\alpha\beta}, \quad (2.46)$$

where \mathbf{E} (\mathbf{H}) is the electric (magnetic) field strength, \mathbf{D} the electric displacement vector and \mathbf{B} the magnetic flux density.

Thus, equations (2.40)-(2.46) along with free energies given in §2.1 and in §2.2 provide a complete Qian-Sheng dynamic description of LCs. These equations can be mapped into the EL equations of motion by inserting the uniaxial \mathbf{Q} tensor given by eq. (2.5) into the governing equations. Then, the following dependencies between the viscosities in both descriptions can be identified:

$$\begin{aligned}
 \alpha_1 &= \frac{9\beta_1 S_0^2}{4} & \alpha_2 &= \frac{3\mu_2 S_0}{4} - \frac{9\mu_1 S_0^2}{4} & \alpha_3 &= \frac{3\mu_2 S_0}{4} + \frac{9\mu_1 S_0^2}{4} \\
 \alpha_4 &= \beta_4 - \frac{\beta_5 S_0}{2} - \frac{\beta_6 S_0}{2} & \alpha_5 &= \frac{3S_0\beta_5}{2} = \frac{3S_0}{4}(\beta_5 + \beta_6 - \mu_2) & & \\
 \alpha_6 &= \frac{3S_0\beta_6}{2} = \frac{3S_0}{4}(\beta_5 + \beta_6 + \mu_2) & \gamma_1 &= \frac{9S_0^2\mu_1}{2} & \gamma_2 &= \frac{3S_0\mu_2}{2}
 \end{aligned} \tag{2.47}$$

Finally, we state the equations imposed on boundaries. As a rule, we impose non-slip boundary conditions on the velocity, which means that the fluid velocity at a boundary is zero. For infinitely strong anchoring, the \mathbf{Q} tensor is specified according to eq. (2.5). For cases of weak anchoring, a surface evolution equation was suggested [63], which, extended to a \mathbf{Q} tensor theory can be written as:

$$\mu_S \partial_t Q_{\alpha\beta} = h_{\alpha\beta}^S - \lambda^S \delta_{\alpha\beta} - \varepsilon_{\alpha\beta\gamma} \lambda_\gamma^S. \tag{2.48}$$

Here $h_{\alpha\beta}^S = -\frac{\partial f_B}{\partial(\partial_\tau Q_{\alpha\beta})} \hat{\nu}_\tau - \frac{\partial f_S}{\partial Q_{\alpha\beta}}$ is a surface molecular field, $\lambda^S = \frac{1}{3} h_{\gamma\gamma}^S$ and $\lambda_\gamma^S = \frac{1}{2} \varepsilon_{\alpha\beta\gamma} h_{\alpha\beta}^S$ are the corresponding Lagrange multipliers, $\hat{\nu}$ is an outward pointing surface unit normal vector and μ_S is the surface viscosity defined through $\mu_S = \mu_1 l_S$, where l_S is a characteristic surface length typically in the range $l_S \approx 100 - 1000 \text{ \AA}$ [64]. The surface viscosity μ_S affects the time derivative in eq. (2.48) and, thus, can be seen as controlling the rate at which surface alignment relaxes to equilibrium.

Chapter 3

Mesoscopic Mesh-free Particle Techniques

In this chapter we review all of the existing mesoscopic mesh-free particle simulation techniques with a special emphasis on the methods we have implemented in the course of this programme of research. Sections §3.2 and §3.3 are directly relevant to the remainder of this Thesis, whereas sections §3.4 and §3.5 are included only for completeness.

3.1 Introduction

Mesh-free particle techniques have been broadly discussed in §1.5.1. In this chapter we concentrate on the subset of mesh-free particle methods which are appropriate for the simulation of mesoscopic phenomena. It should be noted that mesoscopic simulation techniques are a relatively undeveloped area, as compared with continuum simulation techniques and particle based methods such as molecular dynamics.

Mesoscopic simulation techniques can be derived using a number of different approaches. Bottom-up approaches consist of coarse-graining a molecular system, whereby a number of atoms are represented by a single particle and the fast chaotic motion of many atoms is integrated out and replaced by thermal noise. The dissipative particle dynamics (DPD) approach introduced in 1992 by Hoogerbrugge and Koelman [6, 7] can be seen as belonging to this class. Top-down approaches, in contrast, involve discretisation of the continuum equations describing the system and subsequent addition of the thermal noise. We put the smoothed particle hydrodynamics (SPH) simulation technique [9, 10], devised in late 1970's, into this category. Formally, SPH is not a mesoscopic simulation technique in the original formulation. It is not even a continuum numerical method, but rather, initially, a tool for study-

ing astrophysical phenomena. Because SPH is essentially a tool for solving partial differential equations on a set of moving particles, though, it can be regarded as a mesh-free particle technique. The inclusion of thermal fluctuations into the original SPH by Espanol and Revenga [65] in 2003 resulted in a truly top-down mesoscopic technique which is called smoothed dissipative particle dynamics (SDPD).

Finally, there is a third route to deriving mesoscopic simulation techniques, which is based on the kinetic theory. The lattice Boltzmann (LB) method [8], direct simulation Monte Carlo (DSMC) [28, 29] and stochastic rotational dynamics (SRD) [66, 67] methods belong to this class. LB is a particle based mesoscopic simulation technique, but it requires a grid for its operation. Thus, it is not mesh-free and we are not considering it in this chapter.

In spite of the very different routes by which these groups of methods were derived, the end point models are very similar to each other. They all consist of a set of particles moving off-lattice and interacting with each other via pairwise additive interactions. Thermal (random) interactions are also present in each of these methods, except for the SRD technique, which has multi-particle interactions as its foundation.

3.2 Dissipative Particle Dynamics

Dissipative particle dynamics (DPD) has become, over the last decade, a popular method for simulating dynamical and rheological properties of both simple and complex fluids. It is a stochastic simulation technique, which was initially devised by Hoogerbrugge and Koelman [6, 7] to avoid the lattice artifacts of Lattice Gas Automata and to tackle hydrodynamic time and space scales beyond those available to molecular dynamics (MD). It was subsequently reformulated and slightly modified by Espanol [68] to ensure proper thermal equilibration.

DPD is an off-lattice mesoscopic simulation technique which involves a set of particles moving in continuous space and discrete time. Particles represent whole molecules or fluid regions, rather than single atoms, and atomistic details are not considered relevant to the processes addressed. The particles' internal degrees of freedom are then integrated out and replaced by simplified pairwise dissipative and random forces, so as to locally conserve momentum and ensure correct hydrodynamic behaviour. The main advantage of this method is that it gives access to longer time and length scales compared to what is achievable by conventional MD simulations.

3.2.1 DPD Formalism

The basic DPD scheme is based on a set of N particles that move in a continuum two or three-dimensional domain of volume V . As in MD simulations, the system is completely described by specifying the particles' positions \mathbf{r}_i and momenta $\mathbf{q}_i = m_i \mathbf{v}_i$, where $i \in \{1, \dots, N\}$ labels the particles.

Time evolution of the system is governed by Newton's equations of motion

$$\frac{d\mathbf{r}_i}{dt} = \mathbf{v}_i, \quad \frac{d\mathbf{v}_i}{dt} = \frac{1}{m_i} \mathbf{F}_i, \quad (3.1)$$

where the total force \mathbf{F}_i on particle i can be decomposed into the sum of three distinct components – one conservative, one dissipative and one random

$$\mathbf{F}_i = \sum_{j \neq i} \left(\mathbf{F}_{ij}^C + \mathbf{F}_{ij}^D + \tilde{\mathbf{F}}_{ij} \right). \quad (3.2)$$

The first two of these forces are deterministic, whereas the third contribution is stochastic. The sum runs over all particles within a certain cutoff radius r_c , and pairwise additivity is assumed for all force types. The forces are given by

$$\mathbf{F}_{ij}^C = -\nabla \phi_{ij} \quad (3.3)$$

$$\mathbf{F}_{ij}^D = -\gamma m \omega^D(r_{ij}) (\mathbf{e}_{ij} \cdot \mathbf{v}_{ij}) \mathbf{e}_{ij} \quad (3.4)$$

$$\tilde{\mathbf{F}}_{ij} = \sigma m \omega^R(r_{ij}) \xi_{ij} \mathbf{e}_{ij} \quad (3.5)$$

where $\mathbf{r}_{ij} = \mathbf{r}_i - \mathbf{r}_j$ is the relative position, $r_{ij} = |\mathbf{r}_{ij}|$ is the distance, $\mathbf{e}_{ij} = \mathbf{r}_{ij}/r_{ij}$ is the unit vector joining particle centres and $\mathbf{v}_{ij} = \mathbf{v}_i - \mathbf{v}_j$ is the relative particle velocity. ξ_{ij} is a member of a set of symmetric stochastic variables with zero mean and unit variance, obeying Gaussian statistics and uncorrelated for different pairs of particles and different times. The strengths of the dissipative and random forces are determined by the dissipation friction γ and random impulse strength σ respectively, and their interaction range is scaled by the dimensionless radial weighting functions $\omega^D(r_{ij})$ and $\omega^R(r_{ij})$.

For spherical/circular particles, the conservative force \mathbf{F}_{ij}^C is derived from the inter-particle potential $\phi_{ij} = \phi(r_{ij})$ that depends on the separation between two fluid particles. In DPD's mesoscopic description, this is a weak force of relatively long range, which may be interpreted as having emerged from mean field theory. Its main effect is to cause the fluid particles to be reasonably evenly distributed in space. The original DPD formalism specifies that the conservative forces between particles should be softly repulsive, but it does not give their exact form. The most

widely employed form used for this potential in the literature is

$$\phi(r_{ij}) = \begin{cases} \frac{1}{2} \left(\frac{a_{ij}}{r_c} \right) (r_{ij} - r_c)^2 & (r_{ij} < r_c) \\ 0 & (r_{ij} \geq r_c) \end{cases} \quad (3.6)$$

where a_{ij} is a constant defining the strength of the particle-particle interactions. The resulting conservative force

$$\mathbf{F}_{ij}^C = a_{ij}(1 - r_{ij}/r_c)\mathbf{e}_{ij} \quad (3.7)$$

decreases linearly with the inter-particle distance. If only the conservative force is present in the system (i.e. σ and γ are both set to 0), then the algorithm reduces to conventional MD in which particles interact via this soft potential.

Dissipative and random forces are the dominant forces in DPD. The dissipative (or drag) force \mathbf{F}^D is responsible for viscous effects and takes energy out of the system. It is linear in momentum and aims to damp the relative *approaching* velocity of two particles. Thus, the method accounts for velocity gradients, as is necessary in order to be consistent with hydrodynamics. The stochastic Brownian force $\tilde{\mathbf{F}}_{ij}$ represents the thermal fluctuations (thermal noise) in the system. Unlike the viscous force, the random force is independent of the momentum and introduces energy flow from the underlying micro-level of description to DPD's coarse-grained mesoscopic level. Both of these forces act along the line of particle centres, such that linear and angular momenta are conserved, but not energy.

The fluctuation-dissipation theorem derived by Espanol and Warren [68] imposes relations between the force weight functions, amplitudes and $k_B T$. Specifically,

$$\omega^D(r_{ij}) = [\omega^R(r_{ij})]^2, \quad \sigma^2 = 2\gamma k_B T, \quad (3.8)$$

where k_B denotes the Boltzmann constant.

The theorem does not specify the precise form of the weight functions, though, so one of them can be chosen arbitrarily. In their original work, Hoogerbrugge and Koelman [6] used the normalization $n \int \omega(r) d\mathbf{r} = 1$, where $n = N/V$ is the number density, but this approach is no longer widely adopted. Instead, the usual choice is

$$\omega^D(r) = [\omega^R(r)]^2 = \begin{cases} (1 - r/r_c)^2, & r < r_c \\ 0, & r \geq r_c. \end{cases} \quad (3.9)$$

such that there is no discontinuous jump at the cutoff distance.

If the relations in (3.8) are satisfied, then both \mathbf{F}^D and $\tilde{\mathbf{F}}$ act together as a thermostat, which drives the simulated system into the proper equilibrium Gibbs-Boltzman distribution with temperature given only in terms of model parameters

$$k_B T = \frac{\sigma^2}{2\gamma}. \quad (3.10)$$

The number of particles N and volume V used in a typical DP system are constant, so the DPD model produces a well-defined NVT -ensemble with essentially two main virtues: a Galilean invariant thermostat and soft particles. The thermostat conserves momentum locally, such that correct hydrodynamics is recovered on large time and length scales. It should be noted that the given thermostat might also be useful in conventional MD simulations where correct hydrodynamics is important [69]. The second important advantage is the use of soft particles: the soft repulsion forces allow for a much longer time step δt in reduced units in DPD than is possible with MD. Groot and Warren [70] recommended using the value $\delta t = 0.04$, whereas the typical value for MD is $\delta t = 0.002$.

3.2.2 Equilibrium Properties

The first theoretical foundations to DPD were given by Espanol and Warren's [68] formulation of the stochastic differential equations (SDE) and derivation of their equivalent Fokker-Planck equation (FPE), which corresponds to the original algorithm. The equations of motion (3.1) are the Langevin equations, which can be written in the form of SDE as

$$\begin{aligned} d\mathbf{r}_i &= \mathbf{v}_i dt, \\ d\mathbf{v}_i &= \frac{1}{m} \sum_{j \neq i} [\mathbf{F}_{ij}^C - \gamma \omega^D(r_{ij})(\mathbf{e}_{ij} \cdot \mathbf{v}_{ij})\mathbf{e}_{ij}] dt + \frac{1}{m} \sum_{j \neq i} \sigma w^R(r_{ij})\mathbf{e}_{ij} dW_{ij}, \end{aligned} \quad (3.11)$$

where $dW_{ij} = dW_{ji} = \int_t^{t+\delta t} \xi_{ij} d\tau$ are independent increments of the Wiener process. The Ito interpretation is assumed, such that $dW_{ij} dW_{i'j'} = (\delta_{ii'}\delta_{jj'} + \delta_{ij'}\delta_{ji'})\delta t$, i.e. dW_{ij} is infinitesimal of order $\sqrt{\delta t}$.

The equations of motion written in the form of eqs. (3.11) are suitable for immediate use in simulation, whereas the FPE is more convenient to consider in a theoretical analysis. The FPE is the equation governing the time evolution of the probability distribution $P(\mathbf{\Gamma}; t) = P(\mathbf{r}, \mathbf{q}; t)$ of the positions $\mathbf{r} = \{\mathbf{r}_i\}^N$ and momenta $\mathbf{q} = \{\mathbf{q}_i\}^N$ of all particles in the system. It can be derived from the SDE using standard procedures [71] by considering the differential df of an arbitrary function f to

second order and substituting the SDE (3.11) into it. $\langle df/dt \rangle$ can then be obtained, from which the resulting FPE in phase space is extracted:

$$\partial_t P(\mathbf{r}, \mathbf{q}; t) = (\mathcal{L}_C + \mathcal{L}_D)P(\mathbf{r}, \mathbf{q}; t), \quad (3.12)$$

where the evolution operators are defined as

$$\mathcal{L}_C = - \sum_i \left(\mathbf{v}_i \cdot \frac{\partial}{\partial \mathbf{r}_i} + \frac{\mathbf{F}_i}{m} \cdot \frac{\partial}{\partial \mathbf{v}_i} \right) \quad (3.13)$$

$$\mathcal{L}_D = \sum_{i,j \neq i} \frac{1}{m} \mathbf{e}_{ij} \frac{\partial}{\partial \mathbf{v}_i} \left[\gamma \omega^D(r_{ij}) (\mathbf{e}_{ij} \cdot \mathbf{v}_{ij}) + \frac{\sigma^2}{2m} (\omega^R(r_{ij}))^2 \mathbf{e}_{ij} \cdot \left(\frac{\partial}{\partial \mathbf{v}_i} - \frac{\partial}{\partial \mathbf{v}_j} \right) \right]. \quad (3.14)$$

Here \mathcal{L}_C is the conventional Liouville operator of the Hamiltonian system and \mathcal{L}_D is an operator which incorporates the dissipative and random contributions. If dissipative and drag forces are not present, then this reduces to a Hamiltonian system in equilibrium, such that $\partial_t P_{eq} = \mathcal{L}_C P_{eq} = 0$ with a Gibbs distribution as the equilibrium solution. Thus,

$$P_{eq}(\Gamma) = \frac{1}{Z} \exp \left\{ -\frac{H}{k_B T} \right\}, \quad (3.15)$$

where Z is the partition function and H is the unperturbed Hamiltonian. If all of the original DPD forces are present, the equilibrium distribution will be achieved if and only if $\mathcal{L}_D P_{eq} = 0$. It can be shown that this requirement is satisfied when the detailed balance (DB) condition given in eq. (3.8) holds. The DB condition also implies the existence of an H theorem for any DP system, i.e. that the Gibbs distribution is the unavoidable equilibrium distribution. It was shown by Marsh et al. [72] that in this case, the system's free energy must also monotonically approach its equilibrium value.

The thermodynamic description of DPD historically started with the derivation of the equation of state by Groot and Warren [70]. In this, the pressure in the DP

system was measured using the virial theorem

$$\begin{aligned}
 p &= nk_B T + \frac{1}{3V} \left\langle \sum_{j>i} (\mathbf{r}_i - \mathbf{r}_j) \cdot \mathbf{F}_i \right\rangle \\
 &= nk_B T + \frac{1}{3V} \left\langle \sum_{j>i} (\mathbf{r}_i - \mathbf{r}_j) \cdot \mathbf{F}_{ij}^C \right\rangle \\
 &= nk_B T + \frac{2\pi}{3} n^2 \int_0^1 r f(r) g(r) r^2 dr,
 \end{aligned} \tag{3.16}$$

where $g(r)$ is the radial distribution function. The second of these expressions is the most convenient for direct measurement in simulations, and is valid provided that the constraint on the DB parametrization given in eq. (3.8) is met. By varying the density and measuring pressure, the following relation was obtained

$$p = nk_B T + \alpha n^2 \quad (\alpha = 0.101 \pm 0.001), \tag{3.17}$$

which is valid for densities $n > 2$. It should be noted that, as long as conservative forces are relatively weak, this approximation is valid for any choice of the weight functions such that $\omega(r_c) = 0$ [73]. Thus, the dimensionless compressibility

$$\kappa = \frac{1}{k_B T} \left(\frac{\partial p}{\partial n} \right)_T \approx 1 + 0.2an/k_B T \tag{3.18}$$

can be used to adjust the system's compressibility to that of any real system simply by change of the conservative interaction parameter a . For instance, Groot and Warren [70] found that the value $a = 75k_B T/n$ yields a compressibility equivalent to that of water.

3.2.3 Hydrodynamics

The DPD simulation technique emerged originally as a method for modelling the rheological properties of complex fluids. Therefore there has been a substantial effort to recover rigorous hydrodynamic equations [72, 74] and obtain explicit transport coefficients in the terms of DP model parameters using kinetic theory [72, 75, 76].

In this section the kinetic theory derivations by Marsh, Backs and Ernst [72] are summarised, but it should be noted that there is another way to recover the hydrodynamic equations and so obtain the transport coefficients. Espanol in Ref. [74] established linearised Navier-Stokes equations using a Mori-Zwanzig projection operator technique and implicitly obtained transport coefficients in the form of Green-Kubo

formulae.

The starting point in the derivation of the transport equations is to obtain the general rate of change equation. Let us consider the time evolution of an arbitrary macroscopic quantity $A(\Gamma)$, which does not depend on time explicitly. Its average can be written

$$\langle A \rangle = \int d\Gamma A(\Gamma) P(\Gamma, t). \quad (3.19)$$

Then, by substituting the FPE (3.12) into eq. (3.19) and performing integration over all space Γ

$$\partial_t \langle A \rangle = \int d\Gamma A(\Gamma) \partial_t P(\Gamma; t) = \int d\Gamma A(\Gamma) [\mathcal{L}_C + \mathcal{L}_D] P(\Gamma; t), \quad (3.20)$$

the *general rate of change equation* for any macroscopic variable $A(\Gamma)$ is obtained.

Next consider the conserved density fields, which are the mass density $\rho(\mathbf{r}, t) = mn(\mathbf{r}, t)$ and the momentum density $\rho(\mathbf{r}, t)\mathbf{u}(\mathbf{r}, t)$. Here $n(\mathbf{r}, t)$ is the number density field and $\mathbf{u}(\mathbf{r}, t)$ is the velocity field, defined through

$$\begin{aligned} n(\mathbf{r}, t) &= \left\langle \sum_i \delta(\mathbf{r} - \mathbf{r}_i) \right\rangle = \int d\mathbf{v} f(\mathbf{v}, \mathbf{r}, t), \\ n\mathbf{u}(\mathbf{r}, t) &= \left\langle \sum_i \mathbf{v}_i \delta(\mathbf{r} - \mathbf{r}_i) \right\rangle = \int d\mathbf{v} f(\mathbf{v}, \mathbf{r}, t) \mathbf{v}, \end{aligned} \quad (3.21)$$

where $f(\mathbf{v}, \mathbf{r}, t) = f(\mathbf{x}, t)$ is the single-particle distribution function. Application of eq. (3.20) to the conserved mass and momentum densities (3.21) yields appropriate *balance equations*

$$\begin{aligned} \partial_t \rho &= -\nabla \cdot \rho \mathbf{u}, \\ \partial_t (\rho \mathbf{u}) &= -\nabla \cdot (\rho \mathbf{u} \mathbf{u} + \mathbf{\Pi}), \end{aligned} \quad (3.22)$$

which are the standard equations of *continuity* and *momentum conservation*. The stress tensor $\mathbf{\Pi}$ in the local rest frame of the fluid is the sum of kinetic (K), collisional transfer (C) and dissipative (D) contributions

$$\mathbf{\Pi} = \mathbf{\Pi}^K + \mathbf{\Pi}^C + \mathbf{\Pi}^D. \quad (3.23)$$

The first two contributions are present in any conservative system, whereas the last contribution to the momentum flux is due to the dissipative forces between particles. Random forces should not, however, contribute to the momentum flux, and this

expectation is, indeed, born out in simulations: in equilibrium, the time average dissipative contribution is zero, and the equilibrium pressure $\mathbf{\Pi} = p_{eq}\mathbb{I}$ contains only kinetic and collisional contributions, where p_{eq} is the equilibrium pressure given by the virial theorem (3.16). Away from global equilibrium, however, the pressure *does* include extra terms due to the dissipative contribution, i.e. viscosities.

The next step in kinetic theory is to obtain the Fokker-Planck-Boltzmann equation (FPBE) which is an approximate kinetic equation for the single particle distribution function $f(\mathbf{x}; t)$. It is derived by applying the general rate of change equation (3.20) to $f(\mathbf{x}; t)$. Assuming the strong damping limit (large γ), all of the conservative forces are further neglected [72], and making the *molecular chaos* assumption for the two-particle distribution function, $f^{(2)}(\mathbf{x}, \mathbf{x}', t)$ becomes

$$f^{(2)}(\mathbf{x}, \mathbf{x}', t) \approx f(\mathbf{x}, t)f(\mathbf{x}', t). \quad (3.24)$$

The nonlinear FPBE can be solved and analysed using the Chapman-Enskog method. According to this, there are two stages in the evolution of the single-particle distribution function: a rapid kinetic stage and a slow hydrodynamic stage. In the DPD model, the characteristic kinetic time is estimated as $t_0 \sim 1/(\gamma nr_c^3)$ [72]. The balance equations (3.22) correspond to this kinetic stage, whereas for the hydrodynamic stage a *Navier-Stokes equation* can be derived for the slowly varying macroscopic fields $n(\mathbf{r}, t)$ and $\mathbf{u}(\mathbf{r}, t)$

$$\partial_t(\rho\mathbf{u}) + \nabla \cdot (\rho\mathbf{u}\mathbf{u}) = -k_B T \nabla n + \nabla \cdot (2\eta\mathbf{D} + \zeta\nabla \cdot \mathbf{u}\mathbb{I}). \quad (3.25)$$

Here η and ζ are the shear and bulk viscosities, to be discussed in the next section, and \mathbf{D} is the second-rank traceless tensor $D_{\alpha\beta} = \frac{1}{2} (\nabla_\alpha u_\beta + \nabla_\beta u_\alpha - \frac{2}{3} \delta_{\alpha\beta} \nabla \cdot \mathbf{u})$.

The energy density field $e(\mathbf{r}, t)$ is a rapidly varying function of time and, in any DPD system, exhibits rapid relaxation to a local equilibrium state on the time scale t_0 . Therefore, a proper macroscopic equation for $e(\mathbf{r}, t)$ does not exist and no DPD system can maintain a temperature gradient on the hydrodynamic time scale.

Transport Coefficients

The transport coefficients for DPD systems can be calculated using a number of techniques. Originally Hoogerbrugge and Koelman [6] estimated the kinematic viscosity in the continuum limit approximation. Later their results were extended and clarified using the kinetic [72, 75, 77] and Mori [74, 76] theories.

Expressions for the explicit bulk and shear viscosities were obtained by Marsh,

Backx and Ernst (MBE) [72] using kinetic theory in the assumption that conservative forces are absent. This gives

$$\zeta = \zeta_D + \zeta_K = \frac{\gamma mn^2}{2d^2} [r^2\omega] + \frac{k_B T}{\gamma[\omega]} = \frac{1}{d} n k_B T \left(\frac{\omega_0 t_w^2}{2} + \frac{1}{\omega_0} \right), \quad (3.26)$$

$$\eta = \eta_D + \eta_K = \frac{\gamma mn^2}{2d(d+2)} [r^2\omega] + \frac{dk_B T}{2\gamma[\omega]} = \frac{1}{2} n k_B T \left(\frac{\omega_0 t_w^2}{d+2} + \frac{1}{\omega_0} \right), \quad (3.27)$$

where d is the dimensionality of space, $[f(r)] \equiv \int f(r) d\mathbf{r}$ denotes the spatial average for any function f , $\omega_0 = 1/t_0 = \gamma n[\omega]/3$ is the characteristic relaxation rate and $t_w = [r^2\omega]/([w]\bar{v}^2) \sim r_c^2/\bar{v}^2$ is the average traversal time of an action sphere with $\bar{v} = \sqrt{k_B T/m}$ the average thermal velocity. Therefore t_0 and t_w may be seen as two intrinsic time scales of the DPD fluid.

Viscosity coefficients in MBE theory have two contributions, one kinetic and one dissipative, arising from the relevant terms of the stress tensor given in eq. (3.23). The kinetic contribution arises due to the motion of the particles themselves, i.e. it is caused by their momenta. On the other hand, the dissipative contribution results from the momentum transfer originating directly from the dissipative forces. In terms of the intrinsic time scales, if $t_w > t_0$ then dissipative terms are dominant, whereas if $t_w < t_0$ the DPD fluid is in the kinetic regime and dominated by the kinematic viscosities.

Comparison with simulation results [6, 72] reveals that, at large $n\gamma$ and small timestep δt , the viscosities are in very good agreement with theoretical predictions. This corresponds to the hydrodynamic regime, which was originally described by Hoogerbrugge and Koelman.

At small $n\gamma$ and high temperature $k_B T$, the system is in the kinetic regime, where significant discrepancies between theory and simulation are reported [72, 78]. In particular, the dissipative viscosity is still in good agreement with the simulation data, but the predicted kinetic contribution differs from that measured by as much as of a factor of three [75]. A few investigations have been made attempting to understand the origin of this discrepancy. Espanol and Serrano [79] considered correlation effects beyond the scope of MBE theory by looking at the velocity autocorrelation function in the DPD model. From this, they identified two dynamical regimes characterised by dimensionless parameters and successfully tested their theory in two dimensions. Evans [76] derived approximate viscosities based on the expanded basis set of the time evolution operators. Finally, a very plausible explanation was given by Masters and Warren [75], who argued that kinetic transport coefficients are well described by the Boltzmann pair collision theory. In this case,

the theory was in good agreement with the simulation data, and MBE theory was recovered in a Vlasov mean field approximation.

So, in general it is very important to understand which dynamic regime a given simulated system corresponds to. While the explicit transport coefficients given by eqs. (3.26, 3.27) can be very useful in evaluating system parameters and predicting system behaviour, they are only valid for certain dynamic regimes. Also, care must be taken when conservative forces are present, as they will introduce additional terms which are not present in the original derivations given in eqs. (3.26, 3.27).

The self-diffusion coefficient, D , of a DPD system [72, 76] contains only kinetic contributions and does not have dissipative terms

$$D = \frac{dk_B T}{\rho \gamma[\omega]}. \quad (3.28)$$

The Schmidt number $Sc = \nu/D$ is a dimensionless number approximating the ratio of the momentum diffusivity (kinematic viscosity ν) and the mass transfer diffusion coefficient D . It is used to characterise fluid flows in which there are simultaneous momentum and mass diffusion convection processes. For the DPD fluid, it is estimated as

$$Sc = \frac{\nu}{D} = \frac{1}{2} + \frac{n\gamma^2\rho}{2d^2(d+2)k_B T} [r^2\omega][\omega]. \quad (3.29)$$

For the choices of parameters and weight functions (3.9) typically used in simulations, the Schmidt number is of order of unity, that is at least three orders less than that of real fluids. This fact was first noted and quantified in simulations by Groot and Warren [70]. This is an intrinsic problem in DPD that causes flowing fluid particles to have a slow response to rapid changes in the surrounding boundaries. As a result, conventional DPD fails to simulate complex rheology of real fluids due to its slow dynamic response. This issue can be explained by the lack of shear dissipative forces, as the dissipation between two particles always disappears if \mathbf{v}_{ij} is normal to \mathbf{e}_{ij} . This problem has been recently addressed by Fan et al. [80], who proposed a way to resolve the problem by modifying the weight functions and/or by increasing the cut-off radius r_c . The latter method is the more efficient and allows realistic values of the Schmidt number of order $\mathcal{O}(10^3)$ to be achieved with a reasonable increase in the computational cost. This improvement also leads to an increase in the shear viscosity η .

The Reynolds number for a DPD fluid can be estimated as

$$\text{Re} = \frac{\text{Inertia forces}}{\text{Viscous forces}} = \frac{\rho \bar{v} r_c}{\eta}, \quad (3.30)$$

where r_c is chosen to be the fluid's characteristic length. So, in typical non-equilibrium DPD simulations, Reynolds numbers are of order ten, which strictly corresponds to the laminar flow regime.

Finally, the speed of sound in a DPD system has the following form

$$c = \sqrt{\frac{k_B T}{m}} \quad (3.31)$$

3.2.4 Fluid Particle Model

The fluid particle model (FPM) is a generalisation of DPD which was introduced by Espanol [77, 81] in order to capture certain aspects of fluid particle behaviour not present in the original model. Specifically, in the DPD model, two particles moving in opposite directions with parallel velocities will not decelerate each other due to viscous effects. As noted above, this leads, for example, to small values for the shear viscosity and Schmidt number in typical DPD simulations.

FPM extends DPD by introducing non-central shear forces between particles. Then, further angular degrees of freedom are added to the particle descriptions in order to achieve conservation of angular momentum. Consequently, the resulting FPM model has a better founded physical basis than the original DPD approach for modelling Newtonian fluids, especially for low density systems.

The FPM Formalism

FPM is very similar in spirit to DPD, the only significant differences lying in the supplementary spin variable and extra forces between particles. This means that additional care is needed for the treatment of angular coordinates and their conjugate torques. Many arguments relating to DPD are also fully applicable to FPM, so in this section they are omitted and only key results are summarised.

The particle motion is again determined by Newton's equations of motion

$$\frac{d\mathbf{r}_i}{dt} = \mathbf{v}_i, \quad \frac{d\mathbf{v}_i}{dt} = \frac{1}{m_i} \mathbf{F}_i, \quad \frac{d\boldsymbol{\omega}_i}{dt} = \frac{1}{I} \mathbf{N}_i, \quad (3.32)$$

where \mathbf{N}_i is the total torque acting on the fluid particle i , $\boldsymbol{\omega}_i$ is the angular velocity and I is the particle's moment of inertia. It is assumed that particles are

spherical/circular, so the moments of inertia are equal for all axes.

The force between any two particles consists of conservative, dissipative and random parts in much the same way as in DPD. For the sake of convenience, the dissipative part is split here into translational (T) and rotational (R) components

$$\mathbf{F}_{ij} = \mathbf{F}_{ij}^C + \mathbf{F}_{ij}^T + \mathbf{F}_{ij}^R + \tilde{\mathbf{F}}_{ij} \quad (3.33)$$

$$\mathbf{N}_{ij} = -\frac{1}{2}\mathbf{r}_{ij} \times \mathbf{F}_{ij} \quad (3.34)$$

where

$$\mathbf{F}_{ij}^C = -\nabla\phi_{ij} \quad (3.35)$$

$$\mathbf{F}_{ij}^T = -\gamma m \mathbf{M}(r_{ij}) \cdot \mathbf{v}_{ij} \quad (3.36)$$

$$\mathbf{F}_{ij}^R = -\gamma m \mathbf{M}(r_{ij}) \cdot \left(\frac{\mathbf{r}_{ij}}{2} \times [\boldsymbol{\omega}_i + \boldsymbol{\omega}_j] \right) \quad (3.37)$$

$$\tilde{\mathbf{F}}_{ij} = \sigma m (\tilde{A}(r_{ij}) d\mathbf{W}_{ij}^S + \tilde{B}(r_{ij}) \frac{1}{d} \text{tr}[d\mathbf{W}_{ij}] \mathbb{I} + \tilde{C}(r_{ij}) d\mathbf{W}_{ij}^A) \cdot \mathbf{e}_{ij} \quad (3.38)$$

Here $d\mathbf{W}_{ij}$ is the independent matrix of Wiener increments with the superscripts A and S denoting its antisymmetrical and traceless symmetrical parts respectively. $\tilde{A}(r_{ij})$, $\tilde{B}(r_{ij})$ and $\tilde{C}(r_{ij})$ are dimensionless weight functions. Finally, the dimensionless matrix $\mathbf{M}(r_{ij})$ is given by

$$\mathbf{M}(r_{ij}) = A(r_{ij})\mathbb{I} + B(r_{ij})\mathbf{e}_{ij}\mathbf{e}_{ij}, \quad (3.39)$$

where $A(r_{ij})$ and $B(r_{ij})$ are scalar functions discussed below.

The conservative force \mathbf{F}^C is derived from the inter-particle potential ϕ_{ij} and performs exactly the same function as the equivalent term in DPD. Indeed, the form adopted for this potential usually coincides with that used in DPD.

The dissipative force contains two extra contributions as compared with DPD. There are non-central shear forces originating from both translational and rotational particle motions. Their effect can be explained using two simple examples. When two particles are revolving while standing still, rotational dissipative forces are needed to damp the difference between their angular velocities and so give rise to translational motion. Further, when two particles are moving in opposite directions with antiparallel velocities, but along non-intersecting trajectories, viscous translational forces should decrease the particles' relative velocity and so cause them to rotate.

These two additional dissipative forces require the introduction of two extra random forces in order for equilibration to be achieved. The random force in FPM

is specified by a matrix of independent Wiener elements, compared with only one random variable in DPD, so as to be consistent with the tensorial structure of the dissipative force. Wiener matrices are symmetric under particle interchange $d\mathbf{W}_{ij} = d\mathbf{W}_{ji}$, so as to conserve momentum locally. The given choice of torques in eq. (3.34) also implies that the total angular momentum $J = \sum_i \mathbf{r}_i \times \mathbf{q}_i + I\boldsymbol{\omega}_i$ is conserved, i.e. $\dot{J} = 0$.

A fluctuation-dissipation theorem exists for the FPM model, but its form is more complicated than that derived for DPD. Thus,

$$A = \frac{1}{2}(\tilde{A}^2 + \tilde{C}^2), \quad B = \frac{1}{2}(\tilde{A}^2 - \tilde{C}^2) + \frac{1}{d}(\tilde{B}^2 - \tilde{A}^2), \quad \gamma = \frac{\sigma^2 m}{2k_B T}. \quad (3.40)$$

The above relations do not specify the particular forms of the weight functions, so some of them can be chosen arbitrarily. Given that the rheological parameters of a fluid are fully dependent on the above weight functions, as discussed below, their choice is mainly used for mapping the properties of a specific Newtonian fluid onto the model.

It should be also noted that the original DPD model is completely recovered by putting

$$A(r) = 0, \quad B(r) = \omega(r). \quad (3.41)$$

Thus, FPM by itself is very universal. Not only is the DPD model recovered when eq. (3.41) is met, but also conventional MD can be obtained by simply removing dissipative and stochastic forces.

Transport Coefficients

The transport coefficients for FPM can be derived using kinetic theory [77] in much the same way as they are for DPD. As a result of introducing the spin variable, an additional rotational viscosity η_R is included in FPM, which can be significant in systems where rotational diffusion is important. The viscosities are given by

$$\zeta = \gamma m \rho^2 \left(\frac{A_2}{2d} + \frac{(d+2)}{2d} B_2 \right) + \frac{k_B T}{\gamma d (A_0 + B_0)}, \quad (3.42)$$

$$\eta = \frac{1}{2} \gamma m \rho^2 \left(\frac{A_2}{2} + B_2 \right) + \frac{k_B T}{\gamma d (A_0 + B_0)}, \quad (3.43)$$

$$\eta_R = \gamma m \rho^2 \frac{A_2}{2}, \quad (3.44)$$

where η_R is a rotational viscosity and the volume integrals are given by

$$\begin{aligned} A_0 &= \int_0^{r_c} A(r) dr & A_2 &= \frac{1}{d} \int_0^{r_c} r^2 A(r) dr \\ B_0 &= \frac{1}{d} \int_0^{r_c} B(r) dr & B_2 &= \frac{1}{d(d+2)} \int_0^{r_c} r^2 B(r) dr. \end{aligned}$$

Thus, the fluid's predicted rheological properties are completely defined by parameters controlling the inter-particle forces in the model. Again, if eq. (3.41) is satisfied, the viscosities coincide with those predicted for the DPD model.

Discussion

The FPM can be seen as an improvement on DPD which remedies some of its problems and has a better founded theoretical background. In spite of FPM's virtues, the DPD model is still the more widely used technique. There are a few reasons for this. Firstly, most of FPM's advances over the DPD model are only relevant for certain situations, e.g. in flows with complex boundaries, and even in some of those cases these issues can be still resolved using DPD, e.g. by increasing the cut-off radius r_c . Secondly, the FPM is less computationally efficient and is more difficult to implement than DPD due to the added rotational degrees of freedom and the more complex forces. So, DPD continues to be the more likely to be chosen, largely due to its simplicity. Nevertheless, it is important to note that the FPM can still address applications which are beyond the DPD method.

3.2.5 DPD Drawbacks

Most of the success and popularity of the DPD method comes from the method's simplicity and robustness. Further, the great similarity between DPD and molecular dynamic methods, in terms of their technical implementation, allows substantial reuse of the great legacy of available MD codes. Nevertheless, the method's simplicity comes at the expense of more fundamental issues. There are a number of important problems in DPD which need to be resolved in order for the technique to gain wider credibility. Whilst a number of authors have raised individual problems of DPD in separate publications, no comprehensive review of these currently exists. Thus, in this section we make an attempt to outline the major problems with DPD.

(i) Equation of state. Making the standard choice of having conservative forces which depend linearly on the inter-particle distance, see eq. (3.7), imposes a fixed equation of state (EOS), given by eq. (3.17), which is quadratic in density. This fixed EOS is not able to describe non-ideal fluids or fluid-fluid phase transitions. To

counter this, an alternative approach for deriving conservative forces was proposed by Pagonabarraga and Frenkel [73]. In this, conservative forces are calculated from the free-energy density that determines the thermodynamics of the system. Nevertheless, the debate is still open as to which form of DPD is preferable – Groot-Warren [70] or Pagonabarraga-Frenkel [73].

(ii) Upper limit on coarse graining. DPD is a mesoscopic simulation technique which is, inherently, a coarse-grained bottom-up approach. Thus, each particle in DPD can be considered as representing N_m molecules [70]. Keaveny et al. [82] have compared DPD and MD simulations of a simple fluid and particularly studied the effect of the value of the number N_m of molecules representing a DPD bead. Specifically, a Lennard-Jones fluid, simulated by MD, was compared with DPD, the parameters of the latter being varied so as to match the mass density, viscosity and compressibility of the L-J fluid. From this, it was found that good agreement could only be achieved for $N_m < 5$ for both static and hydrodynamic simulations. This low upper limit is a severe limiting factor for what purports to be a mesoscopic simulation technique.

(iii) Physical length and time scales. The interactions between DPD particles were postulated from symmetry principles which effectively ensure correct hydrodynamic behaviour. While this, on its own, does not fix the length and time scales on which a DPD simulation operate, the presence of thermal fluctuations implies the mesoscopic regime [83]. This is actually addressed in a specific context in point (ii), but no general result has been determined.

(iv) Transport coefficients. There is no direct predictive link between a set of DPD simulation parameters and the transport coefficients which emerge from such a simulation. An approximation to kinetic theory is required to enable prediction of these coefficients. Rather, as was shown in §3.2.3, viscosities can be derived for limiting cases in which the role of conservative forces is negligible. This is a manifestation of the fundamental mismatch between the bottom-up DPD method and conventional continuum descriptions.

(v) Configurational temperature. One of the biggest practical advantages of the DPD method is its ability to operate with a long simulation time step, due to the soft inter-particle potentials employed. In the original studies, simulation stability with respect to increasing timestep was addressed by monitoring of the kinetic temperature. However, it has subsequently emerged that, at large time step, systems with stable kinetic temperature can develop configurational temperatures that differ significantly from the desired value [84, 46]. The configurational temperature relates to conservative forces between particles and maintaining it at its

correct value indicates that configurations are being sampled appropriately from the canonical distribution. This is especially important in cases where conservative forces dominate, such as polymers, amphiphile-based membranes etc. While use of modified or hybrid simulation methods can yield some improvements in this regard, the central issue is the choice of timestep.

3.3 Smoothed Particle Hydrodynamics

Smoothed Particle Hydrodynamics (SPH) is the oldest mesh-free method, having originally been introduced in the late 1970's to simulate unbounded three-dimensional problems in astrophysics [9, 10]. It is a truly mesh-free Lagrangian technique, which has successfully been applied to a broad range of problems such as free surface flows [85], underwater explosions [86], problems of heat conduction [87], dynamic response with material strength [88] and many other fluid and mechanical applications [89]. There is an excellent review [90] and a book [89] about the SPH method, in which more specific details can be found. In this section, therefore, we limit ourselves to a brief review of the basics of the SPH method and various enhancements which are directly relevant to the simulations presented later in this Thesis.

3.3.1 SPH Formalism

SPH is a mesh-free method which uses integral interpolation to represent field variables. The basis of this technique can be illustrated by considering a smooth function f over a domain of interest Ω . This function can represent any physical quantity, e.g. temperature. SPH is based on an integral estimate $\langle f \rangle$ of the function f at a point \mathbf{x} , which is defined as

$$\langle f(\mathbf{x}) \rangle = \int f(\mathbf{x}') W(\mathbf{x} - \mathbf{x}', h) d\mathbf{x}'. \quad (3.45)$$

Here, $W(\mathbf{x} - \mathbf{x}', h)$ is an interpolation kernel and h is a smoothing length which defines the domain over which the kernel acts. In the case $W(\mathbf{x} - \mathbf{x}', h) = \delta(\mathbf{x} - \mathbf{x}')$, eq. (3.45) simplifies to the exact relation $\langle f(\mathbf{x}) \rangle = f(\mathbf{x})$ and the interpolant reproduces f exactly. Thus, the integral interpolant $\langle f(\mathbf{x}) \rangle$ can be seen as a smoothed version of the original function f . This is the origin of the term ‘‘smoothed’’ in the moniker SPH.

The interpolation kernel plays a very important role in terms of the accuracy and

stability of the SPH method, since it determines both the interpolation error and the influence volume of the simulated particles. Various kernels have been considered in the published literature and a number of requirements on kernels have also been suggested. From these, the following essential requirements have been identified:

1. The Dirac delta function condition:

$$\lim_{h \rightarrow 0} W(\mathbf{x} - \mathbf{x}', h) = \delta(\mathbf{x} - \mathbf{x}'). \quad (3.46)$$

2. The normalisation condition:

$$\int W(\mathbf{x} - \mathbf{x}', h) d\mathbf{x}' = 1. \quad (3.47)$$

3. The compact support condition, which states that the kernel function should vanish beyond a certain distance defined as the smoothing length, h , multiplied by a scale factor k . This can be written as:

$$W(\mathbf{x} - \mathbf{x}', h) = 0, \quad |\mathbf{x} - \mathbf{x}'| > kh. \quad (3.48)$$

The domain within which the smoothing function is non-zero is called the support domain of the point \mathbf{x} .

4. The kernel function should be a symmetric, or even, function, i.e.

$$W(\mathbf{x} - \mathbf{x}', h) = W(\mathbf{x}' - \mathbf{x}, h). \quad (3.49)$$

The fluid in an SPH simulation is represented as a set of discrete particles, each with a small mass. If we rewrite the interpolation integral (3.45) as

$$\int \frac{f(\mathbf{x}')}{\rho(\mathbf{x}')} W(\mathbf{x} - \mathbf{x}', h) \rho(\mathbf{x}') d\mathbf{x}', \quad (3.50)$$

where $\rho(\mathbf{x}')$ is the density of the fluid at the point \mathbf{x}' then we can identify $\rho(\mathbf{x}') d\mathbf{x}'$ with the mass of that fluid element. This continuous integral can, then, be approximated as a summation over neighbouring mass elements. This yields the discretised interpolant:

$$\langle f(\mathbf{x}) \rangle = \sum_j f_j \frac{m_j}{\rho_j} W(\mathbf{x} - \mathbf{x}_j, h), \quad (3.51)$$

where m_j and ρ_j are, respectively, the mass and density of the j th particle and $f_j = f(\mathbf{x}_j)$. This summation is taken to run over all of the particles which are in

the support domain of the particle at \mathbf{x} . In practice, the kernel W is chosen such that it decreases rapidly with distance and, as stated in requirement (3.48) on kernel functions, vanishes beyond a distance kh . k is typically equal to 2 or 3, depending on the kernel. This effectively reduces the summation over the whole domain to a summation over the finite support domain of a single point. The smoothing length h , on the other hand, needs to be made big enough to ensure that there are sufficient particles in each support domain to enable accurate interpolations to be made.

The simplest example of such a kernel estimate can be provided by estimating the particles' density. Setting $f_j = \rho_j$ in eq. (3.51) yields:

$$\rho(\mathbf{x}) = \sum_j m_j W(\mathbf{x} - \mathbf{x}_j, h), \quad (3.52)$$

which demonstrates how the masses of a set of discrete particles can be smoothed in order to yield an estimate of the density field.

SPH approximates the strong form of PDEs and, thus, its ability to approximate derivatives is of high importance. The calculation of derivatives is based on the interpolation rules given above. In order to estimate the spatial derivative $\partial f(\mathbf{x})/\partial \mathbf{x}$, it should simply be substituted for $f(\mathbf{x})$ in eq. (3.45). Integrating this by parts and, subsequently, applying the divergence theorem then yields

$$\left\langle \frac{\partial f(\mathbf{x})}{\partial \mathbf{x}} \right\rangle = \int_S f(\mathbf{x}') W(\mathbf{x} - \mathbf{x}', h) \mathbf{n} \, dS - \int_{\Omega} f(\mathbf{x}') \frac{\partial W(\mathbf{x} - \mathbf{x}', h)}{\partial \mathbf{x}'} \, d\mathbf{x}'. \quad (3.53)$$

Here, the first term on the right hand side is the so-called residual boundary integral. When the particle's support domain is fully located inside the problem domain Ω , the residual boundary integral is equal to zero. If, on the other hand, the support domain is truncated by a boundary, the residual boundary integral needs to be accounted for. In the conventional SPH approach, however, this term is simply dropped such that boundary conditions need to be considered separately, as discussed below. Setting the residual boundary integral to zero and discretising the continuum equation in the same manner, as in eq. (3.51), yields the following approximation of the spatial derivative:

$$\left\langle \frac{\partial f(\mathbf{x})}{\partial \mathbf{x}} \right\rangle_i = - \sum_j f_j \frac{m_j}{\rho_j} \frac{\partial W(\mathbf{x}_i - \mathbf{x}_j, h)}{\partial \mathbf{x}_j}. \quad (3.54)$$

Thus, the process of approximating derivatives in the SPH method, leads to the differentiation operator being passed from the field variable itself to the known kernel function. One consequence of this is that the form of the derivative given in eq. (3.54) does not necessarily vanish if $f(\mathbf{x})$ is constant. This can be remedied by

employing the following relation:

$$\frac{\partial f}{\partial \mathbf{x}} = \frac{1}{\Phi} \left(\frac{\partial(\Phi f)}{\partial \mathbf{x}} - f \frac{\partial \Phi}{\partial \mathbf{x}} \right), \quad (3.55)$$

where Φ is any differentiable function. Eq. (3.55) can be rewritten in the SPH formalism as follows:

$$\left\langle \frac{\partial f(\mathbf{x})}{\partial \mathbf{x}} \right\rangle_i = \frac{1}{\Phi_i} \sum_j \Phi_j \frac{m_j}{\rho_j} (f_j - f_i) \frac{\partial W_{ij}}{\partial \mathbf{x}_i}, \quad (3.56)$$

where W_{ij} denotes $W(\mathbf{x}_i - \mathbf{x}_j, h)$. Employing this form of the derivative approximation does ensure that it vanishes when the function $f(\mathbf{x})$ is constant.

Ultimately, it is the choice of the function Φ that generates all of the different versions of the derivatives given in the literature. For instance, setting Φ to 1 gives

$$\left\langle \frac{\partial f(\mathbf{x})}{\partial \mathbf{x}} \right\rangle_i = \sum_j \frac{m_j}{\rho_j} (f_j - f_i) \frac{\partial W_{ij}}{\partial \mathbf{x}_i}, \quad (3.57)$$

and the choice $\Phi = \rho$ leads to

$$\left\langle \frac{\partial f(\mathbf{x})}{\partial \mathbf{x}} \right\rangle_i = \frac{1}{\rho_i} \sum_j m_j (f_j - f_i) \frac{\partial W_{ij}}{\partial \mathbf{x}_i}. \quad (3.58)$$

It turns out that this choice of mathematically equivalent SPH discretisations of the differential operator is very important when the SPH is applied to discretise PDEs describing physical phenomena. This will be demonstrated in §3.3.2 using the example of the continuity equation.

Second order derivatives can be estimated by differentiating the SPH interpolant twice. Thus, the straightforward application of this procedure to the field variable function $f(\mathbf{x})$ yields:

$$\left\langle \frac{\partial^2 f(\mathbf{x})}{\partial x^\alpha \partial x^\beta} \right\rangle_i = \sum_j f_j \frac{m_j}{\rho_j} \frac{\partial^2 W_{ij}}{\partial x_i^\alpha \partial x_i^\beta}. \quad (3.59)$$

However, this form is very susceptible to particle disorder. A different, improved version of second-order derivative approximation is obtained by considering a Taylor expansion of the function f and making use of the isotropic nature of the weight

function W_{ij} , which leads to the following identity [65, 91]:

$$\left\langle \frac{\partial^2 f(\mathbf{x})}{\partial x^\alpha \partial x^\beta} \right\rangle_i = \sum_j \frac{m_j}{\rho_j} (f_i - f_j) \left(5 \frac{\Delta x^i \Delta x^j}{r^2} - \delta^{ij} \right) \frac{1}{r} \frac{\partial W_{ij}}{\partial r}, \quad (3.60)$$

where $r = |\mathbf{x}_i - \mathbf{x}_j|$.

3.3.2 SPH Conservation Law Equations

SPH is a numerical technique which solves an initial value problem defined by the conservation laws of continuum mechanics combined with the constitutive relations of the given material. In this section, we consider SPH discretisations of two basic conservation laws which are present in practically every system, namely the continuity equation and the linear momentum equation.

The continuity equation is the fundamental equation of fluid dynamics which states the conservation of mass and is conventionally written in the following form

$$\frac{D\rho}{Dt} = -\rho \nabla \cdot \mathbf{v}, \quad (3.61)$$

where \mathbf{v} is the velocity field. This equation can be discretised using either of the SPH discretisations given by eqs. (3.57, 3.58), which, respectively, yield the two following discretised SPH forms:

$$\left\langle \frac{D\rho}{Dt} \right\rangle_i = \rho_i \sum_j \frac{m_j}{\rho_j} (\mathbf{v}_i - \mathbf{v}_j) \cdot \frac{\partial W_{ij}}{\partial \mathbf{x}_i}, \quad (3.62)$$

$$\left\langle \frac{D\rho}{Dt} \right\rangle_i = \sum_j m_j (\mathbf{v}_i - \mathbf{v}_j) \cdot \frac{\partial W_{ij}}{\partial \mathbf{x}_i}. \quad (3.63)$$

Both of these approximations vanish when the velocity field is constant. It should be noted, though, that eq. (3.63) does not explicitly involve the density, whereas eq. (3.62) clearly does. Although these equations are both mathematically correct, it was shown in [92] that the expression with explicit ρ is more accurate in modelling systems involving two or more fluids with density ratios greater than 2. This can be demonstrated using the example of two different fluids in close contact. Ideally, the estimate of $\nabla \cdot \mathbf{v}$ should be the same for all density ratios of these fluids. However, in practice eq. (3.63) will provide an inaccurate result for different densities, since the summation will involve particles with changed masses. Eq. (3.62), on the other hand, will provide consistent results since the ratio m_j/ρ_j will remain constant.

The linear momentum equation states the conservation of momentum and is

conventionally written in the form

$$\frac{D\mathbf{v}}{Dt} = \frac{1}{\rho} \nabla \cdot \boldsymbol{\sigma}, \quad (3.64)$$

where $\boldsymbol{\sigma}$ is the Cauchy stress tensor. The latter is made up of two parts, namely the isotropic pressure P and the extra-stress tensor $\boldsymbol{\tau}$, such that

$$\sigma^{ij} = -P\delta^{ij} + \tau^{ij}. \quad (3.65)$$

We have written the linear momentum equation (3.64) in the general form. For a conventional Newtonian fluid with bulk viscosity ζ and shear viscosity η , this can be rewritten in a more traditional form:

$$\frac{D\mathbf{v}}{Dt} = -\nabla P + \eta \nabla^2 \mathbf{v} + \left(\zeta + \frac{\eta}{3} \right) \nabla \nabla \cdot \mathbf{v}. \quad (3.66)$$

There are at least three different SPH discretisations of eq. (3.64). The most commonly used of these is the form obtained by noting that

$$\frac{\nabla \sigma}{\rho} = \nabla \left(\frac{\sigma}{\rho} \right) + \frac{\sigma}{\rho^2} \nabla \rho. \quad (3.67)$$

Application of the SPH interpolation rules to the above equation yields, for the α -th component of the velocity field \mathbf{v} , the following approximation rule:

$$\left\langle \frac{Dv^\alpha}{Dt} \right\rangle_i = \sum_j m_j \left(\frac{\sigma_i^{\alpha\beta}}{\rho_i^2} + \frac{\sigma_j^{\alpha\beta}}{\rho_j^2} \right) \frac{\partial W_{ij}}{\partial x_i^\beta}. \quad (3.68)$$

Since $\partial W_{ij}/\partial \mathbf{x}_i = -\partial W_{ij}/\partial \mathbf{x}_j$, the force between two particles i and j is then equal and opposite and acts along the line joining the particle centres. This, in effect, exactly conserves linear and angular momentum, so making the discretisation (3.68) a better alternative to other discretisations which do not possess these properties.

3.3.3 SPH Artificial Viscosity

Artificial viscosity was initially introduced into SPH to avoid spurious oscillations in simulations of shock waves [93]. Since then, the majority of SPH simulations have employed this same approach in order to stabilise the numerical scheme. These spurious oscillations in velocity and pressure fields can occur in SPH due either to discontinuities in the velocity field or to algorithmic pathology in the approximations made to the governing PDEs. Similar numerical instabilities are present in the

finite difference method and finite elements method, and many remedies have been introduced to deal with such problems in the context of these methods. In the finite difference method, for instance, an artificial viscosity is often added to the discrete momentum equation in order to damp out numerical errors. Similar to FDM, SPH also approximates the strong form of PDEs and, thus, the inclusion of an artificial viscosity to suppress instabilities is the most straightforward choice. Many forms have been suggested for this artificial viscosity [9, 93], but the most popular is that of Monaghan and Gingold [93] which is obtained by including an extra term in the parenthesis of eq. (3.68) to give the alternative form

$$\frac{\sigma_i^{\alpha\beta}}{\rho_i^2} + \frac{\sigma_j^{\alpha\beta}}{\rho_j^2} + \Pi_{ij}\delta^{\alpha\beta}. \quad (3.69)$$

Here, the artificial viscous stress Π_{ij} is given as

$$\Pi_{ij} = \begin{cases} \frac{-\alpha\bar{c}_{ij}\mu_{ij} + \beta\mu_{ij}^2}{\bar{\rho}_{ij}}, & \mathbf{v}_{ij} \cdot \mathbf{x}_{ij} < 0 \\ 0, & \mathbf{v}_{ij} \cdot \mathbf{x}_{ij} \geq 0 \end{cases} \quad (3.70)$$

where

$$\mu_{ij} = \frac{h\mathbf{v}_{ij} \cdot \mathbf{x}_{ij}}{\mathbf{x}_{ij}^2 + 0.01h^2}, \quad (3.71)$$

$$\bar{c}_{ij} = \frac{c_i + c_j}{2}, \quad \bar{\rho}_{ij} = \frac{\rho_i + \rho_j}{2}, \quad (3.72)$$

$$\mathbf{v}_{ij} = \mathbf{v}_i - \mathbf{v}_j, \quad \mathbf{x}_{ij} = \mathbf{x}_i - \mathbf{x}_j. \quad (3.73)$$

In eq. (3.70), α and β are constants which are usually of order of unity. The term associated with α includes shear and bulk viscosities [90], and the second term, associated with β , is similar to the von Neumann-Richtmeyer viscosity. It is very important for resolving shocks, where it prevents unphysical particle penetration in high Mach number collisions by introducing an artificial pressure proportional to ρv^2 . The $0.01h^2$ term in the denominator of eq. (3.71) keeps the viscosity bounded when particles approach each other. This artificial viscosity is Galilean invariant. Another advantage of eq. (3.70) is that it guarantees the conservation of angular momentum.

Despite the fact that this artificial viscosity can be used to model many effects related to true viscosity, it has been shown that it provides inaccurate velocity profiles [94]. Nevertheless, both α and β terms have been shown to be important in simulations of viscoelastic free surface flows [95].

3.3.4 Completeness of the SPH

Having so far introduced the SPH approach mostly as a particle-based technique, we now proceed in this section with the consistency (or completeness) analysis of SPH, the basic definitions of which were introduced in §1.5.2.

There are two sources of the accuracy loss in the original SPH method. These come first from the original interpolation given by eq. (3.45) and then from the subsequent particle discretisation of this equation (3.51). Thus, in this section we initially consider kernel consistency before going on to analyse particle consistency.

Kernel Consistency

In order for equation (3.45) to be consistent to order p , it needs to represent polynomials up to this order exactly. It can be shown that the normalisation property (3.47) on kernel functions immediately guarantees that constants (0th order polynomials) will be interpolated exactly:

$$f(\mathbf{x}) = \int cW(\mathbf{x} - \mathbf{x}', h) d\mathbf{x}' = c \int W(\mathbf{x} - \mathbf{x}', h) d\mathbf{x}' = c. \quad (3.74)$$

For a linear function $f(\mathbf{x}) = c_0 + c_1\mathbf{x}$ the following condition should hold:

$$f(\mathbf{x}) = \int (c_0 + c_1\mathbf{x})W(\mathbf{x} - \mathbf{x}', h) d\mathbf{x}' = c_0 + c_1\mathbf{x}. \quad (3.75)$$

This equation can be rewritten by first simplifying it, using eq. (3.74), and then subtracting it from eq. (3.47) with both sides multiplied by \mathbf{x} . This yields:

$$\int (\mathbf{x} - \mathbf{x}')W(\mathbf{x} - \mathbf{x}', h) d\mathbf{x}' = 0. \quad (3.76)$$

This relation is always true since the weight function W is symmetric, as specified by eq. (3.49). Thus, the normalisation and symmetry conditions on weight functions guarantee 1st order consistency.

The following general requirement on weight functions, relating to their ability to represent polynomials of order p , can be obtained by considering the Taylor expansion of the function $f(\mathbf{x})$ [96, 97]:

$$\int (\mathbf{x} - \mathbf{x}')^p W(\mathbf{x} - \mathbf{x}', h) d\mathbf{x}' = 0. \quad (3.77)$$

In simulations of physical phenomena using SPH, the weight function is required always to be positive, to prevent negative unphysical values from being adopted by

certain field variables, e.g. density. Given this, however, it is apparent that the SPH interpolant can not represent 2nd order polynomials exactly, since the expression inside the integral (3.77) can never be negative. Thus, SPH can only achieve 1st order consistency in interior regions. Since the integral (3.77) is not supposed to be truncated by boundaries, it follows that, if no special treatment is introduced, SPH does not have even 0th order consistency near to boundaries.

Particle Consistency

In the previous subsection, it was shown that the continuum kernel approximation in SPH has 0th and 1st order consistencies for interior regions. The SPH particle discretisation of continuum equations further reduces this accuracy, such that the discretised equations may not even attain this order of consistency. The discrepancy in accuracy between a continuum equation and its discretised counterpart is called the particle inconsistency problem [96, 97, 98].

The SPH discretisations of the continuum consistency equations (3.74, 3.76) for uniform particle distribution in the interior region can be written as follows:

$$\sum_{j=1}^N W(\mathbf{x} - \mathbf{x}_j, h) \frac{m_j}{\rho_j} c = c, \quad (3.78)$$

and

$$\sum_{j=1}^N (\mathbf{x} - \mathbf{x}_j) W(\mathbf{x} - \mathbf{x}_j, h) \frac{m_j}{\rho_j} = 0. \quad (3.79)$$

These equations will not always hold for random particle distributions, examples of which can easily be generated. One of the simplest such examples is that of a particle on the boundary of a one-dimensional system. If we again consider the constant function $f(x) = c$, then for this particle the right hand side of eq. (3.78) becomes equal to $c/2$. For interior particles it is also very easy to demonstrate that consistency conditions do not hold in cases of non-uniformly distributed points.

Another important parameter which affects the accuracy of the method is the smoothing length h . For example, in a one dimensional case with uniform particle spacing and with a cubic spline kernel chosen as the smoothing function, SPH has zeroth order consistency for the interior particles if h is equal to the interparticle separation. If h is taken to have a different value, though, eq. (3.78) is not always satisfied and, consequently, the accuracy of results is affected.

Thus, the original SPH method does not even have zeroth order consistency in particle approximations. This is the direct cause of the low accuracy of the

original method, especially when it comes to either boundary particles, irregularly distributed nodes or particles with variable smoothing lengths.

3.3.5 SPH Drawbacks and Improvements

Despite the many virtues of SPH, such as its simple concept, robustness, mesh-free nature, ability to simulate large deformations, etc., it suffers from a number of inherent technical drawbacks. These have stimulated the development of a number of improvements on the original SPH method. The three main drawbacks are:

- the difficulty in enforcing essential boundary conditions [94, 88];
- the tensile instability [99, 100, 101, 102, 103];
- the lack of interpolation consistency [104, 105, 106].

It should be noted, though, that both boundary deficiency and tensile instability problems can be seen as arising directly from the particle inconsistency problem. Solutions to these two problems, which are discussed below, have been introduced at the particle-model level. However, some of these modifications have then gone on to be criticised as being arbitrary and shown to worsen some problems while solving others. On the other hand, corrections aimed directly at the particle inconsistency problem have the capacity to naturally remove the tensile instability problem and, in some cases, the particle deficiency (e.g., boundary condition) problem. In the remainder of this section we consider these issues in more detail along with the available solutions.

Boundary Conditions

Boundary condition implementation is always a nontrivial task in mesh-free methods and there is no universal approach for imposing the same. Since most mesh-free techniques have non-local interpolations as their foundation, the consequent lack of particles near to boundaries usually leads to accuracy deterioration in adjacent regions. The summation integrals for particles near to or at the boundary include only particles located inside the domain and this one-sided contribution causes the integral (3.45) to be truncated by the boundary. This is especially pronounced in the original SPH method, which does not even achieve zeroth-order consistency at boundaries.

A straightforward approach for correctly imposing boundary conditions would be to introduce a correction based on the residual boundary integral (3.53) estimation.

This idea has been considered by Campbell [107], but no numerical results have been presented. A subsequent test of this idea did not produce any satisfactory results [95].

The usual practice in imposing essential boundary conditions in SPH is to use virtual or ghost particles [89, 94, 88, 108]. There are two types of these particles. The virtual particles of the first type represent solid boundaries and are normally kept fixed in space. These are called the “boundary particles”. It has been suggested that an extra repulsive force similar to the Lennard-Jones interatomic potential could be used in the interaction between these particles and the bulk particles, to prevent the latter from penetrating the solid walls [85]. However, it was found by Morris et al. [94] that if boundary particles contribute to the usual expressions for velocity, pressure and gradient, then there is no need to impose this extra repulsive force. This is due to the fact that, when a bulk particle approaches a boundary particle, the densities of both particle types increase. This leads to an increase in the particle pressure and, so, generates a sufficient repulsion.

The virtual particles of the second type are located outside the solid boundary, spanning space to a depth of at least the kernel’s support length $2h$ from the boundary. Such particles are called the “image particle”. Unlike boundary particles, these particles have fixed densities. In order to impose no-slip boundary condition, these image particles also have velocity values set individually for each bulk particle they interact with. These required velocities are found by interpolation, on the assumption that the net velocity on the boundary is zero.

Tensile Instability

Tensile instability is a numerical pathology in the SPH method which can arise in simulations involving any type of elasticity. It was first discovered by Philips and Monaghan [109] and subsequently was extensively studied by a number of authors [99, 110, 111, 112, 102]. From these studies it was found that, in regions under a tensile stress (stretched regions), a small perturbation in particles’ positions can cause exponential growth in their velocities, leading, eventually, to the particles clumping together and exhibiting oscillatory motion. This instability is particularly likely in materials with equation of state which can give rise to negative pressures, but it has been also been observed in materials for which the pressure is always positive, e.g. gases.

Apparently, any mechanism which impedes the inclination of particles to approach one another is able to alleviate the problem. A number of such remedies have been suggested, the most successful of which are the artificial stress method [110, 111]

and the velocity averaging method (XSPH) [112]. Some of the other methods that have been mooted suffer from being a little bit more complicated to implement, e.g. the inclusion of additional stress points [102].

Here, we briefly describe the XSPH approach, which centres on modifying the equation relating the coordinates to the velocities $d\mathbf{x}_i/dt = \mathbf{v}_i$ by replacing the velocity \mathbf{v}_i with the particle averaged velocity at the point \mathbf{x}_i :

$$\langle \mathbf{v} \rangle_i = \mathbf{v}_i + \tilde{\epsilon} \sum_j (\mathbf{v}_j - \mathbf{v}_i) \frac{m_j}{\rho_{ij}} W_{ij}, \quad (3.80)$$

where $\tilde{\epsilon}$ is a parameter which ranges from 0 to 1. This alternative averaging procedure decreases the relative velocities of approaching particles, while conserving both linear and angular momenta.

Particle Inconsistency

Probably the most important numerical shortcoming of the SPH method is the particle inconsistency problem, which arises from the particle approximation process and leads to a low approximation accuracy. This problem was analysed in §3.3.4, where the completeness of the original SPH method was considered and it was shown that the SPH technique does not even have zeroth order consistency. This inaccuracy has motivated the development of a number of improvements to the original SPH approach. As was pointed out previously, negative values of weight functions can lead to unphysical negative values for the field variables, e.g. density. Thus, we only consider approaches which are restricted to positive weight functions, since we are interested in applying the SPH to the simulation of the hydrodynamics of LCs.

In order to alleviate the particle inconsistency problem, Randles and Libersky [88] introduced the following normalised expression for the density:

$$\rho = \frac{\sum_{j=1}^N \rho_j W_{ij} V_j}{\sum_{j=1}^N W_{ij} V_j}, \quad (3.81)$$

and a normalisation for the divergence of the stress tensor σ :

$$\langle \nabla \cdot \sigma \rangle_i = \frac{\sum_{j=1}^N (\sigma_j - \sigma_i) : W_{ij,i} V_j}{\sum_{j=1}^N (\mathbf{x}_j - \mathbf{x}_i) : W_{ij,i} V_j}, \quad (3.82)$$

where $V_j = \frac{m_j}{\rho_j}$, $W_{ij,i} = \frac{W_{ij}}{\mathbf{x}_i}$ and $:$ denotes the tensor product. In these, the accuracy of approximations is improved by explicitly including the particle inconsistency itself

in the final equations.

Two of the more recently introduced corrections, namely corrective smoothed particle hydrodynamics and modified smoothed particle hydrodynamics, are considered in more detail in the following sections.

3.3.6 Corrective Smoothed Particle Method

In an attempt to overcome the particle consistency problem, Chen et al. [113] developed an improvement to the SPH based on a Taylor series expansion. This led to what was called the corrective smoothed particle method (CSPM). In order to demonstrate the idea of this method, we consider a general Taylor expansion of an arbitrary, smooth function f near a fixed point x_i in 1-dimensional space. From this, we obtain, for $f_i = f(x_i)$:

$$f(x) \simeq f_i + f_{i,x}(x - x_i) + \frac{(x - x_i)^2}{2!} f_{i,xx} + \dots \quad (3.83)$$

Multiplying both sides of eq. (3.83) by the weight function W_i and integrating over the whole domain yields:

$$\begin{aligned} \int f(x)W_i(x) dx &= f_i \int W_i(x) dx + f_{i,x} \int (x - x_i)W_i(x) dx \\ &+ \frac{f_{i,xx}}{2} \int (x - x_i)^2 W_i(x) dx + \dots \end{aligned} \quad (3.84)$$

If terms containing derivatives of the function $f(x)$ in the above equation are neglected, then the following corrective kernel expression for the value of the function $f(x)$ at particle x_i is obtained:

$$f_i = \frac{\int f(x)W_i(x) dx}{\int W_i(x) dx}. \quad (3.85)$$

Due to the symmetry condition on conventional weight functions, the second term on the RHS of eq. (3.84) would naturally average to zero for interior particles. However, this is not the case for particles near to or at the boundary, so the neglect of this term in CSPM leads to worse kernel consistency at boundaries. Specifically, the CSPM kernel approximation (3.85) is of first order consistency for interior particles and of zeroth order consistency for particles at the boundaries. It should also be noted that eq. (3.85) is equivalent to the original SPH kernel approximation for interior particles due to the normalisation property on weight functions. The

corresponding particle approximation is written as

$$\langle f \rangle_i = \frac{\sum_{j=1}^N f_j W_{ij} V_j}{\sum_{j=1}^N W_{ij} V_j}. \quad (3.86)$$

This particle approximation is of zeroth order consistency for both interior and boundary particles due to the particle inconsistency problem.

The CSPM correction for derivatives is obtained by substituting the weight function W_i with its derivative $W_{i,x}$ in eq. (3.85). Neglecting terms containing derivatives of second order and higher then gives the following particle approximation for first order derivatives:

$$\left\langle \frac{\partial f}{\partial x} \right\rangle_i = \frac{\sum_{j=1}^N (f_j - f_i) W_{ij,x} V_j}{\sum_{j=1}^N (x_j - x_i) W_{ij,x} V_j}. \quad (3.87)$$

The consistency of particle approximation of derivatives is then of zeroth order consistency for both interior and boundary particles for random particle distributions, similar to CSPM approximations of functions.

3.3.7 Modified Smoothed Particle Hydrodynamics

Recently, modified smoothed particle hydrodynamics (MSPH) has been introduced as a further enhancement over the CSPM. This method was developed simultaneously and independently by Zhang and Batra [114] and by Liu and Liu [97], whose works should be consulted for further details.

Similarly to the derivation of the CSPM method, we again consider a general Taylor expansion of an arbitrary, smooth function f near a fixed point \mathbf{x}_i in d -dimensional space. From this, we obtain, for $f_i = f(\mathbf{x}_i)$:

$$f(\mathbf{x}) \simeq f_i + f_{i,\alpha} (x^\alpha - x_i^\alpha) + \dots, \quad (3.88)$$

where α ranges from 1 to d . Multiplying both sides of eq. (3.88) with a smoothing function (or weight function) $W_i = W(\mathbf{x}_i - \mathbf{x}, h)$ and with its first-order derivatives, and then integrating over the problem space Ω yields

$$\begin{aligned} \int_{\Omega} f(\mathbf{x}) W_i d\mathbf{x} &\simeq f_i \int_{\Omega} W_i d\mathbf{x} + f_{i,\alpha} \int_{\Omega} (x^\alpha - x_i^\alpha) W_i d\mathbf{x}, \\ \int_{\Omega} f(\mathbf{x}) W_{i,\gamma} d\mathbf{x} &\simeq f_i \int_{\Omega} W_{i,\gamma} d\mathbf{x} + f_{i,\alpha} \int_{\Omega} (x^\alpha - x_i^\alpha) W_{i,\gamma} d\mathbf{x}. \end{aligned} \quad (3.89)$$

These integrals can be calculated at an arbitrary set of points i using the standard SPH particle discretisation process. In contrast to both the original SPH and the

CSPM method, the more holistic MSPH approach simultaneously retains all of the terms in eqs. (3.89). This both improves the accuracy of the method and gives a rigorous approach for the implementation of boundaries. This improvement comes, though, at the cost of some extra computational effort, since the values of the function f and its derivatives now need to be evaluated at each point from the set of linear equations

$$\mathbf{B}\mathbf{F} = \mathbf{T}. \quad (3.90)$$

For the three-dimensional case, the matrices \mathbf{B} , \mathbf{F} and \mathbf{T} are

$$B_{IJ} = \sum_{j=1}^N \Phi(I)\Theta(J)\frac{m_j}{\rho_j}, \quad T_I = \sum_{j=1}^N f_j\Phi(I)\frac{m_j}{\rho_j}, \quad (3.91)$$

$$F = \{f_i, f_{i,x}, f_{i,y}, f_{i,z}\}^T, \quad I, J = 1, 2, 3, 4$$

$$\begin{aligned} \Phi(1) &= W_{ij}, & \Phi(2) &= W_{ij,x}, & \Phi(3) &= W_{ij,y}, & \Phi(4) &= W_{ij,z} \\ \Theta(1) &= 1, & \Theta(2) &= x_j - x_i, & \Theta(3) &= y_j - y_i, & \Theta(4) &= z_j - z_i. \end{aligned} \quad (3.92)$$

The system of simultaneous linear equations (3.90) has a solution at each interpolation point, provided that the matrix \mathbf{B} is not ill-conditioned. The method's accuracy can be further improved by retaining higher-order derivatives in the Taylor expansion eqn. (3.88). This, though, again introduces additional computational effort, since the number of linear equations in (3.90) increases accordingly. Also, the stability of the scheme decreases with increase in the number of linear equations included, since the condition number of the matrix \mathbf{B} increases greatly in this case. Thus, there is a trade-off between accuracy and stability.

From the consistency point of view, the accuracy of the MSPH method is increased as compared with both the SPH and CSPM approaches. If k derivatives are retained in the Taylor expansion given by eq. (3.88), then the MSPH approach has $(k-1)$ th order consistency for both interior and boundary regions. Particle disorder does not influence the consistency of this scheme and, thus, the particle consistency is equal to the continuum kernel consistency. The kernel consistency of first- and second-order derivatives is of $(k-2)$ th and $(k-3)$ th orders, respectively.

The MSPH approach is very similar in its derivation to the CSPM method. However, the main difference between the two methods is that the values of field variables and their derivatives are calculated sequentially in the CSPM method, as compared to simultaneous estimation in the MSPH. On the other hand, the higher accuracy of the MSPH method is achieved at the expense of increased computational requirements.

3.4 Smoothed Dissipative Particle Dynamics

In the last two sections, we have described two mesoscopic mesh-free particle techniques, namely DPD and SPH. In both of these approaches, a fluid is represented by a set of particles which are usually seen as lump fluids. Moreover, in both approaches forces are pairwise additive and scaled by weight functions which decrease with increase in the distance between the particles, see e.g. eqs. (3.2-3.5) and eq. (3.51). However, both DPD and SPH have a number of drawbacks. In this section we describe a technique which combines the best ideas from both DPD and SPH and which, at the same time, is free from some of their inherent problems. This simulation technique, derived by Espanol and Revenga [65], is called smoothed dissipative particle dynamics (SDPD). In particular, it represents a Navier-Stokes solver based on the SPH discretisation with includes thermal fluctuations similar to those present in DPD.

The problems peculiar to DPD were discussed in detail in §3.2.5. Employing the SPH discretisation of the Navier-Stokes equation completely removes the following three significant problems: (i) the physical scale simulated by DPD is undefined, (ii) the transport coefficients cannot be specified directly and (iii) the conservative forces do not allow for an arbitrary equation of state. The SPH method, on the other hand, greatly benefits from the inclusion of thermal fluctuations, since it then becomes a truly mesoscopic technique. SPH is also extended in SDPD to explicitly acknowledge the second law of thermodynamics. This makes it physically self-consistent due to close connection between the fluctuation-dissipation theorem and the correct description of hydrodynamic fluctuations in the fluid.

There are two main steps in the derivation of the SDPD model. The first involves introduction of an entropy field variable into the system's description. This then allows for the physically correct introduction of thermal fluctuations into the model during the second step (see below).

The conservation laws present in the standard SPH description, namely the continuity equation and the linear momentum equation, along with their discretisations are given in §3.3.2. An extra equation of hydrodynamics, describing the entropy [46], is given as:

$$T\rho\frac{Ds}{Dt} = \phi + \kappa\nabla^2T, \quad (3.93)$$

where $s = s(\mathbf{r}, t)$ is the entropy per unit mass field, T is the temperature field and κ is the thermal conductivity. The viscous heating field ϕ represents the transfer of energy dissipated by viscous forces into the internal energy of the fluid. This is

given as

$$\phi = 2\eta\overline{\nabla\mathbf{v}} : \overline{\nabla\mathbf{v}} + \zeta(\nabla \cdot \mathbf{v})^2, \quad (3.94)$$

where $\overline{\nabla\mathbf{v}}$ denotes the traceless symmetric part of the velocity gradient tensor. Equation (3.93) for the rate of change of the entropy is then discretised using the standard SPH approximation rules, with second order derivatives being discretised using eq. (3.60).

Next, thermal fluctuations are added into the system. For this, the target equations are first rewritten in terms of the GENERIC framework [115, 116], which then allows for a simple and systematic introduction of thermal noise. This framework incorporates the physics behind the first and second laws of thermodynamics and can be applied to any closed system to describe non-equilibrium processes. Here, we do not describe this framework in detail, but rather state the final form of the stochastic differential equations describing the resulting system. They are

$$d\mathbf{r}_i = \mathbf{v}_i dt \quad (3.95)$$

$$\begin{aligned} m d\mathbf{v}_i = & \sum_j \left(\frac{P_i}{\rho_i^2} + \frac{P_j}{\rho_j^2} \right) \frac{\partial W_{ij}}{\partial \mathbf{x}_i} dt - \sum_j (1 - d_{ij}) a_{ij} \mathbf{v}_{ij} dt \\ & - \sum_j (1 - d_{ij}) \left(\frac{a_{ij}}{3} + b_{ij} \right) \mathbf{e}_{ij} \mathbf{e}_{ij} \cdot \mathbf{v}_{ij} dt + m d\tilde{\mathbf{v}}_i, \end{aligned} \quad (3.96)$$

$$\begin{aligned} T_i dS_i = & \frac{1}{2} \sum_j \left(1 - d_{ij} - \frac{T_j}{T_i + T_j} \frac{k_B}{C_i} \right) \left[a_{ij} \mathbf{v}_{ij}^2 + \left(\frac{a_{ij}}{3} + b_{ij} \right) \right. \\ & \left. \times (\mathbf{e}_{ij} \cdot \mathbf{v}_{ij})^2 \right] dt - \frac{2k_B}{m} \sum_{j \neq i} \frac{T_i T_j}{T_i + T_j} \left(\frac{10}{3} a_{ij} + b_{ij} \right) dt \\ & - 2\kappa \sum_j \frac{T_{ij}}{\rho_i \rho_j} \frac{\partial W_{ij}}{\partial \mathbf{x}_i} dt - 2\kappa \frac{k_B}{C_i} \sum_{j \neq i} \frac{T_j}{\rho_i \rho_j} \frac{\partial W_{ij}}{\partial \mathbf{x}_i} dt + T_i d\tilde{S}_i. \end{aligned} \quad (3.97)$$

Here, C_i denotes the heat capacity at constant volume of particle i and the following notations have been introduced:

$$a_{ij} = \left(\frac{5\eta}{3} - \zeta \right) \frac{1}{\rho_i \rho_j} \frac{\partial W_{ij}}{\partial \mathbf{x}}, \quad b_{ij} + \frac{a_{ij}}{3} = 5 \left(\frac{\eta}{3} + \zeta \right) \frac{1}{\rho_i \rho_j} \frac{\partial W_{ij}}{\partial \mathbf{x}}, \quad (3.98)$$

$$c_{ij} = \frac{2\kappa}{\rho_i \rho_j} \frac{\partial W_{ij}}{\partial \mathbf{x}}, \quad d_{ij} = \frac{T_i T_j}{(T_i + T_j)^2} \left[\frac{k_B}{C_i} + \frac{k_B}{C_j} \right]. \quad (3.99)$$

We now consider these equations in more detail. Equation (3.95), describing variation of particle positions, is the same as that in the original SPH. Strictly speaking, an extra noise term is not necessary here, since thermal fluctuations from the veloc-

ity \mathbf{v} will automatically propagate here. Equation (3.96) for the velocity does now, though, contain three extra terms. The fluctuations themselves are represented by the term containing $\tilde{\mathbf{v}}_i$, which is a combination of independent increments of the Wiener process $d\mathbf{W}_{ij}$. Two other extra terms, containing coefficients a_{ij} , b_{ij} and d_{ij} , follow from the GENERIC framework and represent the irreversible part of the dynamics. Equation (3.97), for the entropy S is extended in a similar way to the equation of motion.

Thus, the SDPD method is derived by introducing thermal fluctuations into the original SPH description by using the GENERIC framework. It should be noted that the same approach can be used to introduce thermal fluctuations into any other particle continuum simulation technique which fulfills two of the laws of thermodynamics. This represents a proper top-down approach to devising mesoscopic simulation models.

3.5 Other Mesoscopic Mesh-free Particle Techniques

3.5.1 Direct Simulation Monte Carlo

The Direct Simulation Monte Carlo (DSMC) method is a particle-based technique for solving the Boltzmann equation by using Monte Carlo simulation. It was first proposed by Bird [28, 29] in the context of simulation of rarefied gas flows, but later it also became popular in simulations of fluids where molecular effects are important.

The fluid in a DSMC simulation is represented by particles, each of which represent a large number of real molecules. The central assumption in DSMC is that molecular motions can be decoupled from the molecular interactions (operator splitting), with the simulation time step Δt being less than the mean collision time. In the DSMC method, molecular motions are modelled deterministically and molecular interactions are modelled probabilistically.

Thus, during each time step, particles are first realistically moved in physical space and time according to their equations of motions. This allows modelling of unsteady phenomena. To calculate the movement of a particle, usually a standard numerical integration technique is used, which can formally be written as

$$\mathbf{r}_i(t + \Delta t) = \mathbf{r}_i(t) + \mathbf{v}_i(t)\Delta t. \quad (3.100)$$

The given boundary conditions are applied when translating particles. During this

step, interactions with other particles are not considered.

Next, collisions of particles are modelled. Exact places and times of these collisions are not calculated, but instead a stochastic algorithm is used. The probabilistic nature of this step is what distinguishes the DSMC technique from deterministic methods, such as molecular dynamics. During the collision step, the domain is first divided into grid of equal cubic cells of volume $V = l_c^d$, where d is the dimensionality of the system and l_c is the side length of a cell. The cell side length l_c is chosen to be smaller than, but of the same order as, the mean free path. Only particles residing within the same cell are chosen to collide, to ensure that only particles which are located close to each other interact. Not all pairs of particles in the same cell collide, as this would be a time consuming process. Instead, a random number M_c of pairs inside each cell is drawn, with M_c given by the following formula

$$M_c = \frac{N_c(N_c - 1)\sigma v_{max}\Delta t}{2V_c}. \quad (3.101)$$

In the above equation, N_c is the total number of particles within the cell, σ is the scattering cross-section (e.g., in two dimensions for spherical particles with radius r $\sigma = 4r$) and v_{max} is the maximum relative velocity of two particles. The maximum relative velocity v_{max} is found from time to time in the simulation by identifying the maximum particle velocity and setting v_{max} to be twice of this value. This greatly saves the computational time.

Having identified colliding pairs of particles inside each cell, the acceptance-rejection method is then applied to each of them. A collision between particles i and j is then performed if

$$\frac{|v_i - v_j|}{v_{max}} < Z, \quad (3.102)$$

where Z is a uniformly distributed random number in the interval $[0, 1]$. Thus, the probability of the collision between two particles effectively depends on their relative velocity.

Finally, the collisions between chosen pairs of particles are performed. Post-collisional velocities need to be found in a consistent way, since collisions take place regardless of the particle positions in the cell. Assuming molecular chaos, in the hard sphere case an impact parameter b is chosen randomly from a uniform distribution. The post-collisional velocities are then calculated as if the particles had collided with the impact parameter b . This algorithm can be generalised to soft sphere potentials, and rotational degrees of freedom can be also introduced [117].

The DSMC method is based on the assumptions which were mentioned above.

These lead to a set of constraints on the technique, which are: (i) the cell size should be comparable with the mean-free path, (ii) the simulation time step should be smaller than the mean time between collisions, (iii) the system should be in a collisional regime, (iv) the number of particles per cell should remain roughly fixed in order to preserve the collisional statistics.

3.5.2 Stochastic Rotational Dynamics

In 1999, Malevanets and Kapral [66, 67, 118] developed a mesoscopic particle based simulation technique which is named either multi-particle collision dynamics (MPC) or stochastic rotational dynamics (SRD) [67]. The SRD technique is essentially an enhanced version of the DSMC technique described in the previous section, with pairwise collisions replaced by multi-particle collisions in order to improve the computational efficiency. In this section, we give a brief description of the principle formalism of the SRD method.

An SRD simulation involves of a set of N particles whose velocities and coordinates vary continuously, i.e. the particles move off-lattice. As in the DSMC method, there are two successive operations during each time step in an SRD simulation, which are called streaming and collision.

During the streaming step, particles are simultaneously propagated according to their velocities, with their coordinates updated as

$$\mathbf{r}_i(t + \Delta t) = \mathbf{r}_i(t) + \mathbf{v}_i(t)\Delta t, \quad (3.103)$$

where Δt is the simulation time step.

The collision step then involves simultaneous transfer of momentum between all particles in each cell. This is the main difference between SRD and the DSMC techniques, because in the DSMC method the momentum is transferred only between certain pairs of particles. In SRD, at each collision step the domain is initially divided into a grid of cubic cells with equal side lengths. Each cell may contain any number of particles, but the total number of particles N is always constant. The centre of mass velocity \mathbf{V} is then calculated for each cell as an average of the particle velocities belonging to that cell. After that, the particle velocities in each cell are rotated by an angle α around a random axis, relative to \mathbf{V} , to yield post-collision velocities. This can be written as the following mathematical transformation of velocities:

$$\mathbf{v}_i(t + \Delta t) = \mathbf{V}(t) + \omega(\mathbf{v}_i(t) - \mathbf{V}(t)), \quad (3.104)$$

where ω is a rotation matrix. The rotation matrix ω is the same for all particles in a given cell, but it varies for different cells.

The collision step by itself is not physical, but it is constructed so as to conserve locally mass, momentum and energy. Thus, in the continuum limit, Navier-Stokes and the hydrodynamic equation for heat transfer are recovered. In their original article, Malevanets and Kapral also showed that the velocity distribution of particles in equilibrium is Maxwellian [66].

Ihle and Kroll [67] subsequently noted that the original SRD method suffers from a lack of Galilean invariance if the grid is chosen to be the same for each time step. This is due to the fact that if particles do not travel significant distances, as compared with the cell size, then the set of particles with which they collide changes only slowly. This leads to a non-physical dependance of transport coefficients on the fluid velocity, which is especially pronounced at low temperatures. This issue is resolved by randomly shifting the position of the grid during each collision step.

Chapter 4

Implementation of Bottom-up Approaches

In this chapter we present results obtained within our development of novel mesoscopic mesh-free techniques for simulation of LCs based on dissipative particle dynamics (DPD) and fluid particle model (FPM) approaches. We initially describe practical implementation aspects of the original DPD/FPM techniques and provide some results validating the codes developed. We then introduce extensions to these techniques and mathematically prove that these are physically correct. Next, we attempt to validate the proposed extensions by reporting simulation results for a number of LC systems.

4.1 Practical Aspects in DPD/FPM Implementation

In this section we describe the particulars of our DPD/FPM implementation. The DPD method has many similarities with the traditional MD technique. This is a big advantage, since most of the well-proven procedures of MD can be reused in DPD. Both methods are particle based, in that particles move off-lattice in a continuum domain but with discrete time steps. The main difference between these two approaches is that the forces in DPD depend on particle velocities and include stochastic terms. This requires utilisation of non-standard integrators.

From an implementation point of view, the FPM is very similar to DPD, apart from one additional issue; rotational degrees of freedom in the FPM require special attention, since forces/torques in the FPM depend on the particles' angular velocities. Unfortunately, articles describing FPM implementation tend not to specify

either the representation used for the treatment of angular coordinates and velocities, or the integration algorithm utilised. We use quaternion parameters for the description of particle orientations and modify the integration algorithm by Martys and Mountain [119] for angular coordinates and velocities.

The remainder of this section is organised as follows. First, we discuss the basic particularities of DPD/FPM implementation, such as reduced units and periodic boundary conditions. We then pay special attention to the choice of integrator. Then, the handling of rotational degrees of freedom and angular velocities is summarised. Next, we describe the implementation of a Verlet neighbour list which we employ in order to speed-up the calculations. The section concludes with a description of the methods used to measure physical quantities in the simulated systems.

4.1.1 Reduced Units

Most computer simulations use reduced units instead of real physical quantities to represent system properties. Apart from the obvious convenience of working with values of order unity, this approach introduces some important technical advantages. Firstly, in real units (SI) some numerical values involved are either much less or much greater than unity. In standard floating-point operations, such as multiplication or division, this significantly increases the risk of numerical errors arising. Secondly, through the law of corresponding states, many different system descriptions can be shown to be identical in reduced units, which allows one to avoid performing redundant simulations. Thirdly, for instance, by setting particle masses to unity, one can achieve simulations in which forces are numerically equal to accelerations and momenta equal to velocities; consequently, savings can be made in running time.

The most straightforward way to specify reduced units is to assign a value of unity to certain key parameters that appear in the model description. Then, all other quantities are expressed in terms of these assigned variables. In the DPD model, the cut-off radius r_c is usually used as the unit of distance, as this is the natural unit of length in the system, and the temperature, via $k_B T$, usually plays the role of the unit of energy. The particle's mass is the unit of mass and, naturally, is set to unity. Given this specific choice of units, the representation of all other units directly follows, e. g. $r_c(m/kT)^{1/2}$ for time, $(1/r_c^3)$ for number density, $(k_B T/m)^{1/2}$ for velocity etc. The full table of unit conversions can be found in Appendix B of [120].

4.1.2 Periodic Boundary Conditions / Minimum Image Convention

In most computer simulations, the number of particles, N , in a system is of order $\mathcal{O}(10^2) - \mathcal{O}(10^5)$ due to the limitations of computing resources, both storage and computational. For instance, the computational expense of a DPD simulation scales with the number of particles as $\mathcal{O}(N^2)$, if no additional measures are taken.

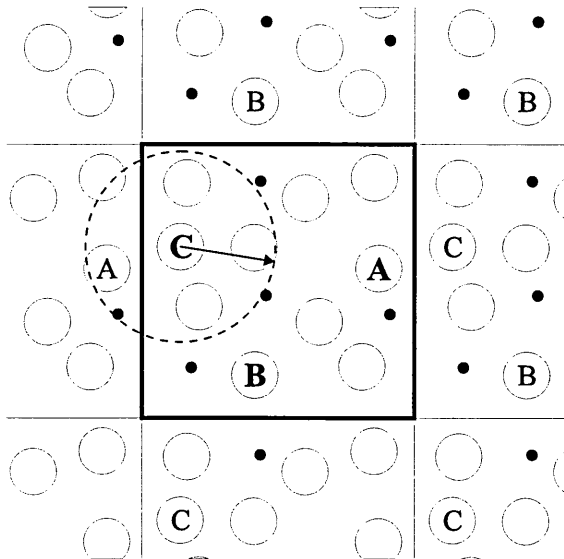


Figure 4.1: Two-dimensional schematic representation of periodic boundary conditions

The aim of most DPD simulations is to inform the macroscopic properties of a given sample. Consequently, it is necessary to account for boundary conditions in simulations. When the number of particles is small, a significant fraction of them are located near the boundary of the simulation box. To deal with this issue, periodic boundary conditions are routinely employed along with the minimum image convention.

In this, the simulated volume, V , is treated as the primitive cell of an infinite periodic lattice of identical cells. A sketch of the two-dimensional case is depicted in Fig. 4.1. Every particle in the cell now has the potential to interact with all other particles in this infinite system, apart from self-images. In practice, though, it is not necessary to keep information about all of the particles in the system. When a particle leaves the central simulation box, an equivalent image then re-enters from the opposite side as a consequence of the periodic boundary conditions. In this way, attention is switched from one image to another whenever a particle crosses a boundary. In the force calculation loop, while going through all pairs of particles,

the minimum image convention is used to define all images within a given particle's interaction range r_c . Provided that $2r_c$ is less than the box length L , then, as shown in Fig. 4.1, for instance, particle C interacts with at most only one of the images of particle A .

Periodic boundary conditions is a widely used and effective method, but unfortunately it suffers a few drawbacks. One consequence of the introduced periodicity is the suppression of fluctuations with wavelengths $\lambda > L$. Therefore, if long wavelengths are important in the simulation, then one should take explicit account of finite system size effects.

4.1.3 Integrators

The velocity-Verlet based integration scheme for DPD, introduced by Groot and Warren [70] (DPD-VV), is a popular variant of the standard MD velocity-Verlet algorithm [120]. As mentioned above, the forces in DPD depend on the particle velocities. This issue is tackled in DPD-VV by using intermediate predicted velocities \mathbf{v}^0 :

$$\mathbf{r}_i(t + \Delta t) = \mathbf{r}_i(t) + \Delta t \mathbf{v}_i(t) + 1/2(\Delta t)^2 \mathbf{F}_i(t), \quad (4.1)$$

$$\mathbf{v}_i^0(t + \Delta t) = \mathbf{v}_i(t) + \lambda \Delta t \mathbf{F}_i(t), \quad (4.2)$$

$$\mathbf{F}_i(t + \Delta t) = \mathbf{F}_i(\mathbf{r}(t + \Delta t), \mathbf{v}^0(t + \Delta t)), \quad (4.3)$$

$$\mathbf{v}_i(t + \Delta t) = \mathbf{v}_i(t) + 1/2\Delta t(\mathbf{F}_i(t) + \mathbf{F}_i(t + \Delta t)). \quad (4.4)$$

Here λ is a phenomenological tuning parameter, which introduces higher-order corrections into the integration procedure. The value $\lambda = 0.5$ corresponds to the original MD velocity-Verlet algorithm, whereas Groot and Warren [70] found that $\lambda = 0.65$ gives the best temperature control in DPD simulations. Generally, λ depends on the model parameters and has to be determined empirically for every specific case. In order for the DPD-VV method to be stable, the time step should be sufficiently small. Marsh and Yeomans [121] derived critical temperatures, densities and model parameters that yield a region where simulations are stable. Due to its simplicity and efficiency, the DPD-VV algorithm is a very popular choice in many DPD simulations. It is used very often, as well, as a basic technique against which to evaluate other integrators [122, 123, 124].

The velocity-Verlet scheme is basically a method for solving the Hamiltonian equations for deterministic dynamical systems. However, the DPD method is actually described by a SDE and has a stochastic underlying basis. Recently, alternative

integrators have been proposed, based on proper stochastic expansions [125, 126, 127]. Here we summarize Shardlow's splitting method [125], the first of these alternative methods. The key idea in this integrator is to factorise the integration process, so that conservative forces can be integrated using conventional integrators. Then, dissipative and random forces are solved separately as SDEs. Two approaches were employed for the integration of the Langevin equations, namely the Trotter expansion [128] (integrator S1) and a second order splitting using the Strang expansion (integrator S2). Both integrators (S1 and S2) give better temperature control than DPD-VV, allowing for a larger time step, and help to avoid some of the artifacts present in the DPD-VV integrator [124]. Integrator S2 is slightly better in characteristics than integrator S1, however, it is more computationally expensive, so integrator S1 has been identified as the optimal choice [125].

Lowe [129] proposed an alternative approach to DPD which involves combining it with Andersen's thermostat. The resulting integration algorithm can be summarised as follows. Firstly, using the velocity-Verlet algorithm, particles' positions and velocities are advanced to time step $t + \Delta t$. The next stage involves system thermalisation. All pairs of particles are considered, where $r_{ij} < r_c$, with probability $\Gamma \Delta t$. Here r_c specifies the interaction range and is similar to the DPD cut-off radius. Then, their component of relative velocity along the line connecting their particle centres is drawn from a distribution $\xi_{ij} \sqrt{2k_B T/m}$, where ξ_{ij} is a Gaussian-distributed random variable with unit variance. The main parameter in Lowe's method is Γ , which is set such that $0 \leq \Gamma \Delta t \leq 1$. If $\Gamma \Delta t$ is close to unity, then all particle velocities are thermalised at each time step. However, if $\Gamma \Delta t \approx 0$, then the system is only weakly coupled to the thermostat. It should be pointed that the main difference between Lowe's method and conventional DPD is that, in Lowe's thermostat, dissipative and random forces are not explicitly calculated. Thus, Lowe's approach is not, in fact, a realisation of the DPD equations, but rather an independent modified thermostat.

A few comparative studies of the efficiency of DPD integrators were performed recently [124, 127]. From these, it was concluded that Shardlow's integrator S1 performs best. Lowe's method was also shown to yield excellent results, in some tests even better than those of integrator S1, even though it is not a proper solution of the DPD equations.

4.1.4 Quaternions

In the FPM, fluid particles possess rotational degrees of freedom and angular velocities, and the forces/torques in the model depend on angular velocities in much the

same way as forces in DPD depend on translational velocities. We use quaternion parameters [130] for the representation of particles' orientations. Since there is no developed integrator yet for angular degrees of freedom for DPD-like algorithms, we have modified the integration algorithm by Martys and Mountain [119] for quaternions in much the same way as the velocity-Verlet algorithm was modified in the DPD-VV integrator derivation.

A quaternion \mathbf{Q} is a set of four scalar quantities

$$\mathbf{Q} \equiv (q_0, q_1, q_2, q_3), \quad (4.5)$$

which satisfy the constraint

$$q_0^2 + q_1^2 + q_2^2 + q_3^2 = 1. \quad (4.6)$$

The four quaternions are not mutually independent, but give an orthogonal representation of space which makes the equations of motion singularity-free, as compared with conventional Euler angle representation that is described in detail by Goldstein [131].

In the quaternion representation, the rotation matrix, which allows transformation between space-fixed and body-fixed coordinates, becomes

$$\mathbf{A} = \begin{pmatrix} q_0^2 + q_1^2 - q_2^2 - q_3^2 & 2(q_1q_2 + q_0q_3) & 2(q_1q_3 - q_0q_2) \\ 2(q_1q_2 - q_0q_3) & q_0^2 - q_1^2 + q_2^2 - q_3^2 & 2(q_2q_3 + q_0q_1) \\ 2(q_1q_3 + q_0q_2) & 2(q_2q_3 - q_0q_1) & q_0^2 - q_1^2 - q_2^2 + q_3^2 \end{pmatrix}. \quad (4.7)$$

Quaternions are connected with principal (in body-fixed coordinates) angular velocities through the following relation

$$\dot{\mathbf{Q}} \equiv \begin{pmatrix} \dot{q}_0 \\ \dot{q}_1 \\ \dot{q}_2 \\ \dot{q}_3 \end{pmatrix} = \frac{1}{2} \begin{pmatrix} q_0 & q_1 & q_2 & q_3 \\ q_1 & q_0 & -q_3 & q_2 \\ q_2 & q_3 & q_0 & -q_1 \\ q_3 & -q_2 & q_1 & q_0 \end{pmatrix} \begin{pmatrix} 0 \\ \omega_x^b \\ \omega_y^b \\ \omega_z^b \end{pmatrix}, \quad (4.8)$$

which can be written in a shorter form $\dot{\mathbf{Q}} = \frac{1}{2}M_{\alpha\beta}W_\beta$ where M and W are the matrices on the right hand side of eq. (4.8). We are now required to derive the second-order time derivative of \mathbf{Q} . For this, let us consider Euler's equations of motion for a rigid body that is fixed and is subject to torques \mathbf{N} in the principal

frame

$$\begin{aligned}\dot{\omega}_x^b &= N_x/I_x + \omega_y^b \omega_z^b (I_y - I_z)/I_x, \\ \dot{\omega}_y^b &= N_y/I_y + \omega_z^b \omega_x^b (I_z - I_x)/I_y, \\ \dot{\omega}_z^b &= N_z/I_z + \omega_x^b \omega_y^b (I_x - I_y)/I_z.\end{aligned}\tag{4.9}$$

Now, if a matrix \mathcal{T} consists of the right-hand side of eq. (4.9) with $\mathcal{T}_4 = 0$, then, after some algebra, the following relation is obtained

$$\ddot{\mathbf{Q}} = \frac{1}{2} M_{\beta\gamma} \mathcal{T}_\gamma - \mathbf{Q}_\beta (\dot{\mathbf{Q}}_\alpha^T \dot{\mathbf{Q}}_\alpha).\tag{4.10}$$

Taking into the account the fact that FPM particles are spherical with equal moments of inertia, the algorithm by Martys and Mountain [119] can be modified to give

$$\mathbf{Q}(t + \Delta t) = \mathbf{Q}(t) + \Delta t \dot{\mathbf{Q}}(t) + 1/2(\Delta t)^2 \ddot{\mathbf{Q}}(t) + 1/2(\Delta t)^2 \mathbf{F}^L(t),\tag{4.11}$$

$$\boldsymbol{\omega}^0(t + \Delta t) = \boldsymbol{\omega}(t) + 1/2\Delta t \mathbf{N}/I,\tag{4.12}$$

$$\mathbf{N}(t + \Delta t) = \mathbf{N}(\mathbf{v}^0(t + \Delta t), \boldsymbol{\omega}^0(t + \Delta t)),\tag{4.13}$$

$$\boldsymbol{\omega}(t + \Delta t) = \boldsymbol{\omega}(t) + 1/2\Delta t (\mathbf{N}(t) + \mathbf{N}(t + \Delta t)).\tag{4.14}$$

Here $\boldsymbol{\omega}^0$ is the predicted angular velocity at time step $(t + \Delta t)$, analogous to the predicted velocity \mathbf{v}^0 in the DPD-VV algorithm. The only significant difference between this modified algorithm and the DPD-VV integrator given in eqs. (4.1-4.4) is that the force $\mathbf{F}^L(t) = -2\Lambda \mathbf{Q}$ maintains the constraints $\mathbf{Q} \cdot \mathbf{Q} = 1$ and $\mathbf{Q} \cdot \dot{\mathbf{Q}} = 0$. This force can be seen as being derived from the Lagrangian multiplier method. The condition (4.6) leads to an explicit expression for the coefficient Λ :

$$(\Delta t)^2 \Lambda = 1 - s_1(\Delta t)^2/2 - \sqrt{1 - s_1(\Delta t)^2 - s_2(\Delta t)^3 - (s_3 - s_1^2)(\Delta t)^4/4},\tag{4.15}$$

where $s_1 = \dot{\mathbf{Q}} \cdot \dot{\mathbf{Q}}$, $s_2 = \dot{\mathbf{Q}} \cdot \ddot{\mathbf{Q}}$ and $s_3 = \ddot{\mathbf{Q}} \cdot \ddot{\mathbf{Q}}$.

4.1.5 Verlet Neighbour List

In simulations, during the force calculation loop, every pair of particles has to be examined in order to determine whether or not they are within the interaction range r_c . This is computationally expensive, as the problem scales with the number of particles as $\mathcal{O}(N^2)$, even though most particle pairs will not satisfy this condition, especially in large or low-density systems. The Verlet neighbour list is a technique

which partially resolves this problem and, so, allows significant speed-up of calculations.

During a simulation, a list of new neighbour particles with distance between them $r_{ij} < r_v$ is created and maintained. Here r_v is an adjustable parameter, which is called the Verlet radius, such that $r_v > r_c$. Now, in the force calculation loop, only pairs on this neighbour list are considered, so cutting out many unnecessary calculations. Obviously, the neighbour list needs to be updated from time to time. This is done by keeping track of particles' maximum displacements, and recalculating the neighbour list whenever one of the particles accumulates a total displacement which exceeds $\frac{1}{2}(r_v - r_c)$.

The Verlet radius r_v should ideally be tailored for every specific case. If it is too small, then the neighbour list recalculation will be required too frequently. If it is too big, however, the frequency of the neighbour list recalculation will be lower, but the list itself will be long and, so, slow the force calculation cycle. For our DPD simulations, we found the value $r_v = 1.7r_c$ to be appropriate.

4.1.6 Calculation of Observables

In a DPD simulation, information about particle positions, velocities and angular velocities (in the FPM technique) is available at every time step, so one has access to a full microscopic picture of the system evolution. However, in practice, we are often interested only in macroscopic quantities, and much of the microscopic detail is redundant. In this section, we describe how typical macroscopic observables and fluid structural properties are calculated by simulation.

The system's potential energy is calculated as a sum of all particle-particle pairwise potentials:

$$E_{pot} = \sum_{i=1}^{N-1} \sum_{j>i}^N \phi_{ij}, \quad (4.16)$$

where ϕ_{ij} is the potential used in DPD simulations, as given in eq. (3.6). The total kinetic energy is given by the sum of translational and rotational (for the FPM) kinetic energies of individual particles:

$$E_{kin} = \sum_{i=1}^N \frac{m\mathbf{v}_i^2}{2} + \sum_{i=1}^N \frac{I\boldsymbol{\omega}_i^2}{2}. \quad (4.17)$$

The the total system energy is then given as

$$E_{tot} = E_{kin} + E_{pot}. \quad (4.18)$$

The DPD model does not conserve energy, so this value is a fluctuating quantity in simulations.

The instantaneous kinetic temperature T of a system can be calculated by applying the equipartition theorem. This states that if the Hamiltonian of a system contains some position or velocity coordinate to quadratic order, the respective degree of freedom will contribute $k_B T/2$ to the mean kinetic energy. Thus, temperature is estimated from

$$E_{kin} = \frac{n}{2} k_B T, \quad (4.19)$$

where $n = 3(N - 1)$ for the DPD model and $n = 6(N - 1)$ for the FPM. DPD/FPM simulations are conducted in NVT -ensembles, so temperature is constant during the simulations. Consequently, the average kinetic energy should remain fixed as well.

Due to the large time steps used in DPD simulations, configurations can be generated which are not canonical [84]. It is therefore advisable to monitor the configurational temperature T_c to assess the degree of equilibrium achieved [132]. This can be determined using the hypervirial relation [133]:

$$k_B T_c = \frac{\sum_i \langle |\nabla_i \phi|^2 \rangle}{\sum_i \langle \nabla_i^2 \phi \rangle}, \quad (4.20)$$

where ∇_i is the gradient and ∇_i^2 is the Laplacian.

The total pressure in simulated systems is calculated by the means of the virial theorem discussed above, using eq. (3.16). The off-diagonal elements of the pressure tensor can also be calculated utilising the virial theorem, by considering products of different cartesian components of the forces and the corresponding inter-particle vectors.

In addition to the average properties discussed above, structural properties of fluids can be extracted from simulations. The radial distribution function is a very important characteristic, which allows comparison of simulation results with experimental data. It is calculated by compiling histograms. The volume around every particle is divided into thin concentric shells and then the number of particles in each shell is divided by the shell volume to give the local density distribution. Then the result is normalised by the total number of particles and the average density, so as to give the radial distribution function. This procedure is usually performed for a number of configurations.

4.2 DPD/FPM Testing and Verification

In this section we describe the simulations undertaken to test and validate our newly developed parallel DPD/FPM codes for isotropic fluids. In these, we tested both equilibrium and non-equilibrium situations against well-proven results so as to make a comprehensive code validation. Initially we used the paper by Groot and Warren [70] for the primary testing, since their results have been verified in a number of subsequent papers. We thereafter follow them in using the following parameter set: conservative force parameter $a = 25$, random force strength $\sigma = 3$ and temperature $k_B T = 1$. The modified VV integrator with parameter $\lambda = 0.65$ was chosen and implemented as the most studied. In all simulations presented in this section we employed 1000 particles.

In every DPD simulation, the first observable to assess is the kinetic temperature, since the method produces NVT -ensembles. A series of simulations were performed to measure the dependance of temperature on the time step. The results, given in Fig. 4.2, are in a good agreement with those provided by Shardlow [125]. The

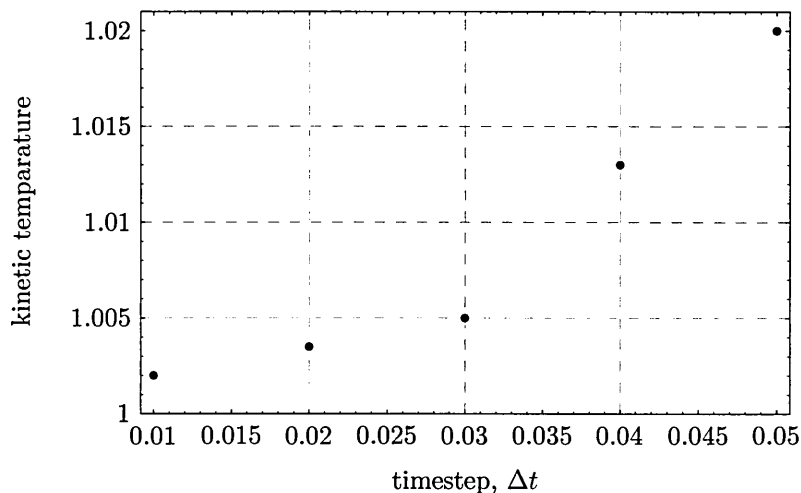


Figure 4.2: Kinetic temperature dependance on timestep Δt in the DPD model.

temperature increases with increase in the timestep, due to the shortcomings of the integrator. In all subsequent simulations we have used a timestep of $\Delta t = 0.02$, since it only gives a 0.4% error in the temperature control.

The DPD method conserves total translational momentum. This quantity is a good checkpoint, since it is an easy observable to monitor and it will readily reveal any errors in the integration algorithm. We monitor the system's centre of mass velocity at every time step. The test run of 50000 steps given in Fig. 4.3 shows that this velocity has the order of the round-up error, which is completely acceptable.

The total error has a tendency to increase, so that, during long simulation runs, particle velocities are rescaled every 25000 steps.

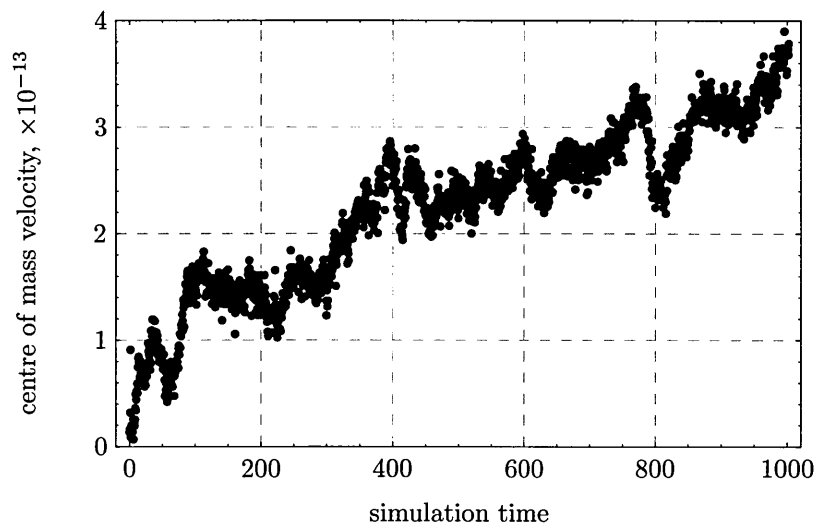


Figure 4.3: Centre of mass velocity.

The radial distribution function is the next important test point, since it provides information about the structural properties of the fluid. First, we measure the radial distribution function in the system without conservative forces as a function of time step, since in this case the relation (3.24) holds and the radial distribution function should be equal to unity for all r . The results are given in Fig. 4.4. Artifacts are present at low values of the inter-particle distance and these increase with time step. This shows one of the other drawbacks of the modified VV integrator. This problem is one of the other reasons why we have set the time step to be $\Delta t = 0.02$ in our simulations, since the lower time step partially eliminates structural artifacts.

We have also measured the radial distribution function in the presence of conservative forces. This is shown in Fig. 4.5 and agrees well with the equivalent result from Groot and Warren [70]. The pressure was recalculated using the last expression from eqs. (3.16) and compared with the measured quantity. Both agreed with accuracy 0.8%, which is negligible in practice.

We have repeated the experiment of Groot and Warren [70] on determination of the equation of state. The resulting plot of excess pressure against density is given in Fig. 4.6 along with the equation of state (3.17). The correspondence is very good.

The last test point we considered for equilibrium simulations is the configurational temperature. A plot of the configurational temperature against time step is given in Fig. 4.7. This shows that the configurational temperature control is very poor in the DPD-VV algorithm as compared with the kinetic temperature. This is

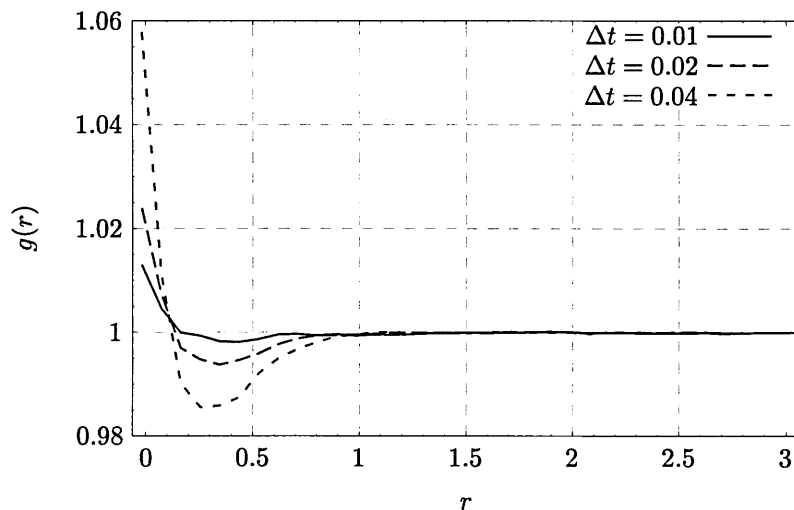


Figure 4.4: Radial distribution functions for the DPD model without conservative forces.

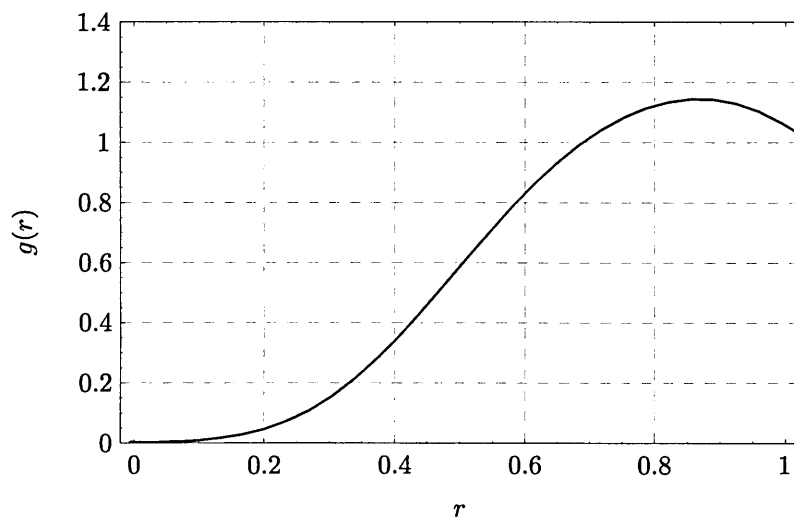


Figure 4.5: Pair correlation function for the DPD model with conservative forces.

caused by the fact that the time step is too large for the conservative force, but the thermostat forces algorithm produces the correct kinetic temperature.

We tested the developed FPM code in the same way as we just described for the DPD model. Both variants (and also all other extensions) differed only in their force calculation routines. Thus, some of the above tests are already applicable to the FPM, e.g. the centre of mass velocity. The FPM model possesses orientational degrees of freedom, so they should be tested in addition to the previous observables. We do this by measuring the orientational kinetic temperature. The dependencies of the configurational, kinetic rotational and translational temperatures on the time step are given in Fig. 4.8. As can be seen from this figure, the configurational temperature increases most markedly with the time step. As noted above, this is

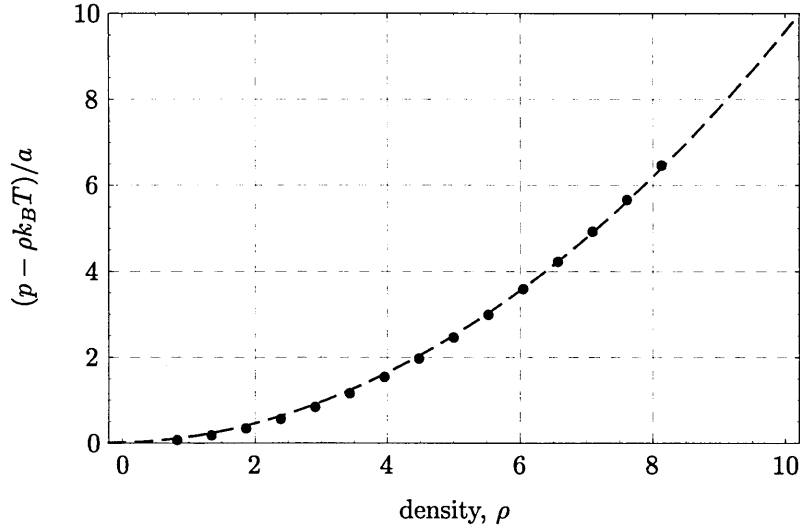


Figure 4.6: Excess pressure obtained from DPD simulations. Points denote simulation data, solid line denotes equation of state.

a general problem for all DPD based methods, since the time step is too big for the conservative forces. The kinetic rotational temperature also increases with the time step. But, surprisingly, the kinetic translational temperature decreases at the same time. This may have been caused by the choice of weight functions and needs to be explored further. Unfortunately, there are no equivalent published numerical results for the FPM model, so we do not have data against which to compare. This implementation was tested further by setting some of the weight functions to zero, so as to recover the original DPD model.

The tests discussed above were used only to assess the models in equilibrium. We have also tested non-equilibrium cases. To test for consistency, we first compare values of the shear viscosity obtained using two different methods: Lees-Edwards boundary conditions and periodic Poiseuille flow. The estimated viscosity is then used to check the velocity profile in Poiseuille flow generated using an external force and boundaries with frozen particles. Additionally, temperature and density profiles are measured across the channel, which is useful in some cases, e.g. when there are density fluctuations near to walls made up of frozen particles.

The initial testing was done by reproducing the results of Backer et al. [134]. Periodic Poiseuille flow was used to measure the viscosity of a system of DPD particles. The system parameters were: $k_B T = 0.5$, $n = 6.0$, $\sigma = 4.5$ and the external force was $g_z = 0.055$. The shear viscosity was thus estimated to be $\eta = 2.1 \pm 0.02$, whereas the value in Ref. [134] is $\eta = 2.09 \pm 0.02$. Thus, the results agree within statistical error.

Next, we tested all three non-equilibrium techniques by measuring the shear

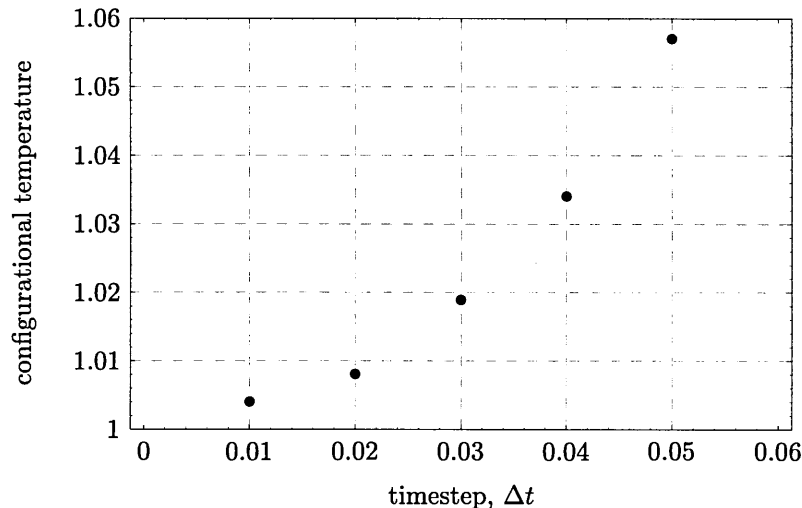


Figure 4.7: Configurational temperature as the function of the time step Δt in DPD.

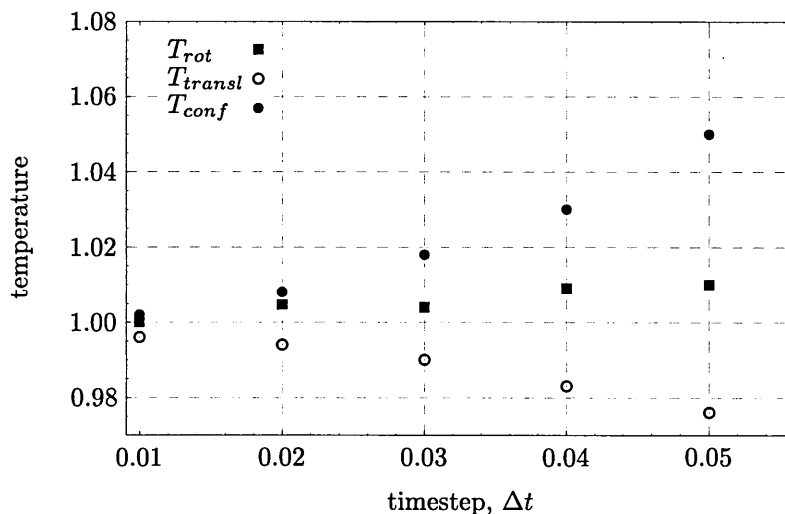


Figure 4.8: Configurational, kinetic translational and kinetic rotational temperatures as the function of the time step Δt in FPM model.

viscosity of the same system. In this case, the conservative forces were present, since they played a significant role in the Poiseuille flow that was generated using boundary conditions by Pivkin [135]. We have chosen the following system parameters for this test: temperature $k_B T = 1.0$, timestep $\Delta t = 0.01$, number density $n = 4.0$, random force strength $\sigma = 3.0$ and conservative force repulsion $a = 25$. The timestep was set rather small so as to avoid possible artefacts in these non-equilibrium simulations. The viscosity calculated using the periodic Poiseuille method was $\eta = 1.07 \pm 0.004$, where the external force was $g_z = 0.055$ in reduced units. The resultant temperature and density profiles across the channel are given in Fig. 4.9. Both profiles are uniform across the channel and their average values correspond well to the input values. The

velocity profile obtained from the same runs is given in Fig. 4.10. Following this, equivalent viscosity calculations were performed using the shear flow generated by Lees-Edwards boundary conditions. Here, the shear rate was set at $\Gamma = 0.05$. The estimated shear viscosity in this case was $\eta = 1.074 \pm 0.004$. Thus, two essentially different techniques have produced the same result.

Finally, we generated a Poiseuille flow by applying an external force $g_z = 0.055$ to the system with added boundaries. The resultant velocity profile is given in Fig. 4.11. The analytical Navier-Stokes solution with viscosity $\eta = 1.03 \pm 0.02$ was fitted to the data, and is also depicted in the figure. This represents a significant discrepancy with the two previous results. The corresponding temperature and density profiles are given in Fig. 4.12. These indicate substantial density fluctuations near the walls, which is a general problem in DPD simulations of systems in which walls are represented by frozen particles. The temperature drops in value near the walls, which is another undesirable effect. It should be also noted that the configurational temperature in this case was estimated as $T_{conf} = 1.086 \pm 0.002$, which is a significant deviation from the input value in spite of the very small time step used.

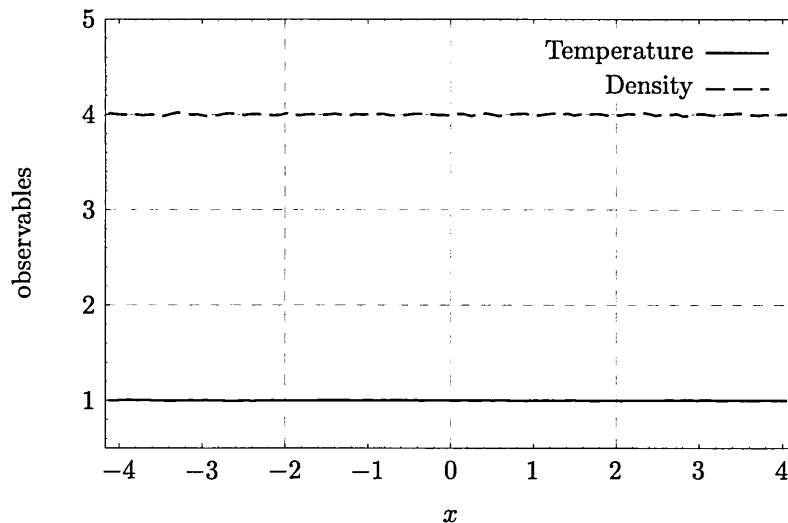


Figure 4.9: The temperature and density profiles in the periodic Poiseuille flow.

4.3 Extending DPD for the Simulation of Liquid Crystals

In this section we introduce anisotropic interaction terms into the DPD simulation technique. We concentrate on a derivation that is applicable only to LCs. Since mesogens are anisotropic, this requires introduction of an additional mesoscopic

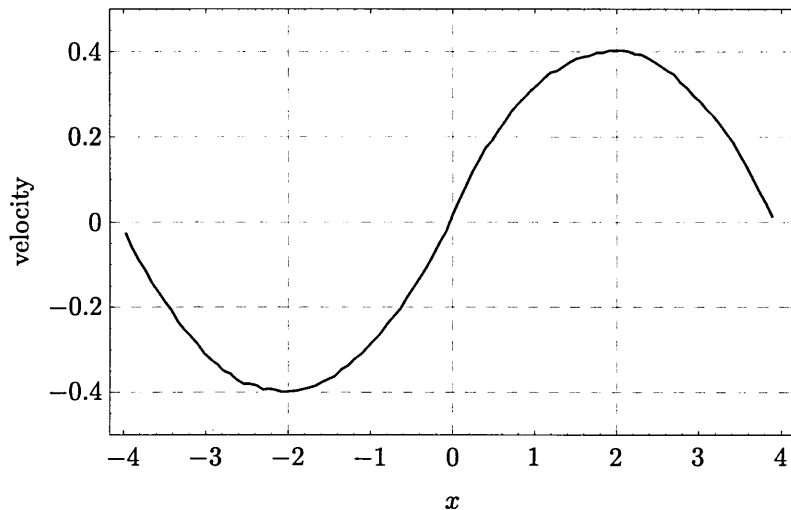


Figure 4.10: The velocity profile in the periodic Poiseuille flow system.

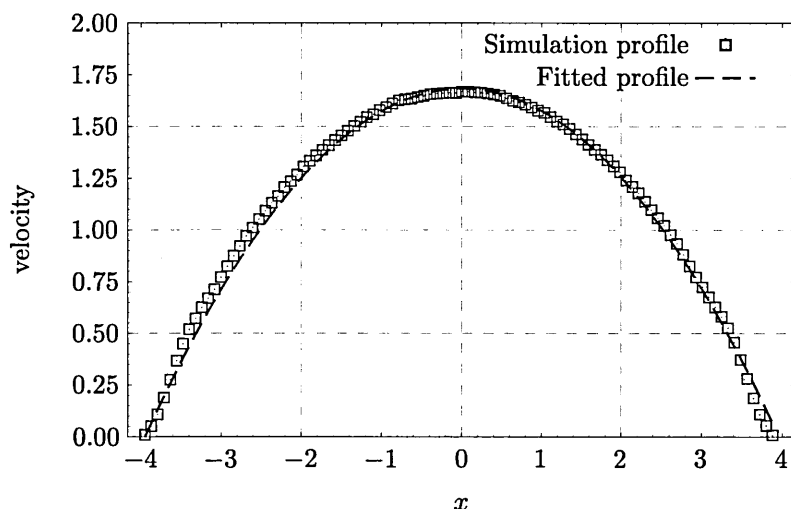


Figure 4.11: The velocity profile in the Poiseuille flow system along with fitted theoretical solution.

variable to the description of the fluid particles. First, we propose to associate a symmetric traceless tensor \mathbf{Q} with each fluid particle, which will carry information about the orientations of the molecules comprising the fluid particle. This is discussed in more detail in the next subsection. Following this, we incorporate dependence on the particles' \mathbf{Q} tensors into the conservative forces, and prove, for a general case, that any arbitrary dependence of the specified form will still lead to the proper equilibrium distribution in simulations. Finally, we introduce anisotropic terms into the thermostat forces in order to recover the correct hydrodynamic behaviour of LCs.

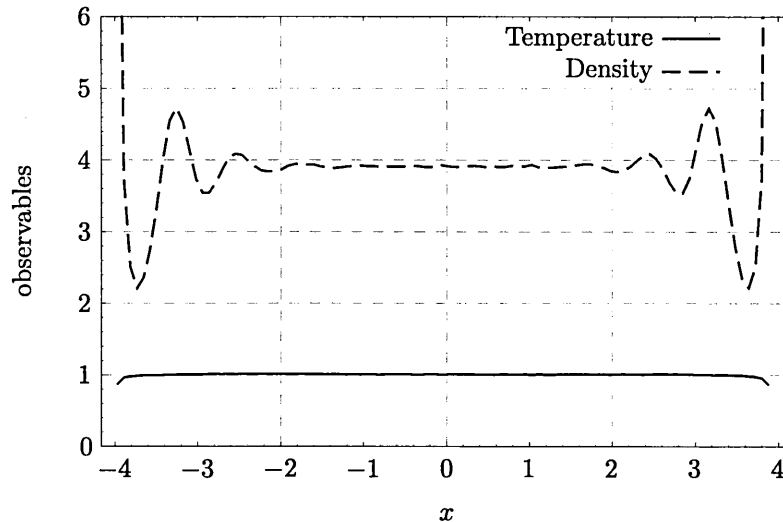


Figure 4.12: The temperature and density profiles in the Poiseuille flow.

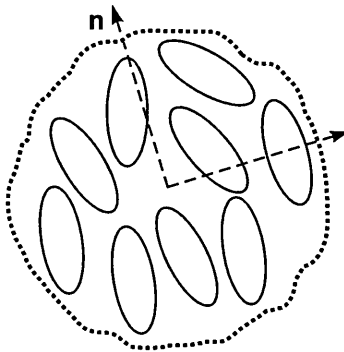


Figure 4.13: Schematic two-dimensional representation of LC bead in DPD.

4.3.1 Incorporation of a Q-tensor into DPD Formalism

DPD particles are usually considered as droplets or beads of fluid. Following this convention, and applying it to LCs, we now consider the use of DPD beads to represent droplets of (locally) ordered fluids, see Fig. 4.13 (in this figure, rod-like mesogens are depicted, but they could equally well be disk-like). The physical dimensions of such fluid particles can be determined, for instance, from pairwise radial distribution functions (positional and/or orientational), making a bottom-up link between microscopic and mesoscopic levels in the spirit of DPD. These fluid droplets are still considered as being spherical in shape, in spite of the fact that their constituent molecules are anisotropic. This can be justified on the grounds that even in the isotropic phase there are significant short-range orientational correlations between mesogenic molecules.

In the mesoscopic DPD description, one is normally interested only in some averaged values and less concerned about the detailed underlying molecular picture.

In LC beads accordingly, we do not need to know the orientation of each molecule, but we still need a means for describing average molecular orientation and order in every bead. The \mathbf{Q} tensor is a very appropriate quantity for this task. Let us assume that there are N molecules in each fluid particle, and that every molecule has orientation described by \mathbf{u} vector. Now let us define the ordering matrix averaged over the fluid particle as

$$\mathbf{Q} = \frac{1}{N} \sum_{i=1}^N \begin{pmatrix} u_{i,x}^2 - \frac{1}{3} & u_{i,x}u_{i,y} & u_{i,x}u_{i,z} \\ u_{i,x}u_{i,y} & u_{i,y}^2 - \frac{1}{3} & u_{i,y}u_{i,z} \\ u_{i,x}u_{i,z} & u_{i,y}u_{i,z} & u_{i,z}^2 - \frac{1}{3} \end{pmatrix}. \quad (4.21)$$

After the diagonalisation of \mathbf{Q} , the director frame can readily be identified, i.e. we obtain the order parameter S as the largest eigenvalue and its conjugated vector gives the director \mathbf{n} . The two other eigenvalues can be used to determine any biaxiality present.

4.3.2 Extending Conservative Forces

Here we make an extension to the conventional DPD conservative forces. We assume that the value of the order parameter of every fluid particle is constant, i.e. $S = 1$. We then define $c_{ij} = \mathbf{n}_i \cdot \mathbf{n}_j$, where \mathbf{n}_i is the orientation of the director of the i th particle. Then we extend the potential energy U_0 from the original DPD model as

$$U_1 = U_0 - \lambda P_2 U_0 = U_0(1 - 0.5\lambda(3c^2 - 1)), \quad (4.22)$$

where λ is some constant in the range $[0, 1]$ and $P_2 \equiv P_2(\cos \theta) = \frac{1}{2}(3c_{ij}^2 - 1)$. This form of the potential is chosen by analogy with the Maier-Saupe mean field potential. This gives an average potential energy U^M of a single molecule in the surroundings of the rest of molecules [2]

$$U^M = -\frac{A}{V^2} S \left(\frac{3}{2} \cos^2 \phi - \frac{1}{2} \right), \quad (4.23)$$

where ϕ is the angle between the long axis of the molecule and the director, V is the volume of the sample and A is a constant independent of temperature.

The revised conservative force needed to implement this extended scheme can be derived from

$$\mathbf{F}_{ij}^{C_1} = -\frac{\partial U_1(r, c)}{\partial r} \mathbf{e}_{ij}. \quad (4.24)$$

The torque exerted on the particle i by particle j is given by

$$\mathbf{N}_{ij} = -\mathbf{n}_i \times \left(\frac{\partial U_1(r, c)}{\partial c} \mathbf{n}_j \right), \quad (4.25)$$

and the torque exerted on the particle j by particle i is given as

$$\mathbf{N}_{ji} = -\mathbf{n}_j \times \left(\frac{\partial U_1(r, c)}{\partial c} \mathbf{n}_i \right). \quad (4.26)$$

One can immediately check that, in this extension, local angular momentum conservation holds, since

$$\mathbf{N}_{ij} + \mathbf{N}_{ji} + \mathbf{r}_{ij} \times \mathbf{F}_{ij} = 0. \quad (4.27)$$

4.3.3 Fokker-Planck Equation and Equilibrium State

The Fokker-Planck equation governs the time evolution of the probability distribution function $\rho(r, v, \varphi, \omega; t)$ of all positions, velocities, orientations and angular velocities of all the particles. The equation of motion for our model in the form of proper stochastic differential equations (SDE) becomes (compare with eq. 3.11):

$$\begin{aligned} d\mathbf{r}_i &= \mathbf{v}_i dt \\ d\mathbf{v}_i &= \frac{1}{m} \sum_{j \neq i} [\mathbf{F}_{ij}^{C_1}(r_{ij}, c_{ij}) - \gamma \omega^D(r_{ij})(\mathbf{e}_{ij} \cdot \mathbf{v}_{ij})\mathbf{e}_{ij}] dt + \frac{1}{m} \sum_{j \neq i} \sigma w^R(r_{ij}) \mathbf{e}_{ij} dW_{ij} \\ d\mathbf{n}_i &= \boldsymbol{\omega}_i dt \\ d\boldsymbol{\omega}_i &= \frac{1}{I} \sum_{j \neq i} \mathbf{N}_{ij}(r_{ij}, c) dt \end{aligned} \quad (4.28)$$

The notations used in the above equations are exactly the same as these in §3.2.2. $dW_{ij} = dW_{ji}$ are independent increments of the Wiener process. Ito interpretation is assumed, which is $dW_{ij}dW_{i'j'} = (\delta_{ii'}\delta_{jj'} + \delta_{ij'}\delta_{ji'})dt$, i.e. dW_{ij} is infinitesimal of order \sqrt{dt} .

Now, following the standard procedures outlined in §3.2.2, let us derive the Fokker-Planck equation that corresponds to the above SDE's.

Consider the differential of the arbitrary function f , keeping all terms of up to

order dt :

$$df = \sum_i \left(d\mathbf{r}_i \cdot \frac{\partial f}{\partial \mathbf{r}_i} + d\mathbf{v}_i \cdot \frac{\partial f}{\partial \mathbf{v}_i} + d\boldsymbol{\omega}_i \cdot \frac{\partial f}{\partial \boldsymbol{\omega}_i} + d\mathbf{n}_i \cdot \frac{\partial f}{\partial \mathbf{n}_i} \right) + \frac{1}{2} \sum_i \sum_j d\mathbf{v}_i d\mathbf{v}_j : \frac{\partial^2 f}{\partial \mathbf{v}_i \partial \mathbf{v}_j}. \quad (4.29)$$

Now substitute the above SDE's into the differential df , obtain $\langle df/dt \rangle$ and extract the Fokker-Planck equation:

$$\partial_t \rho(r, v, \varphi, \omega; t) = [L^C + L^T + L^R] \rho(r, v, \varphi, \omega; t) \quad (4.30)$$

where the operators are given by

$$\begin{aligned} L^C &= - \left[\sum_i \mathbf{v}_i \cdot \frac{\partial}{\partial \mathbf{r}_i} + \sum_i \sum_{j \neq i} \frac{1}{m} \mathbf{F}_{ij}^{C_1} \cdot \frac{\partial}{\partial \mathbf{v}_i} \right] \\ L^T &= \sum_i \sum_{j \neq i} \frac{1}{m} \frac{\partial}{\partial \mathbf{v}_i} \cdot \left[\gamma \omega^D(r_{ij}) (\mathbf{e}_{ij} \cdot \mathbf{v}_{ij}) \mathbf{e}_{ij} + \frac{\sigma^2}{2m} (\omega^R(r_{ij}))^2 \mathbf{e}_{ij} \mathbf{e}_{ij} \cdot \left(\frac{\partial}{\partial \mathbf{v}_i} - \frac{\partial}{\partial \mathbf{v}_j} \right) \right] \\ L^R &= - \left[\frac{1}{I} \sum_i \sum_{j \neq i} \mathbf{N}_{ij}(r_{ij}, c) \cdot \frac{\partial}{\partial \boldsymbol{\omega}_i} + \sum_i \boldsymbol{\omega}_i \cdot \frac{\partial}{\partial \mathbf{n}_i} \right] \end{aligned} \quad (4.31)$$

The operator L^C is the Liouville operator of a Hamiltonian system interacting with conservative forces. The steady state solution of eq. (4.30), $\partial_t \rho \equiv 0$, gives the equilibrium distribution ρ^{eq} . A canonical ensemble:

$$\begin{aligned} \rho^{eq}(r, v, \varphi, \omega) &= \frac{1}{Z} \exp(-H(r, v, \varphi, \omega)/k_B T) \\ &= \frac{1}{Z} \exp \left[- \left(\sum_i \frac{m v_i^2}{2} + \frac{I \omega_i^2}{2} + U_1(r, \varphi) \right) / k_B T \right] \end{aligned} \quad (4.32)$$

will be the solution if the dependencies from the original DPD hold (3.8), since for this distribution $L_{ij}^R \rho \equiv 0$. This means that all equilibrium properties of the original DPD are the same as the properties of the extended model. This, certainly, implies that both the H-theorem and the equipartition theorem hold in this case.

Furthermore, the above derivations can be extended to the general case. Let us consider an arbitrary potential between two fluid particles of the form $U = U(r, \mathbf{n}_i \cdot \hat{\mathbf{r}}, \mathbf{n}_j \cdot \hat{\mathbf{r}}, \mathbf{n}_i \cdot \mathbf{n}_j) = U(r, a, b, c)$, i.e. a function of the centre-centre separation r and all possible scalar products of the unit vectors $\hat{\mathbf{r}}$, $\hat{\mathbf{n}}_i$ and $\hat{\mathbf{n}}_j$. Note that the relative orientation of two linear molecules is completely specified by the set (a, b, c) .

Then we can calculate the conservative force between particles i and j using the chain rule. Thus,

$$\mathbf{F}_{ij}^C = -\nabla_{\mathbf{r}_{ij}} U = -\frac{\partial U}{\partial r} \hat{\mathbf{r}}_{ij} - \frac{\partial U}{\partial a} \hat{\mathbf{n}}_i - \frac{\partial U}{\partial b} \hat{\mathbf{n}}_j. \quad (4.33)$$

From this it can be seen that the total momentum is conserved, since $\mathbf{F}_{ij} = -\mathbf{F}_{ji}$.

Explicitly, the torque exerted on the particle i by particle j is given by

$$\mathbf{N}_{ij} = -\mathbf{n}_i \times \left(\frac{\partial U}{\partial a} \mathbf{r}_{ij} + \frac{\partial U}{\partial c} \mathbf{n}_j \right), \quad (4.34)$$

and the torque exerted on the particle j by particle i

$$\mathbf{N}_{ji} = -\mathbf{n}_j \times \left(\frac{\partial U}{\partial b} \mathbf{r}_{ij} + \frac{\partial U}{\partial c} \mathbf{n}_i \right). \quad (4.35)$$

One can immediately check that the conservation of local angular momentum holds as well

$$\mathbf{N}_{ij} + \mathbf{N}_{ji} + \mathbf{r}_{ij} \times \mathbf{F}_{ij}^C = 0. \quad (4.36)$$

The Fokker-Planck equation is equivalent to equations (4.30-4.31). In this case, again, it could be checked that $L_{ij}^R \rho^{eq} \equiv 0$ by substituting the torques, given by equations (4.34-4.35), into the operator L^R , where ρ^{eq} is given by eq. (4.32). This leads to a very important conclusion – the conservative force can be arbitrarily adjusted, in terms of its dependance on the particles' local directors, and the system will still achieve a proper thermodynamic equilibrium. Thus, ultimately the full elasticity can be recovered for LCs through use of more sophisticated inter-particle interactions than the basic Maier-Saupe-like from eq. (4.22) considered here.

4.3.4 Extending the Thermostat Forces

In the previous subsection we have considered an extension to the DPD conservative forces based on the particles' \mathbf{Q} tensors. This extension was aimed at recovering the isotropic-nematic transition and elasticity of LCs. In this subsection we consider an extension of the DPD thermostat forces with a view of achieving correct hydrodynamic behaviour for a LC fluid.

Transport coefficients in DPD/FPM are not direct input parameters, but, rather, are emergent from a system's behaviour. Analytical expressions for transport coefficients, e.g. those are given by eqs. (3.26-3.29), involve a number of different parameters. Thus, in order to introduce \mathbf{Q} -tensor dependance into transport coeffi-

cients, we need to make one of these parameters \mathbf{Q} -dependant, i.e. make it variable. There are only two possible parameters suitable for this: the spatial average of the dissipative weight function $w^D(r)$ and the dissipation strength parameter γ . Other parameters appearing in the expression for the transport coefficients, such as the dimensionality of the system d , obviously can not be made variable.

In the spirit of the conservative forces extension, we choose, then, to include the \mathbf{Q} -tensor dependance into weight functions of the DPD thermostat. By modifying the random weight function $w^R(r)$ and then setting the dissipative weight function $w^D(r)$ according to eq. (3.8), we ensure that the fluctuation-dissipation theorem is fulfilled. This allows varying transport coefficients while still properly sampling Maxwell-Boltzmann distribution in particles velocities.

In what follows we concentrate on two important transport coefficients, namely the viscosity and the diffusion coefficients. Qualitatively, for a calamatic LC (i.e. comprising rod-like molecules), the effective viscosity measured parallel to the director is lower than that measured perpendicular to the director. Conversely, the diffusion coefficient measured parallel to the director is greater than that measured perpendicular to the director [136]. Thus, in order to replicate this qualitative picture, the dissipative weight function dependencies of the viscosity and the diffusion coefficients should have opposing proportionalities. The diffusion coefficient is always inversely proportional to the dissipative weight function, see eq. (3.28). Thus, the above condition is only possible when the DPD fluid is in the dissipative regime, i.e. it is characterised by a high value of friction coefficient γ and a small temperature $k_B T$. In this case, the first term in the DPD viscosity given by eq. (3.27) is dominant.

We propose, therefore, the following extension to the random DPD force:

$$w_1^R(r) = w^R(r)(1 - 0.5\lambda_t(3c^2 - 1)), \quad (4.37)$$

where $w^R(r)$ is the original weight function given by eq. (3.9) and λ_t is a parameter in the range $[0, 1)$. If $\lambda_t = 0$, then this reverses back to the original DPD function. As λ_t increases in magnitude, conversely, the proposed weight function becomes increasingly influenced by LC's anisotropy. The functional form for the new thermostat weight functions in eq. (4.37) is chosen simply for consistency with the way we extended conservative forces, as can be seen by comparing eq. (4.37) with eq. (4.22).

4.4 Simulation Results

In this section, we present simulation results obtained using the proposed model. DPD is inherently a qualitative model and, thus, we concentrate on examples which can be used to validate the model by showing it to be capable of representing the essential physics of LCs.

4.4.1 Recovering the Isotropic-Nematic Phase Transition

In this subsection we test the ability of the proposed model to recover the isotropic-nematic transition. For this, a series of compression runs were conducted with different values of the λ parameter from eq. (4.22). A plot of the resulting order parameter versus number density behaviour is depicted in Fig. 4.14. The existence of an isotropic-nematic phase transition is clearly demonstrated in the figure. The λ parameter affects the threshold of isotropic-nematic phase transition, but does not significantly change the character of the transition.

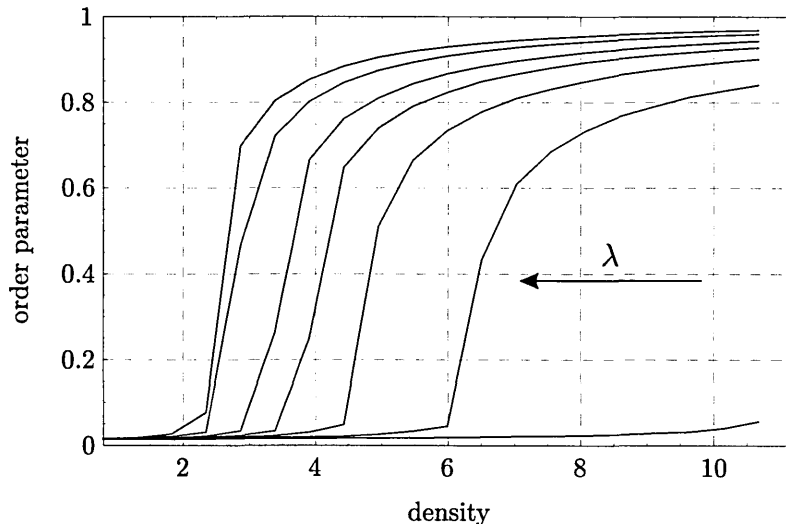


Figure 4.14: Dependence of the order parameter on number density for six different values of λ in the range $[0.3:0.9]$.

4.4.2 Diffusion Coefficients

In this subsection we test the ability of the proposed model to reproduce hydrodynamic behaviour in a qualitatively correct manner. Here, we set $\lambda = 0.8$.

Firstly, agreement with the equipartition theorem was tested. It was found that the rotational kinetic temperature agreed exactly with the translational kinetic temperature.

Next, we measured the diffusion coefficients parallel and perpendicular to the director. For this, we fixed the orientation of the director with a very weak external electric field to lie along one of the box axes. There are two standard approaches for measuring diffusion coefficients in particle-based simulations, one based on the Einstein expression and an alternative route based on the Green-Kubo relation. We have implemented both of these approaches, and, having verified that the two produce equivalent results, have employed the latter. The relevant Green-Kubo expression is based on the integrated velocity autocorrelation function and is given by

$$D = \frac{1}{3N} \int_0^\infty \left\langle \sum_{j=1}^N \mathbf{v}_j(t) \cdot \mathbf{v}_j(0) \right\rangle dt. \quad (4.38)$$

This can then be resolved into components parallel and perpendicular to the fixed director, by estimating the integral (4.38) for the x , y and z directions separately. The measured diffusion coefficient, D , as a function of number density, ρ , is plotted in Fig. 4.15. The diffusion coefficient measured perpendicular to the director decreases as the density increases. This is a typical dependence of the diffusion coefficient on increasing density. On the other hand, the diffusion coefficient measured parallel to the director increases with the density. This counter-intuitive behaviour is peculiar to LCs and has been previously observed in molecular dynamic simulations [136]. The order parameter variation of the LC corresponding to these densities is also plotted with the diffusion coefficients in Fig. 4.15. As expected, there is a direct correspondence between the order parameter variation and the measured diffusion coefficients. This is especially marked for the increasing diffusion coefficient parallel to the director. This is directly attributable to the enhanced orientational order in the system, which promotes diffusion parallel to the director.

4.4.3 Simulation of Colloidal Particles Immersed in LCs

In this section, we present results obtained when we use our proposed mesoscopic model to simulate colloidal particles immersed in LCs. Colloidal particles can be represented using two different approaches in DPD simulations. In the first of those, each colloidal particle is represented as a group of dissipative particles [6, 7, 137]. The second approach involves employing a special potential between the colloidal particles and the dissipative particles [138], such that each colloidal particle is represented by only one particle in the simulations. In our simulations we adopt the latter approach, since it is much more efficient and it allows flexibility in the choice of potential between the different types of particles.

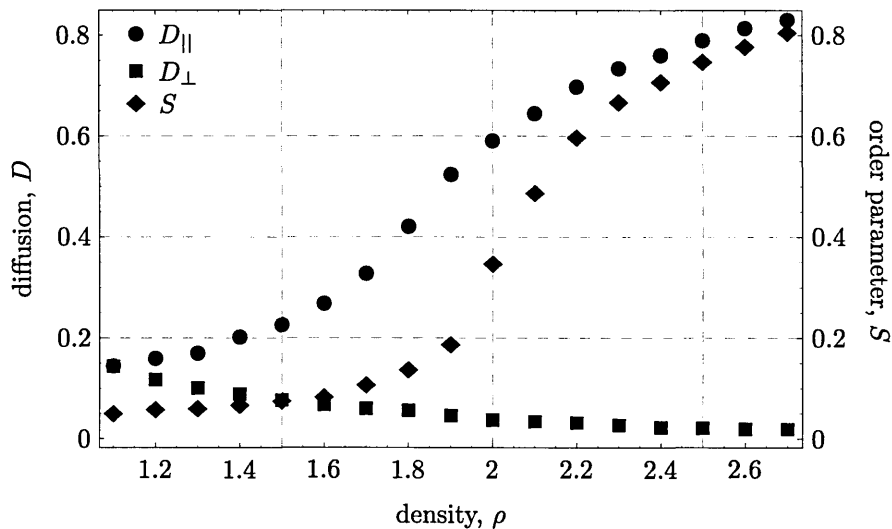


Figure 4.15: Diffusion coefficients measured parallel ($||$) and perpendicular (\perp) to the director as a function of number density ρ . Corresponding order parameter values S are also shown.

We treat each colloidal particle as a spherical particle with radius greater than radius of the DPD fluid particles. In order to simulate the interactions between the colloidal and fluid particles, we employ the interaction mechanism proposed by Satoh and Chantrell [138]. In this, each colloidal particle is regarded as a hard sphere, so that fluid particle velocities are reflected on contact with it. We employ a simple potential to achieve this, namely the Lennard-Jones (LJ) potential. However, if the LJ potential is based on the centres of two particles, this can lead to a significant overlap between colloidal and fluid particles [138]. Thus, an inscribed sphere inside each colloidal particle is considered, with the same diameter as fluid particles and located on the line connecting the centres of the fluid and colloidal particles. This is illustrated in Fig. 4.16. The LJ potential is then effectively applied between each fluid particle F and its correspondingly inscribed virtual particle V . We assume that colloidal particles do not possess any rotational motion and set their angular velocities to zero.

The equations of motion of the colloidal particles are integrated after the total forces acting on them have been calculated. This is achieved in a similar manner to that used for the dissipative particles. The masses of the colloidal particles are set depending on the simulated system. Also, the timestep in simulations involving such colloidal particles needs to be less than that used in generic DPD simulations due to the relatively steep LJ potential employed.

Finally, we needed to develop a route for imposing boundary conditions for \mathbf{Q} . In our simulations, we impose homeotropic boundary conditions on the surfaces of

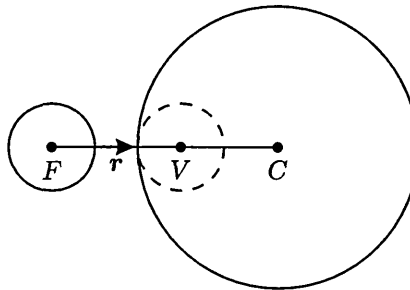


Figure 4.16: Scheme of interaction between colloidal (C) and fluid particles (F), mediated by a virtual particle V .

colloidal particles. For that, we use the same potential as for the fluid-fluid particle interactions, as compared to LJ potential employed for the translational motion. In order to achieve this, we assume that each inscribed virtual particle V has a director which coincides with the line connecting the centres of V and F . Then, the torque acting on the fluid particles is found from eq. (4.22). Consequently, the strength of the homeotropic anchoring can be changed by varying the parameter λ appearing in eq. (4.22).

A typical configuration taken from an equilibrated system of a single colloidal particle immersed in a FPM nematic LC is shown in Fig. 4.17. Here we use $\lambda = 1$ for the LC-colloid interaction so as to impose strong anchoring. In this figure, a cross-section snapshot of the 3D simulated system is shown. This shows that the homeotropic anchoring of the colloidal particle is very pronounced. There is also a Saturn ring defect surrounding the particle. In all our simulations we were only able to achieve defects of this type. Various attempts at obtaining point satellite defects, such as varying the diameter of the colloidal particle or decreasing the anchoring coefficient, did not succeed; the Saturn ring defect formed in all of the simulations considered.

4.5 Discussion

In this chapter we have proposed a novel model for LC simulations based on DPD (FPM) models. This model properly captures the essential physics of LCs, as has been demonstrated in a number of examples. It achieves this through effectively integrating out most of the underlying molecular behaviour. Through this it can be used to easily achieve simulations of complex LC phenomena on meso time- and length-scales thanks to it being computationally very fast.

As compared to other simulation techniques, this model's niche is the ability to quickly simulate dynamic behaviour of systems such as inclusions in LCs. For

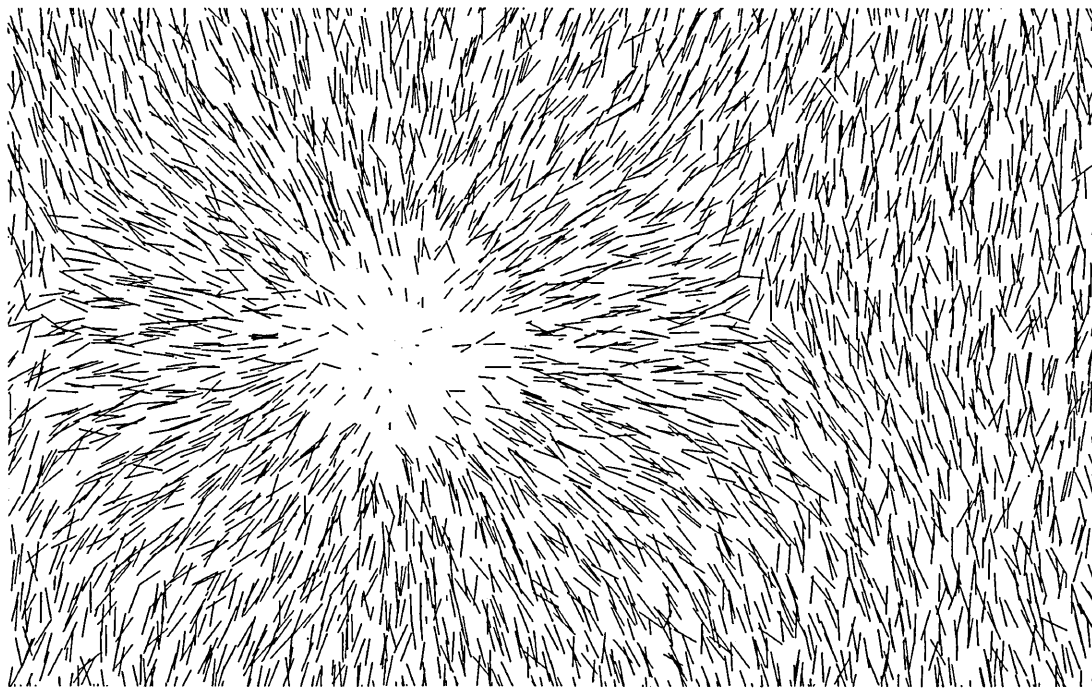


Figure 4.17: Cross-section of a system with a colloidal particle immersed in a LC. The Saturn ring defect lies in a plane perpendicular to this image and is manifested here as just two $1/2$ point defects.

example, a simulation of three colloidal particles immersed in a 3D nematic LC takes around half an hour to complete on a single processor. A snapshot from such a simulation is shown in Fig. 4.18. Similar coarse-grained MD simulation of only one fixed colloidal particle took several months to complete [139]. There are mesoscopic LB models for LC simulations, e.g. [11, 12, 13]. With the help of these, it has proved possible to consider simulations of different inclusions in LC, but this has required a great deal of computational work, not to mention coding time, for detecting the boundaries of these inclusions and taking them into account. If we consider different continuum grid-based techniques, such as FDM and FEM, then these suffer from similar problems to the LB method, i.e. remeshing, in which a significant part of computational time is spent on dealing with moving interfaces.

The proposed model, obviously, is not ideal. There are some problems associated with it, which directly stem from the underlying DPD model. The major issue is the inability to properly connect this mesoscopic model with either molecular or continuum descriptions. For example, it is not clear how to map the elastic constant appearing in eq. (4.22), which is described by only one λ parameter, with its continuum counterpart. Nevertheless, this model's initial goal was to produce a qualitative picture and, thus, this is what one should keep in mind when planning to use it. Notwithstanding this limitation, the system depicted in Fig. 4.18 represents,

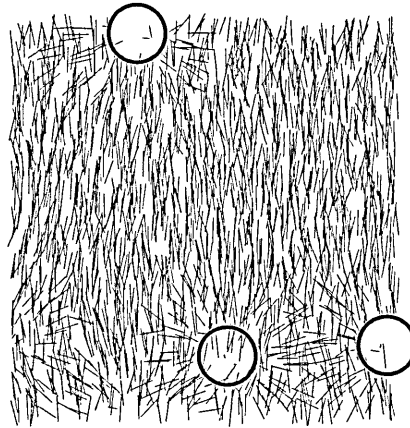


Figure 4.18: Cross-section of a system with colloidal three particles immersed in LC.

to our knowledge, the first 3D dynamic simulation of a LC colloid system.

4.6 Conclusions and Future Work

In this chapter, we have presented a novel mesoscopic simulation technique for LC modelling, which is based on DPD/FPM simulation techniques. We have qualitatively demonstrated that it recovers qualitatively correct LC behaviour, both from the ordering point of view (isotropic-nematic transition) and from its hydrodynamic behaviour. Quantitatively it was proven that both the H-theorem and the equipartition theorem hold for the proposed model. We have also demonstrated how colloidal particles immersed in LCs can readily be simulated using this approach.

Obviously, more work is still needed in this direction. For example, the model could be extended to include more elastic constants. Also, by appropriate modification of the weight functions, five independent Leslie viscosities could be recovered. More research is also needed on the colloidal particle systems in order to gain a greater understanding of the capabilities of the proposed model.

Chapter 5

Implementation of Top-down Approaches

The aim of this chapter is to derive a mesoscopic mesh-free particle technique for LC nematodynamics, in the context of the Qian-Sheng description, using a top-down approach. We initially present our attempts to apply Smoothed Particle Hydrodynamics (SPH) and its variants to the simulation of LCs and show that none of these prove able to produce a numerically stable simulation technique. We then present a generalisation of the Modified Smooth Particle Hydrodynamics (MSPH) simulation technique which is capable of simulating static and dynamic liquid crystalline behaviour. We subsequently validate this technique by reporting the results it yields for a number of numerical test-cases and comparing these results with available analytical solutions.

5.1 Revising the Governing Equations

In mesh-free particle methods, material particles can be either fixed in an Eulerian frame or move in a Lagrangian frame. We are considering flow of LCs and thus we need a description of particles in the Lagrangian frame. The original Qian and Sheng formulation [14] for the flow of a nematic LC whose orientational order is described by a \mathbf{Q} tensor are given in §2. Here, we first alter these governing equations in order to make them suitable for mesh-free simulations and then present the explicit form of the equations used in our simulations. Our derivations are similar to those used for Lattice-Boltzmann simulations of nematodynamics [11].

We use the common assumption that the angular velocity relaxes quickly and, thus, set the moment of inertia equal to zero $J = 0$. With this in view, we substitute

eq. (2.45) into eq. (2.41) to yield

$$h_{\alpha\beta}^B - \frac{\mu_2 A_{\alpha\beta}}{2} - \mu_1 N_{\alpha\beta} - \lambda^B \delta_{\alpha\beta} - \varepsilon_{\alpha\beta\gamma} \lambda_\gamma^B = 0. \quad (5.1)$$

Substitution of the explicit form of the co-rotational derivative $N_{\alpha\beta} = \dot{Q}_{\alpha\beta} - \varepsilon_{\alpha\mu\nu} \omega_\mu Q_{\nu\beta} - \varepsilon_{\beta\mu\nu} \omega_\mu Q_{\alpha\nu}$ into eq. (5.1) and subsequent simplification gives the order evolution equation in the following form:

$$\dot{Q}_{\alpha\beta} = \frac{h_{\alpha\beta}^B}{\mu_1} - \frac{\lambda^B \delta_{\alpha\beta}}{\mu_1} - \frac{\varepsilon_{\alpha\beta\gamma} \lambda_\gamma^B}{\mu_1} - \frac{\mu_2 A_{\alpha\beta}}{2\mu_1} + \varepsilon_{\alpha\epsilon\lambda} \omega_\epsilon Q_{\lambda\beta} + \varepsilon_{\beta\epsilon\lambda} \omega_\epsilon Q_{\alpha\lambda}. \quad (5.2)$$

This is well suited for mesh-free simulations and is the main equation used to implement order evolution.

Next, we consider the main LC momentum evolution (2.40), which we restate here for the sake of self-consistency:

$$\rho \dot{u}_\beta = \partial_\alpha (-P \delta_{\alpha\beta} + \sigma_{\alpha\beta}^v + \sigma_{\alpha\beta}^d + \sigma_{\alpha\beta}^{EM}). \quad (5.3)$$

We first eliminate the time derivatives in the viscous stress tensor σ^v by making the co-rotational derivative $N_{\alpha\beta}$ the subject of the formula (5.1) and further substituting it into the eq. (2.44):

$$\begin{aligned} \sigma_{\alpha\beta}^v = & \beta_1 Q_{\alpha\beta} Q_{\mu\nu} A_{\mu\nu} + \beta_4 A_{\alpha\beta} + \beta_5 Q_{\alpha\mu} A_{\mu\beta} + \beta_6 Q_{\beta\mu} A_{\mu\alpha} \\ & + \frac{\mu_2 h_{\alpha\beta}^B}{2\mu_1} - \frac{\mu_2 \lambda^B \delta_{\alpha\beta}}{2\mu_1} - \frac{\mu_2 \varepsilon_{\alpha\beta\gamma} \lambda_\gamma^B}{2\mu_1} - \frac{\mu_2^2 A_{\alpha\beta}}{4\mu_1} - Q_{\alpha\mu} h_{\mu\beta}^B \\ & + Q_{\alpha\mu} \varepsilon_{\mu\beta\gamma} \lambda_\gamma^B + \frac{\mu_2 Q_{\alpha\mu} A_{\mu\beta}}{2} + Q_{\beta\mu} h_{\mu\alpha}^B - Q_{\beta\mu} \varepsilon_{\mu\alpha\gamma} \lambda_\gamma^B - \frac{\mu_2 Q_{\beta\mu} A_{\mu\alpha}}{2}. \end{aligned} \quad (5.4)$$

The explicit form of the distortion stress tensor σ^d can be found by substituting the bulk free energy (2.9) into eq. (2.42) to give:

$$\begin{aligned} \sigma_{\alpha\beta}^d = & -L_1 \partial_\alpha Q_{\epsilon\lambda} \partial_\beta Q_{\epsilon\lambda} - L_2 \partial_\nu Q_{\epsilon\nu} \partial_\beta Q_{\epsilon\alpha} - L_3 \partial_\beta Q_{\mu\gamma} \partial_\gamma Q_{\mu\alpha} - L_4 Q_{\alpha\mu} \partial_\mu Q_{\epsilon\lambda} \partial_\beta Q_{\epsilon\lambda} \\ & - \frac{4\pi L_1}{P_{ch}} \varepsilon_{\mu\alpha\rho} Q_{\mu\lambda} \partial_\beta Q_{\rho\lambda} + \frac{4\pi L_4}{P_{ch}} \varepsilon_{\mu\alpha\rho} Q_{\mu\epsilon} Q_{\epsilon\lambda} \partial_\beta Q_{\rho\lambda} \\ & + C_1 E_\mu \partial_\beta Q_{\mu\alpha} + C_2 E_\mu Q_{\mu\gamma} \partial_\beta Q_{\gamma\alpha}. \end{aligned} \quad (5.5)$$

Next, we identify the form of the Lagrange multipliers λ^B and λ_γ^B by studying eq. (5.1) and taking the trace of $h_{\alpha\beta}^B$:

$$h_{\alpha\alpha}^B = -h_{\alpha\alpha}^v + 3\lambda^B. \quad (5.6)$$

Substituting the explicit form of the viscous molecular field given by eq. (2.45) into

the above equation, and using the fact that $Q_{\alpha\beta}$ is symmetric and traceless yields:

$$\lambda^B = \frac{1}{3}(h_{\alpha\alpha}^B - \frac{\mu_2}{2}A_{\alpha\alpha}). \quad (5.7)$$

The term $A_{\alpha\alpha}$ is zero for incompressible fluids but it is kept here because we are treating the fluid as slightly compressible; this provides a mechanism for correcting any errors, should they arise.

Analysing the off-diagonal elements of $h_{\alpha\beta}^B$ in eq. (5.1) gives the following result for the Lagrange multipliers:

$$\lambda_\gamma^B = \frac{1}{2}\varepsilon_{\alpha\beta\gamma}h_{\alpha\beta}^B. \quad (5.8)$$

Lastly, we state the explicit form of the molecular field given in eq. (2.43) for phenomenological free energies given in §2.1.4:

$$\begin{aligned} h_{\alpha\beta}^B = & -\alpha_F Q_{\alpha\beta} + 3\beta_F Q_{\alpha\gamma} Q_{\gamma\beta} - 4\gamma_F Q_{\alpha\beta} Q_{\gamma\tau} Q_{\tau\gamma} \\ & + L_1 \partial_\gamma \partial_\gamma Q_{\alpha\beta} + L_2 \partial_\alpha \partial_\gamma Q_{\gamma\beta} + L_3 \partial_\gamma \partial_\beta Q_{\alpha\gamma} \\ & + \frac{L_4}{2} (2Q_{\mu\nu} \partial_\mu \partial_\nu Q_{\alpha\beta} + \partial_\nu Q_{\alpha\beta} \partial_\mu Q_{\mu\nu} + \partial_\mu Q_{\alpha\beta} \partial_\nu Q_{\mu\nu} - \partial_\alpha Q_{\gamma\tau} \partial_\beta Q_{\gamma\tau}) \\ & + \frac{4\pi L_1}{P_{ch}} (\varepsilon_{\mu\lambda\alpha} \partial_\lambda Q_{\mu\beta} - \varepsilon_{\alpha\nu\gamma} \partial_\nu Q_{\gamma\beta}) - \frac{12\pi^2}{P_{ch}^2} L_1 Q_{\alpha\beta} + \frac{18\pi^2}{P_{ch}^2} L_4 Q_{\alpha\gamma} Q_{\gamma\beta} \\ & + \frac{4\pi L_4}{P_{ch}} (Q_{\mu\alpha} \varepsilon_{\mu\nu\gamma} \partial_\nu Q_{\gamma\beta} + Q_{\beta\tau} \varepsilon_{\alpha\nu\gamma} \partial_\nu Q_{\gamma\tau} - \varepsilon_{\mu\lambda\alpha} Q_{\mu\epsilon} \partial_\lambda Q_{\epsilon\beta} - \varepsilon_{\mu\lambda\alpha} Q_{\epsilon\beta} \partial_\lambda Q_{\mu\epsilon}) \\ & + \frac{1}{3} \varepsilon_0 \Delta \varepsilon_a^{max} E_\alpha E_\beta + \frac{1}{3} \mu_0 \Delta \chi_a^{max} H_\alpha H_\beta \\ & - C_1 \partial_\beta E_\alpha + C_2 (E_\alpha \partial_\nu Q_{\beta\nu} - E_\mu \partial_\beta Q_{\mu\alpha} - Q_{\mu\alpha} \partial_\beta E_\mu). \end{aligned} \quad (5.9)$$

We thus have identified the core target equations for our simulations and expressed them in the Lagrangian frame. The target order evolution equation is eq. (5.2) and the target momentum equation is eq. (5.3). These have both been derived using the form of free energy given in §2.1.4 under the assumption that the moment of inertia is negligible.

5.2 Description of the Algorithm

In this section, we describe the key common points of simulation algorithms based on the SPH method and its variants. The specifics of individual methods, e.g. MSPH, will be given in the corresponding subsections.

In order to solve the set of Qian-Sheng equations given in §5.1 we choose to associate a traceless, symmetric, order tensor, $Q_{\alpha\beta}$, with each fluid particle. Microscopically, these order tensors convey information about the state of the average orientational ordering of the molecules which are assumed to be represented by each fluid particle. Mathematically, the Q tensor is just one more field variable describing

the system.

The resulting simulation algorithm centres, then, on solving the set of Qian-Sheng eqs. (5.2)-(5.3) on a set of randomly distributed points in 1-, 2-, or 3-dimensions using the SPH method. Firstly, particles are uniformly located on a problem's domain and are given initial values of velocity, density and \mathbf{Q} . Then, equations (5.2) and (5.3) are considered for each particle, with their right-hand sides replaced by the appropriate kernel estimates.

Thus, the algorithm can be summarised as follows. Firstly, we estimate the velocity gradients, and thus find $A_{\alpha,\beta}$, $N_{\alpha,\beta}$. After that, calculating all \mathbf{Q} derivatives up to second order, we estimate all stress tensors on the right hand side of eq. (5.3) and the molecular field $h_{\alpha\beta}$ on the right hand side of eq. (5.2). Finally, we calculate the right-hand side of eq. (5.3) by estimating the first order derivatives. When the right-hand sides of equations (5.2) and (5.3) are fully estimated, the values of the field variables are propagated using a predictor-corrector integrator discussed in §5.3.2. The differences between the variants of SPH centre on the ways in which the derivatives are calculated.

By its nature, SPH is an adaptive and Lagrangian mesh-free method in which particles are free to move. In some problems, however, the particles can be held fixed in space. This feature is relevant to the simulation of LCs in situations where \mathbf{Q} evolution (governed via eq. (5.2)) needs to be considered but the velocity field (governed via eq. (2.40)) can be neglected. In such cases, we set all velocities to zero and keep the simulated particles fixed in space. This approach significantly reduces the computational effort required, since it avoids the extra loop associated with the estimation of the derivatives in eq. (2.40). In circumstances such as this, SPH is employed as a purely mesh-free strong form numerical technique in which the positivity of the weight function is not exploited.

The original SPH approach uses pressure gradients to drive particles. Thus, it is necessary to use the quasi-incompressible equation of state for incompressible fluids, since fluid pressure is an explicit function of local fluid density, and use of the actual equation of state necessitates adoption of a very small time step. While LCs are incompressible, in our simulations they are treated as slightly compressible via the artificial equation of state. For this, we use the equation of state due to Morris et. al. [94]

$$P = c^2 \rho, \quad (5.10)$$

where c is the speed of sound.

5.3 Major Practical Implementation Aspects

5.3.1 Boundary Conditions

Boundary conditions are usually a source of numerical instability in SPH simulations and, thus, an extra care should be taken when implementing these. The usual practice for imposing boundary conditions is to use techniques based on virtual particles, as was discussed in §3.3.5, and this is the approach we adopt in our SPH simulations.

We employ two different types of boundary particles. Particles of the first type, or “boundary particles”, represent rigid boundaries. Unlike the interior particles, these boundary particles are always held fixed in space, even if they have non-zero prescribed velocities. They contribute in the normal way to the interactions of the interior particles. These are given by SPH summations, calculated from parameters including velocity, pressure, stress tensor and \mathbf{Q} -tensor. We do not evolve densities of boundary particles, unlike Morris et al. [94], since the non-evolving approach was shown to improve free surface flows of viscoelastic fluids near boundaries [95]. In our simulations, boundary particles also exert a penalty force when interior particles closely approach boundary particles. This is implemented in order to prevent interior particles from penetrating the boundary and so leaving the computational domain. This penalty force is similar to the Lennard-Jones interatomic potential [88]. We retain the penalty force in spite of the fact that it was shown to be unnecessary to keep it for Newtonian fluids [94]. The reason for this is that the complex nature of the stress tensor in Qian-Sheng description may lead to configurations where the isotropic pressure due to the artificial equation of state will be offset by terms containing \mathbf{Q} derivatives and, thus, an extra repulsion will be required to keep interior particles away from boundaries.

Particles of the second type are called “image particles” and their purpose is to alleviate the particle deficiency problem near the boundaries. These particles are located outside of the rigid boundaries such that they fill the domain in a range comparable with the support domain kh of the kernel function. These particles, like boundary particles of the first type, have fixed positions and densities. Initially all of the particles, including boundary and image particles, are usually distributed uniformly across the domain so as to avoid significant overlaps at the start of the simulation.

We now consider implementation of simple Dirichlet boundary conditions in a manner similar to Takeda et al. [108] and Morris et al. [94]. This idea is illustrated in Fig. 5.1 using the imposition of no-slip boundary conditions as an example. The

velocities of boundary particles are set to desired values, i.e. to zeros in this example. Then the velocities of the image particles are found by extrapolating the velocities of bulk particles across the boundary. To achieve this, first a normal distance d_A is found from an interior particle A to the rigid boundary, along with a normal distance d_B from an image particle B to the same boundary. The velocity of the image particle is then $\mathbf{v}_B = -(d_B/d_A)\mathbf{v}_A$. Since, in practice, bulk particles can closely

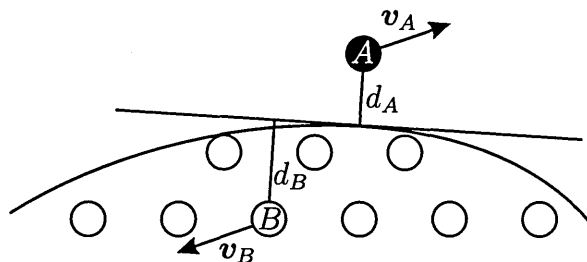


Figure 5.1: An example of setting the velocity of a boundary particle in order to implement no-slip boundary conditions in the original SPH method.

approach the boundary, the maximum value of image particle velocities should be restricted. Consequently, the final formula for the relative velocity of particles A and B is $\mathbf{v}_{AB} = \beta\mathbf{v}_A$, where

$$\beta = \min\left(\beta_{\max}, 1 + \frac{d_B}{d_A}\right). \quad (5.11)$$

Good numerical results are achieved if β_{\max} is set to 1.5 [94]. If the boundary itself is in motion, then \mathbf{v}_A should be replaced by the fluid velocity relative to this boundary. We use the same approach in order to impose boundary conditions for \mathbf{Q} tensors and estimate stress tensors $\boldsymbol{\sigma}$ while calculating forces acting on particles.

5.3.2 Time Integration Scheme

For consistency, we use second order Predictor-Corrector (P-C) methods to integrate both the equations of motion and the \mathbf{Q} -tensor evolution. P-C integration methods are simple, well-established and easy to code. Also, the right hand sides of equations (5.2) and (5.3) are very expensive to calculate and thus it is simply not feasible to employ various other integration methods, e.g. Runge-Kutta methods, for this task.

The final accuracy of solution in second order methods increases as $\mathcal{O}(dt^2)$, where dt is the time step used in the simulations. Thus, if the time step is reduced by a factor of 2, the accuracy is increased by a factor of 4.

We use the P-C algorithm for second order PDEs [140] to evolve the system with time, i.e. to integrate the equations for coordinates and velocity. If we denote the right hand side of eq. (5.3) by F_v , then the integration algorithm can be represented as following:

1: *Predictor step:*

$$2: x^p(t + dt) = x(t) + v(t)dt + \frac{dt^2}{2}a(t)$$

$$3: v^p(t + dt) = v(t) + a(t)dt$$

4: Calculate $F_v(t + dt)$ based on predicted values of $v^p(t + dt)$ and $x^p(t + dt)$.

5: *Corrector step:*

$$6: x^c(t + dt) = x(t) + v(t)dt + \frac{dt^2}{2}(a(t + dt) + 2a(t))/3.0$$

$$7: v^c(t + dt) = v(t) + dt(a(t) + a(t + dt))/2.0$$

Here the superscripts p and c refer to the predicted and corrected values, correspondingly. $a(t)$ denotes particle acceleration at time t and is given by $F_v(t)/m$.

We adopt a simple two step predictor-corrector (P-C) Heun method to integrate the resulting linear ordinary differential equations for Q evolution to second order accuracy. This approach uses Euler's method as a predictor and the trapezoidal rule as a corrector. If F_q is the right-hand side of eq. (5.2), then the scheme can be represented algorithmically as follows:

1: *Predictor step:*

$$2: Q^p(t + dt) = Q(t) + dtF_q(t)$$

3: Calculate $F_q(t + dt)$ based on predicted values of $Q^p(t + dt)$ and $x^p(t + dt)$.

4: *Corrector step:*

$$5: Q^c(t + dt) = Q(t) + dt[F_q(t) + F_q(t + dt)]/2.0$$

The above algorithms are single time step schemes, which means that only the information from the current time step is needed in order to calculate the solution at the next time step. Thus, a variable time step can easily be adopted. If higher accuracy is needed, multistep methods can be used, i.e. the information from previous time steps can be used.

5.3.3 Smoothing Length

The smoothing length h directly affects the accuracy and the efficiency of the SPH algorithm. If h is too small, then there are insufficient particles in the support domain to calculate the field variables' derivatives and, thus, the simulation breaks down. If, on the other hand, h is too big, then the support domain will contain too many particles with a consequence that all of the local properties will be smoothed out. This, in turn, will also affect the accuracy adversely.

If particles are initially distributed evenly inside the domain in a well-ordered fashion, e.g. on a lattice, we then employ a smoothing length h which is 1.1 – 1.5 times larger than the initial inter-particle separation. This also applies to situations in which we distribute points using the Monte-Carlo technique, here again we set the smoothing length to be 1.1 – 1.5 times greater than the average distance between points for the given particle. In both of these situations, the initial number of points in the support domain is monitored so that the smoothing length can be tuned, within the given limits, to provide the best accuracy.

Finally, when particles i and j have different smoothing lengths h_i and h_j , their interaction is symmetrised by using a mean smoothing length $h_{ij} = (h_i + h_j)/2$.

5.3.4 Smoothing Kernel

The choice of the smoothing kernel function in the SPH method is of the utmost importance, since the integral representation of function approximations is at the heart of this method. A number of different smoothing functions have been tried and described in the literature, and a number of requirements have been discussed. Here, we use the B-spline weight function due to Monaghan and Lattanzio [141] in our simulations

$$W(R) = \alpha_d \times \begin{cases} \frac{2}{3} - R^2 + \frac{1}{2}R^3 & 0 \leq R < 1 \\ \frac{1}{6}(2 - R)^3 & 1 \leq R < 2 \\ 0 & R \geq 2 \end{cases} \quad (5.12)$$

where R is the distance between two particles normalised by h and α_d is a normalisation factor which is equal to $1/h$, $15/(7\pi h^2)$ and $3/(2\pi h^3)$ in 1-, 2- and 3-dimensions, respectively. The support domain is equal to $2h$ when using this kernel function.

The first derivative of the B-spline can easily be obtained

$$W'(R) = \alpha_d \times \begin{cases} \frac{1}{h}(-2R + \frac{3}{2}R^2) & 0 \leq R < 1 \\ -\frac{1}{2h}(2 - R)^2 & 1 \leq R < 2 \\ 0 & R \geq 2 \end{cases} \quad (5.13)$$

As can be seen from the analysis of this first derivative, it has its maximum at $R = 2/3$ and then decreases with decrease in the inter-particle distance. This is clearly unphysical and has sometimes lead to instability [99]. Nevertheless, to date this has been the most widely used kernel function in the SPH literature and was shown to give good results in the MSPH simulations of Ref. [142].

5.3.5 Reduced Units

In computer simulations of physical phenomena, values of physical quantities very often take values which differ by many orders of magnitude. This clearly presents a problem for computer simulations where numbers are represented with a fixed precision. To avoid these problems, so-called reduced units are used. In these, dimensional values of physical quantities are scaled into reduced units. This is especially relevant in computer simulations of LCs, where, for example, the values of the elastic constants are of order 10^{-12} whereas those of the Landau coefficients are of order 10^5 .

In our simulations, we introduce a characteristic length \hat{l}_0 , a characteristic time \hat{t}_0 and a characteristic mass \hat{m}_0 . Typical values used are $\hat{l}_0 = 10^{-7}$ m, $\hat{t}_0 = 10^{-7}$ s and $\hat{m}_0 = 10^{-20}$ kg. When using this set of parameters, all other numerical quantities lie within a numerical range suitable for stable and reliable computer calculations, namely $10^{-2} - 10^3$.

Having introduced these characteristic quantities, we then scale all other physical quantities according to their dimensions. For instance, values of elastic constants are scaled to $\frac{\hat{t}_0^2}{\hat{m}_0 \hat{l}_0}$, which transforms their order of magnitude from 10^{-12} to 1. When outputting the observables, though, the values are scaled back to their original dimensional units.

5.4 Implementation Details For Individual Methods

5.4.1 Smoothed Particle Hydrodynamics

A review of the original SPH methodology was given in §3.3. Major implementation aspects which we adopted were described both in §5.2 and in §5.3. In this section, then, we describe a few remaining practical details which directly relate to our implementation of the original SPH approach.

The \mathbf{Q} tensor evolution is described by eq. (5.2), which involves second order derivatives of \mathbf{Q} . There are at least two different ways of estimating second order derivatives, which were presented in §3.3.1. As an obvious choice, we employ the form which is given by eq. (3.60) due to its improved accuracy.

We have also coded the possibility of including the XSPH averaging procedure, which was described in §3.3.5, into our SPH simulations. XSPH was shown to overcome the tensile instability problem which is very likely to arise in simulations

involving any sort of elasticity. We judged that this might be relevant for simulations of LCs, in which the stress tensor is given by the complex equation (5.4). The value of this expression is strongly dependant on the state of ordering, especially in regions with high Q gradients, and, thus, might trigger undesirable system behaviour. The XSPH approach, on the other hand, is very straightforward to implement and has been shown to produce smooth velocity fields [143].

5.4.2 Modified Smoothed Particle Hydrodynamics

We now describe details of the algorithm we have developed to simulate LC behaviour using the MSPH technique. All general implementation issues peculiar to the original SPH technique also hold for the MSPH method. The only major difference is the way in which derivatives are calculated, and thus this is the point we describe in detail in this section.

The way that derivatives are calculated in the MSPH method was described in §3.3.7. In brief, the system of linear equations (3.90) needs to be solved in accord with the matrix entries given by eqs. (3.91)-(3.92). In the MSPH approach, like in the original SPH, higher order derivatives can be calculated in two different ways. Firstly, the derivatives can be calculated directly by retaining all terms up to the required order in the Taylor expansion of the field function (3.88). This approach is computationally expensive, since the number of equations in (3.90) increases rapidly with both the number of expansion terms and the problem's dimensionality. An alternative approach is to calculate higher order derivatives directly as first-order derivatives of the lower order derivatives. This nested approximation retains the same order of accuracy as the full solution and is, therefore, our preferred approach in the calculations presented here.

We use the nested approach to calculate the derivatives involved, and retain all of the derivatives in the Taylor expansion up to the second order. We have found that retaining third order derivatives does not significantly improve the model's accuracy, whereas it does add an appreciable computational overhead.

In the MSPH formulation, there is no need to use an artificial viscosity since proper viscosity terms appear in eq. (5.3). It is also pertinent that there are no large velocities in typical LC simulations. Although we implemented an artificial viscosity, in case we needed it to stabilise the numerical scheme, we found that there was no need to include it in any of the simulations presented here.

As was discussed in §5.2, in some LC problems, the velocity field is not considered and thus the SPH method is employed purely as a mesh-free method. The same

is true for the MSPH method. In such a circumstance, the computational effort involved in MSPH is greatly decreased, since the matrix \mathbf{B} in eq. (3.90) needs to be estimated only once. The method's accuracy can be further improved by appropriate tuning of the smoothing length h and by achieving a uniform distribution of the particle positions [97]. It has been shown that, in such circumstances, the method's accuracy can exceed that of FEM approaches [142].

We treat boundary conditions in MSPH in the same way as we do in SPH, i.e. by employing virtual particles. However, we only use particles of the first type (boundary particles) to represent rigid boundaries, and do not need to use image particles to fill in the region outside of the boundary. This is due to the fact that the situation with boundaries is greatly improved in the MSPH method, as compared to SPH, where the consistency condition at and near to a boundary depends on both the number of higher order derivatives retained in eq. (3.88) and the placement of the boundary particles. Thus, in order to impose Dirichlet boundary conditions, we just need to set the desired values of the field variables at the boundary particles. For instance, in the case of infinitely strong orientational anchoring, the required \mathbf{Q} -tensor is achieved by setting $Q_{\alpha\beta} = \text{const}$ at the boundary particles.

In the case of weak anchoring, however, the \mathbf{Q} -tensor at the boundary particles is left free to evolve in accordance with eq. (2.48). Since eq. (2.48) is based on first order derivatives, the accuracy of its solution at the boundary is the same as that achieved in the bulk when using the MSPH. This consistency makes the implementation of weak anchoring boundary conditions reasonably straightforward.

5.5 Electric Field Solvers

In §2.2.2 we noted that LCs interact with applied electric or magnetic fields and, thus, it is often necessary to solve Maxwell's equations of electromagnetism when considering LC device behaviour. In LCs, the diamagnetism is small and thus we treat applied magnetic fields as constant. The dielectric parameters, on the other hand, are much larger and, thus, when an external voltage is applied, the dielectric contribution must be treated appropriately for accurate results to be achieved.

Maxwell's equations, with electro-hydrodynamic ion convection being deliberately ignored, are written in the following form:

$$\partial_\alpha D_\alpha = \sigma_f \quad (5.14)$$

$$D_\alpha = \epsilon_0 \epsilon_{\alpha\beta} E_\beta + P_\alpha \quad (5.15)$$

$$E_\beta = -\partial_\beta \phi \quad (5.16)$$

By subsequently substituting eq. (5.16) into eq. (5.15) and then further into eq. (5.14), and setting the free charge to zero $\sigma_f = 0$ we get:

$$-\partial_\alpha (\epsilon_0 \epsilon_{\alpha\beta} \partial_\beta \phi) + \partial_\alpha P_\alpha = 0. \quad (5.17)$$

Substitution of the dielectric tensor given by eq. (2.7) into the above equation with subsequent rearrangement gives the final equation to be solved for the potential ϕ :

$$\begin{aligned} \partial_\gamma \partial_\gamma \phi = \frac{1}{\epsilon_0 \epsilon_{\gamma\gamma}} [& -2\epsilon_0 \Delta \epsilon_a^{max} Q_{\alpha\beta} \partial_\alpha (\partial_\beta \phi) - 2\epsilon_0 \Delta \epsilon_a^{max} \partial_\alpha (Q_{\alpha\beta}) \partial_\beta (\phi) - \epsilon_0 \partial_\beta (\phi) \partial_\beta (\epsilon_{\gamma\gamma}) \\ & - 2\epsilon_0 Q_{\alpha\beta} \partial_\beta (\phi) \partial_\alpha (\Delta \epsilon_a^{max}) + 3\partial_\alpha P_\alpha]. \end{aligned} \quad (5.18)$$

Here a pure, single-component LC has been assumed and, thus, $\partial_t \epsilon_\perp = \partial_t \epsilon_\parallel = \partial_\alpha \epsilon_\perp = \partial_\alpha \epsilon_\parallel = 0$. The above equation for ϕ is a Poisson equation which reduces to the Laplace equation in the isotropic fluid limit.

As we are working with an off-lattice numerical method, eq. (5.18) needs to be solved at a randomly distributed set of points. This effectively limits the scope of the available numerical methods for the SPH technique. We have initially used a standard successive over relaxation (SOR) scheme for solving this equation. In developing our methodology, we subsequently adopted the mesh-free collocation technique which is more efficient and accurate. Both of these schemes are described further below.

SOR scheme. In order to solve eq. (5.18), we employ the SPH approach to calculate all of the derivatives appearing in this equation using the values of the potential ϕ determined at the previous time step. We then solve eq. (5.18) numerically using a SOR method at each time-step, when the Q -tensors are known for each particle. Thus, the scheme can be summarised as

$$\phi^{g+1} = \phi^g - \omega \Lambda, \quad (5.19)$$

where ϕ^{g+1} denotes the successive approximation to the current value of the potential ϕ^g , Λ is the calculated difference between the right and left hand sides of eq. (5.18) and ω is a convergence constant. Usually, only a few iterations are needed at each time-step in order to achieve the required accuracy. An external electric field is applied by imposing boundary conditions of the form $\phi = \text{const}$. This potential is then solved at each time step, which significantly reduces the computational efficiency.

MLSRK collocation technique. Using the mesh-free shape functions which are discussed in Appendix A, we can approximate functions and their derivatives

using eqs. (A.8–A.14). Thus, for any non-boundary internal node x_i with n nodes in its support domain, eq. (5.18) is discretised by simple collocations at x_i :

$$\left(\partial_\gamma \partial_\gamma \Phi^T - \frac{1}{\epsilon_0 \epsilon_{\gamma\gamma}} \left[-2\epsilon_0 \Delta \epsilon_a^{max} Q_{\alpha\beta} \partial_\alpha \partial_\beta \Phi^T - 2\epsilon_0 \Delta \epsilon_a^{max} \partial_\alpha Q_{\alpha\beta} \partial_\beta \Phi^T - \epsilon_0 \partial_\beta (\epsilon_{\gamma\gamma}) \partial_\beta \Phi^T - 2\epsilon_0 Q_{\alpha\beta} \partial_\alpha \Delta \epsilon_a^{max} \partial_\beta \Phi^T \right] \right) \phi = \frac{3\partial_\alpha P_\alpha}{\epsilon_0 \epsilon_{\gamma\gamma}}, \quad (5.20)$$

where ϕ is a vector that collects unknown potentials at nodes located in the support domain of x_i and Φ is the vector of shape functions:

$$\phi^T = \{\phi_1, \phi_2, \dots, \phi_n\} \quad (5.21)$$

$$\Phi^T = \{\Phi_1, \Phi_2, \dots, \Phi_n\} \quad (5.22)$$

Equation (5.20) can be equivalently written in the matrix form:

$$\mathbf{K}_i \phi = p_i, \quad (5.23)$$

where \mathbf{K}_i is the nodal matrix of node x_i with dimensions $1 \times n$, and represents the expression in brackets of eq. (5.20). The value of p_i is simply the right-hand side of eq. (5.20), i.e. $p_i = \frac{3\partial_\alpha P_\alpha}{\epsilon_0 \epsilon_{\gamma\gamma}}$. When there is no flexoelectricity involved in the simulated system, p_i is just set to zero.

Next, we consider the treatment of boundary conditions in the collocation technique. An external voltage is usually applied by setting a specified value of the potential ϕ at boundary nodes. Thus, eq. (A.9) for a boundary node x_b should read as

$$\Phi^T \phi = \phi_b, \quad (5.24)$$

where ϕ_b is the voltage applied at the boundary. It can be easily seen that, for boundary nodes, the nodal matrix \mathbf{K}_b then consists of only shape functions, i.e. $\mathbf{K}_b = \Phi$.

Finally, by assembling eqs. (5.23) and (5.24) for all nodes, we obtain the following system of linear equations:

$$\mathbf{K}_{N \times N} \phi_{N \times 1} = \mathbf{P}_{N \times 1}, \quad (5.25)$$

where the rows of the global matrix $\mathbf{K}_{N \times N}$ consist of nodal vectors \mathbf{K} , the global vector $\mathbf{P}_{N \times 1}$ consists of both p_i for internal nodes and values of applied voltage ϕ_b for boundary particles, and $\phi_{N \times 1}$ is the vector of unknown potentials at the nodes. By solving this system of linear equations, the value of the potential at each node

can be found. The global matrix $\mathbf{K}_{N \times N}$ is sparse and is very large for a big number of nodes N in the system. We use the numerical library PETSc [144] to effectively store and solve this system. This numerical library routine also provides a means of solving this system in parallel, which fits very well with our developed codes.

5.6 SPH Simulation Attempts

No simulation attempts of LCs using the SPH method have been previously reported. In this section, we present the ultimately fruitless attempts we have made to apply the SPH technique to the simulation of the Qian-Sheng equations outlined in §5.1.

The focus of these efforts are a set of simulations aimed at modelling Couette flow between two flat plates which impose infinite homeotropic anchoring. In the nematic phase, this shear flow has an aligning effect because the director aligns itself so as to minimise its torque. In these systems, elasticity can usually be ignored in the centre of the channel if the shear is strong and the channel has a large width; consequently the effects of the boundaries on \mathbf{Q} can be neglected. Olmsted [55] has shown that, in this limit, this flow is biaxial and the director angle is given by

$$\cos(2\theta) = -\frac{\mu_1}{\mu_2}(3S + P_B), \quad (5.26)$$

where θ is the angle which the director makes with the flow. This angle depends only on the viscosity ratio and is independent of the elastic constants.

We therefore consider a system which is initially at rest with \mathbf{Q} tensor set to be uniform across the cell. The cell width is $L = 1.2 \mu\text{m}$. At time $t = 0$, the upper plate starts to move at constant velocity $v_0 = 0.012 \text{ m/s}$ parallel to the x -axis. Thus, the first part of the simulation solely tests the SPH as a solver for the Newtonian fluid, since the \mathbf{Q} tensor is uniform and no gradients are present. The time scales for velocity and \mathbf{Q} evolution are of different orders of magnitude, and, thus, the velocity field is able to fully equilibrate before \mathbf{Q} develops any changes. We have not experienced any numerical problems in this part of the modelling; SPH simulations of this early stage proved robust and stable, as would be expected from the published literature. Typical examples of the time-dependant velocity profiles achieved during this rearrangement are shown in Fig. 5.2; the LC velocity gradually develops a linear profile with time. We compare these profiles with the available analytical solution by Morris [94], which is based on series solutions and is given by:

$$v_x(y, t) = \frac{v_0}{L}y + \sum_{n=1}^{\infty} \frac{2v_0}{n\pi} (-1)^n \sin\left(\frac{n\pi}{L}y\right) \exp\left(-\nu \frac{n^2\pi^2}{L^2}t\right), \quad (5.27)$$

where ν is the shear viscosity of the Newtonian fluid. Here, we substitute ν with the LC apparent viscosity which is equal to one of the Miesowicz viscosities, because Q is uniform. Here, the simulation results are in close agreement with the corresponding theoretical solutions.

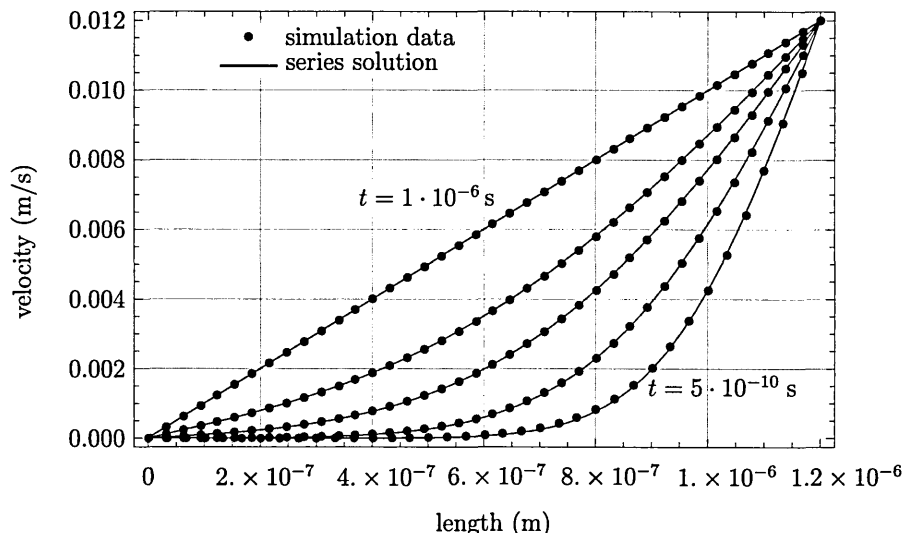


Figure 5.2: Time-dependant velocity profiles for Couette flow between two flat plates, obtained from SPH simulation and from analytical calculation [94].

As this system develops further, the director profile realigns itself so as to minimise the torque. The dependence of the angle between the director profile and the direction of flow as a function of time is shown in Fig. 5.3. This shows that the interfacial region grows markedly as the central region realigns with the flow. However, during this stage of the simulation we observed significant numerical instabilities which were manifested as spurious oscillations in both the velocity and pressure fields. These oscillations eventually led to diverging velocity values which ultimately caused most of these simulations to abort. An example of the velocity profile of one such simulation is given in Fig. 5.4, where a snapshot is given from the early stage of a breaking simulation. In all failed simulations, the numerical pathologies originated in regions located near to the boundaries, as can be seen in Fig 5.4. Fig. 5.3 represents a rare example of a successful run which produced a result set consistent with the analytical solution eq. (5.27) and did not fail.

Here, it should be noted that, in these test cases, gradients of Q gradually increased with simulation time, as can be clearly seen from Fig. 5.3. Further, the highest gradients in Q always developed near to the boundaries. Thus, with time, the simulations became increasingly prone to instabilities, especially next to boundaries, since the requirement on the order of approximation (consistency) for SPH only increases with time. In addition, SPH is of lower consistency order near to

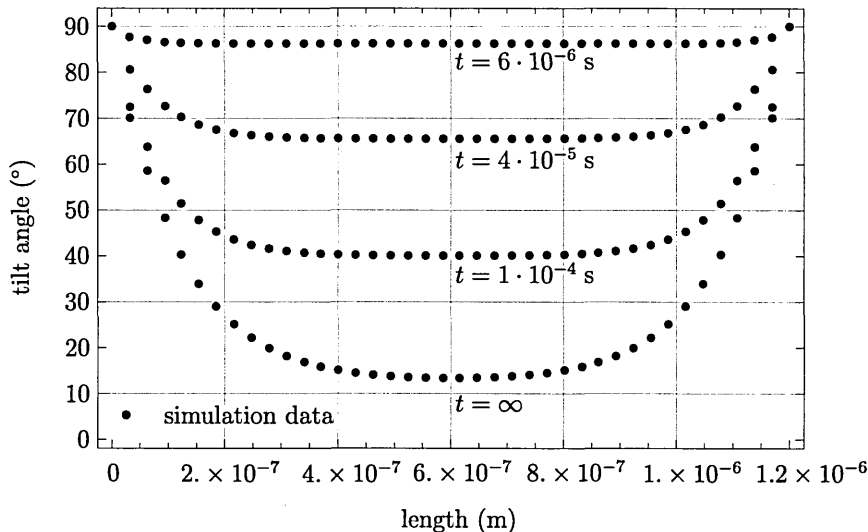


Figure 5.3: Time-dependant \mathbf{Q} tensor profiles for the Couette flow between two flat plates.

boundaries than it is in bulk (as was discussed in §3.3.4). That is why all of the simulation failures originated in regions adjacent to the boundaries.

In attempting to tackle these numerical instabilities, we took the following steps. First of all, since the instabilities occurred in velocities, we introduced particle-based improvements such as an artificial viscosity and velocity averaging (XSPH). These improvements directly influence the velocities, and are easy to implement and sometimes these techniques have been found to resolve instability problems [90, 143]. Unfortunately, however, they did not work for our particular case. While slightly improving the situation, in that instabilities occurred later in the simulation than they did with the original SPH, these remedies still failed to completely stabilise the scheme. The main reason for this is that none of these improvements directly target the core reason of the failure, i.e. the lack of consistency of the SPH method. Also, while the aforementioned improvements alleviated the consistency problem of the momentum equation (5.3), they did not have any effect on the order evolution equation (5.2). Consequently, the instabilities persisted.

As a second step, we imposed initial arrangements in which all particles were arranged on a uniform grid. In this case, the consistency of the SPH method increased, as would be expected, see §3.3.4. This had a direct effect on both the momentum and order evolution equations. By tweaking the smoothing length h as a function of initial particle spacing Δx we then tried to achieve numerically stable simulations, but again this was unsuccessful. In all of the above cases we tested a number of different kernel functions, namely quintic, cubic spline and Gaussian, but all of these produced equally unstable simulations. Thus, although these measures

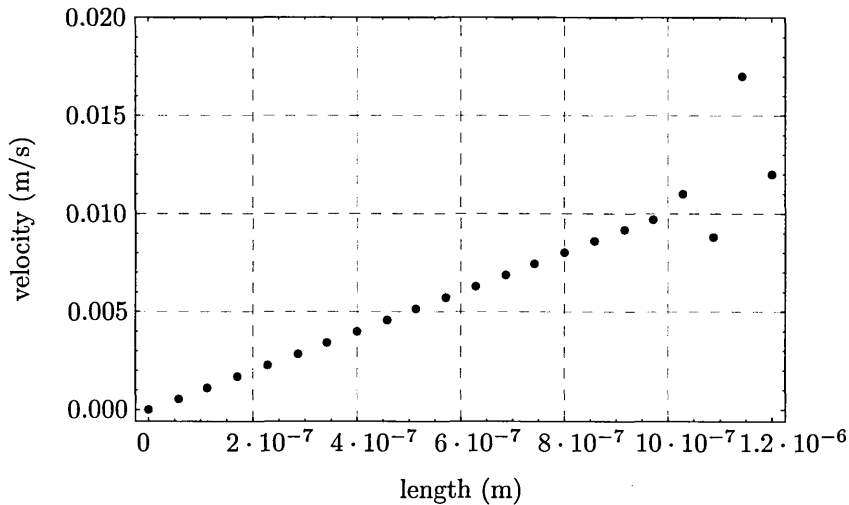


Figure 5.4: An example of unsuccessful simulation using the SPH technique.

improved the consistency of the SPH approximation, the order of the consistency increase was not sufficient to make it possible to model the target equations (5.2) and (5.3).

Having failed with particle-based improvements, we started to implement and test methods targeted at the improvement of the consistency of the original SPH method. The first obvious choice for this was the CSPM technique, outlined in §3.3.6, since this improves the consistency of the SPH near to or at the boundaries. The use of this technique did not, however, yield an LC simulator fit for purpose. This line of work was therefore abandoned in favour of the more complex MSPH approach described in §3.3.7. This did finally prove sufficiently stable for simulations of the Qian-Sheng equations of nematodynamics to be achievable. This is demonstrated in more detail in the following sections.

To conclude this section, we stress that the numerical instabilities observed here originate from algorithmic pathologies in the approximations used for parabolic or hyperbolic systems. In our case, these proved to derive from the rather complex nature of the driving equations. Thus, the consistency of the original SPH method is fundamentally inadequate for simulation of the Qian-Sheng equations. Also, the low accuracy of the SPH method near to or at system boundaries makes it impossible to impose anything more complex than Dirichlet boundary conditions. This too would be a big drawback for any mesoscopic simulation method of LC behaviour.

5.7 MSPH Testing and Verification

In this section we present results of numerical simulations which test the accuracy of the MSPH technique and assess its applicability to the modelling of electro-optical devices. Due to the relatively complex nature of the partial differential equations describing LC phenomena, we limit ourselves initially to quasi 1-dimensional examples which can be compared either exactly with analytical solutions or partially with previous simulations.

We test our solver step-by-step, initially starting only with Landau-de Gennes terms and gradually introducing elastic constants, flow and electromagnetic fields. First, in §5.7.1 we model the LC phase transition using only Landau-de Gennes theory and compare it with analytical results. Then, in §5.7.2 we demonstrate application of the method to the simulation of the classic Fréedericksz transition scenario in order to assess both electric field and Q -solvers, while neglecting flow. Next, in §5.7.3 we further test the MSPH solver by considering a situation which involves isolated LC flow in the transverse flow effect. Finally, in §5.7.4 we simulate the behaviour of a dual-frequency chiral hybrid aligned nematic LC cell, in order to validate the full implementation of the MSPH solver.

5.7.1 Equilibrium Phase Behaviour

The nematic-isotropic phase transition was considered in §2.1.4 using the Landau-de Gennes description. In this section we test the ability of our solver to properly reproduce LC phase behaviour. For this, we consider an unrestricted LC sample with material parameters suitable for 5CB [14], in which $a = 65000 \text{ J m}^{-3} \text{ K}^{-1}$, $B = 530000 \text{ J m}^{-3}$, $C = 980000 \text{ J m}^{-3}$. Periodic boundary conditions are assumed in each direction. We vary the temperature T in the system and measure the order parameter, the analytical value of which is given by eq. (2.12). The results are plotted in Fig. 5.5. When there is no applied electric field, heating the LC leads to an analytically predicted behaviour of the order parameter. The dependance in this case is the same as that plotted in Fig. 2.4, with the error being the round-off error and not exceeding 0.001%. The cooling process of the LC sample, starting from the isotropic phase with $S = 0$, clearly exhibits a jump at the lower limit of supercooling. Below this temperature the behaviour of the order parameter is identical to that in the previously described heating regime. We also plot the dependance of the order parameter on temperature when an external electric field is applied. The application of large electric field ($20 \cdot 10^6 \text{ V/m}$ with $\Delta\epsilon_a = 10.3$) makes the transition continuous.

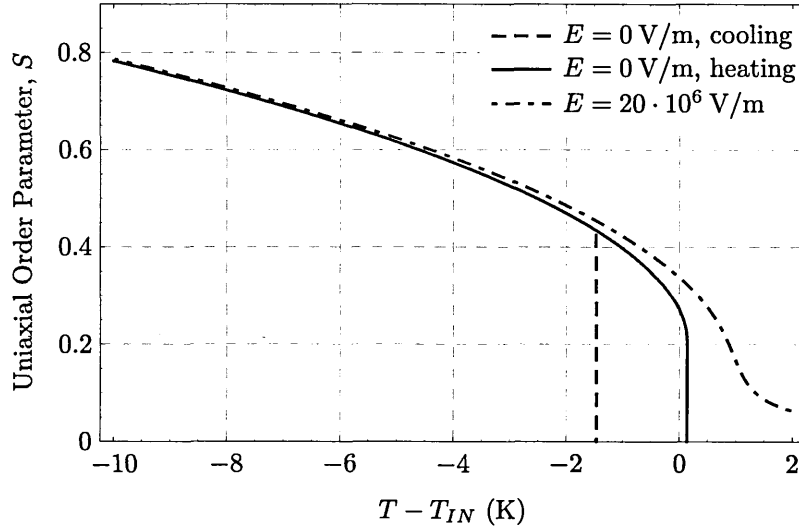


Figure 5.5: The dependance of the order parameter on the temperature, both with an applied electric field and without.

5.7.2 Fréedericksz Transition

We consider the splay geometry variant of the well known Fréedericksz transition behaviour. In this, we switch off the velocity field and consider only the evolution of the Q -tensor and electric field as the applied voltage is varied. In order to maintain consistency with analytical treatments, we assume infinite anchoring boundary conditions on both plates, with the director fixed parallel to the plates.

In the splay geometry, the critical Fréedericksz voltage V_c is given by

$$V_c = \pi \sqrt{\frac{K_1}{\epsilon_0 \Delta \epsilon}}, \quad (5.28)$$

where d is the distance between plates, $\Delta \epsilon$ is the LC's dielectric anisotropy and K_{11} is the splay elastic constant.

For an applied voltage $\bar{V} > V_c$ the maximum distortion angle θ_m of the director in the centre of the cell can be found numerically from the following equation [145, 146]

$$\frac{V}{V_c} = \frac{2(1 + \gamma \sin^2 \theta_m)^{\frac{1}{2}}}{\pi} \int_0^{\frac{\pi}{2}} \frac{G(\theta_m, \kappa, \gamma, \lambda)}{(1 + \gamma \sin^2 \theta_m \sin^2 \lambda)^2} d\lambda, \quad (5.29)$$

where $\gamma = \Delta \epsilon / \epsilon_{\perp}$, $\kappa = (K_{33} - K_{11}) / K_{11}$ and

$$G(\theta_m, \kappa, \gamma, \lambda) = \frac{(1 + \kappa \sin^2 \theta_m \sin^2 \lambda)(1 + \gamma \sin^2 \theta_m \sin^2 \lambda)}{1 - \sin^2 \theta_m \sin^2 \lambda}. \quad (5.30)$$

The resulting equilibrium director profile can then be determined from

$$\bar{z} = \frac{1}{2} \frac{\int_0^\phi G(\theta_m, \kappa, \gamma, \lambda)^2 d\lambda}{\int_0^{\frac{\pi}{2}} G(\theta_m, \kappa, \gamma, \lambda)^2 d\lambda}, \quad \phi = \sin^{-1} \left(\frac{\sin \theta}{\sin \theta_m} \right), \quad (5.31)$$

where $\bar{z} = z/d$ is the reduced distance. In the above equation $0 \leq \bar{z} \leq \frac{1}{2}$, the solution for $\frac{1}{2} \leq \bar{z} \leq 1$ being obtained from the symmetry condition $\theta(\bar{z}) = \theta(1 - \bar{z})$. Equations (5.29,5.31) were derived using an assumption of fixed order parameter. Despite this, we use them here to compare with our results since, in our simulations of this system, the maximal change in order parameter we have observed is 0.002.

As in the previous section, we use the following values of the Landau-de Gennes coefficients: $a = 65000 \text{ J m}^{-3} \text{ K}^{-1}$, $B = 530000 \text{ J m}^{-3}$, and $C = 980000 \text{ J m}^{-3}$, with elastic constant values ($K_{11} = 17$, $K_{22} = 13$, $K_{33} = 30$) $\times 10^{-12} \text{ N}$, we have simulated the Fréedericksz effect for a cell of width $d = 1 \mu\text{m}$ at temperature $T = T_{IN} - 4(T_{IN} - T^*)$. In order to achieve a marked response to the applied field, we have set the dielectric anisotropy to be relatively large $\Delta\epsilon = 10.3$, with $\epsilon_{\parallel} = 12.87$ and $\epsilon_{\perp} = 2.57$. For this choice of parameters, the critical Fréedericksz voltage is 1.36 V.

The evolution of the director profile for a uniformly-spaced 100 point simulation of this system on application of a 3 V potential to an initially uniform LC cell is shown in Fig. 5.6. These profiles represent snapshots taken from a run performed with a time-step of 10^{-7} s . The corresponding equilibrium director profile, determined from eq. (5.31), is also shown, and is in excellent agreement with the long-time simulation profile. The Q-solver element of this simulation was computationally very efficient, and the bulk of the run-time was taken up by the relatively rudimentary E-field solver used here.

In order to assess the effect of the number and distribution of the interpolation points on the accuracy of this simulation, we have performed a number of equivalent runs and found that small discrepancies can arise when regions with high director gradients have low point density. We quantify this effect in Table 5.1 which shows the percentage overshoot in the central director angle obtained for different choices of point distribution. This error is reduced below 0.5% for 100 uniformly spaced points or 70 non-uniformly spaced points. Here, a simple arithmetic progression was used to concentrate the non-uniform point distribution in the regions with high director gradient, but it would be straightforward to implement a scheme which iteratively distributed points according to their local Q gradients.

Finally, in this section, we note that time-dependant profiles of the electric potential are routinely determined in our method. We illustrate this behaviour in

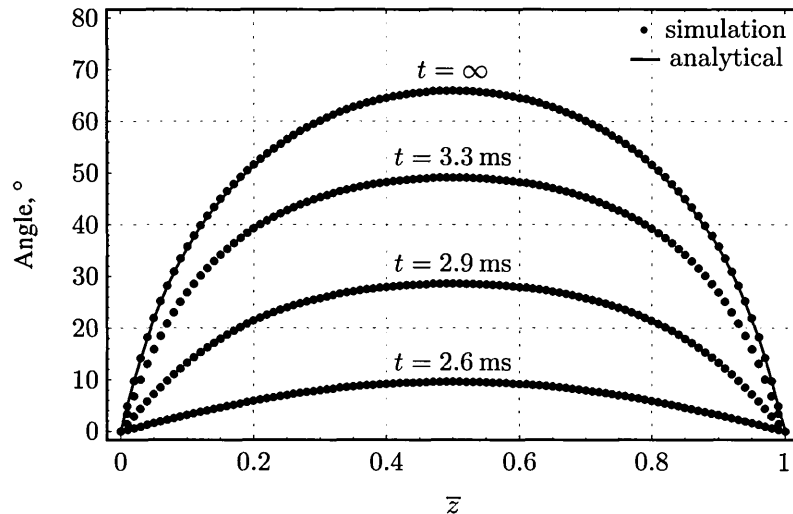


Figure 5.6: Time evolution of the angle which director makes with x -axis across the cell. Analytical curve in equilibrium is found from eq. (5.31).

Number of points	Uniform distribution, percentage error	Non-uniform distribution, percentage error
30	3.4	1.1
50	1.4	0.7
70	0.8	0.5
100	0.5	0.3

Table 5.1: Table of the percentage error in the simulated director angle in the cell centre depending on the number of interpolation points and their distribution (uniform and non-uniform). An analytical value of 65.66° is found from eqn. (5.29).

Fig. 5.7. Initially, when Q is uniform across the cell, the electric field is necessarily constant, leading to a linear potential profile. As $Q(\bar{z})$ develops splay-bend distortions, however, the field becomes concentrated in those regions with highest dielectric constant, leading to marked nonlinearities in the electric potential $V(\bar{z})$. There is no analytical formula for the electric potential across the Fréedericksz cell.

5.7.3 Transverse Flow Effect

In this numerical example, we study the combined effect of both external applied magnetic field and LC flow. We consider the flow of a LC whose director is fixed by a strong magnetic field parallel to the bounding plates. This setup is shown schematically in Fig. 5.8.

An external pressure is applied to the LC along the x -direction. The strong magnetic field \mathbf{H} is applied, in the plane of the bounding plates and makes an angle

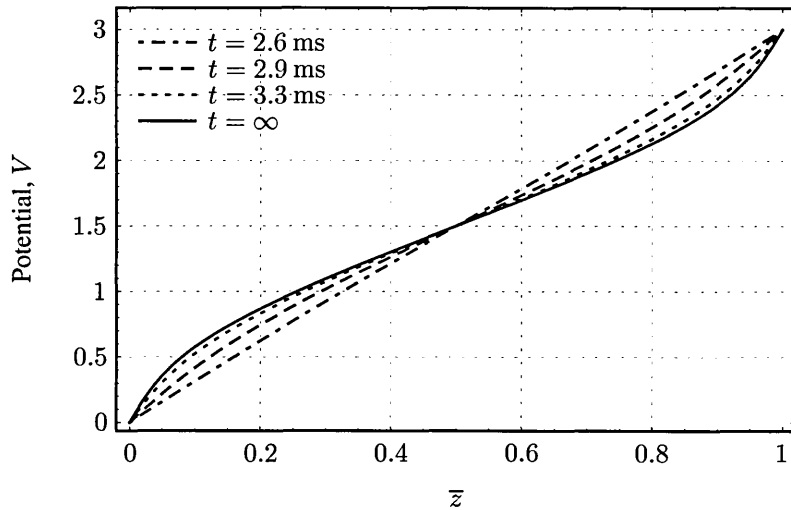


Figure 5.7: Time evolution of the electric potential across the Fréedericksz cell.

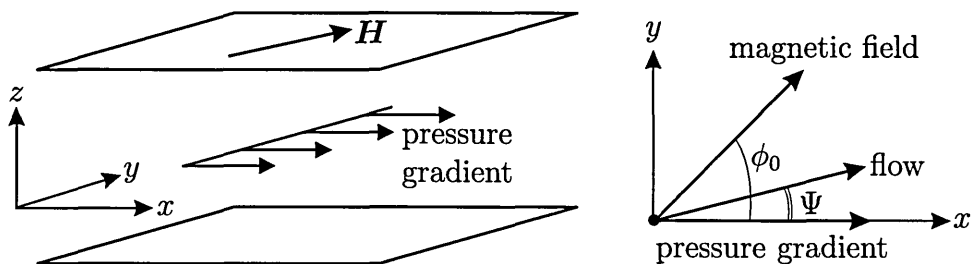


Figure 5.8: A schematic illustration of the transverse flow effect.

$\phi_0 > 0$ with the direction of the external pressure gradient. It is assumed that the magnetic field is sufficiently strong for \mathbf{Q} gradients to be neglected. Thus, the LC's velocity develops a y -component due to the director orientation, and the velocity adopts some angle $\Psi > 0$ with the x -axis. The analytical expression for this angle is [145]:

$$\tan \Psi = -\frac{(\alpha_3 + \alpha_6) \sin \phi_0 \cos \phi_0}{\alpha_4 + (\alpha_3 + \alpha_6) \sin^2 \phi_0}. \quad (5.32)$$

We have set-up a three-dimensional geometry to simulate this example. Periodic boundary conditions were applied in the x and y directions. No-slip boundary conditions were assumed at the bounding plates in the z -direction, i.e. the LC velocity was set to zero at $z = 0$ and $z = d$, where d is the channel width.

Initially, all components of the LC velocity were set to zero. During the simulation, the applied external pressure in the x -direction creates a velocity field distribution. After a sufficiently long equilibration time has passed, the LC velocity field converges to some steady value, and we can calculate the angle Ψ which the LC velocity makes with the x -direction.

ϕ_0 angle, degrees	Analytical Ψ angle	Simulated angle	% error
10	04.294	04.289	0.1
20	08.345	08.337	0.1
30	11.883	11.870	0.1
40	14.568	14.552	0.1
50	15.966	15.946	0.1
60	15.533	15.512	0.1
70	12.711	12.692	0.2
80	07.283	07.271	0.2

Table 5.2: Table of theoretical (equation 5.32) and simulated angles at the transverse flow effect.

The simulation results along with the analytical values are provided in Table 5.2. The relative error of the simulation results do not exceed 0.2%, as compared with the analytical solution given by eq. (5.32). The simulation was conducted in a channel of width $2\ \mu\text{m}$ and with the LC viscosity coefficients ($\alpha_1 = -21.2$, $\alpha_2 = -153$, $\alpha_3 = -0.773$, $\alpha_4 = 109.5$, $\alpha_5 = 107.1$, $\alpha_6 = -46.673$) $\times 10^{-3}\ \text{kg m}^{-1}\ \text{s}^{-1}$. The LC density was $\rho = 1.01 \times 10^3\ \text{kg m}^{-3}$.

5.7.4 Fast Switching Dual-Frequency Chiral HAN Cell

Having validated different order-tensor aspects of our MSPH approach in previous subsections, we now assess the full model by turning on the flow effects. To illustrate this, we consider the switching of a dual-frequency chiral hybrid aligned nematic (CHAN) LC cell (CHAN) [147, 148]. In such a device, a chiral LC with a frequency-dependant dielectric permittivity is used, so as to achieve fast switching times. The principles underlying the operation of this device are that both of its switching behaviours are field driven, whereas the relaxation of a simple Fréedercksz cell is a passive process whose speed is dictated by material properties such as elastic constants and viscosity coefficients. The two states of the CHAN device are a zero field chiral HAN arrangement and a high-frequency-field-induced twisted nematic arrangement. Both states are accessed from the same intermediate vertically aligned state, induced by a low frequency field pulse.

This CHAN system was chosen as a test for our full MSPH LC simulator because, as we demonstrate below, its behaviour is strongly dependant on the velocity field. It therefore gives us an opportunity to assess the ability of the MSPH approach to properly recover the physical nature of the partial differential equations describing LC flow (i.e. eqn. (2.40)). Note that the partial differential equations governing the LC description used for this system also necessarily contain terms introducing

chirality. A further reason for considering the CHAN set-up is that it has recently been the subject of a combined experimental and theoretical study by Sambles and Jewell [147, 148]. Here, therefore, we are able to adopt the same cell and material parameters as were used in refs [147, 148] and make a direct comparison with their results. Thus, the cell width is set at $4.94\ \mu\text{m}$, with homeotropic anchoring on one surface and planar anchoring on the other. The elastic constants used are $(K_{11} = 16.7, K_{22} = 10, K_{33} = 20.9) \times 10^{-12}\ \text{N}$ and the pitch is $P_{ch} = 13.0\ \mu\text{m}$. The viscosity coefficients are $(\alpha_1 = -10, \alpha_2 = -300, \alpha_3 = 25, \alpha_4 = 170, \alpha_5 = 190, \alpha_6 = -85) \times 10^{-3}\ \text{kg m}^{-1}\ \text{s}^{-1}$ and the density is $\rho = 1.01 \times 10^3\ \text{kg m}^{-3}$. The dielectric anisotropies are $\Delta\epsilon = 2.6$ at low frequency and $\Delta\epsilon = -2.3$ at high frequency. The modelling work presented in refs [147, 148] was based on the Leslie-Eriksen-Parodi director-based description of nematodynamics, and achieved by iteratively time-stepping through the velocity and orientation profile variations.

Initially, we have obtained the CHAN cell's equilibrium configuration by setting the LC alignment to be uniform except at the boundaries, which were fixed at homeotropic and planar, and letting the Q tensor evolve in the absence of an applied field. In the course of time, the order tensor arrangement then relaxed to the equilibrium configuration. To allow meaningful comparison of our data with those of [147], we have used our particle Q tensors to construct director tilt and azimuthal angle profiles; for the equilibrium configuration, these are plotted in Figs. 5.9 (a,b) with the time label $t = 0$. Slight non-linearities are apparent here, reflecting the difference in the splay and bend elastic constants.

Following [147], we then applied a low-frequency 7 V pulse to the system for 20 ms immediately followed by a high frequency pulse with the same voltage for 80 ms. The twist and tilt profiles obtained during these two time windows are shown in Figs. 5.9. Like ref [147], we have held all z -components of the velocity at zero in our 1-dimensional modelling of this device. In contrast to [147], however, we have embedded dielectric permittivities within our model and simply imposed constant applied voltages. Due to both this and the Q -tensor nature of our model, while we expect the qualitative behaviour observed here to be equivalent to that seen by Sambles and Jewell, small quantitative discrepancies can be anticipated.

When the low-frequency voltage was applied to this CHAN system, the director tilt profile (Fig. 5.9a) switched monotonically from approximately linear to tanh-like, the action of the applied field being to promote homeotropic alignment in the upper half of the cell. The accompanying changes in the associated twist profiles (Fig. 5.9b) have little physical significance since they predominate in the growing homeotropic region in which twist is relatively meaningless. When we ran an equiv-

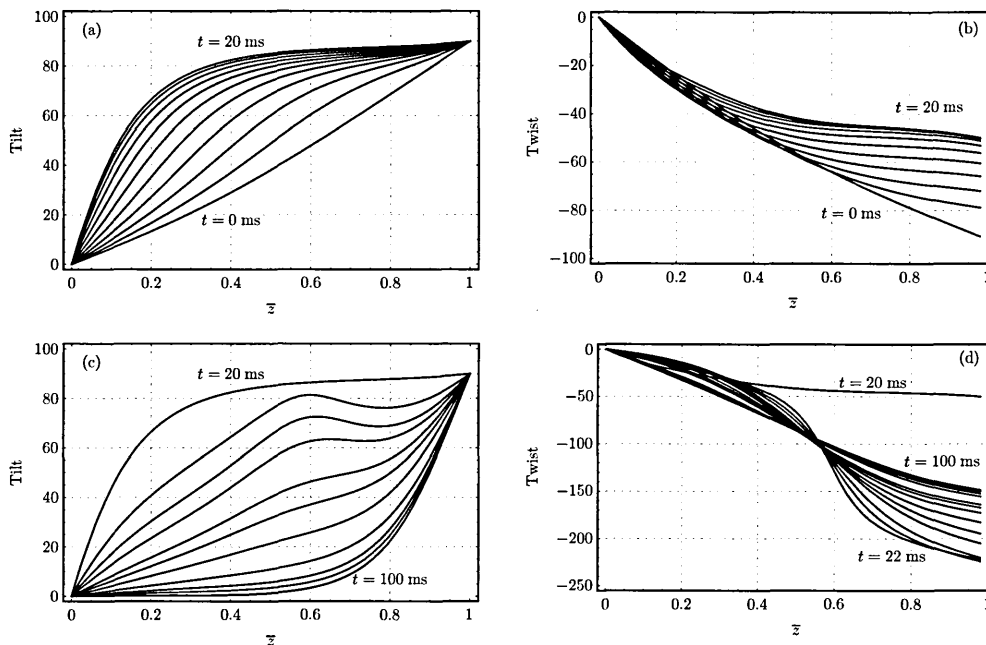


Figure 5.9: Time evolution of the director twist and tilt angle profiles when the low-frequency voltage is applied (a,b) and when the high-frequency voltage is applied (c,d).

alent simulation with all velocities set to zero, no differences were apparent in the initial and final profiles, but the intermediate profiles showed slower convergence in the homeotropic region.

When the frequency of the applied voltage was changed, at $t = 20$ ms, a backflow effect was produced which significantly influenced the director profiles. This is particularly apparent from Fig. 5.9 (d) which shows a large jump in the twist profile immediately after the frequency shift. Physically, this corresponds to the director tilting backwards, leading to an instantaneous 180 degree step in the twist values observed at high z . This led to a region with high twist gradient forming in the central region of the cell, which itself promoted formation of a maximum in the associated tilt profile. Subsequently, these high twist gradient and high tilt features dilated and the cell relaxed into what was, predominantly, a twisted nematic arrangement. To illustrate the backflow behaviour responsible for these director profile rearrangements, we plot, in Fig. 5.10, a series of profiles of the x -component of the velocity during application of the high frequency applied field. By comparing these with Fig. 5.9 (c), it can be seen that the peaks in the director tilt profiles correspond to the maxima in this velocity field. Furthermore, by conducting equivalent simulations with the velocity field switched off, we have found that no twist jumps or tilt maxima are observed when backflow is suppressed. This is entirely consistent

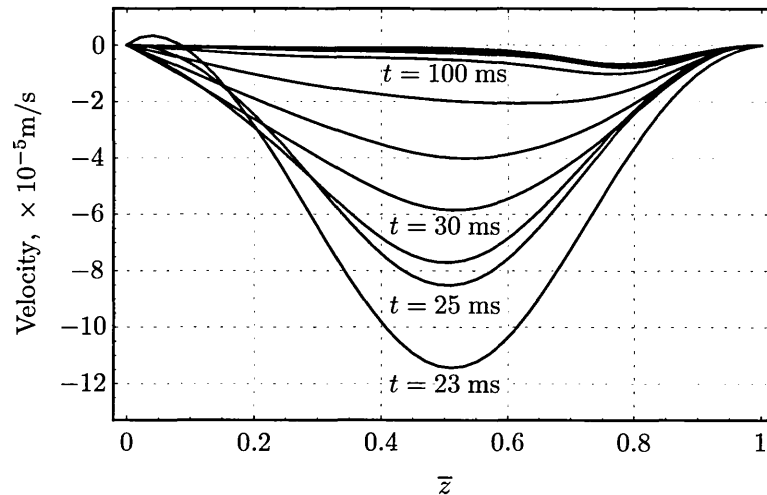


Figure 5.10: Time evolution of the x -velocity across the CHAN cell as a function of reduced distance \bar{z} .

with the findings of Sambles and Jewell.

5.8 Conclusions

In this chapter we have presented our attempts to apply the SPH method along with its different improvements to the simulation of LCs. We have shown that the order of the consistency of the original SPH method is insufficient for it to simulate the Qian Sheng equations of nematodynamics. Further, various improvements of SPH, such as introduction of an artificial viscosity, are not sufficient to overcome this fundamental failing. Ultimately, after many attempts, we have found that the MSPH technique is capable of simulation of Qian-Sheng equations describing the LC behaviour. This has been validated against a number of test cases in which it was shown to be in good agreement with previous analytical and numerical results. The set-ups considered here have been restricted to quasi-one dimensional behaviour involving little order parameter variations. To assess the full capabilities of the MSPH methodology developed here, therefore, requires consideration of more complex scenarios.

Chapter 6

Modelling of the PABN Device

6.1 Overview of PABN Operation

In this section we consider current status of research of the PABN device. We first briefly review the developments in experimental investigations and then we consider the advancements in theoretical studies.

6.1.1 Experimental Studies

The PABN device consists of a LC cell with one surface flat and the opposite one populated with an array of microscopic posts, as depicted in the micrograph Fig. 6.1. The PABN cell shares many features with conventional LCD cells, the key difference being the substrate decorated by microscopic posts. The upper substrate has homeotropic boundary conditions, i.e. it fixes the director to be strictly perpendicular to the surface plane. The boundary conditions on the lower substrate are of a tangent type, which restricts the director locally to be in the plane of the surface.

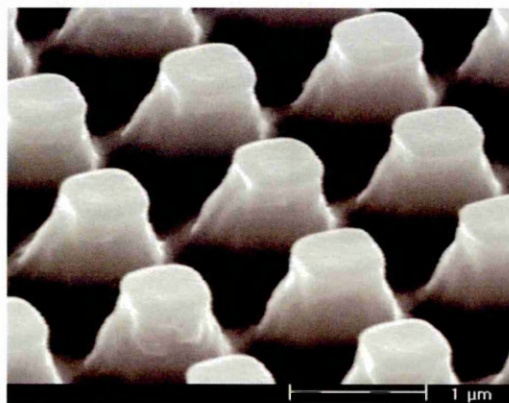


Figure 6.1: The PABN device [24, 149].

It has been experimentally observed that a LC confined between such a patterned substrate and a fixed homeotropic substrate exhibits two long-lasting field-off states [24]. When viewed between crossed polarisers, these states are found to give an optical contrast – one state is bright and another one is dark. These configurations correspond to minima in the LC’s free energy and are separated by a free energy barrier, i.e. they are bistable.

Initially, optical modelling [150] suggested that the dark state corresponds to the LC director tilting around the post, while the bright state corresponds to the LC director laying planar around the post, as depicted in Fig. 6.2. The former state is further referred to as tilted (\mathcal{T}) state and the latter state is referred to as planar (\mathcal{P}) state. In Fig. 6.2, only the LC which is adjacent to the post surface is shown. If there were no posts, the director profile would bend linearly from bottom to top. This is what is observed experimentally when post heights are small, i.e. only the planar state is achieved. Increasing post heights leads to two stable states. In these, the tilted state has the LC director at the patterned surface tilting more strongly than is the case with the linear profile, while in the planar state this surface-region tilt is greatly reduced. For large post heights only the tilted state is observed. Thus, bistability is only observed for post heights in a certain range [24].

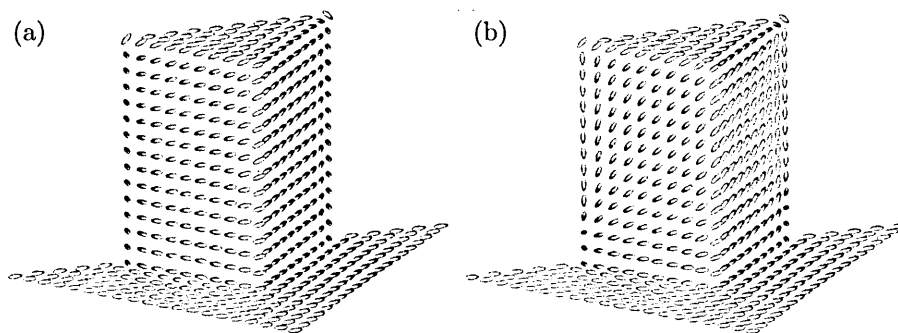


Figure 6.2: Schematic illustration of LC alignment close to post surface for (a) planar and for (b) tilted states [150].

The switching between these bistable states is achieved via the application of monopolar square electric field pulses, the sign of which dictates the final state. Bidirectional switching is only possible with negative dielectric LC materials. A positive pulse is needed in order to achieve $\mathcal{T} - \mathcal{P}$ switching, while a negative pulse is needed to switch from \mathcal{P} to \mathcal{T} state. The dependance on field sign suggests that the primary mechanism driving at least one of the switching processes may be flexoelectricity, but this has yet to be fully demonstrated. There is also some asymmetry, in that a lower voltage is needed to switch from \mathcal{T} to \mathcal{P} than is the case for switching in the opposite direction [150].

In the original experimental studies of this class of system, cuboidal posts were used [24]. In these systems, the degeneracy between symmetry-related alignment directions was removed by tilting the post in a preferred direction, leaning angles as small as 5° proving sufficient. More recent work [151], however, has considered reducing the symmetry of the cross section of the post, thus eliminating the need for post-tilting. This was found to help to achieve finer alignment control and open up the possibility of having multidomains in a single pixel.

6.1.2 Theoretical and Simulation Studies

Previous theoretical attempts to understand the operation of the PABN device are limited to a small number of articles, most of which only consider static director configurations of the PABN cell.

Newton and Spiller [152] have shown that appropriate control of the shapes of the surface features of the PABN device plays a crucial role in establishing its bistability, the periodicity of these features being of lesser importance. This conclusion was obtained by considering how a LC aligns around posts.

More recent theoretical studies of stable static states have been conducted using a three-dimensional finite-element implementation of Oseen-Frank theory [24, 149, 150]. In these simulations, the post shape was approximated by a rectangular bar, with the director's orientation being fixed on its edges. In [24] and [150] it was suggested that the planar state is characterised by a pair of $1/2$ defect lines along the leading and trailing edges in the director field, whereas in more recent publication [149] it was suggested that the planar state \mathcal{P} is free of such defects. Four distinct locally stable director topologies were also identified in [149] by explicitly constructing the trial configurations and then minimising their free energies.

The most recent publication by Willman et al. [18] deals with the switching behaviour between two energy minimum states. In this, a dynamic finite-element implementation of Landau-de Gennes theory was used, which allows for variable order parameter. The post geometry in this case was represented in 3D by a rectangular post with rounded corners and edges. From this, it was found that switching of the PABN device is a two step process. During the first step, the director field adopts a defect configuration due to the negative anisotropy of the LC. During the second step, the director field develops either a continuous or a discontinuous configuration at the post edges depending on the sign of the applied field, due to flexoelectricity.

6.2 Post Geometry Representation

In this section we describe the model which we have used to represent the post shape and the approach we have used to discretise it.

6.2.1 Geometry Model

All previous efforts at PABN device modelling have employed a rectangular geometry for post representation. This is largely due to the constraints of the standard mesh generators used: namely, they require a geometry made of simple primitives as their input. By comparison, the MSPH technique described in §5 is a mesh-free technique and so does not require a mesh for its operation. As such, it is able to accommodate the use of smooth functions in the post model description. We have exploited this advantage by using smooth functions to match the post geometry as closely as possible to the real one. In particular, we have been able to avoid the imposition of unrealistically sharp substrate features.

We impose periodic boundary conditions in the x and y directions. We then describe the height h of a single post as a function of the x and y coordinates, $h = h(x, y)$. For this, we use a hyperbolic tangent function as a basic building block for all of our post models. All geometries are given on the interval $[-0.5 : 0.5]$ in x and y dimensions and are given unit height. Thus, they can easily be scaled to represent any desired dimensions.

The simplest example of a post-like geometry is the circularly shaped feature depicted in Fig. 6.3. This surface is described by the following equation:

$$h(x, y) = \frac{1}{2} \left(\tanh \left(0.1 - 15 \left(\sqrt{x^2 + y^2} - 0.25 \right) \right) + 1 \right). \quad (6.1)$$

Effectively, the only variable in the above equation is the reduced distance $r = \sqrt{x^2 + y^2}$ from the axes origin $(0, 0)$.

More sophisticated, alternative post shapes involve x and y coordinates as separate terms in the surface equations. For example, a smooth rectangle-like post can be described by the following equation:

$$f(x, y) = \tanh(\pi(s_1x - p_1) - \tanh(\pi(s_2x + p_2))) \times \tanh(\pi(s_1y - p_1) - \tanh(\pi(s_2y + p_2))). \quad (6.2)$$

Here the p_i control the post's width and length and the s_i determine the smoothness of the structure. An example of a such surface is given in Fig. 6.4. The surface shape can be modified in any way by modifying the parameters appearing in eq. (6.2), e.g.

in order to introduce asymmetry.

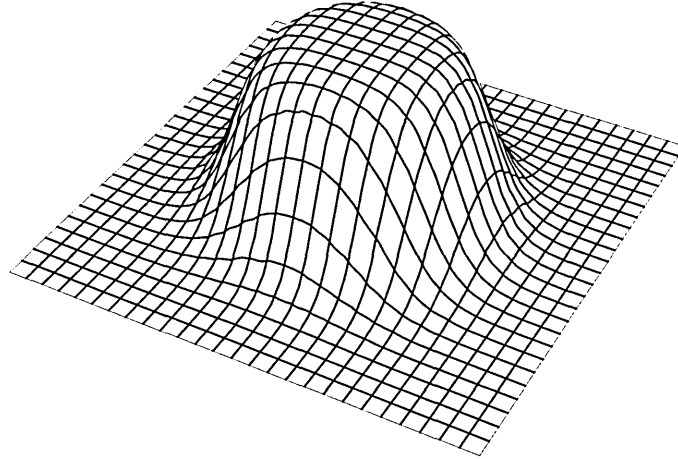


Figure 6.3: An example of the analytical circular post shape given by eq. (6.1).

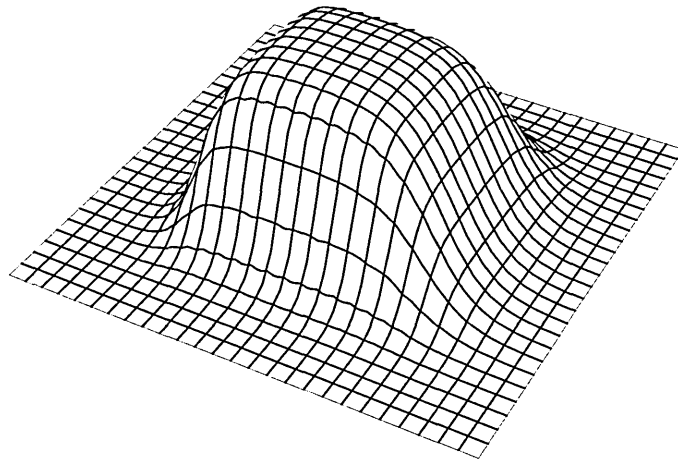


Figure 6.4: An example of the analytical rectangular post shape given by eq. (6.2), with $p_1 = 0.825$, $p_2 = 1.375$, $s_1 = 4p_1$ and $s_2 = 4p_2$.

Many such post shapes can be generated by appropriate variation of the parameters p_i and s_i in eq. (6.2). The biggest advantage of such a representation is the absence of any unrealistically sharp corners. Avoiding such artefacts reduces the likelihood of unphysical defects developing in the system. Another advantage comes from the fact that we can both closely represent the geometry and, at the same time, precisely know the normal at each point on the surface. This has a consequence that the numerical calculation of planar anchoring is more accurate than that achieved, e.g., with traditional grid-based methods.

6.2.2 Geometry Discretisation

Having described the way we construct post surfaces, we now proceed to a description of the discretisation process. Very often, standard mesh generators are used to set the nodes' distribution in meshless methods. Thus, in this section we briefly consider distribution of nodes in domains of interest for mesh-based methods and out attempts to use these. Then, we describe the technique we have employed for initial node distribution and its implementation.

In mesh-based methods, such as finite elements and finite volume methods, the mesh generation is an important process which controls the convergence and the accuracy of results. Domains in these methods are discretised into smaller elements by using nodes which are connected in a predefined matter. Triangulation is the most adaptable way of creating meshes. An example of a standard Delaunay triangulation, which is very widely used in FEM, is given in Fig. 6.5.

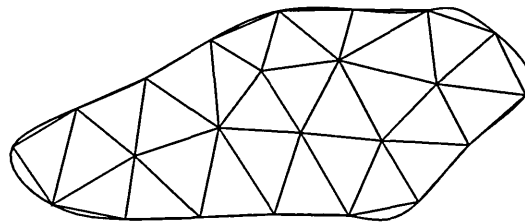


Figure 6.5: An example of Delaunay triangulation for a random 2D area.

In mesh-free methods, the domain and its boundaries are represented by a set of scattered nodes without any connectivity between them. Points which represent boundaries are usually kept fixed in space. As such, any geometry can be represented very accurately, even if the shape functions in the mesh-free method are of low order. An example of such a discretisation is given on the right side of Fig 6.6. The nodes' distribution and their density directly controls the accuracy of the final solution. Thus, a reliable and robust technique for achieving uniform node placement is highly desirable. The possibility of fine tuning nodal densities in different domain regions is also advantageous, as this can save computational resources while increasing the solution's accuracy.

Unfortunately, node generation methodology for mesh-free methods is a relatively unexplored area and, usually, standard mesh generator algorithms for mesh-based methods are used for the distribution of nodes [89]. Mesh generation has been an active area of research and there are plenty of tools/libraries available for inputting a geometry into a computer model and further meshing it. Transformation of such a mesh into a set of nodes can then be achieved in a number of ways. The

simplest of these is to discard all connections between nodes in the mesh. Another possibility is to use the barycenters of the elements as the nodes; this leads to a more uniform node distribution but does not represent boundaries exactly. Using both of these methods sometimes can, though, give an optimal solution. An example of the application of the latter technique is depicted in Fig. 6.6.

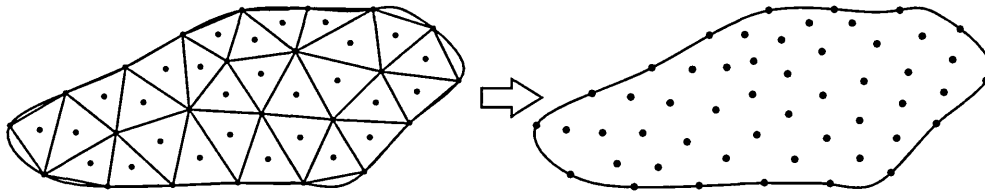


Figure 6.6: An example of the transformation of a mesh into a set of nodes.

In our work on simulating PABN systems, we initially used standard mesh generators to discretise the post geometries. While this approach yielded satisfactory results for simple geometries, it proved inflexible and inefficient for complex 3-D surfaces. The central issue in this proved to be that, before discretising any given complex geometry, one needs first to digitally represent it in order to use it as an input to a mesh generator. Thus, mesh generators need some sort of “coarse mesh” which they can then use to divide a given geometry into elements. For complex cases, we found that this double discretisation had a tendency to yield undesirable results. For example, consider the analytical post structure depicted in Fig. 6.4. After inputting this geometry into the Gmsh generator [153] and meshing it, we obtained the result depicted in Fig. 6.7. This shows only the vertices of the elements, the connections between them having been removed. Here, some points are arranged in lines on the surface due to the initial domain representation. This type of arrangement, though, should be avoided in mesh-free methods, as was first found by Nayroles et al. [154], because it will not guarantee stability in the construction of mesh-free functions. Additionally, it is also very difficult to represent periodic boundary conditions using this type of approach. The need to alleviate these major problems therefore motivated us to look for alternative ways for achieving geometry discretisations.

To this end, we applied a standard Monte Carlo simulation approach – Grand Canonical Monte Carlo (GCMC) [120] – to uniformly distribute nodes in a given space. This approach was first suggested by Zhang and Smirnov [155] as a solution to this problem. In this method, the chemical potential μ of a system is fixed (we set $\mu = 0$ for our systems) and the number of particles N is a fluctuating quantity. It should be emphasised that the GCMC approach is employed only for nodes distribution in this Thesis. Thus, we select values of the governing physical

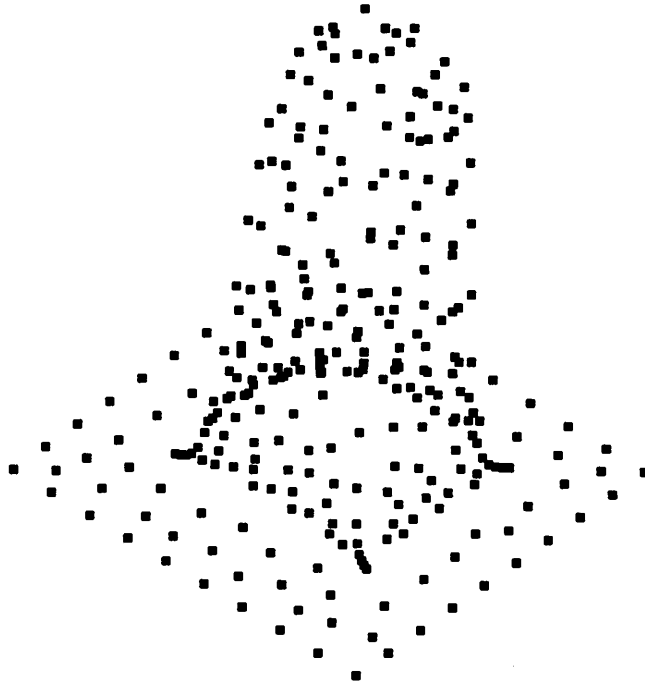


Figure 6.7: An example of an unsatisfactory geometry discretisation achieved using the Delaunay triangulation approach of the Gmsh generator [153].

parameters so as to achieve a fast convergence of the method, rather than to ensure the proper representation of any physical phenomena.

The node points determined in the GCMC method are treated as particles interacting through with some prescribed repulsive pair-wise potential. After running a GCMC simulation for a sufficient time, the particles naturally redistribute themselves so as to achieve a uniform but disordered distribution in a given domain. Further, a distribution of particles with a specified average distance between them can be achieved by adding an attractive tail to the prescribed inter-particle potential. In the GCMC method, node distributions can readily be generated for any number of dimensions, because the potential between any two particles can be made to depend purely on the distance between those particles, i.e. on the Euclidian norm. From our point of view, this represents an efficient, controllable and effective route by which to generate node distributions. It is also fully consistent with the spirit of mesh-free methods. It can, therefore, also be seen as a pragmatic physical solution to a mathematical problem.

In our implementation, we use the standard 12-6 Lennard-Jones pair-wise potential to generate the inter-particle interaction:

$$\phi(r) = 4\varepsilon \left[\left(\frac{\sigma}{r} \right)^{12} - \left(\frac{\sigma}{r} \right)^6 \right]. \quad (6.3)$$

The σ parameter controls the optimal distance between nodes at which energy is minimal, which equals approximately 1.122σ , ε is an energy scale parameter, but its precise value has little effect in this particular situation and so it is just set to $1/4$.

The procedure of generating a nodal distribution using the GCMC method consists of attempting a series of random moves to explore the configurational space of the system of nodes. When generating the boundary nodes for, e.g. a PABN post, the GCMC particles are constrained to the space defined by the alignment surface expression, e.g. eq. (6.2). The rules for accepting or rejecting changes to the nodal arrangement are then based, in part, on the corresponding potential energy function

$$\varphi = \sum_i \sum_{j>i} \phi(r_{ij}). \quad (6.4)$$

We use three types of trial moves to explore the system:

1. Insertion of particles. A particle is inserted into the system at a random position. The potential energy change of the system, $\Delta\varphi$, is calculated and the insertion is accepted or rejected based on the following criterion:

$$\text{accept if } \frac{zV}{N+1} e^{-\beta\Delta\varphi} > R \quad (6.5)$$

$$\text{reject if } \frac{zV}{N+1} e^{-\beta\Delta\varphi} \leq R \quad (6.6)$$

2. Removal of particles. A particle is chosen at random and the energy change of the system, $\Delta\varphi$, is calculated on the assumption that the particle was removed. The move is accepted or rejected based on the following criterion:

$$\text{accept if } e^{-\beta\Delta\varphi} > R \quad (6.7)$$

$$\text{reject if } e^{-\beta\Delta\varphi} \leq R \quad (6.8)$$

3. Displacement of particles. A particle is chosen at random and is given a random displacement within certain limits. Then, the energy change of the system, $\Delta\varphi$, is calculated, and the move is accepted or rejected based on the following criterion:

$$\text{accept if } e^{-\beta\Delta\varphi} > R \quad (6.9)$$

$$\text{reject if } e^{-\beta\Delta\varphi} \leq R \quad (6.10)$$

In the above equations, R is a uniform random number in the $(0, 1)$ interval generated

during each trial move, N is the total number of nodes in the system before the trial move, V is the volume of the system, $\beta = 1/k_B T$, where k_B is the Boltzmann constant and T is the temperature of the system, $z = e^{\beta\mu}/\Lambda^3$, where μ is the system's chemical potential which we set to zero and Λ is the thermal de Broglie wavelength.

Provided that T is kept sufficiently high to ensure liquid-like behaviour from the node points, this GCMC approach readily generates configurations in which nearest neighbour separations are $\sim 1.1\sigma_0$ but there is no long-ranged position order. In practice these simulations are run until N has reached a steady state; following this, nodal configurations are taken. Finally, we note that whilst our use of this approach was motivated by the desire to reliably generate node locations for complex system boundaries, it can equally well be utilized to produce the positions of bulk sites for a mesh-free simulation.

6.2.3 Implementation Details

In this subsection we give a brief description of the implementation details of the GCMC method. In this, all technical details are virtually the same as those used in standard molecular dynamic (MD) and Monte Carlo (MC) simulations and, thus, here we only briefly provide relevant specifics.

Initial configuration. We start with an initially empty domain, points being sequentially added, removed and moved as per a conventional GCMC simulation. The original article [155] suggests making an initial guess to the particles' distribution. However, we found that this was unnecessary. Indeed, the extra few minutes of GCMC simulation required by this were far easier to perform than any other methods for preparing an initial guess for the complex geometries involved here.

Boundaries. The complex boundary walls were discretised first. Following this, the bulk was discretised with the boundary particles kept fixed. In this way, the boundary particles participated in the calculation of the bulk system's total potential, but were not liable to GCMC trial moves. Periodic boundary conditions were implemented in the usual way, as in standard MC or MD simulations.

Node spacing. Variable node resolution can be achieved in this GCMC approach by imposing spatial dependance on the particle interaction parameter σ . If two particles i and j have different σ parameters, then the resultant parameter σ_{ij} , appearing in their potential calculation, is given by the standard mixing rules as $\sigma_{ij} = (\sigma_i + \sigma_j)/2$.

Simulation parameters. The parameters appearing in eqns. (6.5-6.10) do not carry the same meaning as they do in simulations of physical systems. Here, one is

only interested in the fast convergence of the method. Thus, parameters should be adjusted simply to achieve associated acceptance and rejection criteria that lead to the effective distribution of points. We found that values of $\beta = 35$, $z = 10^5$ and $V = 1$ gave good convergence rates.

Speeding up the algorithm. During each step of the GCMC method, a change in the total potential energy, given by eq. (6.4), needs to be calculated. Determining this by calculating eq. (6.4) for all pairs of particles in the system is an expensive process, which takes $\mathcal{O}(N^2)$ calculation time, where N is the total number of particles in the system. The Lennard-Jones is not a long-ranged interaction, though, and, thus, the algorithm can be significantly improved. Approaches for achieving such efficiencies are routinely employed in particle-based MD and MC simulations. Here, we use the linked cell method [156]. In this, the simulation domain is divided into cells with sizes which are equal to or slightly larger than the cut-off radius r_c , which we set to $r_c = 2.5\sigma_{max}$. Here, σ_{max} is the maximum coarsening distance set in the domain. Then, each particle in the given cell interacts only with particles in the same cell or with particles in neighbouring cells. Since the number of neighbouring cells and their sizes are independent of the system's size, the final algorithm scales linearly with the number of points considered.

6.3 Static Configurations

In this section we present the results we have obtained for energy minimum configurations of a LC confined in a PABN cell geometry. In all presented simulations, we have used the following LC parameters. The elastic constants were set to ($K_{11} = 13.7$, $K_{22} = 7.3$, $K_{33} = 22.1$, $K_{24} = 3$) pN and, except where stated otherwise, the following set of Landau thermotropic coefficients was used: $\alpha_F = 65000 \text{ J m}^{-3} \text{ K}^{-1}$, $\beta_F = 533000 \text{ J m}^{-3}$ and $\gamma_F = 975000 \text{ J m}^{-3}$. In order to impose the planar degenerate anchoring on the post surface, we use the free energy term given by eq. (2.33). In this, we set $c_1 = -80 \cdot 10^{-5} \text{ J/m}^2$ and $c_2 = c_3 = 0$. This chosen value of c_1 was found to be strong enough to maintain planar alignment but not so strong that the surface nodes showed marked biaxiality.

All of our simulations were initiated in one of a set of trial configurations from which the system was allowed to relax into a local free energy minimum. The initial trial configurations used were constructed in a similar way to those described in [149]. This effectively set the initial orientational topology of each simulation. Explicitly, each particle \mathbf{Q} tensor was set such that the principal direction of the order tensor followed a specified vector field $\mathbf{n} = \{n_x, n_y, n_z\}$ whose non-normalised components

are given below.

In all trial configurations, the x and y components of the vector \mathbf{n} were given by

$$\begin{aligned} n_x &= \left[\sin \left(\frac{\pi x}{L_p} \right) \right] \left(\frac{H-z}{H} \right), \\ n_y &= \left[\sin \left(\frac{\pi y}{L_p} \right) \right] \left(\frac{H-z}{H} \right), \end{aligned} \quad (6.11)$$

where H is the cell height and L_p the post's cross-sectional dimension. For particles above the top of post (height h), the z -component of \mathbf{n} was also the same for all trial configurations and given by

$$n_z = \frac{z-h}{H-h}. \quad (6.12)$$

Four different configurations were considered for the z -component of the vector \mathbf{n} for particles below the top of the post. These were given by

$$n_z = \begin{cases} z(h-z)/h^2, & T, \\ z(h-z) \left[1 + \cos \left(\frac{\pi x}{L_p} \right) + \cos \left(\frac{\pi y}{L_p} \right) \right] / h^2, & P_1, \\ z(h-z) \cos \left(\frac{\pi x}{L_p} \right) / h^2, & P_2, \\ z(h-z) \cos \left(\frac{\pi x}{L_p} \right) \cos \left(\frac{\pi y}{L_p} \right) / h^2, & P_3. \end{cases}$$

where the labels T and P denote tilted and planar states. These four arrangements correspond to the distinct arrangements identified from the finite element simulations presented in [149].

The simulations we have performed using these 4 different initial configurations have equilibrated to only two stable configurations – T and P_1 . In comparison, the finite element simulations presented in [149] found distinct energy minima for all four configurations. All of the simulations that we have initiated with P_3 and P_4 initial configurations have converted into either the P_1 state or the tilted state T , which we have found to be the state with the lowest elastic free energy. These interconversion simulations have all involved the depinning of highly distorted regions from the post faces and, ultimately, changes in the orientational topology. In contrast, the continued stability of the P_1 arrangement suggests it as the most plausible arrangement for the experimentally observed planar state. Below we describe the observed states P_1 and T in more detail.

6.3.1 Tilted State \mathcal{T}

First, we consider the tilted state, \mathcal{T} . Experimentally, PABN cells cooled from the isotropic LC phase always adopt this state [24]. Our simulations are consistent with this observation since we find that this state is adopted from a wide range of starting configurations and topologies. We show a slice through the tilted state order field obtained from our simulations in Fig. 6.8. This is a periodic cross-section taken along the post diagonal. Between the posts, this configuration shows a relatively rapid orientational rearrangement from planar to near-vertical, but little elastic distortion above the post. The other significant distortions associated with the tilted state are

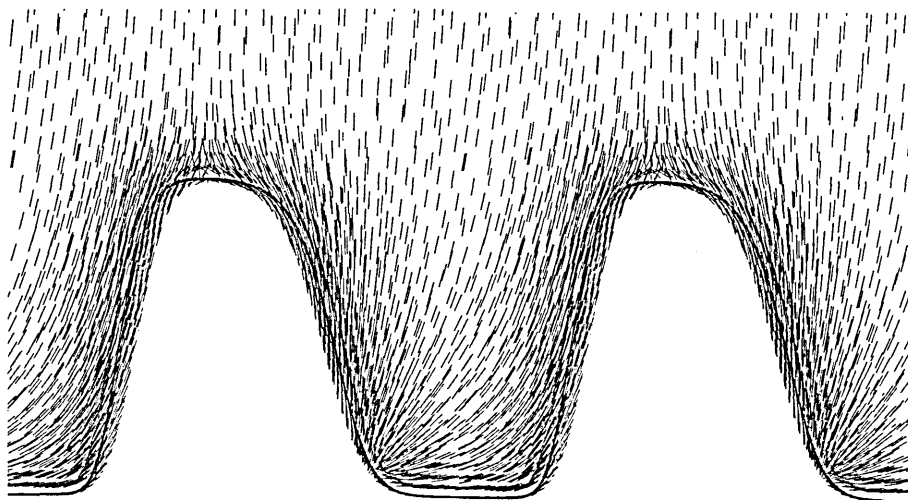


Figure 6.8: Periodic cross-section of the tilted state \mathcal{T} along the post diagonal.

topological in nature. As shown in Fig. 6.9, which shows the order field around a single post from a slightly oblique viewing angle, the state contains three defects – two at the base of the leading edge and a third at the top of the trailing corner. The defects at the base are half integer defects. It should be noted that, in previous simulation studies, only one full integer defect was identified at the base of the post. In our simulations, defects are not pinned to any sharp features and, thus, they are more able to adopt the configuration with the lowest free energy. We suggest, then, that two half integer defects are observed here since the free energy of a defect is proportional to square of its strength, as was discussed in §2.2.6 and, consequently, sum of squares of two halves is less than the square of one.

6.3.2 Planar State \mathcal{P}_1

The planar state \mathcal{P}_1 has a higher elastic free energy than the tilted state \mathcal{T} described in the previous section. Initially, all of our attempts to find this state by precon-

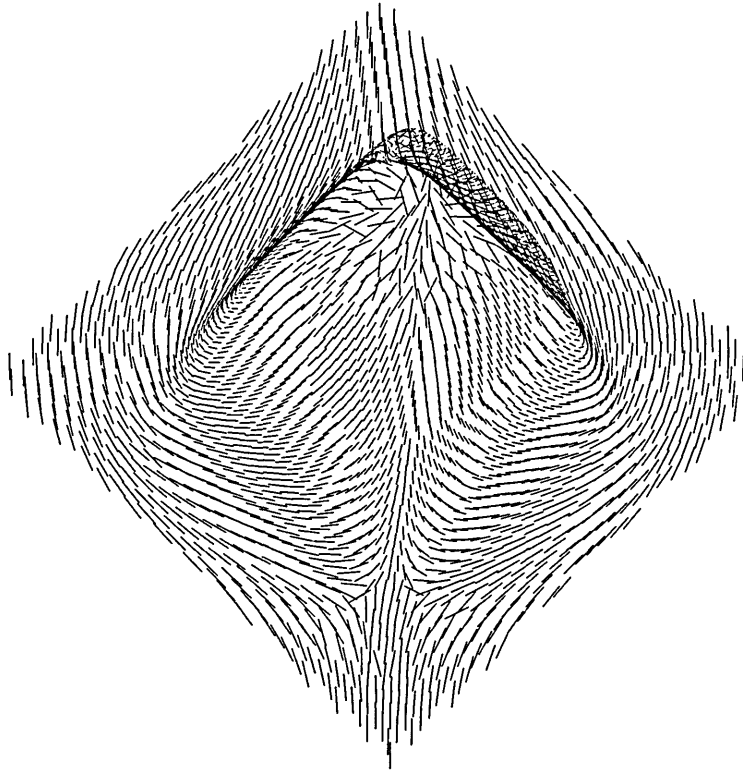


Figure 6.9: Near-top-down view of the equilibrated tilted state in the vicinity of a single post, showing defects at the base of the leading corner and the top of the trailing corner.

structing a director field very close to that of \mathcal{P}_1 failed to stabilise; the director field first adopted the \mathcal{P}_1 state, but slowly reoriented itself into the tilted state \mathcal{T} .

A series of simulation snapshots demonstrating this \mathcal{P}_1 - \mathcal{T} rearrangement are shown in Fig. 6.10, where the post diagonal cross-section is depicted. In this simulation, no electric field was applied and the transition was driven solely by elastic and Landau free energy contributions. Initially, as is depicted in Fig. 6.10.2, two defects form in the upper middle of the trailing edge. Then, these separate and move towards the top and the bottom corners, accordingly, where they eventually stop. This is accompanied by bulk director reorienting towards the tilted state.

We can draw a few conclusions from the nature of this rearrangement. First, large values of the elastic constants destabilise the planar state. This is inferred from the fact that, as mentioned before, this process is driven only by elasticity. Decreasing the elastic constants would therefore be expected to decrease the torque exerted on the surface and, so, stabilise the planar state. A second observation is that increasing the Landau-de Gennes free energy of the defect line on the post surface, given by eq. (2.9), will enhance the stability of the planar state, since this has the effect of raising the free energy barrier between the two stable states. This

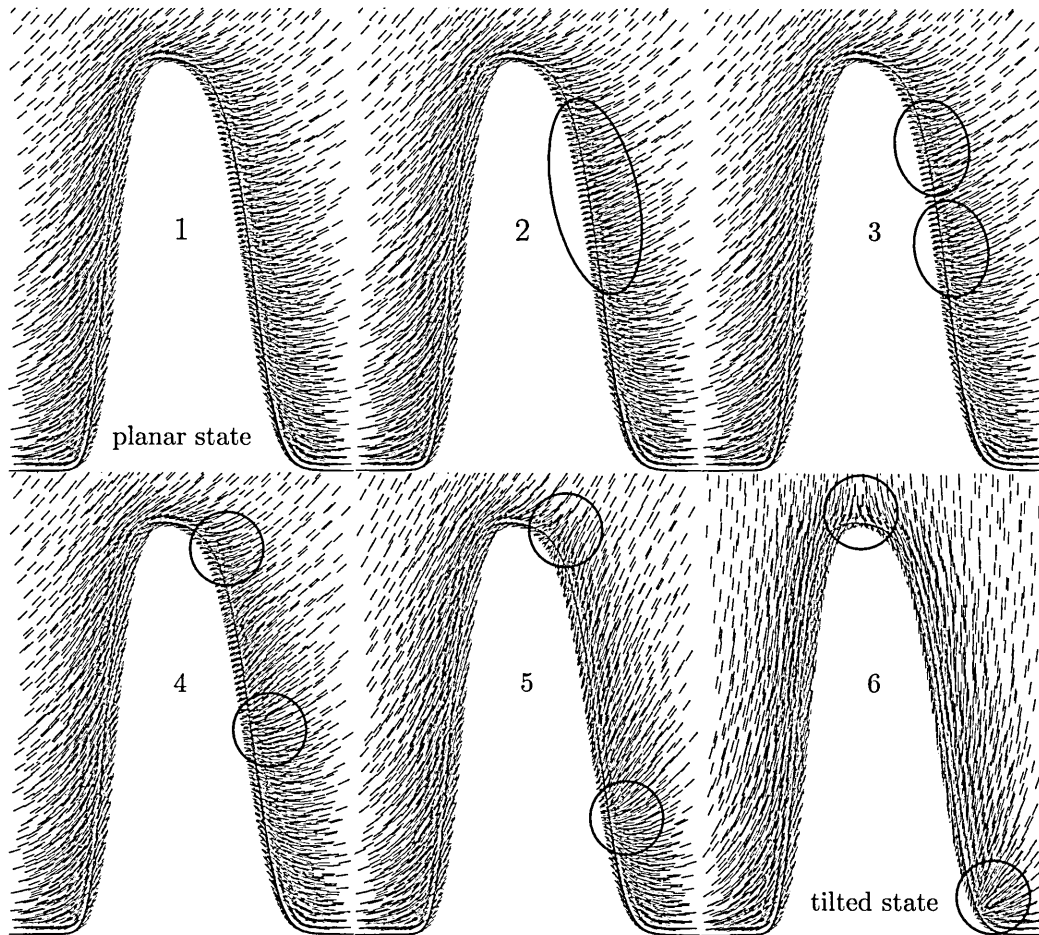


Figure 6.10: Series of snapshots depicting $\mathcal{P}_1 - \mathcal{T}$ transition driven solely by elasticity.

can be achieved by increasing values of the thermotropic coefficients α_F , β_F and γ_F .

At the beginning, we used the following values of Landau coefficients in our modelling: $\alpha_F = 650 \text{ J m}^{-3} \text{ K}^{-1}$, $\beta_F = 5330 \text{ J m}^{-3}$ and $\gamma_F = 9750 \text{ J m}^{-3}$. These values were chosen to insure a greater stability of simulations. In the light of the above findings, we have modified the simulation parameters in an attempt to stabilise the \mathcal{P}_1 state. Specifically, we have used the following elastic constant set ($K_{11} = 13.7$, $K_{22} = 7.3$, $K_{33} = 22.1$, $K_{24} = 3$) pN and the following set of Landau thermotropic coefficients: $\alpha_F = 65000 \text{ J m}^{-3} \text{ K}^{-1}$, $\beta_F = 533000 \text{ J m}^{-3}$ and $\gamma_F = 975000 \text{ J m}^{-3}$. Using these parameters, simulations initiated with the planar \mathcal{P}_1 starting configuration adopted a stable planar \mathcal{P}_1 arrangement. However, the other two planar configurations, namely \mathcal{P}_2 and \mathcal{P}_3 , were still found to be unstable in our simulations with the above parameters.

In the planar \mathcal{P}_1 configuration, the order field cross-section across the post diagonal took the form depicted in Fig. 6.11. Here, the LC director adopts an asym-

metrical U-shaped profile between the posts. This asymmetry derives from the differences in the configurations adopted at the leading and trailing faces. This finding is in qualitative agreement with the topological and configurational results provided in [149]. In this state, we observe a small degree of biaxiality adjacent to the post's leading and trailing edges, the value of which does not exceed 0.05. This biaxiality has been predicted in earlier works [24] but was not found in the finite element simulation of [149].

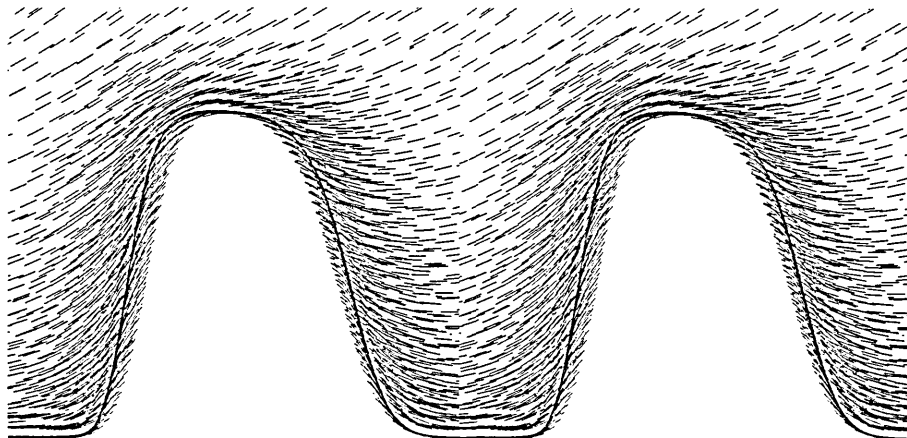


Figure 6.11: Periodic cross-section of the planar state P_1 across posts' diagonals.

6.4 Studying Effects of the Post Topography

In this section we consider the effect of different post topographies on the stable static configurations of the PABN device.

6.4.1 Circular Posts

In order to determine whether the post's sharp features have any effect on the bistability of the PABN device, we consider the behaviour of a circularly shaped post given by eq. (6.1). By preconstructing starting configurations as described in §6.3, we observed two stable states, which are \mathcal{T} and \mathcal{P}_1 . Two other planar states, namely \mathcal{P}_2 and \mathcal{P}_3 , were found to be unstable in our simulations. Specifically, a preconstructed \mathcal{P}_2 configuration always converged to the planar \mathcal{P}_1 state, whereas a preconstructed \mathcal{P}_3 configuration always converged to the tilted state \mathcal{T} . The two stable states are depicted in Fig. 6.12. From these it can be seen that the stable configurations for both of these states are very similar to those determined using the rectangle-like posts described in the previous section. In the tilted state, there are

two half-defects at the bottom of the post. The top defect, however, resides exactly at the top of the structure, unlike in the rectangular posts where it develops at the high-curvature corner. The orientational character of the bulk LC for both states is very similar to that described in the previous subsection.

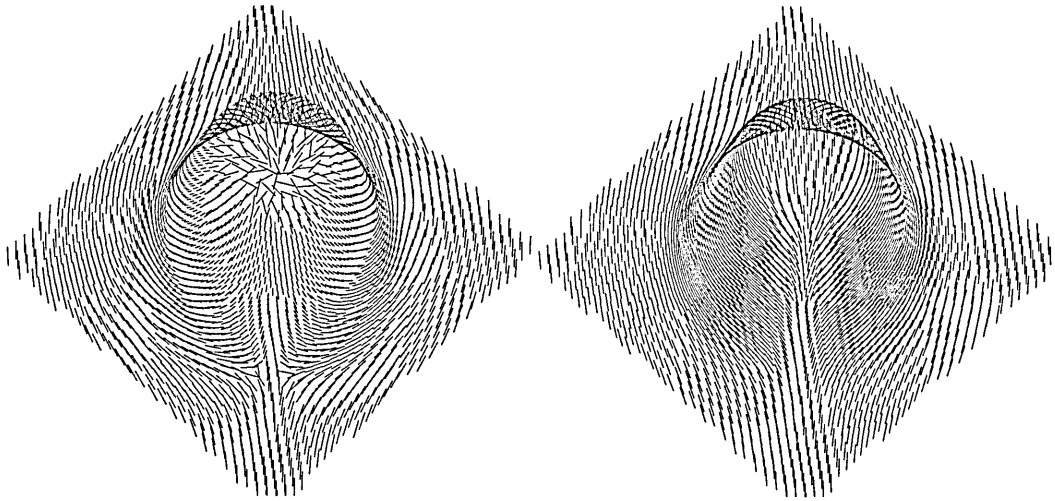


Figure 6.12: Equilibrium configurations obtained using circular posts: tilted (left) and planar (right) states.

Note that, despite the high symmetry of the circular post, this class of system can still readily select the required azimuthal alignment directions – these are set by the diagonals of the regular array of posts.

These results indicate, therefore, that the primary cause of bistability in the PABN device is the periodic arrangement of the post-like features on the substrate. Details of the shapes of these features are not crucial to the bistability but can be used to break the degeneracy of the two diagonal directions and modify details of the switching characteristics.

6.4.2 Effect of the Post Smoothness

In this subsection we study the effect of the post smoothness on the difference between the two minimal states. In device engineering, it is very important to have highly distinct states since this leads directly to improved contrast ratio. In practice, there is some scope in the manufacturing process to modify the post's smoothness to some extent. Thus, here we consider whether it is likely that this will have a significant effect on the difference between two stable states.

In order to represent posts with different smoothness, we vary the s_i parameters appearing in eq. (6.2). Here, we employ the following p_i values: $p_1 = 0.605$ and $p_2 = 1.155$. We set the s_i parameters as $s_1 = 2.2(s - 1)$ and $s_2 = 2.2s$, where s

ranges from 2.1 to 2.9 in our simulations. Higher values of this s parameter lead to posts with sharper features. Three posts with different values of the smoothness parameter are depicted in Fig. 6.13.

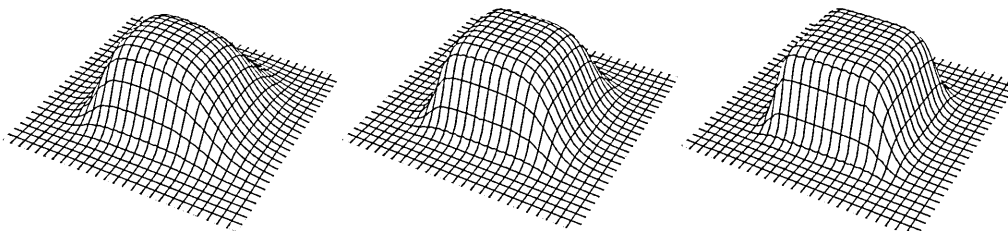


Figure 6.13: Posts with different values of the smoothness parameter s (2.1, 2.5 and 2.9, respectively, going from left to right).

To assess the effect of post smoothness, we have first calculated the difference in free energies between the planar and tilted states. These results are plotted in Fig. 6.14 as a function of the smoothness parameter s . Here, the low energy tilted state was taken as the baseline, relative to which the percentage increase in free energy of the planar state was calculated. As can be seen from Fig. 6.14, the post smoothness has a modest effect on the relative difference between these free energies, the range of variation being only 3.5%.

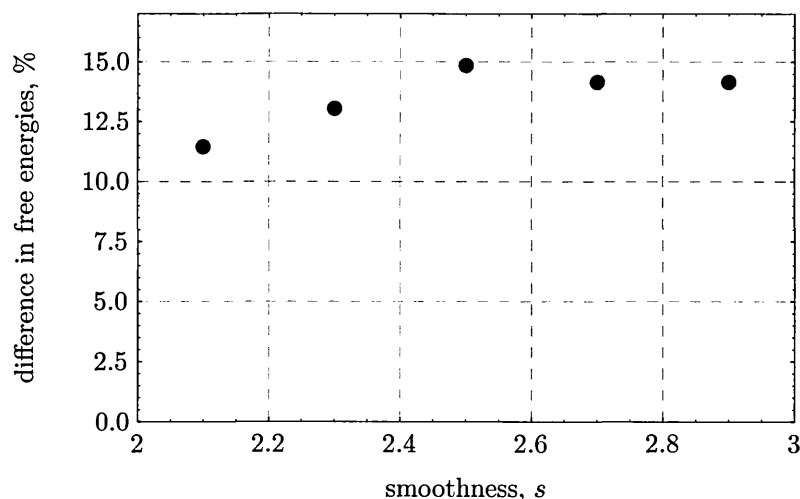


Figure 6.14: Relative difference in free energies between the two minimal states of the PABN device for square posts with varying smoothness s .

Next, we calculate the average profile of the angle which the LC director makes with the z -axis for both stable states and then find the difference between these. These results are plotted in Fig. 6.15 for a number of different values of the smoothness parameter s . It can be seen that difference is larger for posts with higher smoothness. When the post features become sharper, the difference in the director

tilt angle profiles reduces. Unsurprisingly, the largest variance is achieved near the post top, though even here the range for different posts only of order a few degrees. In the bulk, there is no significant distinction between the director profiles achieved using posts with different smoothness values.

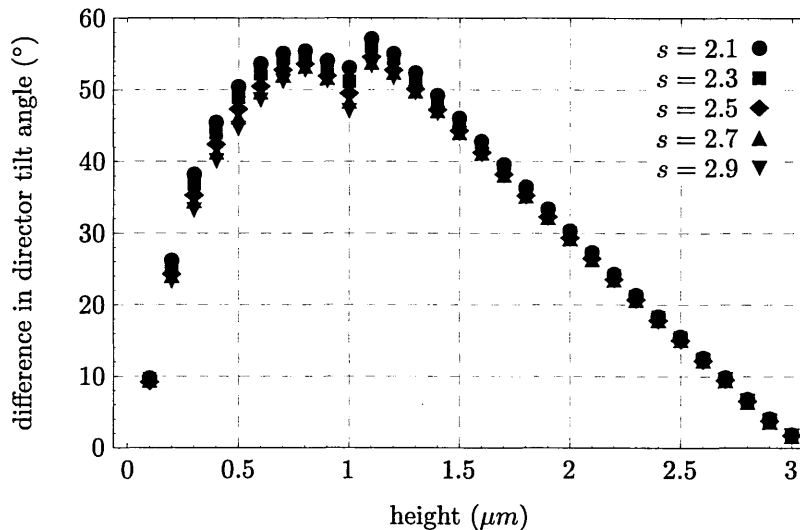


Figure 6.15: Difference in director tilt angle profiles of the two minimal states of the PABN device for posts with different smoothness values s (post occupies the first $1 \mu\text{m}$ of the height range).

Thus, based on the analysis of free energies and average director tilt angle profiles, it can be concluded that post's smoothness has no significant effect on the distinction between the PABN device's two stable states. Any differences, if there are any, will be barely noticeable in a practical setup.

6.4.3 Effect of the Post Height

In this section we study the effect of the post height on the difference between two minimal states of the PABN device. For this, we study different configurations obtained using the rectangle-like post depicted in Fig. 6.2.

We first calculate the free energies of the two states. These are plotted in Fig. 6.16, for both planar \mathcal{P}_1 and tilted \mathcal{T} states.

In the tilted state \mathcal{T} , there are three defects present, one at the top and the other two the bottom of the post. The planar state \mathcal{P}_1 , on the other hand, has a defect line running along the trailing edge. Thus, as the post becomes taller, the free energy of the tilted state stays approximately constant, since there are still only three defects present in the system. The free energy of the planar state, on the other hand, increases with the post's height, since the defect line length increases

proportionately. This effect is clearly depicted in Fig. 6.16, where our calculations show that the free energy of the tilted state stays approximately fixed and the free energy of the planar state increases linearly with the post height.

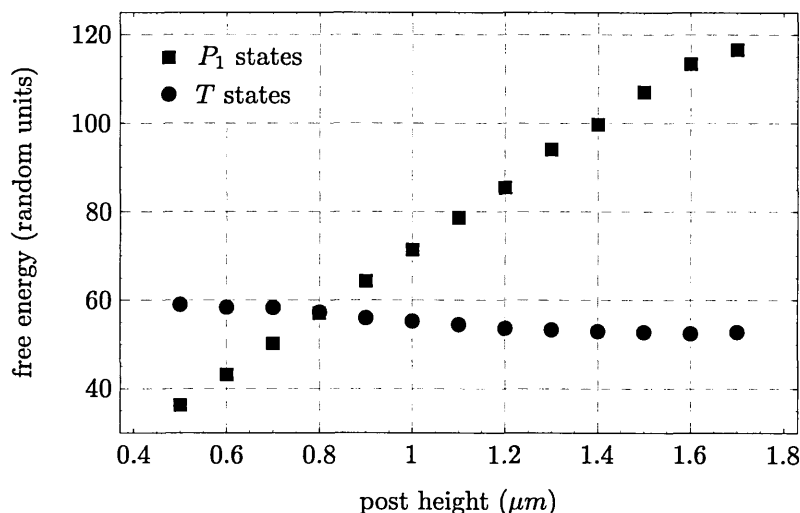


Figure 6.16: Free energies of different states depending on a post height.

The free energies of both states are equal when the post height is $0.8 \mu\text{m}$. For systems with posts below this height, the free energy of the planar state is lower than that of the tilted state. This contradicts the previous FEM simulation findings [149], in which free energy of the planar state was always found to be larger than that of the tilted state. This difference is due to the way the geometries were constructed in [149], where simple rectangular posts with sharp vertices were employed.

We have observed that the planar state becomes unstable and rearranges into the tilted state when the post height exceeds $1.7 \mu\text{m}$. This is fully consistent with experimental observations, in which the bistability was found only for a certain range of post heights [149].

Next, for a single post height, we consider the average tilt angle which the LC director makes with the z -axis. Tilt angle profiles for both stable states are plotted in Fig. 6.17, for a PABN system with the post height equal to $1.1 \mu\text{m}$. There is a distinct difference between two states in the area of the post, whereas in the bulk this difference becomes less pronounced due to elasticity. In each of these states, there is a dip of the tilt angle which coincides to the coordinate which is just above the post height. This happens because in both states the LC configuration takes local planar character in this region due to its interaction with the post's top boundary condition.

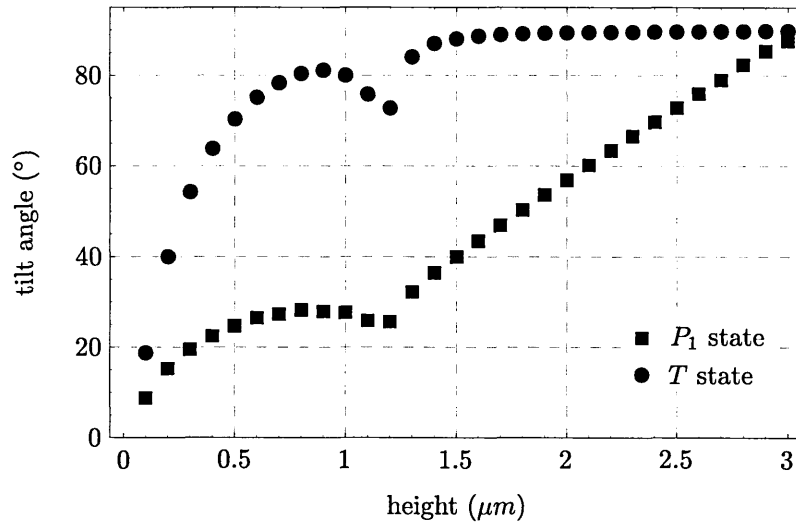


Figure 6.17: Average tilt angle of the LC director as a function of the z coordinate in the PABN cell, post height is $1.1 \mu m$.

6.5 Switching Behaviour

In this section we describe our study of the switching dynamics of the PABN device. In our simulations, we use an identical basic setup similar to that described in §6.2.1. To this we have added an extra layer of an isotropic dielectric placed below and inside the post, the thickness of which is $0.5 \mu m$. We set the dielectric permittivity of this isotropic dielectric to be $\epsilon = 5.0$. It was added in order to represent the bottom transparent electrode of the PABN device. We have not represented the top electrode in our simulations, since doing so would introduce an unnecessary computational effort without making any practical difference, given the uniform field and director arrangements in this region.

We apply an external field by fixing the potential on the ground electrode and on the upper homeotropic layer of the LC. The bottom electrode is set to have the zero potential and the upper plate potential is set to be equal to $\pm 20 V$, depending on the switching direction. During each time step, we solve Maxwell's equations of electromagnetism with the method described in §5.5, in order to obtain a distribution of the electric field inside the PABN cell. We apply the external potential difference for 3 ms time period and, after having removed it, we allow the LC to relax into an equilibrium configuration. The LC has negative dielectric anisotropy, which we set to $\Delta\epsilon = -4.85$. Also, the LC has values of elastic constants and Landau thermotropic coefficients equal to those given in §6.3.

In all simulations of the PABN device switching, we use the equilibrated static configurations described in §6.3 as initial starting conditions for the LC director

distribution.

6.5.1 $\mathcal{T} - \mathcal{P}$ Transition

In order to simulate this transition, we took an equilibrated \mathcal{T} configuration system and set the potential of the upper plate to +20 V. Fig. 6.18 shows a series of snapshots of the director field on the cross-section of the post's diagonal during the subsequent $\mathcal{T} - \mathcal{P}$ transition, and Fig. 6.19 shows snapshots of the LC director on the PABN post itself. The corresponding snapshots in Figs. 6.18 and 6.19 are taken at the same moments in time.

These snapshots show that, following application of the electric field, the bulk LC quickly reorients itself into a planar arrangement due to the negative dielectric anisotropy of the simulated LC. The director field of the PABN post itself, on the other hand, changes only insignificantly on this time-scale, as can be seen in Fig. 6.19.2. This is due to the LC surface viscosity, which makes this region respond more slowly to external influences. If the applied electric field is removed at this point, then the director field reverts to the tilted state \mathcal{T} . This is consistent with experimental observations.

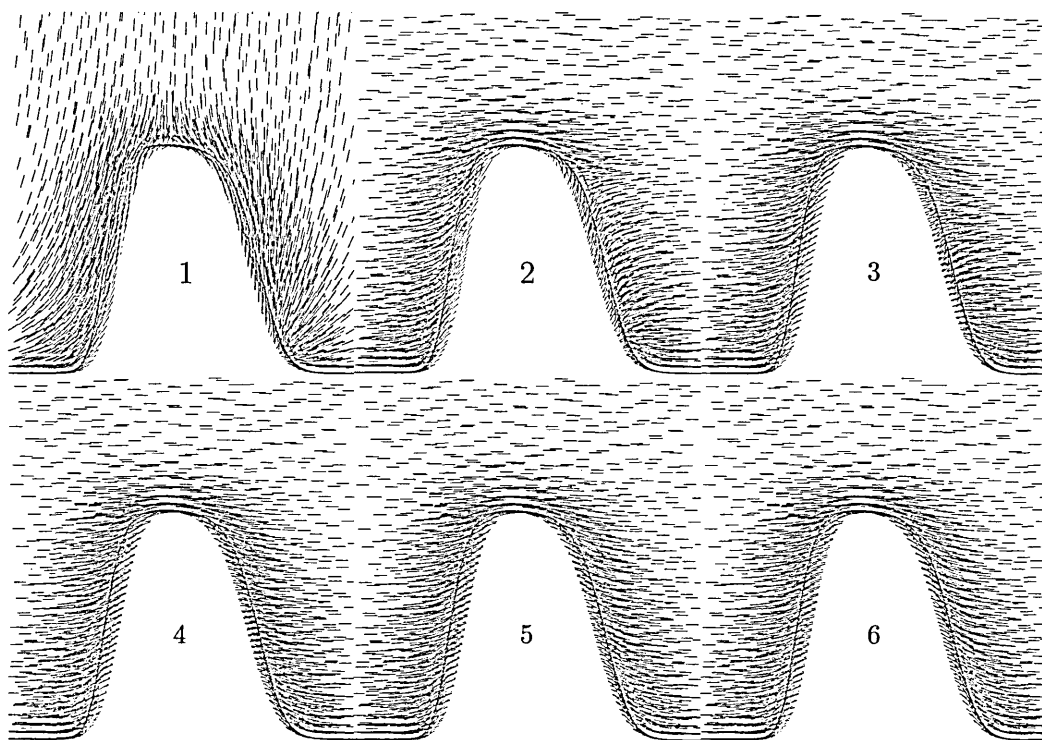


Figure 6.18: Series of snapshots depicting switching between tilted and planar states. Post's cross-section is shown. In these, $t_1 = 0$ ms, $t_2 = 0.9$ ms, $t_3 = 1.4$ ms, $t_4 = 1.5$ ms, $t_5 = 2.5$ ms, $t_6 = 3.0$ ms

Alternatively, continued application of the applied electric field reorients the LC on the post's surface into the planar configuration, as can be seen in Figs. 6.19(3-6). This then affects the adjacent bulk LC, which correspondingly transforms from an inflection-like configuration in-between the posts into a U-like one. Fig. 6.19 depicts the PABN post from such an angle that post's edge, which has the defect line in the planar state, is clearly visible. Initially, when the LC on the post just starts to adopt the planar configuration, the LC on the edge still maintains the 'tilted state' arrangement. Later, though, the adjacent faces become increasingly planar aligned, and the defect line develops along this edge.

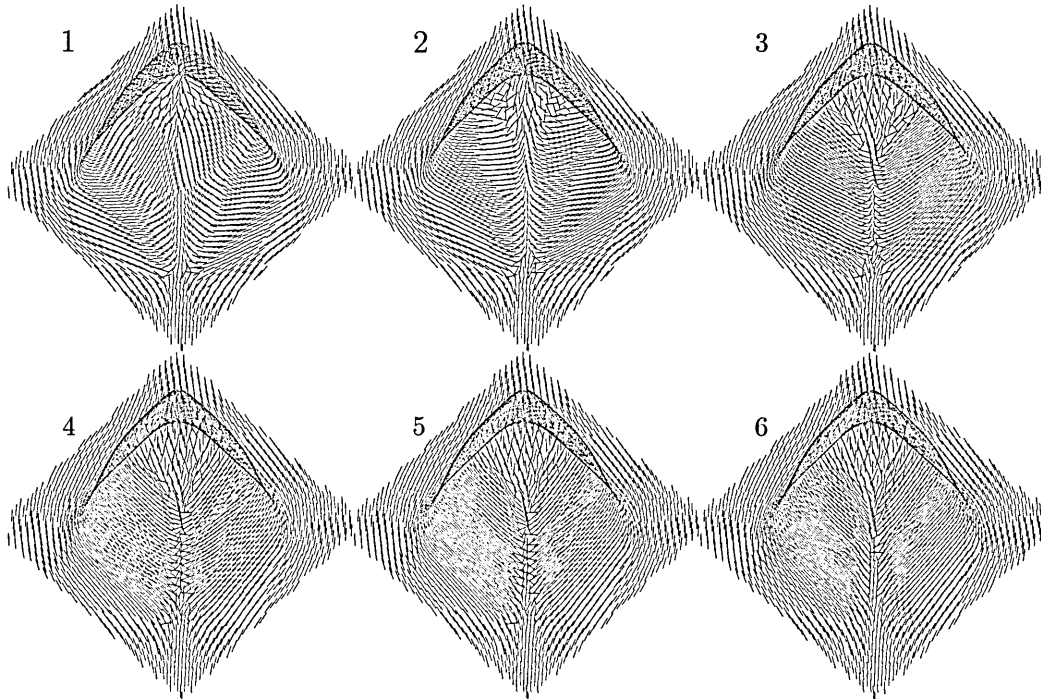


Figure 6.19: Series of snapshots depicting switching between tilted and planar states. Post's surface is shown. In these, $t_1 = 0$ ms, $t_2 = 0.9$ ms, $t_3 = 1.4$ ms, $t_4 = 1.5$ ms, $t_5 = 2.5$ ms, $t_6 = 3.0$ ms

When the electric field is completely removed, the LC in these simulations relaxes into the planar state. It should be noted that the optical switching between these states is very fast, since once the electric field has been applied the bulk LC almost immediately adopts the planar state. The later stages of this switching, i.e. the reorientation of the LC on the post and equilibration of the bulk LC into the planar state, do not lead to significant optical change.

It should finally be noted that we observed the planar \mathcal{P}_1 state as the final outcome of this switching. This further supports our finding that this equilibrium state is the one which is observed experimentally in the planar configuration.

6.5.2 $\mathcal{P} - \mathcal{T}$ Transition

In this section we describe our attempts to simulate the $\mathcal{P} - \mathcal{T}$ transition. For this, we have employed the same simulation setup as that described in the previous section. Naturally, we employ an equilibrated \mathcal{P}_1 state as the starting configuration in these simulations. The voltage applied to the top plate in this switching direction was set to -20 V, as compared with the positive applied field used for the switching in the opposite direction.

We additionally introduce flexoelectric terms into the continuum description of the LCs, because these were demonstrated to play an important role in the reverse switching process [18]. For this, we employ the flexoelectric free energy density term given by eq. (2.29). We assume that the bend and the splay flexoelectric terms are equal and we choose $e_{11} = e_{33} = 3S_0/(2e)$, with $e = 10^{-12} \text{ cm}^{-1}$. These values were shown to successfully promote the reverse switching in FEM modelling of the PABN device [18].

However, in all of our attempts to achieve $\mathcal{P} - \mathcal{T}$ switching, the system has equilibrated back into the planar state \mathcal{P}_1 after the removal of the electric field. We have observed the following effects during our attempts to achieve this switching process. First, the bulk LC adopts the planar configuration. This is entirely consistent with what we observe in the early stages of the forward switching process, and gives the configuration depicted in Fig. 6.20.2. This result is expected, since the simulated LC has negative dielectric anisotropy. Next, the LC on the post surface starts to adopt an arrangement consistent with the planar configuration. In this, defect lines on both leading and trailing edges form, similar to the forward switching process. Following this, the director on the leading edge starts to slowly reorient itself so as to point upwards, i.e. into an arrangement more consistent with the tilted state. This behaviour is expected due to the flexoelectric terms present. However, this reorientation is very slow and we have observed that over the 3 ms time period the surface director does not get close to achieving the fully upward arrangement. This is very apparent from the 3 ms configuration shown in Fig. 6.20.3. Consequently, when the external electric field is removed, the system relaxes back into the planar state.

6.6 Conclusions

In this chapter we have described a study of the characteristics and operation of the PABN device which we have performed using our newly developed MSPH solver.

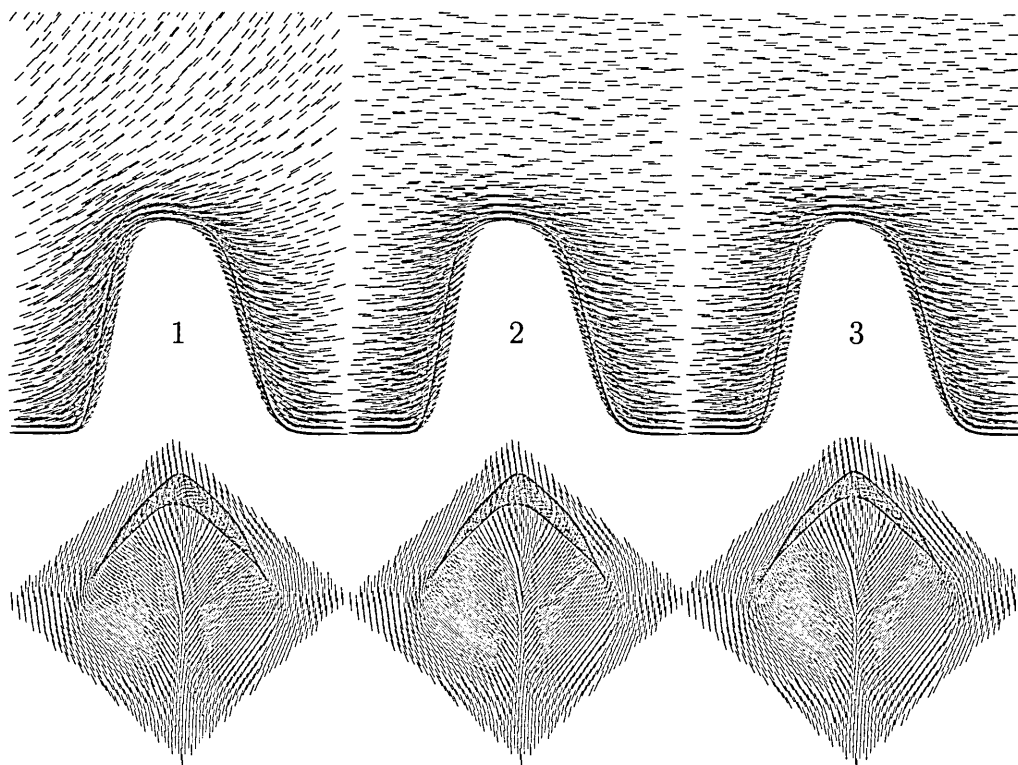


Figure 6.20: Series of snapshots depicting our simulation attempt of switching between planar and tilted states. Top row: Post's cross-section is shown. Bottom row: Post's surface is shown. In these, $t_1 = 0$ ms, $t_2 = 0.9$ ms, $t_3 = 3.0$ ms

First, we have presented a novel smooth geometry model for representing the post in a PABN device. This can be used to represent an arbitrary smooth post geometry without any sharp features. We have then described the attempts we have made to discretise complex smooth geometries. Of these, the GCMC simulation approach has proven to be the most effective technique for domain discretisation.

Next, we have studied the static stable configurations of the LC in the PABN device. In this, we have identified two distinct stable configurations, which are planar and tilted. In contrast with previous simulation results [149], we have identified only one stable planar configuration, the \mathcal{P}_1 state. Next, we have demonstrated that bistability in PABN devices arises due to the arrangement rather than the shape of the posts by considering the effect of using circular-like post. This is concluded because, in this setup, the two stable states identified, were very similar to those obtained using rectangle-like post geometries. We have then studied the effect of post smoothness on the difference between the two states. It was found that the post smoothness plays a minimal role in this. Then, we have undertaken a quantitative study of the effect of the post height on the stable states by comparing their free energies and corresponding director tilt profiles.

Finally, we have studied the switching process in the PABN device. In this, we have been able to achieve the forward $\mathcal{T} - \mathcal{P}$ switching direction, in which the system always equilibrated into the \mathcal{P}_1 state after the external field was removed. The core of this switching was found to be in the reorientation of the LC on the post surface. The reverse switching direction ($\mathcal{P} - \mathcal{T}$), on the other hand, was not achieved, even after the introduction of flexoelectricity. Further exploration of parameter space is needed in respect of this.

Recalling the conclusion drawn at the end of Chapter 5, it is now appropriate to comment on the performance of the MSPH simulation method in the context of this complex device. Here, this technique has proven capable of effectively simulating LC behaviour in 3D systems with complex geometries, including the representation of LC defects. The mesh-free character of this technique allows for easy distribution of nodes in a problem domain, including the variable resolution of nodes in specified regions. These represent practical and computational advantages over rival methods. Another potential advantage, which we have not explored here, is that thermal fluctuations can potentially be incorporated using the SDPD approach of Espanol [65]. However, the MSPH method is a relatively young technique and, thus, it also has some disadvantages as compared to conventional numerical techniques, such as FEM and FDM. From these, the increased computational demand and lower stability can be identified. The former disadvantage is pertinent to all mesh-free methods, whereas the latter one arises due to the strong-form character of the MSPH method. Taking these strengths and weaknesses in the round, therefore, we conclude that MSPH offers a viable alternative to FEM and FDM methods, particularly in simulations involving moving interfaces or defects.

Chapter 7

Conclusions and Further Work

In this Thesis we have described our implementation of a set of simulation techniques for LCs capable of tackling mesoscopic phenomena. We have employed mesh-free particle techniques derived from both bottom-up and top-down approaches. When following the bottom-up approach, we have generalised the DPD/FPM simulation technique, which ultimately allowed us to recover the qualitative behaviour of LCs. When following the top-down route, we have used the SPH technique and its variants, which allowed us to rigorously solve the full set of Qian-Sheng equations. This methodology was consequently applied to simulations of the PABN device operation.

In this chapter we summarise the conclusions drawn from all previous chapters and we also suggest possible directions for further research.

7.1 Conclusions and Discussions

In Chapter 4 we described aspects of our work dedicated to following a bottom-up approach. In this, we initially implemented the DPD simulation technique and one of its extensions – the FPM method, which additionally includes rotational degrees of freedom. Then, we incorporated a \mathbf{Q} -tensor description into the particles and extended the inter-particle forces so as to take \mathbf{Q} -tensors into account. We then demonstrated that the resultant algorithm qualitatively recovers the physics of LCs, including the isotropic-nematic phase transition and proper hydrodynamical behaviour (diffusion coefficient). Subsequently, we demonstrated how the proposed technique can be applied to a challenging task – simulation of colloidal particles immersed in a nematic LC.

Chapter 5 is devoted to a description of our efforts in following top-down approach. Specifically, we have used the SPH simulation techniques and its variants to solve a full set of Qian-Sheng equations. In this, we have first rewritten the Qian-

Sheng equations in the Lagrangian frame of reference so that they became suitable for mesh-free simulations. We have then described our attempts to simulate the governing equations with the original SPH technique, the CSPM method and with both of these techniques along with some of their improvements. These attempts have proved fruitless. We then have finally advanced with the MSPH simulation technique. We have also described the way we have solved for externally applied electromagnetic fields. We have provided a number of test cases, both analytical and numerical, in order to thoroughly test the developed mesh-free numerical LC solver. In these, we have tested all the aspects of the numerical solver, ranging from the Landau free energy to fully coupled velocity fields with all elastic constants and with externally applied fields.

Chapter 6 has addressed our study of the PABN device operation. First, a new smooth geometry representation has been presented. Then, we have described the implementation of a discretisation technique exploiting the GCMC simulation approach. Next, we have studied the static configurations of the PABN device. Specifically, we have been able to identify two stable states, tilted and planar. For the planar state, though, we have found only one stable configuration, namely \mathcal{P}_1 , whereas the previous works have identified three distinct planar configurations [149]. This has been explained by the smooth geometry used, which avoids sharp surface features. We have demonstrated that bistability in the PABN device arises for topological reasons by simulating circular-like post in a PABN device geometry. We have then studied the effect of post smoothness on the difference between the two stable states. From this, we have concluded that post smoothness has a very little effect in this matter. We have also studied the effect of post height on static configurations and have compared free energies between two states. Finally, we have studied the switching process between two states. Tilted-planar direction switching has been easily achieved, with the system moving into the \mathcal{P}_1 stable state. This is consistent with the fact that \mathcal{P}_1 is the more easily observable state in practice. We have not been able to achieve planar-tilted switching – this issue requires further consideration.

The work presented in this Thesis has largely been directed by the objectives which were set at the beginning of this project and which are listed in §1.1. Thus, as a result of this work the following broader conclusions can be drawn. When trying to bridge the gap between atomistic and mesoscopic time- and length-scales, the most promising technique is the DPD method. This allows one to readily simulate mesoscopic phenomena which are not achievable by any other simulation techniques, in terms of both simplicity and simulation time required. The disadvantages of

this technique are linked directly to its advantages, with the lack of quantitative rigour being the most serious. When following top-down approaches, mesh-free particle techniques have been found to offer a promising route. When applied to the solution of continuum problems, these numerical techniques are already capable of producing solutions for problems involving complex geometries in 3D. This has been demonstrated using simulations of the PABN device. However, it should be noted that these techniques are not yet as well developed as competitor methods such as FEM and FDM. Generally, they are less effective in terms of computational cost, but they gain for being able to use a range of node resolutions in a single simulation.

7.2 Further Work

The work presented in this Thesis has increased our understanding of mesoscopic simulation techniques and of their capabilities in relation to the simulation of nematic LCs. From there, the following three separate directions for further research can be identified:

- Bottom-up approach. We applied DPD/FPM modelling techniques to LC simulation and showed that this is a very viable and promising direction. Thus, it would be interesting to further extend our description so as to additionally include three elastic constants and anisotropic viscosities. The high efficiency of this approach suggests that it might be appropriate for more in-depth investigation of the dynamical behaviour of colloidal particles in LCs, including forces between these arising due to the LC medium and their self-assembly. This is an area which has been inaccessible to simulations.
- Top-down approach. We have found out that the SPH simulation technique is not capable of simulating complex governing equations due to its low consistency. On the other hand, positive smooth functions are required for mesh-free LC modelling so that the node points represent physically valid particles. Thus, a first step in this direction might be to use a mixed scheme for solving the governing LCs equations. This might involve using the SPH technique for solving the velocity field equation, along with other more stable mesh-free technique used for solving Q -tensor equations. The second step in this would be to introduce thermal noise into the velocity field, so as to achieve a proper mesoscopic description.
- Simulation of the PABN device operation. We have just started to study the PABN device operation using the MSPH method. The straightforward

further work in this direction would be to study the flexoelectricity effects in the PABN switching process between two stable states. If this can be achieved, and the reverse switching process simulated, then our technique will be directly applicable to device design issues relevant to the PABN and related devices.

Appendix A

Moving Least Squares Shape Functions

In this work we employ a framework of collocation mesh-free methods in which the moving least-square reproducing kernel (MLSRK) method [98, 157] is used to construct shape functions for the numerical solution of Maxwell's equations of electromagnetism. The basic idea of the collocation approach is to seek the solution of a partial differential equation on a set of independent points in space by constructing an interpolation function constructed using the values at those points.

According to the MLSRK [157] method, the approximation of a smooth field variable $f(\mathbf{x})$ (e.g., the \mathbf{Q} -tensor) at some point in space $\bar{\mathbf{x}}$ can be given as

$$f^h(\mathbf{x}, \bar{\mathbf{x}}) = \sum_{i=1}^m p_i \left(\frac{\bar{\mathbf{x}} - \mathbf{x}}{\rho} \right) a_i(\bar{\mathbf{x}}, \rho) = \mathbf{p}^T \left(\frac{\bar{\mathbf{x}} - \mathbf{x}}{\rho} \right) \mathbf{a}(\bar{\mathbf{x}}, \rho), \quad (\text{A.1})$$

where ρ is a dilatation parameter, $\mathbf{p}^T(\mathbf{x}) = \{p_1(\mathbf{x}), p_2(\mathbf{x}), \dots, p_m(\mathbf{x})\}$ is a vector of complete basis functions of order m and $\mathbf{a}^T(\bar{\mathbf{x}}, \rho) = \{a_1(\bar{\mathbf{x}}, \rho), a_2(\bar{\mathbf{x}}, \rho), \dots, a_m(\bar{\mathbf{x}}, \rho)\}$ is a vector of unknown coefficients that depends on $\bar{\mathbf{x}}$. For example, for 3-D problems

$$\mathbf{p}^T(\mathbf{x}) = \{1, x, y, z\} \text{ for } m = 4. \quad (\text{A.2})$$

These basis functions should not necessarily be polynomials, but could, alternatively, include functions which are anticipated to be present in the final solution.

The unknown coefficient vector $\mathbf{a}^T(\bar{\mathbf{x}}, \rho)$ is determined by minimising the weighted squared difference with a window function $W(\bar{\mathbf{x}} - \mathbf{x}, \rho)$, i.e.

$$J(\mathbf{a}) = \sum_{i=1}^n W(\bar{\mathbf{x}} - \mathbf{x}_i, \rho) \left[\mathbf{p}^T \left(\frac{\bar{\mathbf{x}} - \mathbf{x}_i}{\rho} \right) \mathbf{a}(\bar{\mathbf{x}}) - f_i \right]^2, \quad (\text{A.3})$$

where f_i is the value of function f at the point i and n is the number of nodes in the support domain of $\bar{\mathbf{x}}$. We use the B-spline function discussed in §5.3.4 as a window function in our simulations. The minimisation of eq. (A.3), $\partial J/\partial \mathbf{a} = 0$, leads to the following set of linear equations

$$\mathbf{M}(\bar{\mathbf{x}})\mathbf{a}(\bar{\mathbf{x}}) = \mathbf{B}(\bar{\mathbf{x}}). \quad (\text{A.4})$$

Here, $\mathbf{M}(\bar{\mathbf{x}})$ is called the moment matrix and is defined as

$$\mathbf{M}(\bar{\mathbf{x}}) = \sum_{i=1}^n W(\bar{\mathbf{x}} - \mathbf{x}_i, \rho) \mathbf{p} \left(\frac{\bar{\mathbf{x}} - \mathbf{x}_i}{\rho} \right) \mathbf{p}^T \left(\frac{\bar{\mathbf{x}} - \mathbf{x}_i}{\rho} \right). \quad (\text{A.5})$$

The matrix $\mathbf{B}(\bar{\mathbf{x}})$ in eq. (A.4) is a $m \times n$ matrix and it has the following form:

$$\mathbf{B}(\bar{\mathbf{x}}) = [W_1 \mathbf{p}_1, \quad W_2 \mathbf{p}_2, \quad \dots, \quad W_n \mathbf{p}_n], \quad (\text{A.6})$$

where $W_i = W(\bar{\mathbf{x}} - \mathbf{x}_i, \rho)$ and $\mathbf{p}_i = \mathbf{p} \left(\frac{\bar{\mathbf{x}} - \mathbf{x}_i}{\rho} \right)$.

We solve eq. (A.4) for $\mathbf{a}(\bar{\mathbf{x}})$ using the LU-factorisation method, the final solution of which can be written in the following form

$$\mathbf{a}(\bar{\mathbf{x}}) = \mathbf{M}^{-1}(\bar{\mathbf{x}})\mathbf{B}(\bar{\mathbf{x}}). \quad (\text{A.7})$$

In this, the condition number of the matrix \mathbf{M} can be used to control the quality of nodal distribution.

Having found optimal values for the coefficients \mathbf{a} , we then directly find the vector of the MLSRK shape functions:

$$\Phi^T(\bar{\mathbf{x}}) = \mathbf{p}^T \left(\frac{\bar{\mathbf{x}} - \mathbf{x}}{\rho} \right) \mathbf{a}(\bar{\mathbf{x}}) = \mathbf{p}^T \left(\frac{\bar{\mathbf{x}} - \mathbf{x}}{\rho} \right) (\mathbf{M}^{-1}(\bar{\mathbf{x}})\mathbf{B}(\bar{\mathbf{x}})). \quad (\text{A.8})$$

These shape functions ultimately lead to the following form of function interpolation:

$$f^h(\bar{\mathbf{x}}) = \sum_{j=1}^n \Phi_j(\bar{\mathbf{x}}) f_j = \Phi^T(\bar{\mathbf{x}}) \mathbf{F}_s, \quad (\text{A.9})$$

where $\mathbf{F}_s = \{f_1, f_2, \dots, f_n\}$ is the vector which collects the function values of all points in the support domain.

Next, we obtain the partial derivatives of the shape functions following the route described in [158]. For this, we introduce a γ matrix which is found from the

following equation:

$$\boldsymbol{\gamma}^T = \mathbf{p}^T \mathbf{M}^{-1}. \quad (\text{A.10})$$

The partial derivatives of $\boldsymbol{\gamma}$ are then obtained by solving the following equations:

$$\mathbf{M}\boldsymbol{\gamma}_{,i} = \mathbf{p}_{,i} - \mathbf{M}_{,i}\boldsymbol{\gamma} \quad (\text{A.11})$$

and

$$\mathbf{M}\boldsymbol{\gamma}_{,ij} = \mathbf{p}_{,ij} - (\mathbf{M}_{,i}\boldsymbol{\gamma}_{,j} + \mathbf{M}_{,j}\boldsymbol{\gamma}_{,i} + \mathbf{M}_{,ij}\boldsymbol{\gamma}). \quad (\text{A.12})$$

In these, comma denotes a partial derivative with respect to the indicated cartesian coordinate.

Finally, partial derivatives of the MLSRK shape functions are found from the following expressions:

$$\boldsymbol{\Phi}_{,i}^T = \boldsymbol{\gamma}_{,i}^T \mathbf{B} + \boldsymbol{\gamma}^T \mathbf{B}_{,i} \quad (\text{A.13})$$

and

$$\boldsymbol{\Phi}_{,ij}^T = \boldsymbol{\gamma}_{,ij}^T \mathbf{B} + \boldsymbol{\gamma}_{,i}^T \mathbf{B}_{,j} + \boldsymbol{\gamma}_{,j}^T \mathbf{B}_{,i} + \boldsymbol{\gamma}^T \mathbf{B}_{,ij}. \quad (\text{A.14})$$

Bibliography

- [1] P. G. De Gennes and J. Prost. *The Physics of Liquid Crystals*. Clarendon press, Oxford, 2nd edition, 1993.
- [2] P. J. Collings and M. Hird. *Introduction to Liquid Crystals*. Taylor & Francis, 1997.
- [3] P. R. Kishore, N. V. S. Rao, P. B. K. Sarma, T. F. S. Raj, M. N. Avadhanlu, and C. R. K. Murty. Field and frequency effects in a nematic mixture of negative and positive dielectric anisotropy. *Molecular Crystals and Liquid Crystals*, 45(3-4):231–241, 1978.
- [4] F. C. Frank. On the theory of liquid crystals. *Discussions of the Faraday Society*, 25:19–28, 1958.
- [5] C. M. Care and D. J. Cleaver. Computer simulation of liquid crystals. *Reports on Progress in Physics*, 68(11):2665–2700, 2005.
- [6] P. J. Hoogerbrugge and J. M. V. A. Koelman. Simulating microscopic hydrodynamic phenomena with dissipative particle dynamics. *Europhysics Letters*, 19(3):155–160, 1992.
- [7] J. M. V. A. Koelman and P. J. Hoogerbrugge. Dynamic simulations of hard-sphere suspensions under steady shear. *Europhysics Letters*, 21(3):363–368, 1993.
- [8] S. Succi. *The Lattice Boltzmann Equation for Fluid Dynamics and Beyond*. Oxford University Press, Oxford, 2001.
- [9] L. B. Lucy. Numerical approach to testing of fission hypothesis. *Astronomical Journal*, 82(12):1013–1024, 1977.
- [10] R. A. Gingold and J. J. Monaghan. Smoothed particle hydrodynamics - theory and application to non-spherical stars. *Monthly Notices of the Royal Astronomical Society*, 181(2):375–389, 1977.

- [11] T. J. Spencer and C. M. Care. Lattice Boltzmann scheme for modeling liquid-crystal dynamics: Zenithal bistable device in the presence of defect motion. *Physical Review E*, 74(6):061708, 2006.
- [12] C. M. Care, I. Halliday, and K. Good. Lattice Boltzmann nemato-dynamics. *Journal of Physics-Condensed Matter*, 12(43):L665–L671, 2000.
- [13] C. Denniston, E. Orlandini, and J. M. Yeomans. Simulations of liquid crystal hydrodynamics in the isotropic and nematic phases. *Europhysics Letters*, 52(4):481–487, 2000.
- [14] T. Z. Qian and P. Sheng. Generalized hydrodynamic equations for nematic liquid crystals. *Physical Review E*, 58(6):7475–7485, 1998.
- [15] A. N. Beris and B. J. Edwards. *Thermodynamics of Flowing Systems with Internal Microstructure*. Oxford University Press, Oxford, 1994.
- [16] A. M. Sonnet, P. L. Maffettone, and E. G. Virga. Continuum theory for nematic liquid crystals with tensorial order. *Journal of Non-Newtonian Fluid Mechanics*, 119(1-3):51–59, 2004.
- [17] R. Pecher, S. Elston, and P. Raynes. Meshfree solution of Q-tensor equations of nematostatics using the MLPG method. *Cmes-Computer Modeling in Engineering & Sciences*, 13(2):91–101, 2006.
- [18] E. Willman, F. A. Fernandez, R. James, and S. E. Day. Switching dynamics of a post-aligned bistable nematic liquid crystal device. *Journal of Display Technology*, 4(3):276–281, 2008.
- [19] M. Schadt and W. Helfrich. Voltage-dependent optical activity of a twisted nematic liquid crystal. *Applied Physics Letters*, 18(4):127, 1971.
- [20] G. D. Boyd, J. Cheng, and P. D. T. Ngo. Liquid-crystal orientational bistability and nematic storage effects. *Applied Physics Letters*, 36(7):556–558, 1980.
- [21] D. W. Berreman and W. R. Heffner. New bistable cholesteric liquid-crystal display. *Applied Physics Letters*, 37(1):109–111, 1980.
- [22] D. K. Yang, J. L. West, L. C. Chien, and J. W. Doane. Control of reflectivity and bistability in displays using cholesteric liquid-crystals. *Journal of Applied Physics*, 76(2):1331–1333, 1994.

- [23] G. P. Bryan-Brown, M. J. Towler, M. S. Bancroft, and D. G. McDonnell. Bistable nematic alignment using bigratings. *SID*, pages 209–212, 1994.
- [24] S. Kitson and A. Geisow. Controllable alignment of nematic liquid crystals around microscopic posts: Stabilization of multiple states. *Applied Physics Letters*, 80(19):3635–3637, 2002.
- [25] G. R. Liu. *Mesh Free Methods: Moving Beyond the Finite Element Method*. CRC Press Inc, 2002.
- [26] G. R. Liu and Y. T. Gu. *An Introduction to Meshfree Methods and Their Programming*. Springer, 2005.
- [27] Li Shaofan and Kam Wing Liu. *Meshfree Particle Methods*. Springer-Verlag Berlin, 2004.
- [28] G. A. Bird. *Molecular gas dynamics*. Oxford, Clarendon Press, 1976.
- [29] G. A. Bird. Recent advances and current challenges for DSMC. *Computers & Mathematics with Applications*, 35(1-2):1–14, 1998.
- [30] F. H. Harlow. The particle-in-cell computing method for fluid dynamics, in methods in computational physics. *Fundamental Methods in Hydrodynamics*, 3, 1964.
- [31] J. S. Chen, C. H. Pan, C. T. Wu, and W. K. Liu. Reproducing kernel particle methods for large deformation analysis of non-linear structures. *Computer Methods in Applied Mechanics and Engineering*, 139(1-4):195–227, 1996.
- [32] T. Belytschko, Y. Krongauz, J. Dolbow, and C. Gerlach. On the completeness of meshfree particle methods. *International Journal for Numerical Methods in Engineering*, 43(5):785–819, 1998.
- [33] L. D. Landau. In collected papers. *Gordon and Breach, New York*, page 193, 1965. (ed. D. Ter Haar).
- [34] E. F. Gramsbergen, L. Longa, and W. H. Dejeu. Landau theory of the nematic isotropic-phase transition. *Physics Reports*, 135(4):195–257, 1986.
- [35] W. Helfrich. The strength of piezoelectricity in liquid crystals. *Z. Naturforsch*, 26A(5):833–835, 1971.
- [36] R. B. Meyer. Piezoelectric effects in liquid crystals. *Physical Review Letters*, 22(18):918–921, 1969.

- [37] A. L. Alexe-Ionescu. Flexoelectric polarization and second order elasticity for nematic liquid crystals. *Physics Letters A*, 180(6):456–460, 1993.
- [38] G. Barbero and L. R. Evangelista. *An elementary course on the continuum theory for nematic liquid crystals*. World Scientific, 2001.
- [39] M. Nobili and G. Durand. Disorientation-induced disordering at a nematic-liquid-crystal solid interface. *Physical Review a*, 46(10):R6174–R6177, 1992.
- [40] M. Rapini and M. Papoular. Distortion d’une lamelle nematique sous champ magnetique, conditions d’ancrage aux parois. *J. de Physique*, 30(C4-54):C4–56, 1969.
- [41] M. A. Osipov and S. Hess. Density-functional approach to the theory of interfacial properties of nematic liquid-crystals. *Journal of Chemical Physics*, 99(5):4181–4190, 1993.
- [42] H. Stark. Physics of colloidal dispersions in nematic liquid crystals. *Physics Reports - Review Section of Physics Letters*, 351(6):387–474, 2001.
- [43] J. L. Ericksen. Anisotropic fluids. *Archive for Rational Mechanics and Analysis*, 4(1):231–237, 1959.
- [44] F. M. Leslie. Some constitutive equations for anisotropic fluids. *The Quarterly Journal of Mechanics & Applied Mathematics*, 19(3):357–370, 1966.
- [45] O. Parodi. Stress tensor for a nematic liquid crystal. *Journal De Physique*, 31(7):581–584, 1970.
- [46] S. R. de Groot and P. Mazur. *Non-Equilibrium Thermodynamics*. Dover Publications, 1984.
- [47] A. M. Sonnet and E. G. Virga. Dynamics of dissipative ordered fluids. *Physical Review E*, 64(3):031705, 2001.
- [48] D. Forster, T. C. Lubensky, P. C. Martin, J. Swift, and P. S. Pershan. Hydrodynamics of liquid crystals. *Physical Review Letters*, 26(17):1016–1019, 1971.
- [49] D. W. Berreman. Liquid-crystal twist cell dynamics with backflow. *Journal of Applied Physics*, 46(9):3746–3751, 1975.
- [50] J. L. Ericksen. Liquid-crystals with variable degree of orientation. *Archive for Rational Mechanics and Analysis*, 113(2):97–120, 1991.

- [51] A. Kilian and S. Hess. Derivation and application of an algorithm for the numerical-calculation of the local orientation of nematic liquid-crystals. *Zeitschrift Fur Naturforschung Section*, 44(8):693–703, 1989.
- [52] P. G. De Gennes. Short range order effects in the isotropic phase of nematics and cholesterics. *Molecular Crystals and Liquid Crystals*, 12(3):193–214, 1971.
- [53] T. C. Lubensky. Molecular description of nematic liquid crystals. *Physical Review A*, 2(6):2497–2514, 1970.
- [54] S. Hess. Irreversible thermodynamics of nonequilibrium alignment phenomena in molecular liquids and in liquid-crystals. 1. Derivation of nonlinear constitutive laws, relaxation of alignment, phase-transition. *Zeitschrift Fur Naturforschung Section*, 30(6-7):728–738, 1975.
- [55] P. D. Olmsted and P. Goldbart. Theory of the nonequilibrium phase-transition for nematic liquid-crystals under shear-flow. *Physical Review A*, 41(8):4578–4581, 1990.
- [56] S. Hess and I. Pardowitz. On the unified theory for nonequilibrium phenomena in the isotropic and nematic phases of a liquid-crystal – spatially inhomogeneous alignment. *Zeitschrift Fur Naturforschung Section*, 36(6):554–558, 1981.
- [57] S. Hess. Transport phenomena in anisotropic fluids and liquid-crystals. *Journal of Non-Equilibrium Thermodynamics*, 11(3-4):175–193, 1986.
- [58] C. P. Borgmeyer and S. Hess. Unified description of the flow alignment and viscosity in the isotropic and nematic phases of liquid crystals. *Journal of Non-Equilibrium Thermodynamics*, 20(4):359–384, 1995.
- [59] S. Hess. Fokker-Planck equation approach to flow alignment in liquid-crystals. *Zeitschrift Fur Naturforschung Section*, 31(9):1034–1037, 1976.
- [60] M. Doi. Molecular-dynamics and rheological properties of concentrated-solutions of rodlike polymers in isotropic and liquid-crystalline phases. *Journal of Polymer Science Part B - Polymer Physics*, 19(2):229–243, 1981.
- [61] M. Grosso, P. L. Maffettone, and F. Dupret. A closure approximation for nematic liquid crystals based on the canonical distribution subspace theory. *Rheologica Acta*, 39(3):301–310, 2000.

- [62] T. Tsuji and A. D. Rey. Effect of long range order on sheared liquid crystalline materials. 1. Compatibility between tumbling behavior and fixed anchoring. *Journal of Non-Newtonian Fluid Mechanics*, 73(1-2):127–152, 1997.
- [63] A. I. Derzhanski and A. G. Petrov. Flexoelectricity in nematic liquid-crystals. *Acta Physica Polonica A*, 55(5):747–767, 1979.
- [64] M. Vilfan, I. D. Olenik, A. Mertelj, and M. Copic. Aging of surface anchoring and surface viscosity of a nematic liquid crystal on photoaligning poly-(vinyl-cinnamate). *Physical Review E*, 63(6):061709, 2001.
- [65] P. Espanol and M. Revenga. Smoothed dissipative particle dynamics. *Physical Review E*, 67(2):026705, 2003.
- [66] A. Malevanets and R. Kapral. Mesoscopic model for solvent dynamics. *Journal of Chemical Physics*, 110(17):8605–8613, 1999.
- [67] T. Ihle and D. M. Kroll. Stochastic rotation dynamics: A galilean-invariant mesoscopic model for fluid flow. *Physical Review E*, 63(2):020201, 2001.
- [68] P. Espanol and P. B. Warren. Statistical-mechanics of dissipative particle dynamics. *Europhysics Letters*, 30(4):191–196, 1995.
- [69] T. Soddemann, B. Dunweg, and K. Kremer. Dissipative particle dynamics: A useful thermostat for equilibrium and nonequilibrium molecular dynamics simulations. *Physical Review E*, 68(4):046702, 2003.
- [70] R. D. Groot and P. B. Warren. Dissipative particle dynamics: Bridging the gap between atomistic and mesoscopic simulation. *Journal of Chemical Physics*, 107(11):4423–4435, 1997.
- [71] C. W. Gardiner. *Handbook of Stochastic Methods for Physics, Chemistry and the Natural Sciences*. Springer-Verlag Berlin, 2nd edition, 1985.
- [72] C. A. Marsh, G. Backx, and M. H. Ernst. Static and dynamic properties of dissipative particle dynamics. *Physical Review E*, 56(2):1676–1691, 1997.
- [73] I. Pagonabarraga and D. Frenkel. Dissipative particle dynamics for interacting systems. *Journal of Chemical Physics*, 115(11):5015–5026, 2001.
- [74] P. Espanol. Hydrodynamics from dissipative particle dynamics. *Physical Review E*, 52(2):1734–1742, 1995.

- [75] A. J. Masters and P. B. Warren. Kinetic theory for dissipative particle dynamics: The importance of collisions. *Europhysics Letters*, 48(1):1–7, 1999.
- [76] G. T. Evans. Dissipative particle dynamics: Transport coefficients. *Journal of Chemical Physics*, 110(3):1338–1342, 1999.
- [77] P. Espanol. Fluid particle model. *Physical Review E*, 57(3):2930–2948, 1998.
- [78] I. Pagonabarraga, M. H. J. Hagen, and D. Frenkel. Self-consistent dissipative particle dynamics algorithm. *Europhysics Letters*, 42(4):377–382, 1998.
- [79] P. Espanol and M. Serrano. Dynamical regimes in the dissipative particle dynamics model. *Physical Review E*, 59(6):6340–6347, 1999.
- [80] X. J. Fan, N. Phan-Thien, S. Chen, X. H. Wu, and T. Y. Ng. Simulating flow of DNA suspension using dissipative particle dynamics. *Physics of Fluids*, 18(6):063102, 2006.
- [81] P. Espanol. Fluid particle dynamics: A synthesis of dissipative particle dynamics and smoothed particle dynamics. *Europhysics Letters*, 39(6):605–610, 1997.
- [82] E. E. Keaveny, I. V. Pivkin, M. Maxey, and G. E. Karniadakis. A comparative study between dissipative particle dynamics and molecular dynamics for simple- and complex-geometry flows. *Journal of Chemical Physics*, 123(10):104107, 2005.
- [83] M. Serrano and P. Espanol. Thermodynamically consistent mesoscopic fluid particle model. *Physical Review E*, 64(4):046115, 2001.
- [84] W. K. Den Otter and J. H. R. Clarke. The temperature in dissipative particle dynamics. *International Journal of Modern Physics C*, 11(6):1179–1193, 2000.
- [85] J. J. Monaghan. Simulating free-surface flows with SPH. *Journal of Computational Physics*, 110(2):399–406, 1994.
- [86] J. W. Swegle and S. W. Attaway. On the feasibility of using smoothed particle hydrodynamics for underwater explosion calculations. *Computational Mechanics*, 17(3):151–168, 1995.
- [87] J. K. Chen, J. E. Beraun, and T. C. Carney. A corrective smoothed particle method for boundary value problems in heat conduction. *International Journal for Numerical Methods in Engineering*, 46(2):231–252, 1999.

- [88] P. W. Randles and L. D. Libersky. Smoothed particle hydrodynamics: Some recent improvements and applications. *Computer Methods in Applied Mechanics and Engineering*, 139(1-4):375–408, 1996.
- [89] G. R. Liu and M. B. Liu. *Smoothed Particle Hydrodynamics: A Meshfree Particle Method*. World Scientific, 2003.
- [90] J. J. Monaghan. Smoothed particle hydrodynamics. *Reports on Progress in Physics*, 68(8):1703–1759, 2005.
- [91] P. W. Cleary and J. J. Monaghan. Conduction modelling using smoothed particle hydrodynamics. *Journal of Computational Physics*, 148(1):227–264, 1999.
- [92] A. Colagrossi. A meshless lagrangian method for free-surface and interface flows with fragmentation. *Universita di Roma, La Sapienza, Italy*, 2004. PhD Thesis.
- [93] J. J. Monaghan and R. A. Gingold. Shock simulation by the particle method SPH. *Journal of Computational Physics*, 52(2):374–389, 1983.
- [94] J. P. Morris, P. J. Fox, and Yi Zhu. Modeling low Reynolds number incompressible flows using SPH. *Journal of Computational Physics*, 136(1):214–26, 1997.
- [95] J. Fang, R. G. Owens, L. Tacher, and A. Parriaux. A numerical study of the SPH method for simulating transient viscoelastic free surface flows. *Journal of Non-Newtonian Fluid Mechanics*, 139(1):68–84, 2006.
- [96] M. B. Liu, G. R. Liu, and K. Y. Lam. Constructing smoothing functions in smoothed particle hydrodynamics with applications. *Journal of Computational and Applied Mathematics*, 155(2):263–284, 2003.
- [97] M. B. Liu and G. R. Liu. Restoring particle consistency in smoothed particle hydrodynamics. *Applied Numerical Mathematics*, 56(1):19–36, 2006.
- [98] T. Belytschko, Y. Krongauz, D. Organ, M. Fleming, and P. Krysl. Meshless methods: An overview and recent developments. *Computer Methods in Applied Mechanics and Engineering*, 139(1-4):3–47, 1996.
- [99] J. W. Swegle, D. L. Hicks, and S. W. Attaway. Smoothed particle hydrodynamics stability analysis. *Journal of Computational Physics*, 116(1):123–134, 1995.

- [100] J. P. Morris. A study of the stability properties of smooth particle hydrodynamics. *Publications Astronomical Society of Australia*, 13(1):97–102, 1996.
- [101] C. T. Dyka and R. P. Ingel. An approach for tension instability in smoothed particle hydrodynamics (SPH). *Computers & Structures*, 57(4):573–580, 1995.
- [102] C. T. Dyka, P. W. Randles, and R. P. Ingel. Stress points for tension instability in SPH. *International Journal for Numerical Methods in Engineering*, 40(13):2325–2341, 1997.
- [103] T. Belytschko, Y. Guo, W. K. Liu, and S. P. Xiao. A unified stability analysis of meshless particle methods. *International Journal for Numerical Methods in Engineering*, 48(9):1359–1400, 2000.
- [104] W. K. Liu, S. Jun, and Y. F. Zhang. Reproducing kernel particle methods. *International Journal for Numerical Methods in Fluids*, 20(8-9):1081–1106, 1995.
- [105] G. A. Dilts. Moving-least-squares-particle hydrodynamics – I. Consistency and stability. *International Journal for Numerical Methods in Engineering*, 44(8):1115–1155, 1999.
- [106] G. A. Dilts. Moving least-squares particle hydrodynamics II: conservation and boundaries. *International Journal for Numerical Methods in Engineering*, 48(10):1503–1524, 2000.
- [107] P. M. Campbell. Some new algorithms for boundary value problems in smoothed particle hydrodynamics. *DNA Report DNA-TR-88-286*, 1989.
- [108] H. Takeda, S. M. Miyama, and M. Sekiya. Numerical-simulation of viscous-flow by smoothed particle hydrodynamics. *Progress of Theoretical Physics*, 92(5):939–960, 1994.
- [109] G. J. Phillips and J. J. Monaghan. A numerical-method for 3-dimensional simulations of collapsing, isothermal, magnetic gas clouds. *Monthly Notices of the Royal Astronomical Society*, 216(4):883–895, 1985.
- [110] J. J. Monaghan. SPH without a tensile instability. *Journal of Computational Physics*, 159(2):290–311, 2000.
- [111] J. P. Gray, J. J. Monaghan, and R. P. Swift. SPH elastic dynamics. *Computer Methods in Applied Mechanics and Engineering*, 190(49-50):6641–6662, 2001.

- [112] J. J. Monaghan. On the problem of penetration in particle methods. *Journal of Computational Physics*, 82(1):1–15, 1989.
- [113] J. K. Chen, J. E. Beraun, and T. C. Carney. A corrective smoothed particle method for boundary value problems in heat conduction. *International Journal for Numerical Methods in Engineering*, 46(2):231–252, 1999.
- [114] G. M. Zhang and R. C. Batra. Modified smoothed particle hydrodynamics method and its application to transient problems. *Computational Mechanics*, 34(2):137–146, JUL 2004.
- [115] M. Grmela and H. C. Ottinger. Dynamics and thermodynamics of complex fluids. I. Development of a general formalism. *Physical Review E*, 56(6):6620–6632, 1997.
- [116] H. C. Ottinger. Relativistic and nonrelativistic description of fluids with anisotropic heat conduction. *Physica A - Statistical Mechanics and its Applications*, 254(3-4):433–450, 1998.
- [117] K. Nanbu. Direct simulation scheme derived from the Boltzmann-equation. 3. Rough sphere gases. *Journal of the Physical Society of Japan*, 49(5):2055–2058, 1980.
- [118] A. Malevanets and R. Kapral. Solute molecular dynamics in a mesoscale solvent. *Journal of Chemical Physics*, 112(16):7260–7269, 2000.
- [119] N. S. Martys and R. D. Mountain. Velocity Verlet algorithm for dissipative-particle-dynamics-based models of suspensions. *Physical Review E*, 59(3):3733–3736, 1999.
- [120] M. P. Allen and D. J. Tildesley. *Computer Simulation of Liquids*. Oxford University Press, 1993.
- [121] C. A. Marsh and J. M. Yeomans. Dissipative particle dynamics: The equilibrium for finite time steps. *Europhysics Letters*, 37(8):511–516, 1997.
- [122] G. Besold, I. Vattulainen, M. Karttunen, and J. M. Polson. Towards better integrators for dissipative particle dynamics simulations. *Physical Review E*, 62(6):R7611–R7614, 2000.
- [123] I. Vattulainen, M. Karttunen, G. Besold, and J. M. Polson. Integration schemes for dissipative particle dynamics simulations: From softly interacting

- systems towards hybrid models. *Journal of Chemical Physics*, 116(10):3967–3979, 2002.
- [124] P. Nikunen, M. Karttunen, and I. Vattulainen. How would you integrate the equations of motion in dissipative particle dynamics simulations? *Computer Physics Communications*, 153(3):407–423, 2003.
- [125] T. Shardlow. Splitting for dissipative particle dynamics. *Siam Journal on Scientific Computing*, 24(4):1267–1282, 2003.
- [126] G. De Fabritiis, M. Serrano, P. Espanol, and P. V. Coveney. Efficient numerical integrators for stochastic models. *Physica A-Statistical Mechanics and its Applications*, 361(2):429–440, 2006.
- [127] M. Serrano, G. De Fabritiis, P. Espanol, and P. V. Coveney. A stochastic trotter integration scheme for dissipative particle dynamics. *Mathematics and Computers in Simulation*, 72(2-6):190–194, 2006.
- [128] D. Frenkel and B. Smit. *Understanding Molecular Simulation: From Algorithms to Applications*. Academic Press, 2nd edition, 2002.
- [129] C. P. Lowe. An alternative approach to dissipative particle dynamics. *Europhysics Letters*, 47(2):145–151, 1999.
- [130] D. J. Evans. Representation of orientation space. *Molecular Physics*, 34(2):317–325, 1977.
- [131] H. Goldstein. *Classical mechanics*. Addison-Wesley, Reading, MA, 2nd edition, 1980.
- [132] M. P. Allen. Configurational temperature in membrane simulations using dissipative particle dynamics. *Journal of Physical Chemistry B*, 110(8):3823–3830, 2006.
- [133] J. G. Powles, G. Rickayzen, and D. M. Heyes. Temperatures: old, new and middle aged. *Molecular Physics*, 103(10):1361–1373, 2005.
- [134] J. A. Backer, C. P. Lowe, H. C. J. Hoefsloot, and P. D. Iedema. Poiseuille flow to measure the viscosity of particle model fluids. *Journal of Chemical Physics*, 122(15):154503, 2005.

- [135] I. V. Pivkin and G. E. Karniadakis. A new method to impose no-slip boundary conditions in dissipative particle dynamics. *Journal of Computational Physics*, 207(1):114–128, 2005.
- [136] M. P. Allen. Diffusion-coefficient increases with density in hard ellipsoid liquid-crystals. *Physical Review Letters*, 65(23):2881–2884, 1990.
- [137] E. S. Boek, P. V. Coveney, H. N. W. Lekkerkerker, and P. van der Schoot. Simulating the rheology of dense colloidal suspensions using dissipative particle dynamics. *Physical Review E*, 55(3):3124–3133, 1997.
- [138] Akira Satoh and Roy W. Chantrell. Application of the dissipative particle dynamics method to magnetic colloidal dispersions. *Molecular Physics*, 104(20-21):3287–3302, 2006.
- [139] D. Andrienko, G. Germano, and M. P. Allen. Computer simulation of topological defects around a colloidal particle or droplet dispersed in a nematic host. *Physical Review E*, 63(4):041701, 2001.
- [140] J. V. Franz. *Computational Physics: An Introduction*. Springer; 2nd edition, 2001.
- [141] J. J. Monaghan and J. C. Lattanzio. A refined particle method for astrophysical problems. *Astronomy and Astrophysics*, 149(1):135–143, 1985.
- [142] G. M. Zhang and R. C. Batra. Wave propagation in functionally graded materials by modified smoothed particle hydrodynamics (MSPH) method. *Journal of Computational Physics*, 222(1):374–390, 2007.
- [143] W. G. Hoover, C. G. Hoover, and E. C. Merritt. Smooth-particle applied mechanics: Conservation of angular momentum with tensile stability and velocity averaging. *Physical Review E*, 69(1):016702, 2004.
- [144] S. Balay, K. Buschelman, W. D. Gropp, D. Kaushik, M. G. Knepley, L. C. McInnes, B. F. Smith, and H. Zhang. PETSc Web page, 2001. <http://www.mcs.anl.gov/petsc>.
- [145] Iain W. Stewart. *The Static and Dynamic Continuum Theory of Liquid Crystals: A Mathematical Introduction*. Taylor & Francis Ltd, 2003.
- [146] H. J. Deuling. Deformation of nematic liquid-crystals in an electric-field. *Molecular Crystals and Liquid Crystals*, 19(2):123–131, 1972.

- [147] S. A. Jewell and J. R. Sambles. Dynamic response of a dual-frequency chiral hybrid aligned nematic liquid-crystal cell. *Physical Review E*, 73(1):011706, 2006.
- [148] S. A. Jewell and J. R. Sambles. Measurement of azimuthal backflow in a dual-frequency chiral HAN cell. *Molecular Crystals and Liquid Crystals*, 477:551–559, 2007.
- [149] A. Majumdar, C. J. P. Newton, J. M. Robbins, and M. Zyskin. Topology and bistability in liquid crystal devices. *Physical Review E*, 75(5):051703, 2007.
- [150] S. C. Kitson and A. D. Geisow. Bistable alignment of nematic liquid crystals around microscopic posts. *Molecular Crystals and Liquid Crystals*, 412(1):153–161, 2004.
- [151] S. C. Kitson, E. G. Edwards, and A. D. Geisow. Designing liquid crystal alignment surfaces. *Applied Physics Letters*, 92(7):073503, 2008.
- [152] C. J. P. Newton and T. P. Spiller. *Proceedings of the International Displays Research Conference (SID)*, page 13, 1997.
- [153] C. Geuzaine and J. F. Remacle. Gmsh: a three-dimensional finite element mesh generator with built-in pre- and post-processing facilities, 2009. <http://www.geuz.org/gmsh/>.
- [154] B. Nayroles, G. Touzot, P. Villon, and A. Ricard. Diffuse approximation and Diffuse Elements. *New Advances in Computational Structural Mechanics*, 32:143–157, 1992.
- [155] H. Z. Zhang and A. V. Smirnov. Node placement for triangular mesh generation by Monte Carlo simulation. *International Journal for Numerical Methods in Engineering*, 64(7):973–989, 2005.
- [156] R. W. Hockney and J. W. Eastwood. *Computer Simulation Using Particles*. McGraw-Hill Education, 1981.
- [157] W. K. Liu, S. F. Li, and T. Belytschko. Moving least-square reproducing kernel methods. 1. Methodology and convergence. *Computer Methods in Applied Mechanics and Engineering*, 143(1-2):113–154, 1997.
- [158] T. Belytschko, Y. Krongauz, M. Fleming, D. Organ, and W. K. S. Liu. Smoothing and accelerated computations in the element free Galerkin method. *Journal of Computational and Applied Mathematics*, 74(1-2):111–126, 1996.